Advances in Reverse Electrodialysis for Renewable Energy Generation

Catarina Simões

ADVANCES IN REVERSE ELECTRODIALYSIS FOR RENEWABLE ENERGY GENERATION

Catarina Cerqueira da Silva Simões

ADVANCES IN REVERSE ELECTRODIALYSIS FOR RENEWABLE ENERGY GENERATION

DISSERTATION

to obtain
the degree of doctor at the Universiteit Twente,
on the authority of the rector magnificus,
prof. dr. ir. A. Veldkamp,
on account of the decision of the Doctorate Board
to be publicly defended
on Friday 10 March 2023 at 14.45 hours

by

Catarina Cerqueira da Silva Simões

born on the 28th of April, 1995
in Almada, Portugal

This dissertation has been approved by:

Supervisor

prof. dr. ir. D.W.F. Brilman

Co-supervisor

dr. M. Saakes

Cover design:	C. Simões, A. Simões, G. Doornbusch & Ipskamp
Printed by:	Ipskamp Printing
Lay-out:	Catarina Simões
ISBN (print):	978-90-365-978-90-365-5518-0
ISBN (digital):	978-90-365-5519-7
URL:	https://doi.org/10.3990/1.9789036555197

Graduation Committee:

Chair / secretary:	prof.dr. J.L. Herek
Supervisor:	prof.dr.ir. D.W.F. Brilman Universiteit Twente, TNW, Sustainable Process Technology
Co-supervisor:	dr. M. Saakes Wetsus, European Centre of Excellence for Sustainable Water Technology
Committee Members:	prof.dr.ir. R.G.H. Lammertink Universiteit Twente, TNW, Soft matter, Fluidics and Interfaces
	prof.dr. G. Mul Universiteit Twente, TNW, Photocatalytic Synthesis
	prof. dr. ir. H.V.M. Hamelers Wageningen Universiteit
	prof. dr. J.G. Crespo Universidade Nova de Lisboa

"Try and leave this world a little better than you found it"

Robert Baden-Powell

Contents

Summary

Salinity gradient energy (SGE) is the energy released from the mixing of two solutions with different salinity, such as seawater and river water. SGE is a renewable and sustainable energy source that integrates the hydrological cycle, having an important role in the transition to renewable and clean energies without CO_2 emissions. Reverse electrodialysis (RED) is the electro-membrane process used in this thesis to harvest SGE. In RED, ions migrate through ion exchange membranes (IEMs), selective to either anions or cations, from the seawater compartment to the river water compartment due to a salinity gradient between these solutions. The concentration gradient across the IEMs results in a potential difference over each membrane. The potential difference generated, when connecting an external load to the two electrodes (one at each end of the stack's membrane pile), drives an ionic current through the stack and an electrical current through the external circuit. Usually, the ionic current is converted at the electrodes to an electrical current using a redox couple. This thesis aims to optimize and scale up the RED process for energy generation using seawater and river water.

Chapter 2 demonstrates the implementation of electrode segmentation to strategically optimise the output power density and energy efficiency of RED. Using a validated RED model and investigating experimentally the RED process with a scaled-up cross-flow stack of 0.22 x 0.22 m^2, it was possible to achieve higher performance results with a four-electrode segments stack than with a stack with unsegmented electrodes or single electrodes. The highest overall yield concerning gross power production was obtained by "saving the gradient" in the first two segments for the last two segments (along the river water path). Fixing the same net power density (the maximum value achieved with a single electrode was 0.92 $W{\cdot}m^{-2}$), electrode segmentation increased the energy efficiency relatively by 43 %, from 17 % to 25 %. While realising an overall 40 % energy efficiency, the net power density achieved with electrode segmentation was 39 % higher than measured for a single electrode (0.47 $W{\cdot}m^{-2}$). Electrode segmentation allows the current density to be tuned locally, thereby improving the overall process performance without trade-offs. This can contribute to reducing operating costs, with higher energy efficiencies, or to reducing capital investment, with higher net power densities.

Chapter 3 discusses the potential and flexibility of multistage RED. Hereto the validated model from Chapter 2 is exploited, in combination with an experimental study using two electrically independent cross-flow stacks of 0.22 x 0.22 m^2. These are arranged in series in terms of seawater and river water inflow. The influences of residence time and electrical control were studied experimentally and compared with the model outcome. The model proved to be successful in describing the different flow arrangements and electrical control.

It was found that multistage RED yields a higher gross power density and energy efficiency than a single stage. Depending on the power consumption required for pumping, adding an extra stack in series may or may not increase the net power production. This underlines the need for focus on low-pressure drop stack designs.

The electrode pairs of each stage in the multistage arrangement were tuned individually, like with the segmented electrodes. Applying the "saving the gradient" strategy (i.e., lowering the discharge current value in the first stage by consuming less of the salinity gradient) increased the gross overall performance of the two stages by up to 17 % relative to a single-stage and up to 6 % relative to a sequentially optimized two-stage system. Lastly, different multistage configurations were simulated using the model, which revealed that two stages are sufficient for feeding seawater and river water. With a third stage, the improvements achieved would not offset additional pressure drop losses. Multistage RED configuration is increasingly beneficial for higher residence times and higher salinity gradients, preventing voltage losses and brisk salinity changes.

Chapter 4 shows, for the first time, the multistage RED approach using natural waters at the piloting location at the Afsluitdijk, the Netherlands. Two cross-flow stacks of 0.22 x 0.22 m^2 connected in series, were used, each with a different number of cell pairs, respectively 32 cell pairs for stage 1 and 64 cell pairs for stage 2. The configuration's performance was evaluated for over 30 days. Natural waters introduced new variables to the process, such as the presence of several divalent ions, conductivity fluctuations and (bio-)fouling. The influence of divalent ions is explained in Chapter 1. A distinct behaviour was found for divalent ions in each stage. While in stage 1, Ca^{2+} and SO_4^{2-} were transported from the river to the seawater side (uphill transport), in stage 2, no uphill transport occurred. Mg^{2+}, another divalent ion present, was not transported against the gradient at any stage. The first stage delivered a gross power density of around 0.60 $W \cdot m^{-2}$, and the second stage delivered around 0.25 $W \cdot m^{-2}$. The actual total gross power density achieved at the available salinity gradient was stable at values around 0.35-0.40 $W \cdot m^{-2}$. The total net power density, corrected for the initial pressure drop of the stacks, was 0.25 $W \cdot m^{-2}$ at an energy efficiency of 37 %. Throughout the operation, due to increasing stack pressure drop, the actual total net power density lowered finally to 0.10 $W \cdot m^{-2}$. At the end of the experimental campaign, a stack autopsy revealed the presence of microorganisms with sizes ten times larger than the cartridge filter nominal pore size (5 µm) and biofilm covering part of the spacer open area, both contributing to the increased pressure drop in the stacks. Remarkably, it did not affect the achieved electrical gross power density. Pressure drop monitoring, -minimization and fouling control, is confirmed as a crucial element for the success of the technology.

Chapter 5 focuses on the electrode system by using carbon-based slurries to replace the common, less environmentally friendly, redox solutions typically used as the electrode rinse

solution. Carbon-based slurry electrodes (CSEs) allow a continuous reverse electrodialysis process in a more clean and sustainable way. At the laboratory scale (0.1 x 0.1 m^2), six CSEs made from activated carbon mixed with either carbon black or graphite powder (conductive additives) were characterized both physically and electrochemically and tested in RED operation. The CSEs containing a total of 20 wt% mixture of activated carbon and carbon black showed the best electrical performance, but also the highest viscosities. The use of CSEs made it possible to avoid Faradaic reactions at the anode and cathode and eliminated voltage losses caused by water electrolysis. A continuous test of the best CSE resulted in a stable output for 17 days, using a stack with a single membrane configuration. To show the versatility of CSEs, higher current densities up to 350 $A{\cdot}m^{-2}$ were tested in an electrodialysis setting and were shown to be feasible until current densities of 150 $A{\cdot}m^{-2}$ without abrupt pH changes.

Lastly, Chapter 6 presents an outlook on the potential of reverse electrodialysis as a sustainable renewable energy source. It discusses the process' achievability accounting for what is currently known and draws future developments. Also, the sustainability of RED is reviewed, explaining what will influence the surrounding environment during the lifetime of a RED facility. And the last point discussed is the development agenda for the technology considering IEMs advances, current energy trends, and automatic control in dynamic environments.

Samenvatting

Zoutgradiënt energie (*salinity gradient energy, SGE*) is energie die vrijkomt bij het mixen van zout en zoetwater, zoals bijvoorbeeld zeewater en rivierwater. SGE is een hernieuwbare en duurzame energiebron die geïntegreerd kan worden in de hydrologische cyclus. Daarom kan SGE een belangrijke rol gaan innemen in de energietransitie naar duurzame en schone energiebronnen zonder CO_2 uitstoot. Omgekeerde elektrodialyse (*reverse electrodialysis, RED*) is het membraanproces dat in dit proefschrift gebruikt wordt om SGE te winnen. In RED migreren ionen door ion uitwisselingsmembranen (*ion exchange membranes, IEMs*). Deze membranen zijn selectief voor anionen of kationen. De positief geladen kationen en de negatief geladen anionen migreren vanuit het zeewater compartiment naar het rivierwater compartiment gedreven door de zoutgradiënt tussen deze twee oplossingen. De concentratiegradiënt over de IEMs resulteert in een potentiaalverschil over de membranen. Het potentiaalverschil dat gegenereerd wordt kan, zodra het verbonden wordt met een externe belasting over de elektrodes (aan beide uiteindes van de membraanstapel), omgezet worden van een ionische stroom naar een elektrische stroom door middel van redoxreacties. Het doel van dit proefschrift is het optimaliseren en opschalen van het RED proces voor energiewinning uit zeewater en rivierwater.

In Hoofdstuk 2 is de implementatie van elektrode segmentatie onderzocht om strategisch de stroomdichtheid en energetische efficiëntie van RED te optimaliseren. Gebruikmakend van een gevalideerd RED model en experimentele resultaten van een opgeschaalde kruisstroom stack van 0,22 x 0,22 m^2, was het mogelijk om hogere prestaties te behalen met een vier-electrode gesegmenteerde stack vergelijken dan met een enkele elektrode stack. De hoogste opbrengst is behaald in termen van bruto stroomproductie bij de modus “saving the gradient”, waarbij de eerste twee elektrode segmenten minder belast werden dan de laatste twee elektrode segmenten (gezien in de richting van de rivierwater stroomrichting). Bij dezelfde netto stroomdichtheid (maximumwaarde behaald met een enkele elektrode was 0,92 $W{\cdot}m^{-2}$), steeg de energetische efficiëntie met electrode segmentatie relatief gezien met 43 % namelijk van 17 % naar 25 %. Het doel was om een totale energetische efficiëntie van 40 % te halen. De netto stroomdichtheid behaald met electrode segmentatie was 39% hoger dan gemeten bij een enkele elektrode (0,47 $W{\cdot}m^{-2}$). Met elektrode segmentatie kon de stroomdichtheid lokaal ingesteld worden waardoor de procesprestaties verbeterden zonder compromissen. Dit kan bijdragen aan het verlagen van de operationele kosten, met hogere energetische efficiëntie, of door het reduceren van kapitaalinvesteringen, met hogere netto stroomdichtheden.

In Hoofdstuk 3 is de potentie en flexibiliteit van meertraps RED. Hiervoor is het gevalideerde model dat ook gebruikt is in hoofdstuk 2 verder benut, in combinatie met een experimentele

studie van twee kruisstroom stacks van 0,22 x 0,22 m^2, georiënteerd in serie in termen van de zeewater en de rivierwater stroomrichting. De effecten van verblijftijd en elektrische controle zijn experimenteel onderzocht en vergeleken met het model. Het model bleek succesvol te zijn om verschillende vloeistofstroom mogelijkheden en elektrische controle te beschrijven. Deze studie heeft bewezen dat de meertraps RED een hogere bruto stroomdichtheid en energie efficiëntie heeft dan een enkele stack. Afhankelijk van het stroomverbruik voor pompen, kan het toevoegen van een tweede stack in serie de netto stroomproductie verhogen. Dit bevestigt de noodzaak om een stackontwerp te gebruiken met een lage drukval.

De elektrodeparen van elke stack in meertraps arrangement zijn individueel afgestemd, vergelijkbaar met de gesegmenteerde elektrode stack. Door hetzelfde principe van "saving the gradient" toe te passen verhoogt de totale netto prestatie van de tweetraps RED tot 17 % vergeleken met een enkele trap RED en tot 6 % vergeleken met een opeenvolgend geoptimaliseerd tweetraps systeem. Tenslotte zijn verschillende meertraps configuraties gesimuleerd met het model, waaruit geconcludeerd kan worden dat bij gebruik van zeewater en rivierwater de toepassing van twee trappen het meest efficiënt is. Een derde trap genereert niet voldoende energie om de toegevoegde drukval te compenseren. Meertraps RED is voordelig voor hoge verblijftijden en hoge zoutgradiënten, daarnaast voorkomt het spanningsverliezen en abrupte zoutconcentratie verschillen.

Hoofdstuk 4 demonstreert voor het eerst een meertraps RED benadering gebruikmakend van oppervlaktewater bij de pilotlocatie op de Afsluitdijk in Nederland. Twee kruisstroom stacks van 0,22 x 0,22 m^2 in serie geschakeld, met elk een verschillend aantal celparen, namelijk 32 celparen in de eerste trap en 64 celparen in de tweede trap. Deze configuratie werd onderzocht gedurende 30 dagen. Oppervlaktewater introduceerde nieuwe variabelen in het proces, zoals bijvoorbeeld tweewaardige kationen en anionen, fluctuaties in geleidbaarheid en bio(fouling). Het effect van tweewaardige ionen is uitgelegd in hoofdstuk 1. Een apart gedrag van meerwaardige ionen werd geobserveerd per trap. Terwijl in de eerste trap calciumionen en sulfaationen werden getransporteerd van de rivierwater compartimenten naar de zeewater compartimenten (zogenaamd *uphill transport*), werd er in de tweede trap geen *uphill transport* waargenomen. Magnesium, een ander tweewaardig ion, werd niet getransporteerd in beide RED trappen. De eerste trap leverde een bruto vermogensdichtheid van 0,60 $W \cdot m^{-2}$, en de tweede trap leverde een bruto vermogensdichtheid van 0,25 $W \cdot m^{-2}$. De totale bruto vermogensdichtheid behaald bij de beschikbare zoutgradiënt was stabiel tussen 0,35-0,40 $W \cdot m^{-2}$. De totale netto vermogensdichtheid, gecorrigeerd voor de initiële drukval van de stacks, was 0,25 $W \cdot m^{-2}$ bij een energetische efficiëntie van 37 %. Gedurende de bedrijfsvoering nam, door de opbouw van drukval, de totale netto vermogensdichtheid af tot 0,10 $W \cdot m^{-2}$. Na het experiment werd de stack geopend en de autopsie onthulde een eerste vervuiling namelijk micro-organismen

in afmetingen 10 keer groter dan de nominale poriegrootte (5 µm) van de cartridge. Een tweede vervuiling die werd geconstateerd was een biofilm die een deel van het spaceroppervlak bedekte. Beide vervuilingen hebben bijgedragen aan het toenemen van de drukval in de stacks. Opvallend genoeg heeft dit niet de bruto vermogensdichtheid beïnvloed. Drukvalmonitoring, vermindering en controle op vervuiling zijn noodzakelijke elementen voor het succesvol opereren van de RED technologie.

In Hoofdstuk 5 ligt de focus op koolstof gebaseerde slurries om de meest gebruikte, minder milieuvriendelijke, redox oplossingen te vervangen die typisch gebruikt worden als elektrode spoelvloeistof. Koolstof gebaseerde slurry elektrodes (carbon based slurries, CSEs) kunnen gebruikt worden in een continue RED proces op een schone en duurzame manier. Op laboratoriumschaal (0,1 x 0,1 m^2) werden zes CSEs gemaakt van aktieve koolstof gemengd met roet of grafietpoeder (beide elektrisch geleidende additieven om de elektrische geleidbaarheid van de slurry te verhogen). De slurries werden gekarakteriseerd door zowel de viscositeit, porositeit als het elektrochemisch gedrag te meten onder RED omstandigheden. De CSEs die een 20 gewichtspercentage mengsel van actieve kool en roet bevatten, lieten de beste elektrochemische en elektrische prestaties zien, maar deze mengsels vertoonden ook de hoogte viscositeit. Het gebruik van CSEs maakt het mogelijk om elektrochemische reacties aan de anode of kathode te voorkomen en elimineren spanningsverliezen veroorzaakt door water elektrolyse. Een continue test van de beste CSE resulteerde in een stabiele celspanning gedurende 17 dagen, gebruikmakend van een enkele membraan opstelling. Om de veelzijdigheid van CSEs aan te tonen werden hogere stroomdichtheden getest tot 350 $A{\cdot}m^{-2}$ onder elektrodialyse omstandigheden en lieten daarbij de gewenste stabiliteit zien van de celspanning tot 150 $A{\cdot}m^{-2}$ zonder pH veranderingen.

Afsluitend belicht Hoofdstuk 6 de potentie van RED als een nieuwe duurzame hernieuwbare energiebron. De haalbaarheid van het RED proces wordt besproken op basis van de kennis van nu en bespreekt daarbij toekomstige ontwikkelingen ter verbetering van de technologie. Ook is de duurzaamheid van RED bestudeerd en is uitgelegd wat de invloeden in de directe omgeving van de technologie zijn gedurende de levensduur van een RED faciliteit. Als laatste is de onderzoek agenda besproken voor de technologie met in acht name van de ontwikkelingen in IEMs, energietrends en automatisering van besturing van het RED proces in dynamische omgevingen.

Resumo

A Energia de Gradiente Salino (*Salinity Gradient Energy*, SGE) é a energia libertada pela mistura de águas com diferentes salinidades, como por exemplo, a água do mar (salgada) e a água do rio (doce). SGE é uma fonte de enegia renovável que integra o ciclo hidrológico, tendo um papel importante na transição para energias renováveis e limpas sem emissão de CO2. A Electrodiálise Inversa (*Reverse Electrodialysis*, RED) é o processo electromembranar usado nesta dissertação para extrair a SGE. Em RED, os iões migram através das membranas de permuta iónica (*Ion Exchange Membranes*, IEMs), selectivas a aniões ou catiões, que se movem do compartimento de água salgada para o compartimento de água doce devido ao gradiente salino entre estas soluções. O gradiente de concentração através das IEMs resulta numa diferença de potencial em cada membrana. Quando uma carga externa é conectada aos dois elétrodos (um em cada extremidade da stack), a diferença de potencial gerada conduz uma corrente iónica através da stack e uma corrente eléctrica através do circuito externo. Geralmente, a corrente iónica é convertida nos elétrodos em corrente elétrica recorrendo a um par de oxirredução. A presente tese visa a otimização e aumento de escala do processo de RED para geração de energia a partir da mistura de água do mar com água do rio.

O Capítulo 2 demonstra a implementação da segmentação do elétrodo para estrategicamente otimizar a densidade de potência e a eficiência energética de RED. Utilizando um modelo validado de RED e investigando experimentalmente com uma stack de fluxo cruzado (0,22 x 0,22 m^2), foi possível alcançar altas performances com uma stack com quatro segmentos de elétrodo comparando com uma stack com um único elétrodo. O rendimento mais elevado com respeito à densidade de potência bruta foi obtido através da estratégia de "salvar o gradiente" nos primeiros dois segmentos para utilizar nos dois seguintes (na direção da água do rio). Para a mesma densidade de potência líquida (com o valor máximo obtido para um único elétrodo de 0,92 $W{\cdot}m^{-2}$), a segmentação aumentou a eficiência energética relativamente em 43 %, de 17 % para 25 %. Enquanto visando para 40 % de eficiência energética, a densidade de potência líquida alcançada com a segmentação foi 39 % mais elevada que a eficiência medida para um único elétrodo (0,47 $W{\cdot}m^{-2}$). A segmentação do elétrodo permite que a densidade de corrente seja afinada localmente, melhorando a performance do processo sem trocas. Isto contribuiu para reduzir os custos de operação, com eficiências energéticas mais altas, ou para reduzir os capitais de investimento, com densidades de potência líquidas mais altas.

O Capítulo 3 discute o potencial e a flexibilidade de RED em estágios. Aqui o modelo validado do capítulo anterior é explorado e combinado com um estudo experimental com duas stacks de fluxo cruzado (0,22 x 0,22 m^2), conectadas em série. As influências do tempo

de residência e do tipo de controlo elétrico foram estudadas experimentalmente e comparadas com os resultados do modelo. O modelo mostrou-se bem-sucedido a descrever os diferentes arranjos de alimentação das águas e tipos de controlo elétrico. Ao utilizar dois estágios em RED fornece-se mais densidade de potência bruta e eficiência energética que um só estágio. Dependendo da potência necessária para as bombas, adicionar uma stack extra em série poderá ou não aumentar a produção da densidade de potência líquida. Evidencia-se, assim, a necessidade de apostar em designs da célula que diminuíam as perdas de potência para as bombas.

Os elétrodos de cada estágio foram afinados individualmente, como na segmentação. Aplicando a estratégia de "salvar o gradiente" (nomeadamente, baixando o valor da corrente de descarga no primeiro estágio consumindo menos gradiente de salinidade e deixando para o segundo estágio) a performance do sistema bruta aumentou até 17 % relativamente ao um único estágio e até 6 % relativamente a dois estágios sequencialmente otimizados. Por último, diferentes configurações dos estágios foram simuladas recorrendo ao modelo que revelaram que alimentar água do mar e do rio em dois estágios é suficiente, enquanto num terceiro estágio os benefícios em bruto não seriam suficientes para contrabalançar as perdas de potência nas bombas. Os benefícios da RED em estágios aumentam para tempos de residência longos e gradientes de salinidade maiores, prevenindo perdas de voltagem e mudanças de salinidade súbitas.

O Capítulo 4 mostra, pela primeira vez, RED em estágios utilizando águas naturais na estação piloto no Afsluitdijk, nos Países Baixos. A performance de duas stacks em fluxo cruzado (0,22 x 0,22 m^2) conectadas em série, com um número diferente de pares de membranas, 32 pares para o primeiro estágio e 64 pares para o segundo estágio, foi avaliada por mais de 30 dias. A alimentação com águas naturais introduziu novas variáveis no processo, tais como a presença de iões multivalentes, flutuação da condutividade e deposição de matéria indesejada nas membranas e compartimentos (fouling). A influência dos iões multivalentes no processo é explicada no capítulo 1. Um comportamento distinto foi descoberto para os iões multivalentes em cada estágio. Enquanto no primeiro estágio, Ca^{2+} e SO_4^{2-} foram transportados do rio para o lado do mar (*uphill transport*), no segundo estágio, não ocorreu *uphill transport*. Mg^{2+}, outro ião divalente presente, não foi transportado contra o gradiente em nenhum estágio. O primeiro estágio produziu cerca de 0,60 $W \cdot m^{-2}$ de densidade de potência bruta e o segundo estágio produziu cerca de 0,25 $W \cdot m^{-2}$. A densidade de potência bruta total atingida com o gradiente de salinidade disponível foi estável entre valores de 0,35 – 0,40 $W \cdot m^{-2}$. A densidade de potência líquida total, corrigida para a perda de pressão inicial das bombas, foi de 0,25 $W \cdot m^{-2}$ com 37 % eficiência energética. Durante a operação, devido ao acréscimo da pressão nas stacks, a densidade de potência líquida total diminuiu para 0,10 $W \cdot m^{-2}$. No final da campanha experimental, a autópsia à célula revelou a presença de microrganismos com tamanhos dez vezes maiores que o filtro de cartucho com

poro nominal de 5 µm e biofilme cobrindo parte da área aberta do espaçador. Ambos contribuindo para o aumento da pressão das stacks e consequente aumento das perdas de potência nas bombas. Notavelmente, isto não afetou a densidade de potência bruta. Monitorização e minimização da pressão das stacks e controlo do fouling foram confirmados como elementos cruciais para o sucesso da tecnologia.

O Capítulo 5 foca-se no sistema do elétrodo utilizando pastas à base de carvão para substituir as reações comuns de oxirredução, tipicamente usadas como solução para enxaguar o elétrodo, mas menos amigas do ambiente. Elétrodos baseados em pastas de carvão (*carbon-based slurry electrodes*, CSEs) permitem um processo RED contínuo de maneira mais limpa e sustentável. À escala de laboratório (0,1 x 0,1 m^2), seis CSEs compostos por carvão ativado (*activated carbon*) misturado com ou carvão preto (*carbon black*) ou grafite em pó (*graphite powder*), dois aditivos condutivos, foram caracterizados física- e electroquimicamente e testados operando o sistema de RED. Os CSEs que continham misturas de carvão ativado e carvão preto (20 wt%) resultaram nas mais elevadas performances elétricas, mas também nas mais elevadas viscosidades. Usando CSEs foi possível evitar reações secundárias no ânodo e cátodo e eliminar perdas de voltagem causadas pela reação de eletrólise da água. O melhor CSE foi testado continuamente por 17 dias com resultados estáveis, numa configuração de uma membrana. Para demonstrar a versatilidade dos CSEs, correntes mais elevadas (até 350 $A \cdot m^{-2}$) foram testadas para eletrodiálise e provou-se exequível até correntes de 150 $A \cdot m^{-2}$ sem mudanças abruptas de pH.

Finalmente, o Capítulo 6 apresenta o panorama sobre o potencial de eletrodiálise inversa como uma fonte sustentável e renovável de energia. É discutido o alcance do processo tendo em conta o conhecimento gerado e propõe-se futuros desenvolvimentos. Além do mais, a sustentabilidade de RED é revista, explicando que mudanças irão influenciar o ambiente circundante durante o tempo de vida de uma instalação RED. O último ponto discutido é a agenda de desenvolvimento para a tecnologia, considerando os avanços em IEMs, tendências energéticas atuais e controlo automático em ambientes dinâmicos.

Chapter 1

Introduction

1.1. Renewable energy generation

The International Panel on Climate Change stated, *"Human influence has warmed the climate at a rate that is unprecedented in at least the last 2000 years"* [1]. Climate change is a growing concern of the 21st century. One major cause for it is the combustion of fossil fuels to meet the global energy demand. The combustion of fossil fuels greatly increases the emission of greenhouse gases (GHG) in the atmosphere which consequently increases the Earth's temperature, in particular the emission of CO_2 [2]. Future scenarios predict the need not only to reduce GHG emissions but also to use technologies that have neutral or negative GHG emissions [3]. Given that energy became essential to humankind, the transition to renewable energy sources is the most prompting solution to decrease fossil fuel combustion and consequently reduce fossil GHG emissions.

The transition to renewable energies is accelerated by political agreements, such as the Paris Agreement, where countries pledge to take action to stay well under the 2°C temperature increase until 2100 [4]. Currently, renewable energy sources only generate 13 % of the global energy demand. Most of the renewable energy produced originates from hydropower (54 %). Hydroelectric dams must be built in specific places with significant height differences. In the most suitable locations, they have already been implemented. Therefore, in recent years, hydropower capacity has barely increased. Hydropower is followed by wind and solar energy, with a share of 24 % and 13 %, respectively. From 2010 to 2021, the growth of both technologies was steep with 437 % and 2945 % more energy generation, for wind and solar respectively [5]. The fact that these are intermittent energy sources is a serious drawback. They either depend on wind or the sun, resulting in major fluctuations in electrical energy production. The options to balance the electrical energy produced and the energetic demand rely on large-scale energy storage systems [6].

Energy from water is a renewable energy source that has multiple ways to be harvested. In the oceans, rivers and seas, there is a lot of energy potential to be utilized. Besides previously introduced hydropower, other technologies such as tidal, wave and salinity gradient energy (SGE) are considered suitable renewable energy sources. They also offer the option for a continuous supply and additionally have a low environmental impact. SGE is one of these emerging renewable energy options to complement the energy demand of modern society [7]. In SGE, energy is released from mixing water streams with different salinity while increasing the entropy, i.e., when the river meets the sea. This thesis focuses on improving harvesting SGE.

1.2. Salinity gradient energy

SGE is a renewable energy source that integrates the hydrological cycle, as schematized in Figure 1.1. Applying SGE allows a continuous power output, by using, for example, a river that continuously flows to the sea. The integration in the hydrological cycle ensures the sustainability of SGE, without CO_2, SO_2 or NO_x-related (GHG) emissions during operation [8].

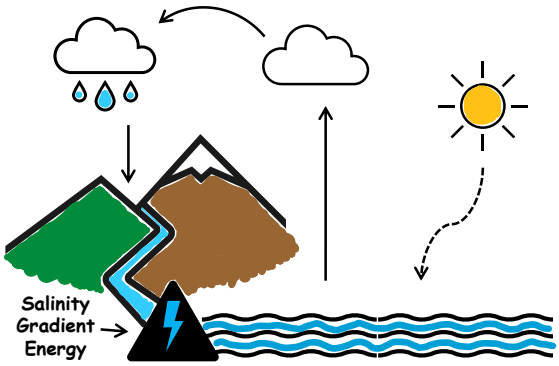

Figure 1.1 Simplified schematic of the hydrological cycle. Salinity gradient energy is a renewable source, integrated into the natural water cycle.

A remarkable amount of energy is available from mixing waters with different salinity. The theoretical potential was estimated at 1.72 TW, and the technical potential was at 0.98 TW, looking into only rivers discharging into the sea [8]. This technical potential is equivalent to 8617 TWh/year, which corresponds to 32.7 % of the global en"ergy demand in 2021 [9]. Another potential salinity gradient source, besides the hydrological cycle, is the use of industrial salt brines and closed-loop systems [10,11]. This is not accounted for in the estimation above, increasing the total technical potential. The theoretically available energy (Gibbs free energy of mixing) is equal to the variation of the Gibbs free energy as a result of the mixing process, and it is calculated according to equation 1.1:

$$\Delta G_{mix} = G_B - (G_{RW} + G_{SW}) \quad \text{(Eq. 1.1)}$$

Where G is the Gibbs free energy (J) and the subscripts, B is the brackish solution resulting from mixing, RW is the river water, and SW is the seawater [12]. The Gibbs free energy can be calculated as:

$$G = \Delta H - T \cdot \Delta S = -T \cdot (S_B - S_{RW} - S_{SW}) \quad \text{(Eq. 1.2)}$$

$$S = -R \cdot n_T \cdot \sum_i x_i \ln(x_i \cdot \gamma_i) \quad \text{(Eq. 1.3)}$$

Where S is the entropy (J·K^{-1}), T is the temperature (K), R is the universal gas constant (J·mol·K^{-1}), n_T is the total number of moles (mol), x_i is the fraction of component i (-) and γ_i is the molar activity coefficient of the component i (-), which accounts for non-ideal solutions. The change in enthalpy ΔH (J) is assumed negligible compared to the change in entropy, or equal to zero (in the case of ideal solutions).

Different processes can capture SGE by using a "controlled mixing" device. The most known SGE capturing processes are pressure retarded osmosis (PRO), capacitive mixing (CAPMIX) and reverse electrodialysis (RED). In PRO, the driving force is the osmotic pressure difference across a semipermeable membrane [13]. In CAPMIX, the driving force is the adsorption and desorption of ions in capacitive layers [14]. And, in RED, the driving force is the salinity gradient that creates a potential difference across ion exchange membranes [15]. CAPMIX works in charge-discharge cycles since the feedwater needs to be switched periodically, making it less attractive than the other two processes. Between PRO and RED, Post et al. investigated and compared the applicability of each. It was concluded that RED shows more potential for the concentration gradient existing between seawater and river water since higher power density and energy efficiency are retrieved [16]. In this thesis, RED is the investigated process, using the salinity gradient between seawater and river water.

1.3. Reverse electrodialysis

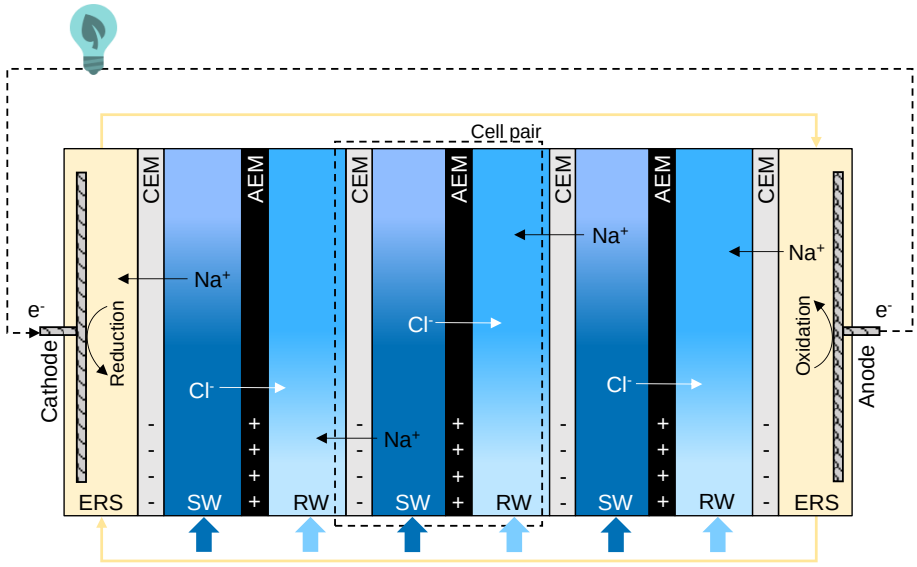

Figure 1.2 Schematic of the reverse electrodialysis process. An alternate pile of CEMs and AEMs is used with seawater and river water being alternately fed through the compartments. At each end of the pile, an electrode rinse solution is used to convert the ionic current into an electrical current.

RED is an electro-membrane process that uses a RED stack to capture energy (illustrated in Figure 1.2). The concept was introduced in 1954 by Pattle [7]. Since then, the technology has been brought to a pilot scale with four pilot plants worldwide (The Netherlands, Italy, Japan, and South Korea) [17–20].

The stack comprises ion exchange membranes (IEMs), specifically anion exchange membranes (AEMs) and cation exchange membranes (CEMs) piled alternately. Between the membranes, fresh and saltwater also flow alternately through the compartments. The compartments can be made using spacers or by profiling the membranes [21,22]. One AEM, one CEM, one salty and one freshwater compartment form a cell pair. A RED stack can comprise hundreds to thousands of cell pairs. The ions present will be transported from the concentrated to the diluted solution, according to their charge and membrane selectivity. Anions will cross the AEMs while cations will cross the CEMs.

Due to the difference in concentration between the compartments, a potential difference arises over each membrane. This leads to an accumulated potential difference across the membrane pile. For enclosing the membrane pile, an extra shielding membrane and two electrode compartments are needed, one at each end, where the ionic current is converted into electrical current using electrodes and a redox couple [23].

1.4. Challenges and opportunities in reverse electrodialysis

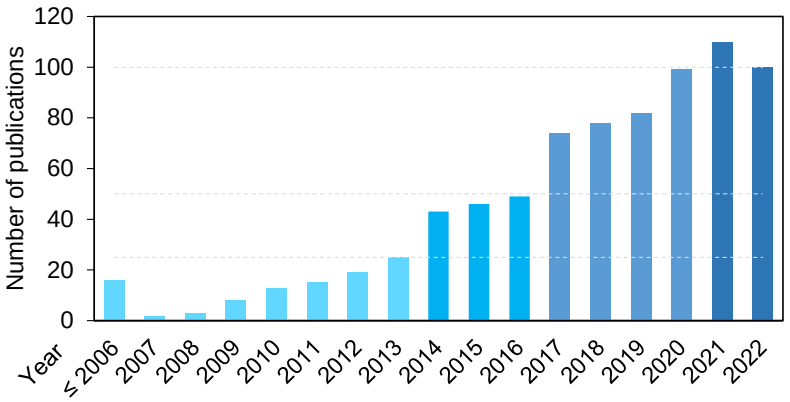

Figure 1.3 Number of reverse electrodialysis publications through the years. Source: Scopus (November 2022)

Figure 1.3 shows the growing interest in RED, particularly in recent years, by displaying the number of scientific publications associated with the keyword "reverse electrodialysis". Given the high number of publications recently, one might ask "What are the challenges in RED?"

1.4.1. Reverse electrodialysis power density and energy efficiency

The theoretical value of the potential difference generated across an ion exchange membrane pair by the salinity gradient can be calculated using the modified Nernst equation:

$$E_{IEM} = \alpha_{IEM} \cdot \frac{RT}{zF} \cdot \ln\left(\frac{c_{SW} \cdot \gamma_{SW}}{c_{RW} \cdot \gamma_{RW}}\right) \quad \text{(Eq. 1.4)}$$

Where α_{IEM} is the IEM permselectivity (-), R is the gas constant (J.mol^{-1}.K^{-1}), T is the absolute temperature (K), z is the ion valency (-), F is the Faraday constant (C.mol^{-1}), c is the solution concentration (mol·L^{-1}) and γ is the molar activity coefficient (-). To calculate the voltage of the membrane pile at zero current, the overall electromotive force (EMF, V) is the sum of individual membrane voltages:

$$EMF = N \cdot (E_{AEM} + E_{CEM}) \quad \text{(Eq. 1.5)}$$

Where N is the number of cell pairs in a stack (-). The value of EMF can also be measured experimentally and is named open circuit voltage (OCV), which might differ slightly from the theoretical value [12]. The internal stack resistance (R_i, Ω), is defined as:

$$R_i = R_{elect} + N \cdot (R_{AEM} + R_{CEM} + R_{SW} + R_{RW}) \quad \text{(Eq. 1.6)}$$

Where, R_{elect} is the electrode compartment resistance, including the extra shielding membrane (Ω), R_{AEM} and R_{CEM} are the membranes' resistances (Ω) and R_{SW} and R_{RW} are the water compartment resistances (Ω). The stack gross power (P_{gross}, W) is given as the current times the terminal voltage in equation 1.7.

$$P_{gross} = I \cdot U \quad \text{(Eq. 1.7)}$$

Where I is the current (A) and U is the terminal voltage (V). The electrical current I can be deduced from the electrical circuit from the EMF, internal stack resistance R_i and external load resistance R_{load} (equation 1.8). The terminal voltage is a function of the EMF, the current and the stack's internal resistance (equation 1.9).

$$I = \frac{EMF}{R_i + R_{load}} \quad \text{(Eq. 1.8)}$$

$$U = EMF - I \cdot R_i \quad \text{(Eq. 1.9)}$$

Therefore, the power produced by the stack depends on the value of the EMF and the internal stack resistance. By using Ohm's law and equations 1.8 and 1.9, equation 1.7 becomes:

$$P_{gross} = I^2 \cdot R_{load} = \left(\frac{EMF}{R_i + R_{load}}\right)^2 \cdot R_{load} \quad \text{(Eq. 1.10)}$$

Assuming no dependency on the location in the stack, the maximum power (P_{max}, W) is achieved when the terminal voltage is equal to half of the EMF and if the resistances are equal ($R_i = R_{load}$), and equation 1.10 becomes:

$$P_{max,gross} = \frac{(EMF)^2}{4 \cdot R_i} \quad \text{(Eq. 1.11)}$$

Figure 1.4 shows the typical curves that are obtained when applying several current density steps. The current density is defined as the current per electrode area (A·m^{-2} electrode). The I-V curve in Figure 1.4A shows that in OCV conditions, the current is zero and the stack has a maximum voltage (EMF). With increasing discharge current, the stack voltage reduces, and the slope obtained from the I-V curve is the stack's internal resistance (R_i). At higher current densities, larger voltage drops occur across the feedwater compartments and the IEMs give a lowered stack voltage. At the short circuit current condition, the stack voltage reaches zero volt, and no power is produced. Figure 1.4B shows the calculated power density versus the current density curve. The maximum power is obtained at P_{max}, which corresponds to a stack voltage half of EMF, and is displayed as EMF/2 in Figure 1.4A.

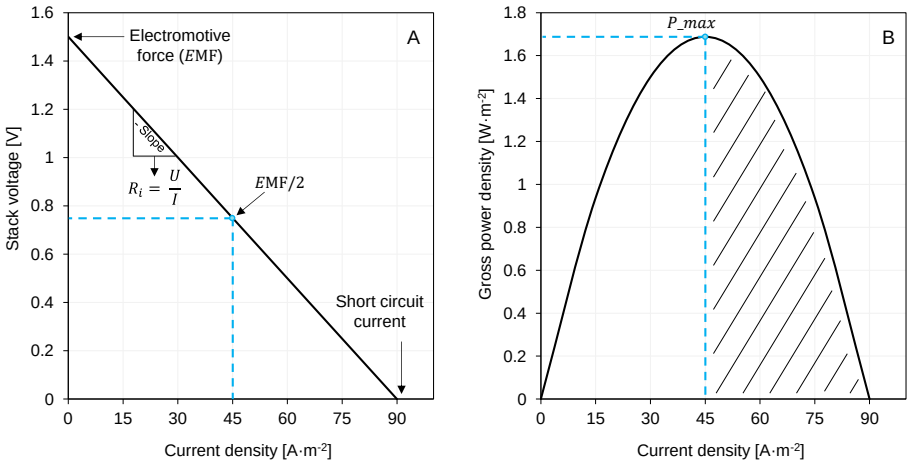

Figure 1.4 Example of a typical current-voltage (I-V) curve measured with a RED stack (A) and the corresponding power density versus current density curve response (B). Feeding 0.5 and 0.017 M NaCl solutions. R_i = 0.0356 Ω and R_{elect} = 0 Ω. Cross-flow stack with 0.22 x 0.22 m^2 dimension, flow velocity of 1 cm·s^{-1}, 155 µm net-woven spacer and Type 10 Fujifilm AEM and CEM.

From equation 1.11, to achieve maximum power, half of the EMF is dissipated on the external load. Thus, only 50 % efficiency is achievable at maximum power (equation 1.12) [24].

$$Eff = \frac{I^2 \cdot R_u}{I^2 \cdot R_i + I^2 \cdot R_u} = 0.5 \qquad \text{(Eq. 1.12)}$$

In practice, some internal resistance components (R_{AEM}, R_{CEM}, R_{RW} *and* R_{SW}) will change throughout the stack length due to the change in concentration. Therefore, the system is more complex than initially described. Consequently, RED systems will not be limited to achieving 50 % efficiency at maximum power. It will also depend on operating conditions, such as flow velocity [25]. The energy efficiency (η_{energy}, %) is calculated as the gross power produced (P_{gross}, W) over the Gibbs free energy (equation 1.1) per second (ΔG_{in}, W):

$$\eta_{energy} = \frac{P_{gross}}{\Delta G_{in}} \qquad \text{(Eq. 1.13)}$$

To understand the limits of mixing, Figure 1.5 shows the theoretical Gibbs free energy calculated from mixing 1 L of 0.513 M NaCl and 1 L of 0.017 M NaCl (assumed as reference concentrations for seawater and river water, 30 and 1 g NaCl·L^{-1}) with the change in concentration and electromotive force caused by further mixing. The change in concentration and the Gibbs free energy are not proportional. In Figure 1.5, when 25 % mixing has occurred, meaning the salinity concentration difference is reduced by 25 % (ΔC = 0.372 M), already 50 % of the available energy is used. And when 50 % mixing has occurred (ΔC = 0.248 M), 80 % of the available energy is used. Therefore, if half of the energy is dissipated at the stack and mixing halfway already released 80 % of the available energy, the process will reach 40 % efficiency at maximum power conditions. For a continuous RED process operating at maximum power, aiming for 40 % energy efficiency is a realistic target.

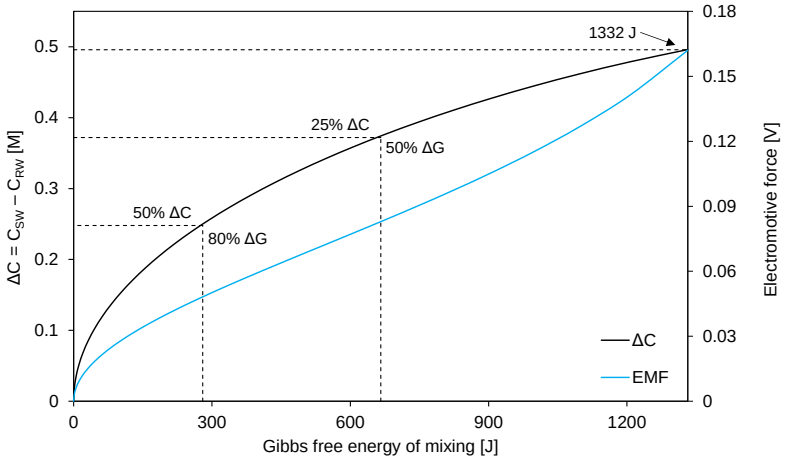

Figure 1.5 Theoretical Gibbs free energy of mixing compared to the change in concentration (starting concentrations: 0.513 M NaCl and 0.017 M NaCl) and electromotive force available from the salinity gradient through one cell pair. Calculations were made for mixing 1 L of each solution and assuming equal mixing.

From equation 1.13, it is concluded that the energy efficiency will increase with increasing gross power. However, other parameters can influence both energy efficiency and gross power in opposite ways. For example, using higher flow rates will reduce the concentration polarization at the membranes and the change in concentration along the stack will be smaller [26]. This contributes to lower voltage losses and results in increased power. However, when increasing the flow rate also ΔG_{in} increases substantially resulting in lower energy efficiency. The other way around, with lower flow rates, concentration polarization increases, as well as the co-ion and water transport. This results in less power obtained. At the same time, more of ΔG_{in} as provided is harvested and the energy efficiency is therefore increased.

Since the IEMs are a big fraction of the RED capital of investment, the power is usually defined as power density (Pd_{gross}, W·m^{-2}). The gross power (P_{gross}, W) is divided by the total active (ion exchange) membrane area installed (A_{mem}, m^2).

$$Pd_{gross} = \frac{P_{gross}}{A_{mem}} \qquad \text{(Eq. 1.14)}$$

The active membrane area is defined as the total area of installed AEMs and CEMs of all cell pairs (not accounting for the extra shielding membrane).

Since the feedwaters are pumped into the system, this pumping power needs to be accounted for, as a loss, reducing the gross electrical power generated by the stack. The pumping power loss (P_{pump}, W) is calculated by multiplying the pressure drop across the seawater and river water compartments by the flow rate of the seawater and river water, respectively:

$$P_{pump} = \varphi_{RW}\Delta P_{RW} + \varphi_{SW}\Delta P_{SW} \qquad \text{(Eq. 1.15)}$$

Where φ is the flow rate of the feedwater (m^3·s^{-1}) and ΔP is the pressure drop across the seawater or river water compartment (Pa). The net power (P_{net}, W) is now obtained by subtracting the pumping power losses from the gross power:

$$P_{net} = P_{gross} - P_{pump} \qquad \text{(Eq. 1.16)}$$

From the previous discussion, it is concluded that to increase the gross power density and energy efficiencies obtained with RED new operating strategies are needed. In this thesis, electrode segmentation and multistage operation are studied for their potential to optimize the RED system by having either more than one electrode in one stack (Figure 1.6A) or by combining the operation in multiple stacks (Figure 1.6B). This results in an efficient electrical control that harnesses the salinity gradient further.

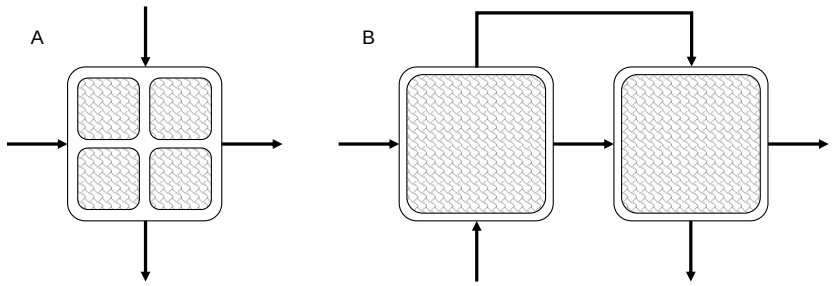

Figure 1.6 Schematic representation of electrode segmentation (A) and multistage RED (B).

1.4.2. Reverse electrodialysis with natural waters

To upscale reverse electrodialysis, testing in natural conditions is an important step in the development of the technology. While at the laboratory all conditions are precisely controlled, in natural conditions many challenges arise [18–20,27–30]. Natural feedwaters contain, besides Na^+ and Cl^- ions, multivalent ions like Mg^{2+}, Ca^{2+}, SO_4^{2-}, and foulants, such as natural organic matter, inorganic particulates and microorganisms, which contribute negatively to the obtained power density [31]. Experiments with natural waters showing the occurrence and (relative) importance of these phenomena are, however, scarce.

Multivalent ions can reduce the stack voltage, increase the IEMs' electrical resistance, and decrease the IEMs' permselectivity [15,32]. Figure 1.7 schematizes how the multivalent ions influence the process (only done with Mg^{2+} and SO_4^{2-} representing multivalent ions). Due to their higher valency, the voltage generated by multivalent ions is lower than for monovalent ions (half the voltage in the case of divalent ions, assuming similar activity coefficients and membrane permselectivity, see equation 1.4).

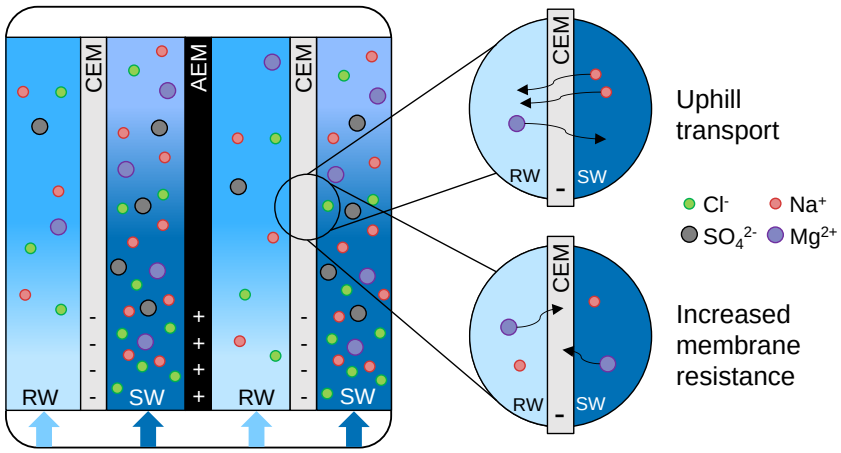

Figure 1.7 Schematic of the influence of divalent ions, present in natural waters, in RED.

Multivalent ions present in natural waters may also affect the ion transport through the IEMs. The reason is that multivalent ions are not only exchanged through the IEM due to the salinity gradient but also migrate from low to high concentration (from river water to seawater) to obtain a chemical equilibrium potential at both sides of the IEM [33]. This phenomenon is named uphill transport [34]. For example, two Na^+ ions can exchange through a CEM from the seawater to the river water with one Mg^{2+} ion that migrates from the river water to the seawater, to achieve chemical equilibrium. In this exchange, no net charge is transported.

IEMs are characterized by their charged functional groups. CEMs contain negatively charged groups (e.g., sulphonate group $-SO_3^-$) and AEMs contain positively charged groups (e.g., quaternary ammonium group $-NR_3+$). Consequently, e.g., for the CEM, the higher valency of multivalent cations increases the membrane's electrical resistance and can lead to multivalent cation trapping. This may permanently affect the CEM [31]. Studies often do not show the fate of multivalent ions in upscaled RED stacks using natural waters.

In addition to the interactions of the multivalent cations and anions with the cation and anion exchange membranes respectively, also fouling can affect the IEMs' performance. For example, humic acids, often present in freshwater, are negatively charged and can bind to the AEMs [35]. More importantly, fouling has a negative impact on RED as it can accumulate on the spacers used to maintain the distance between the membranes. This leads to an increase in pressure drop across the compartments, which increases pumping power losses, reduces net power production (equation 1.16) and can eventually clog the water compartments. Overcoming fouling requires feed water pre-treatment or in-situ cleaning at the stack, but, at the same time, cleaning must be done with the lowest energy consumption possible.

1.4.3. Towards redox free reverse electrodialysis

Typically the conversion of the ionic current into an electric current in RED is done utilizing dimensionally stable electrodes (for example Ti/Pt; Ti/Pt-Ir; Ti/Ru-Ir) at the end compartments in combination with an electrode rinse solution, like redox couples (e.g., Fe^{2+}/Fe^{3+} or hexacyanoferrate $[Fe(CN)_6]^{3-}/[Fe(CN)_6]^{4-}$ mixed with 0.25 M NaCl or anthraquinone or by using seawater electrolysis) [23].

On one hand, these redox couples have a fast charge transfer rate (except seawater electrolysis) enabling the electrode system resistance to be negligible compared to the membrane pile resistance [36]. On the other hand, their sustainability, stability and economic viability are debatable for large-scale applications. The Fe^{2+}/Fe^{3+} couple is only stable at pH values below 2 [37], requiring that shielding membranes, positioned at the ends of the membrane pile, must be resistant to acidic environments. Furthermore, continuous pH

monitoring combined with acid dosing is necessary to avoid the precipitation of iron compounds around the cathode. The hexacyanoferrate couple decomposes in the presence of sunlight and oxygen partially releasing cyanide ions that can harm the environment [38]. In case of leakage, CN^-, $Fe(CN)_6^{3-}$ and, $Fe(CN)_6^{4-}$ can strongly bind with the AEMs thus reducing their performance [23,39]. Recently, this couple was also found to be unstable in scaled-up RED stacks in the presence of Mg^{2+} and Ca^{2+} causing scaling [28]. In the case of water electrolysis, or electrolysis using NaCl solutions (or seawater), gas evolution occurs with gaseous chlorine gas (Cl_2) that evolves at the anode and hydrogen (H_2) gas at the cathode. Chlorine gas is corrosive while hydrogen gas increases the risk of explosion and must be removed from the system. Furthermore, gas bubbles at the electrode compartments will increase the electrical resistance leading to higher ohmic voltage losses [40]. And the formation of chlorine requires the use of expensive fluorinated end membranes like PFSA (perfluorinated sulphonic acid) type membranes.

Ideally, the redox couple is replaced by an eco-friendlier alternative, having similar or better performance. Vermaas et al. proposed a cleaner RED process using fixed capacitive carbon paste, coated in Pt-coated Ti-mesh electrodes (CRED) [41]. The charge transfer mechanism is no longer based on redox reactions, but instead, is based on Na^+ and Cl^- ions being adsorbed onto the active carbon electrodes' surface area because of the electrostatic field of the electrical double layer [42]. However, once the carbon has become saturated with ions, it is necessary to reverse the polarity of the electrodes to trigger ion desorption by switching the river water and seawater. Thus, the process is not continuous, and it is mandatory to frequently switch feedwaters. To avoid this switching, Fei et al. studied the use of flow electrodes for RED (FE-RED) [43], where an active carbon-based slurry electrode flowed through the electrode compartment chambers. Once these slurries are mixed, the charges are neutralized. These carbon-based slurry systems have clear advantages. However, rather low power densities were achieved. Thus, carbon-based slurry electrodes need further investigation and development, before such systems are viable for application at large-scale RED facilities.

1.5. Thesis Aim and Outline

The research presented in this thesis originates from the need to optimize and scale-up the reverse electrodialysis process for energy generation. Harvesting salinity gradient energy using reverse electrodialysis allows for a continuous renewable energy supply which does not compete with other energy sources but complements them and reduces the need for energy storage systems. This research aims to understand how electrode segmentation and multistage operation, using scaled-up stacks with artificial and natural seawater and river water can improve the obtained power density and energy efficiency. Another aim is to evaluate carbon-based slurries' performance to replace the redox solution at the electrodes.

Chapter 2 reports on the use of segmented electrodes in a scaled-up RED stack. The experimental study with pure NaCl solutions was done by dividing a single electrode into four equal segments and was complemented with modelling of the power output. For the first time, the beneficial effect of segmented electrodes on power density and energy efficiency was shown, for a cross-flow stack, as well as how to improve the overall maximum power, by "saving the salinity gradient" as the leading principle.

Chapter 3 focuses on a multistage approach with pure NaCl solutions using two scaled-up cross-flow stacks in series for enhancing the energy efficiency without trading off the power density. Experimental tests and modelling analyses were performed for various flow rates and configurations to optimize the multistage configuration and to understand when the multistage approach is most beneficial for RED. The gross power density and energy efficiency are improved. However, the increase of pressure drop due to adding a second stage decreased the net power density compared to a single stage.

Chapter 4 investigates the multistage approach with scaled-up cross-flow stacks feeding natural waters by testing a two-stage configuration in series at the Afsluitdijk, The Netherlands. Testing was performed continuously by feeding natural waters for over a month. In this study the fate of multivalent ions in a multistage configuration was unveiled for the first time as well as fouling consequences for the configuration were discovered. Gross electrical power production was found to be independent of fouling.

Chapter 5 pursues a more sustainable RED process by replacing the redox solution with carbon-based slurry electrodes. Carbon-based slurry electrodes provide a stable and safe use and remove hazards such as gas evolution or harmful liquids for aquatic life. The slurry electrodes tested appeared successful at the laboratory scale.

Lastly, Chapter 6, gives an outlook on RED, discussing the process achievability and future improvements. It also reviews the sustainability of RED in the surrounding environment and the development agenda for the technology.

Figure 1.8 provides a visual representation of the thesis outline, connecting the different chapters.

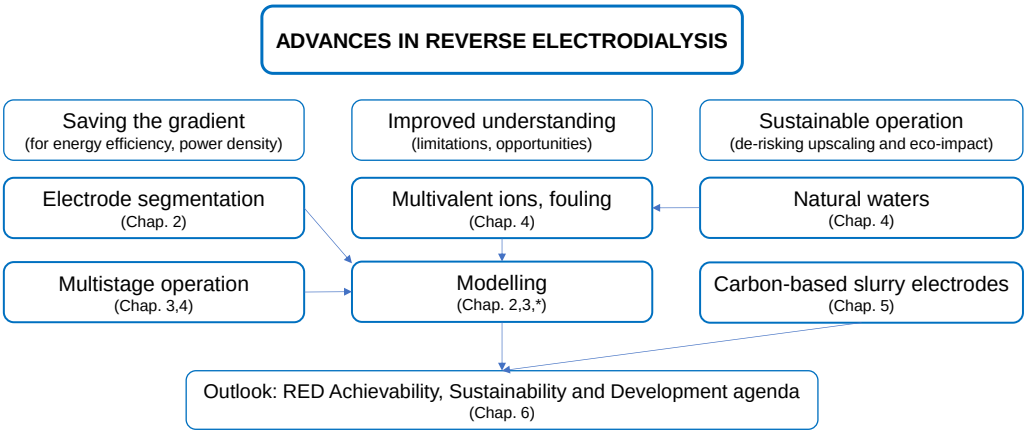

Figure 1.8 Visual representation of the thesis outline. * Publication not included in this thesis connecting modelling and multivalent ions [44].

References

[1] V. Masson-Delmotte, P. Zhai, A. Pirani, S.L. Connors, C. Péan, S. Berger, N. Caud, Y. Chen, L. Goldfarb, M.I. Gomis, Summary for Policymakers. In: Climate Change 2021: The Physical Science Basis. Contribution of Working Group I to the Sixth Assessment Report of the Intergovernmental Panel on Climate Change, New York, 2021. https://doi.org/10.1017/9781009157896.001.

[2] P. Friedlingstein, M.W. Jones, M. O'Sullivan, R.M. Andrew, J. Hauck, G.P. Peters, W. Peters, J. Pongratz, S. Sitch, C. le Quéré, D.C.E. Bakker, J.G. Canadell, P. Ciais, R.B. Jackson, P. Anthoni, L. Barbero, A. Bastos, V. Bastrikov, M. Becker, L. Bopp, E. Buitenhuis, N. Chandra, F. Chevallier, L.P. Chini, K.I. Currie, R.A. Feely, M. Gehlen, D. Gilfillan, T. Gkritzalis, D.S. Goll, N. Gruber, S. Gutekunst, I. Harris, V. Haverd, R.A. Houghton, G. Hurtt, T. Ilyina, A.K. Jain, E. Joetzjer, J.O. Kaplan, E. Kato, K. Klein Goldewijk, J.I. Korsbakken, P. Landschützer, S.K. Lauvset, N. Lefèvre, A. Lenton, S. Lienert, D. Lombardozzi, G. Marland, P.C. McGuire, J.R. Melton, N. Metzl, D.R. Munro, J.E.M.S. Nabel, S.-I. Nakaoka, C. Neill, A.M. Omar, T. Ono, A. Peregon, D. Pierrot, B. Poulter, G. Rehder, L. Resplandy, E. Robertson, C. Rödenbeck, R. Séférian, J. Schwinger, N. Smith, P.P. Tans, H. Tian, B. Tilbrook, F.N. Tubiello, G.R. van der Werf, A.J. Wiltshire, S. Zaehle, Global Carbon Budget 2019, Earth Syst Sci Data. 11 (2019) 1783–1838. https://doi.org/10.5194/essd-11-1783-2019.

[3] 2100 Warming Projections: Emissions and expected warming based on pledges and current policies, Climate Analytics and NewClimate Institute. (2022). https://climateactiontracker.org/global/temperatures/ (accessed November 27, 2022).

[4] U.N.F. Convention on Climate Change, Paris Agreement, (2015). https://unfccc.int/files/essential_background/convention/application/pdf/english_paris_agreement.pdf (accessed January 21, 2020).

[5] BP, Statistical Review of World Energy 2022, 2022. https://www.bp.com/en/global/corporate/energy-economics/statistical-review-of-world-energy/downloads.html (accessed September 2, 2022).

[6] M. Yekini Suberu, M. Wazir Mustafa, N. Bashir, Energy storage systems for renewable energy power sector integration and mitigation of intermittency, Renewable and Sustainable Energy Reviews. 35 (2014) 499–514. https://doi.org/10.1016/j.rser.2014.04.009.

[7] R.E. Pattle, Production of electric power by mixing fresh and salt water in the hydroelectric pile, Nature. (1954). https://doi.org/10.1038/174660a0.

[8] J. Kuleszo, C. Kroeze, J. Post, B.M. Fekete, The potential of blue energy for reducing emissions of CO2 and non-CO2 greenhouse gases, Journal of Integrative Environmental Sciences. (2010). https://doi.org/10.1080/19438151003680850.

[9] IEA, Electricity Market Report, July 2022, 2022. https://www.iea.org/reports/electricity-market-report-july-2022 (accessed August 19, 2022).

[10] W. Li, W.B. Krantz, E.R. Cornelissen, J.W. Post, A.R.D. Verliefde, C.Y. Tang, A novel hybrid process of reverse electrodialysis and reverse osmosis for low energy seawater desalination and brine management, Appl Energy. 104 (2013) 592–602. https://doi.org/10.1016/j.apenergy.2012.11.064.

[11] M. Tedesco, A. Cipollina, A. Tamburini, W. van Baak, G. Micale, Modelling the Reverse ElectroDialysis process with seawater and concentrated brines, Desalination Water Treat. 49 (2012) 404–424. https://doi.org/10.1080/19443994.2012.699355.

[12] A. Cipollina, G. Micale, Sustainable Energy from Salinity Gradients, 2016. https://doi.org/10.1016/C2014-0-03709-4.

[13] N.Y. Yip, M. Elimelech, Thermodynamic and energy efficiency analysis of power generation from natural salinity gradients by pressure retarded osmosis, Environ Sci Technol. (2012). https://doi.org/10.1021/es300060m.

[14] D. Brogioli, R. Ziano, R.A. Rica, D. Salerno, F. Mantegazza, Capacitive mixing for the extraction of energy from salinity differences: Survey of experimental results and electrochemical models, J Colloid Interface Sci. 407 (2013) 457–466. https://doi.org/10.1016/j.jcis.2013.06.050.

[15] R.E. Lacey, Energy by reverse electrodialysis, Ocean Engineering. 7 (1980) 1–47. https://doi.org/10.1016/0029-8018(80)90030-x.

[16] J.W. Post, J. Veerman, H.V.M. Hamelers, G.J.W. Euverink, S.J. Metz, K. Nymeijer, C.J.N. Buisman, Salinity-gradient power: Evaluation of pressure-retarded osmosis and reverse electrodialysis, J Memb Sci. 288 (2007) 218–230. https://doi.org/10.1016/j.memsci.2006.11.018.

[17] J.W. Post, C.H. Goeting, J. Valk, S. Goinga, J. Veerman, H.V.M. Hamelers, P.J.F.M. Hack, Towards implementation of reverse electrodialysis for power generation from salinity gradients, Desalination Water Treat. 16 (2010) 182–193. https://doi.org/10.5004/dwt.2010.1093.

[18] M. Tedesco, A. Cipollina, A. Tamburini, G. Micale, Towards 1 kW power production in a reverse electrodialysis pilot plant with saline waters and concentrated brines, J Memb Sci. 522 (2017) 226–236. https://doi.org/10.1016/j.memsci.2016.09.015.

[19] J.Y. Nam, K.S. Hwang, H.C. Kim, H. Jeong, H. Kim, E. Jwa, S.C. Yang, J. Choi, C.S. Kim, J.H. Han, N. Jeong, Assessing the behavior of the feed-water constituents of a pilot-scale 1000-cell-pair reverse electrodialysis with seawater and municipal wastewater effluent, Water Res. 148 (2019) 261–271. https://doi.org/10.1016/j.watres.2018.10.054.

[20] S. Mehdizadeh, M. Yasukawa, T. Abo, M. Kuno, Y. Noguchi, M. Higa, The effect of feed solution temperature on the power output performance of a pilot-scale reverse electrodialysis (RED) system with different intermediate distance, Membranes (Basel). (2019). https://doi.org/10.3390/membranes9060073.

[21] D.A. Vermaas, M. Saakes, K. Nijmeijer, Doubled power density from salinity gradients at reduced intermembrane distance, Environ Sci Technol. (2011). https://doi.org/10.1021/es2012758.

[22] D.A. Vermaas, M. Saakes, K. Nijmeijer, Power generation using profiled membranes in reverse electrodialysis, J Memb Sci. (2011). https://doi.org/10.1016/j.memsci.2011.09.043.

[23] J. Veerman, M. Saakes, S.J. Metz, G.J. Harmsen, Reverse electrodialysis: Evaluation of suitable electrode systems, J Appl Electrochem. 40 (2010) 1461–1474. https://doi.org/10.1007/s10800-010-0124-8.

[24] J. Veerman, J.W. Post, M. Saakes, S.J. Metz, G.J. Harmsen, Reducing power losses caused by ionic shortcut currents in reverse electrodialysis stacks by a validated model, J Memb Sci. (2008). https://doi.org/10.1016/j.memsci.2007.11.032.

[25] D.A. Vermaas, J. Veerman, N.Y. Yip, M. Elimelech, M. Saakes, K. Nijmeijer, High efficiency in energy generation from salinity gradients with reverse electrodialysis, ACS Sustain Chem Eng. (2013). https://doi.org/10.1021/sc400150w.

[26] A.M. Weiner, R.K. McGovern, J.H. Lienhard V., A new reverse electrodialysis design strategy which significantly reduces the levelized cost of electricity, J Memb Sci. 493 (2015) 605–614. https://doi.org/10.1016/j.memsci.2015.05.058.

[27] S. Mehdizadeh, Y. Kakihana, T. Abo, Q. Yuan, M. Higa, Power generation performance of a pilot-scale reverse electrodialysis using monovalent selective ion-exchange membranes, Membranes (Basel). 11 (2021) 1–25. https://doi.org/10.3390/membranes11010027.

[28] C. Simões, B. Vital, T. Sleutels, M. Saakes, W. Brilman, Scaled-up multistage reverse electrodialysis pilot study with natural waters, Chemical Engineering Journal. 450 (2022) 138412. https://doi.org/10.1016/j.cej.2022.138412.

[29] A. D'Angelo, M. Tedesco, A. Cipollina, A. Galia, G. Micale, O. Scialdone, Reverse electrodialysis performed at pilot plant scale: Evaluation of redox processes and simultaneous generation of electric energy and treatment of wastewater, Water Res. 125 (2017) 123–131. https://doi.org/10.1016/j.watres.2017.08.008.

[30] B. Vital, E. v. Torres, T. Sleutels, M.C. Gagliano, M. Saakes, H.V.M. Hamelers, Fouling fractionation in reverse electrodialysis with natural feed waters demonstrates dual media rapid filtration as an effective pre-treatment for fresh water, Desalination. 518 (2021). https://doi.org/10.1016/j.desal.2021.115277.

[31] D.A. Vermaas, D. Kunteng, M. Saakes, K. Nijmeijer, Fouling in reverse electrodialysis under natural conditions, Water Res. (2013). https://doi.org/10.1016/j.watres.2012.11.053.

[32] J.W. Post, H.V.M. Hamelers, C.J.N. Buisman, Influence of multivalent ions on power production from mixing salt and fresh water with a reverse electrodialysis system, J Memb Sci. (2009). https://doi.org/10.1016/j.memsci.2008.12.042.

[33] M. Higa, A. Tanioka, K. Miyasaka, Simulation of the transport of ions against their concentration gradient across charged membranes, J Memb Sci. 37 (1988) 251–266. https://doi.org/10.1016/S0376-7388(00)82432-1.

[34] D.A. Vermaas, J. Veerman, M. Saakes, K. Nijmeijer, Influence of multivalent ions on renewable energy generation in reverse electrodialysis, Energy Environ Sci. (2014). https://doi.org/10.1039/c3ee43501f.

[35] T. Rijnaarts, J. Moreno, M. Saakes, W.M. de Vos, K. Nijmeijer, Role of anion exchange membrane fouling in reverse electrodialysis using natural feed waters, Colloids Surf A Physicochem Eng Asp. 560 (2019) 198–204. https://doi.org/10.1016/j.colsurfa.2018.10.020.

[36] Y. Mei, C.Y. Tang, Recent developments and future perspectives of reverse electrodialysis technology: A review, Desalination. (2017). https://doi.org/10.1016/j.desal.2017.10.021.

[37] O. Scialdone, C. Guarisco, S. Grispo, A.D. Angelo, A. Galia, Investigation of electrode material - Redox couple systems for reverse electrodialysis processes. Part I: Iron redox couples, Journal of Electroanalytical Chemistry. 681 (2012) 66–85. https://doi.org/10.1016/j.jelechem.2012.05.017.

[38] E. Jaszczak, Ż. Polkowska, S. Narkowicz, J. Namieśnik, Cyanides in the environment—analysis—problems and challenges, Environmental Science and Pollution Research. 24 (2017) 15929–15948. https://doi.org/10.1007/s11356-017-9081-7.

[39] S. Ašperger, I. Murati, D. Pavlović, Kinetics of oxidation and of catalytic decomposition of hexacyanoferrate(II) ion, Journal of the Chemical Society A: Inorganic, Physical, Theoretical. 0 (1969).

[40] J. Hyung, H. Kyo, H. Jeong, S. Yong, B. Joo, Y. Nam, C. Soo, Electrode system for large-scale reverse electrodialysis : water electrolysis , bubble resistance , and inorganic scaling, J Appl Electrochem. 49 (2019) 517–528. https://doi.org/10.1007/s10800-019-01303-4.

[41] D.A. Vermaas, S. Bajracharya, B.B. Sales, M. Saakes, B. Hamelers, K. Nijmeijer, Clean energy generation using capacitive electrodes in reverse electrodialysis, Energy Environ Sci. 6 (2013) 643. https://doi.org/10.1039/c2ee23562e.

[42] E. Avraham, M. Noked, I. Cohen, A. Soffer, D. Aurbach, The Dependence of the Desalination Performance in Capacitive Deionization Processes on the Electrodes PZC, J Electrochem Soc. 158 (2011) P168. https://doi.org/10.1149/2.078112jes.

[43] F. Liu, O. Coronell, D.F. Call, Electricity generation using continuously recirculated flow electrodes in reverse electrodialysis, J Power Sources. 355 (2017) 206–210. https://doi.org/10.1016/j.jpowsour.2017.04.061.

[44] D. Pintossi, C. Simões, M. Saakes, Z. Borneman, K. Nijmeijer, Predicting reverse electrodialysis performance in the presence of divalent ions for renewable energy generation, Energy Convers Manag. 243 (2021). https://doi.org/10.1016/j.enconman.2021.114369.

Chapter 2

Electrode segmentation in reverse electrodialysis: Improved power and energy efficiency

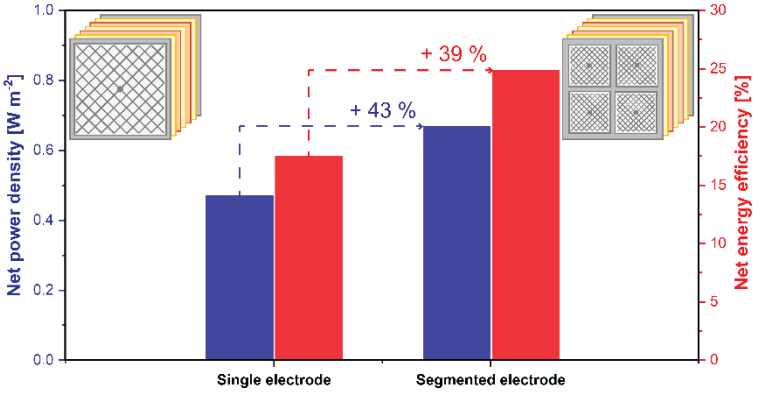

Abstract

Reverse electrodialysis harvests energy from salinity gradients establishing a renewable energy source. High energy efficiencies are fundamental to up-scale the process and to minimize feedwater pre-treatment and pumping costs. The present work investigates electrode segmentation to strategically optimise the output power density and energy efficiency. Electrode segmentation allows the current density to be tuned per electrode segment. Segmentation experiments were performed with a dedicated electrode configuration in a cross-flow stack using a wide range of residence times. Moreover, an experimentally validated model was extended and used to further compare single and segmented electrode configurations. While operating the electrode segments, the highest efficiencies were obtained when considering the overall power, i.e., not maximized by segment. Results show that at a given net power density (0.92 $W \cdot m^{-2}$), electrode segmentation increases the net energy efficiency from 17 % to 25 %, which is a relative increase of 43 %. Plus, at 40 % net energy efficiency the net power output for a segmented electrode configuration (0.67 $W \cdot m^{-2}$) is 39 % higher than in a single electrode configuration. Higher power density reduces capital investment and higher energy efficiency reduces operating costs. Electrode segmentation increases these parameters compared to a single electrode and can be potentially applied for up-scaling.

This chapter has been published as:

C. Simões*****, D. Pintossi*****, M. Saakes, Z. Borneman, W. Brilman and K. Nijmeijer, 2020. Electrode segmentation in reverse electrodialysis: Improved power and energy efficiency. Desalination, 492, p.114604, https://doi.org/10.1016/j.desal.2020.114604

***** these authors contributed equally

2.1. Introduction

Given the growing global energy demand, there is a great societal need for clean and renewable energy sources to replace the use of polluting fossil fuels and reduce CO_2 emissions [1]. One promising source of renewable energy is the salinity gradient energy (also known as blue energy), where the energy results from the reversible mixing of two streams with different salinities. The salinity gradient is widely available anywhere a river runs into the sea, being a non-intermittent renewable energy source, opposite to solar and wind energy [2]. The theoretical energy that can be generated from mixing 1 m^3 of river water (1 g $NaCl \cdot L^{-1}$) with 1 m^3 of seawater (30 g $NaCl \cdot L^{-1}$) is 1.7 MJ [3]. Worldwide the technical potential for salinity gradient energy was estimated at 983 GW [4]. With its implementation, energy-related emissions could be reduced by 25 %, 27 %, and 8 % of CO_2, CH_4, and N_2O, respectively [4].

One main technology to harvest salinity gradient energy is reverse electrodialysis (RED) [5]. The RED process consists of a stack with an alternating series of cation (CEM) and anion (AEM) exchange membranes (Figure 2.1). Compartments are established with spacers between the membranes, where seawater and river water flow alternately alongside the membrane. Since ion exchange membranes (IEMs) have selectivity either toward cations (CEMs) or anions (AEMs), a Donnan potential is generated across the membranes. One cell pair comprises one AEM, one CEM, one river compartment, and one seawater compartment. When multiple cell pairs are stacked, this potential is accumulated. The potential difference over the membranes drives the transport of ions through the membranes from the seawater towards the river water compartment. Finally, enclosing the membrane pile, an electrode is placed at each end of the stack. A redox solution is recirculated to convert the ionic current into an electrical current, which powers an external load [6].

In the past years, several studies were conducted to improve the process' power density as well as its efficiency. This includes membrane modification, such as monovalent-ion-selective membranes, surface modifications and profiled membranes [7–10], fouling prevention and monitoring [11–15], spacer thickness effect or no spacer present by using corrugated membranes [16,17], flow velocity of the feedwaters [18], scalability of the cross-flow stack [19], prevention of ionic shortcut currents [20], modelling of the RED process with different flow strategies (co-flow, counter-flow and cross-flow) and model optimization of the RED process [21–24]. Furthermore, the potential for large-scale application has been proven with pilot plants [25,26].

To establish RED as a commercial technology, it is crucial to use large-scale stacks with sufficient energy efficiency [27]. With more ion exchange, to allow sufficient energy efficiency, the salt concentration in the river water increases significantly along the length of the stack,

resulting in a drastic decrease of the local ohmic electrical resistance and a drop of electromotive force inside the stack along the flow path length. This leads to a non-homogeneous current distribution over the length of the active membrane area [22]. When using a stack with a single pair of electrodes, i.e., one anode and one cathode, only one external load can be set to harvest the energy. While this single load can be tuned for maximum power production, this represents a compromise between the optimal loads of different sections of the active area [28].

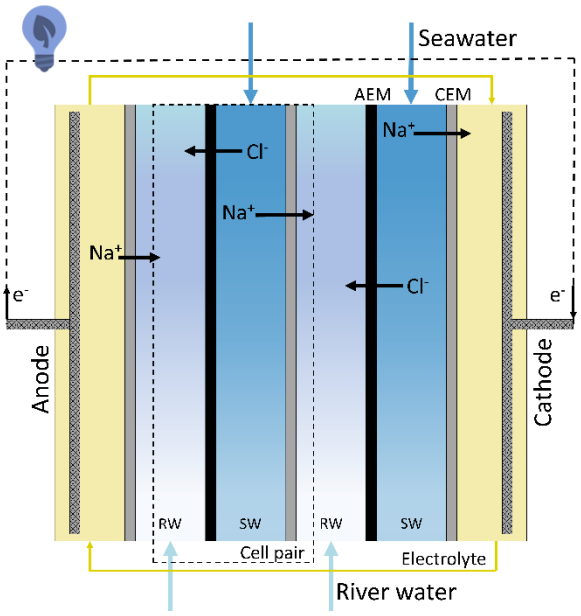

Figure 2.1 Working principle of RED. Two cell pairs are present in the scheme plus an extra CEM to shield the feedwater from the electrode rinse solution. One cell pair is composed of one AEM, one CEM, one river compartment and one seawater compartment. In a RED stack, multiple cell pairs are placed between the electrodes.

For a given stack size, the required pumping energy is reduced at longer residence times due to a lower flow velocity [19]. Moreover, feedwaters need to be pre-treated to avoid fouling inside the RED stacks [29]. The extraction of more energy per m^3 of seawater and river water compensates the energy consumption associated with pumping and pre-treatment of the feedwaters. In brief, the operation of stacks to achieve sufficient energy efficiency introduces new challenges that limit the maximum RED power output [30].

A promising strategy to increase energy efficiency without incurring additional power output losses is electrode segmentation. Segmentation has been used before to map the current density inside electrochemical cells, such as proton-exchange membrane fuel cells [31,32] or redox flow batteries [33,34], and for process optimization in electrodialysis [35,36]. In RED, segmentation allows the optimization of the performance by tuning the resistive load per segment. In this way, the external load can be adjusted to the local electrode segment

electrical resistance. Such adjustment enables a higher power density output and energy efficiency. Veerman et al. [28] made the first experimental study of segmentation in RED with a scaled-up stack (active area of 25 cm x 75 cm). Segmentation was studied using three-electrode segments (25 cm x 25 cm, each). The stack was operated horizontally with a co-flow feed configuration. The optimal resistance was found for each electrode segment and the corresponding current was extracted. This resulted in a power density increase of 11 %, from 0.44 to 0.49 $W \cdot m^{-2}$, when compared with the same stack with the three-electrode segments connected as one electrode. The same author published a model regarding electrode segmentation [21], which proved an increase of power by about 15 % when using an infinite number of segments. In this model, the non-ideal behaviour of membranes was accounted for and the stack (10 cm x 10 cm) was operated with a co-flow feed configuration. Besides infinite segmentation, the model also predicted the effect of 2 to 5 electrode segments, with a power increase between 13 and 17 %, respectively. While surprising, the higher increase for a limited number of segments rather than for an infinite number of electrode segments can be explained by the trade-off between high power in the first stages and the need to preserve gradient for the last segments. More recently, Vermaas et al. [22] modelled a RED stack to study the influence of the feed flow configuration, the seawater fraction and the electrode segmentation on the energy efficiency. The model of Vermaas et al. assumed ideal IEMs, no concentration polarization effects and considered a fixed residence time for river water. The results showed that for all configurations higher efficiencies were achieved when the electrode was segmented. The energy efficiency increases by approximately 15 % for the same ratio of seawater and river water when using two electrode segments compared to a single electrode.

The present research aims to investigate experimentally and by modelling the behaviour of electrode segmentation in a RED cross-flow stack. This includes the integration of previous modelling works [21,22] into a new dedicated model, able to characterize the cross-flow stack either with a single electrode or different electrode segments. Furthermore, besides studying the interaction between electrode segments, the overall maximum power density of the electrode segments was optimized.

2.2. Materials and methods

2.2.1. RED modelling

To model the RED stack with segmented electrodes in a cross-flow configuration, two models presented in the literature were combined: the model proposed by Veerman et al [21] and the model by Vermaas et al [22]. Veerman's model includes membrane properties, osmosis and salt transport, but it is limited to co-flow and counter-flow configurations, while

Vermaas' model includes the cross-flow configuration, but it only considers ideal membranes (having zero electrical resistance and perfect permselectivity).

The models were combined and used as reported with the addition of segmentation along the seawater direction to simulate a 2 by 2 segmented electrode configuration. Figure S2.1a describes the segmented cross-flow stack, while Figure 2.2 depicts the discretization scheme.

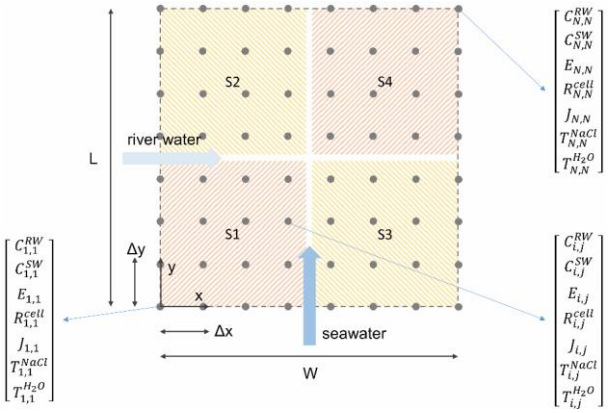

Figure 2.2 Scheme of the discretization strategy adopted in the RED model. The cell pair is reduced to a matrix where to each point a set of properties relative to the feedwaters and membranes is associated.

The modified Nernst equation expresses the electromotive force (V) available at each point in the grid:

$$E_{i,j} = (\alpha_{AEM} + \alpha_{CEM}) \frac{RT}{zF} ln\left(\frac{\gamma_{i,j}^{SW} C_{i,j}^{SW}}{\gamma_{i,j}^{RW} C_{i,j}^{RW}}\right) \quad \text{(Eq. 2.1)}$$

Where $\boldsymbol{\alpha}$ is the permselectivity of AEM and CEM (-), $\boldsymbol{R}$ is the universal gas constant (J·mol^{-1}·K^{-1}), $\boldsymbol{T}$ is the absolute temperature (K), $\boldsymbol{z}$ is the ion valence (-), $\boldsymbol{F}$ is the Faraday constant (C·mol^{-1}), $\boldsymbol{\gamma}$ is the molar activity coefficient (-) estimated with the TCPC model of Ge et al. (a semi-empirical model combining Pitzer long-range interactions and short-range solvation effect) [37], and $\boldsymbol{C}$ is the salt concentration (mol·m^{-3}).

The area resistance (Ω·m^2) of the cell was given by:

$$R_{i,j}^{cell\ pair} = R_{AEM} + R_{CEM} + \frac{1}{f}\frac{d_{RW}}{\kappa_{i,j}^{RW}} + \frac{1}{f}\frac{d_{SW}}{\kappa_{i,j}^{SW}} + \frac{R_{blank}}{N_{CP}} \quad \text{(Eq. 2.2)}$$

$$\kappa = \Lambda \cdot C \quad \text{(Eq. 2.3)}$$

Where $\boldsymbol{R_{AEM}}$ and $\boldsymbol{R_{CEM}}$ are the area electrical resistance of the AEM and CEM (Ω·m^2), respectively, $\boldsymbol{f}$ is the spacer shadow factor (-), a fitting parameter accounting for the presence of non-conductive spacers in the water compartments, $\boldsymbol{d}$ is the water compartment

thickness (m), κ is the conductivity of feedwaters (S·m^{-1}), R_{blank} is the area electrical resistance of the shielding CEMs and electrodes (Ω·m^2), N_{CP} is the number of cell pairs (-), and Λ is the molar conductivity of NaCl (S·m^{-1}·mol^{-1}).

To implement electrode segmentation in the model, the four load voltages (U_{S1}, U_{S2}, U_{S3}, and U_{S4}) were used for the four segments (S1, S2, S3, and S4 in Figure 2.2). The load voltages (V) applied to the segments were:

$$U_{i,j}^{load} = U_{S1} \quad for\ 0 \le i < \frac{N}{2}, \qquad 0 \le j < \frac{N}{2}$$

$$U_{i,j}^{load} = U_{S2} \quad for\ 0 \le i < \frac{N}{2}, \qquad \frac{N}{2} \le j \le N$$

$$U_{i,j}^{load} = U_{S3} \quad for\ \frac{N}{2} \le i \le N, \qquad 0 \le j < \frac{N}{2}$$

$$U_{i,j}^{load} = U_{S4} \quad for\ \frac{N}{2} \le i \le N, \qquad \frac{N}{2} \le j \le N$$

When the loads were applied to the segments, the current density (A·m^2) at all points was:

$$J_{i,j} = \frac{E_{i,j} - U_{i,j}^{load}}{R_{i,j}^{cell}} \qquad \text{(Eq. 2.4)}$$

The salt flux (mol·m^{-2}·s^{-1}) at each point of the discretization grid was expressed as the sum of current transport and co-ion transport through the AEM and CEM:

$$T_{i,j}^{NaCl} = \frac{J_{i,j}}{F} + 2\left(C_{i,j}^{SW} - C_{i,j}^{RW}\right)\frac{D_{NaCl}}{l_m} \qquad \text{(Eq. 2.5)}$$

Where D_{NaCl} is the average diffusion coefficient of NaCl through the AEM and CEM (m^2·s^{-1}), l_m is the membrane thickness (m), and factor 2 is introduced to account for the diffusion through both membrane types.

The volumetric flux of water through the membranes (m·s^{-1}) was given by [21]:

$$T_{i,j}^{H_2O} = -2\left(C_{i,j}^{SW} - C_{i,j}^{RW}\right)\frac{D_{H_2O}}{l_m}\frac{MW_{H_2O}}{\rho_{H_2O}} \qquad \text{(Eq. 2.6)}$$

Where D_{H_2O} is the average diffusion coefficient of water through the AEM and CEM (m^2·s^{-1}), the factor 2 was introduced to account for the diffusion through both membrane types, MW_{H_2O} is the molecular weight of water (kg·mol^{-1}), and ρ_{H_2O} is the density of water (kg·m^{-3}).

The change in concentration in the active area can be described by the sum of the salt transport due to migration and diffusion (co-ions), plus water transport, as in the following partial differential equations (PDEs):

$$\frac{\partial C_{i,j}^{SW}}{\partial y} = -\frac{\Delta x}{\Delta \phi_{SW}} T_{i,j}^{NaCl} + C_{i,j}^{SW} \frac{\Delta x}{\Delta \phi_{SW}} T_{i,j}^{H_2O} = -\frac{W}{\phi_{SW}} T_{i,j}^{NaCl} + C_{i,j}^{SW} \frac{W}{\phi_{SW}} T_{i,j}^{H_2O} \quad \text{(Eq. 2.7)}$$

$$\frac{\partial C_{i,j}^{RW}}{\partial x} = +\frac{\Delta y}{\Delta \phi_{RW}} T_{i,j}^{NaCl} - C_{i,j}^{RW} \frac{\Delta y}{\Delta \phi_{RW}} T_{i,j}^{H_2O} = +\frac{L}{\phi_{RW}} T_{i,j}^{NaCl} - C_{i,j}^{RW} \frac{L}{\phi_{RW}} T_{i,j}^{H_2O} \quad \text{(Eq. 2.8)}$$

Where Δx and Δy are the discretization intervals (m), ϕ is the feed flow rate ($m^3 \cdot s^{-1}$), $\Delta \phi$ is the feed flow rate in Δx or Δy ($m^3 \cdot s^{-1}$), L is the length of the active area (m), and W is its width (m). The two governing PDEs are solved numerically using the Forward Euler method (equations 2.9 and 2.10), thus obtaining the matrix of the concentrations at a steady state.

$$C_{i+1,j}^{SW} = C_{i,j}^{SW} + dy \left(-\frac{W}{\phi_{SW}} T_{i,j}^{NaCl} + C_{i,j}^{SW} \frac{W}{\phi_{SW}} T_{i,j}^{H_2O} \right) \quad \text{(Eq. 2.9)}$$

$$C_{i,j+1}^{RW} = C_{i,j}^{RW} + dx \left(+\frac{L}{\phi_{RW}} T_{i,j}^{NaCl} - C_{i,j}^{RW} \frac{L}{\phi_{RW}} T_{i,j}^{H_2O} \right) \quad \text{(Eq. 2.10)}$$

From the solution concentrations, the electromotive force, cell resistance, current density, power (and power density), and efficiencies were calculated. Custom Python 3.6 scripts and functions were developed for this purpose. The grid size was 500 x 500 points. Further grid refinement did not significantly affect the model results, while it increased the computation time.

The total power output was maximized by varying the ohmic loads applied to the four segments using an SLSQP (sequential least squares programming) algorithm. The scypy.optimize.minimize function was used for this purpose (- P_{gross} was the minimized function).

Table S1 summarizes all the model input parameters used in the present work and how they were evaluated.

For both model and experimental data, the gross power produced by the stack was given by:

$$P_{gross} = U_{load} I \quad \text{(Eq. 2.11)}$$

Where U_{load} is the voltage drop measured if a load is applied to the stack (V) and I is the current extracted from the stack (A).

To calculate the efficiency of the stack operation, the total Gibbs energy available in the salinity gradient (J), was considered:

$$\Delta G = T \cdot \Delta S = T \cdot (S_{mix} - S_{SW} - S_{RW}) \quad \text{(Eq. 2.12)}$$

$$S = -Rn_{TOT}\sum_i x_i ln(\gamma_i x_i) \; with \; i = Na^+, Cl^-, H_2O \quad \text{(Eq. 2.13)}$$

Where S is the entropy (J·K^{-1}), n_{TOT} is the total number of moles (mol), x_i is the fraction of element i (-).

Considering in equation 2.13 the flow rates of the feedwaters (m^3·s^{-1}) rather than the compartment volumes (m^3), n_{TOT} becomes the number of moles per second (mol·s^{-1}). The entropy was calculated per unit of time (W·K^{-1}), and equation. 2.12 expressed the available power (W), which can be directly compared to the stack power output to calculate the energy efficiency.

The (gross) energy efficiency (%) considered the gross power produced compared to the total available Gibbs energy at the inlet (complete mixing was assumed):

$$\eta_{energy} = 100\frac{P_{gross}}{\Delta G_{in}} \quad \text{(Eq. 2.14)}$$

The pumping losses (W) were calculated as the energy consumed to pump the seawater and the river water respectively [21]:

$$P_{pump} = \phi_{SW} dP_{SW} + \phi_{RW} dP_{RW} \quad \text{(Eq. 2.15)}$$

$$dP_{RW} = K\frac{W\phi_{RW}}{L{d_{RW}}^3} \quad \text{(Eq. 2.16)}$$

$$dP_{SW} = K\frac{L\phi_{SW}}{W{d_{SW}}^3} \quad \text{(Eq. 2.17)}$$

Where dP is the pressure drop between the feedwater inlet and outlet (Pa), K is the fitting coefficient (Pa·s) used to describe the pumping energy, and ϕ is the flow rate of the feedwater (m^3·s^{-1}).

By subtracting the pumping losses from the gross power, the net power (W) was obtained:

$$P_{net} = P_{gross} - P_{pump} \quad \text{(Eq. 2.18)}$$

From the net power, the net energy efficiency (%) was determined:

$$\eta_{net} = 100\frac{P_{net}}{\Delta G_{in}} \quad \text{(Eq. 2.19)}$$

All power figures were converted to power densities by dividing the power values by the total membrane area ($A_{total} = 2W \cdot L \cdot N_{CP}$, accounting for the area of CEMs and AEMs in all cell pairs).

$$P_d = \frac{P}{2W \cdot L \cdot N_{CP}} \quad \text{(Eq. 2.20)}$$

2.2.2. Stack configuration & electrodes

A cross-flow reverse electrodialysis stack (REDstack BV, The Netherlands) was used to investigate the effect of electrode segmentation on performance. The stack design details can be found in previous research [16,29,38]. The stack, with 22 cm x 22 cm active membrane area, contained 10 cell pairs (0.968 m^2 of total active membrane area). The number of cell pairs was chosen according to the desired experiment duration and volume of the feedwater reservoirs (at the highest flow rate, water consumption is approximately 2.5 $L \cdot h^{-1}$ per cell pair). Each cell pair consisted of one Fujifilm type 10 CEM and one Fujifilm type 10 AEM (FUJIFILM Manufacturing Europe BV, The Netherlands). The properties of these membranes are reported by Moreno et al. [19]. To close the electrode compartments, two CEMs are placed at each end, for double-shielding purposes, adding a total of three extra Fujifilm type 10 CEMs, instead of one extra CEM. The membranes were separated by 155 µm thick woven net-spacers (Deukum GmbH, Germany), with netting Saatifil PES 153/55 (Saati SpA, Italy). For the model validation, standard 22 cm x 22 cm (Figure 2.3b) Ti-mesh 1.0 electrodes with 2.5 µm Pt galvanic coating were used as anode and cathode (MAGNETO Special Anodes BV, The Netherlands).

For segmentation, a dedicated electrode configuration was manufactured (REDstack BV, The Netherlands) with four 10 cm x 10 cm electrodes placed at the endplates with 1.5 cm distance between each other (Figures 2.3d and S2.1b), while the total active membrane area was kept at 0.968 m^2. The electrodes were made of Ti-mesh with a Ru/Ir mixed metal oxide coating for anode and cathode (MAGNETO Special Anodes BV, The Netherlands). As electrode rinse solution a mixture of 0.2 M $K_4Fe(CN)_6$, 0.2 M $K_3Fe(CN)_6$ and 0.15 M NaCl was used (96 %, 96 % and 100 % purity, respectively, VWR Chemicals, Belgium). Due to the special electrode configuration, the electrode rinse solution was pumped independently into each electrode compartment (Figure S2.1b) at a flow rate of 150 $mL \cdot min^{-1}$ using a peristaltic pump (Cole-Palmer, Masterflex L/S Digital drive, USA) with two double pump heads to avoid pulsations (Cole-Palmer, Masterflex L/S Two-Channel Easy-Load II, USA). Figure 2.3a provides a schematic illustration of the feed water directions, electrical connections and sensors during the segmented electrode stack operation.

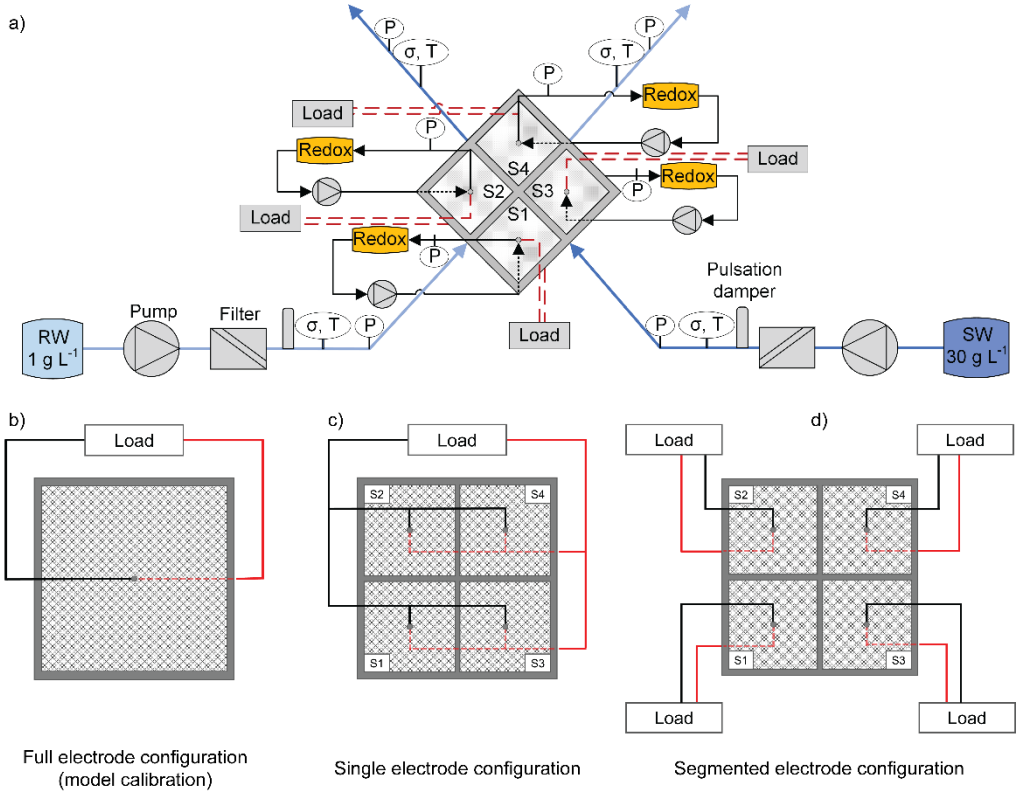

Figure 2.3 a) Flow diagram for the operation of the segmented electrode stack configuration. b) Electrode and external load representation of the stack with a 22 cm x 22 cm electrode (full electrode configuration). c) Electrode and external load representation of the stack with four 10 cm x 10 cm electrode segments connected to a single external load (single electrode configuration). d) Electrode and external load representation of the stack with four 10 cm x 10 cm electrode segments connected to four separate external ohmic loads (segmented electrode configuration).

2.2.3. Feedwaters and sensors

Artificial feedwaters were made of 30 g NaCl·L^{-1} and 1 g NaCl·L^{-1} (99.9 % purity, Regenit, Esco, The Netherlands), for seawater and river water, respectively. The two solutions were pumped at the same flow velocity using diaphragm pumps (Grundfos DDA220, Denmark). Pulsation dampers (PDS250 PVC/FKM, Prominent GmbH, Germany) were placed between the pumps and the stack to mitigate the pump pulsation. Also, cartridge filters with 1 µm pore size (Filter Technics, Belgium) were placed before the stack (Figure 2.3a). Outlet flow velocities were measured gravimetrically. Conductivity and temperature were measured in-line (VStar22, Thermo Fisher Scientific, USA) at the inflow and outflow of each stream. The inlet temperatures were set to 25 °C. The absolute pressure was measured with calibrated sensors (MIDAS SW, JUMO GmbH, Germany) at the same points as the conductivity and at the electrode rinse solutions. The data were collected with a data logger (Memograph M, Endress

+ Hauser, Germany). Salt concentrations were calculated from conductivity values based on an experimental calibration curve (Figure S2.2). The hydrodynamic losses were determined as the product of the differential pressure across the stack and the flow rate (equation 2.15) [28].

2.2.4. Experimental procedure

2.2.4.1. Experiments for model validations with standard stack

To identify the spacer shadow factor and the average salt diffusion coefficient values through the membranes, a separate experiment with full electrode configuration (Figure 2.3b) was performed and data were fitted with the model. The 22 cm x 22 cm electrode stack (Figure 2.3b) was used to determine the power density and energy efficiency at different current densities fixing the residence time at 22 s (flow velocity of 1.0 cm·s^{-1}). This was done by increasing the current density in 6.2 A·m^{-2} steps (0.3 A in current over 22 cm x 22 cm area) for 10 minutes each, taking the average of the last 2 minutes of the current and voltage values as measured with the potentiostat (IVIUM.XRi, IVIUM Technologies BV, The Netherlands) to obtain the power (equation 2.11). The blank resistance was measured to be 0.071 Ω, given by REDstack [39], which comprised the resistance of the electrodes, the rinse solution and the three extra CEMs. This was used to discard the contribution of the electrodes to the stack resistance, which would be negligible when using hundreds of cell pairs. To validate the model, experimental power data were corrected for the blank resistance [39], to avoid the presence of the blank resistance (equation. 2.2) as an additional fitting parameter. Pumping losses across the stack were determined experimentally, and the model parameter K (equations 2.16 and 2.17) was adjusted to fit the experimental data. The shadow factor f was adjusted to fit the experimental data, starting with 0.55, corresponding to the open area of the spacer netting.

2.2.4.2. The relation between electrode segments

To understand the mutual response of the electrode segments, the relation between electrode segments (Figure 2.3d) was established by measuring the potential of each segment with a multi-channel potentiostat (IVIUM n-stat, IVIUM Technologies BV, The Netherlands) at a fixed residence time of 22 s (flow velocity of 1.0 cm·s^{-1}). This consisted in operating one electrode segment, first at open-circuit voltage (OCV) conditions for 60 s followed by a stepwise increase in the extracted current with 16.5 A·m^{-2} current density steps (0.2 A in current over 11 cm x 11 cm area), for 120 s each, until the stack voltage crossed 0 V. Simultaneously, the OCV of the other three electrode segments was measured continuously. Segment current densities were calculated by dividing the applied current (in A) by one-fourth of the active membrane area.

2.2.4.3. Comparison between single and segmented electrode configurations

The performance of four-electrode segments electrically connected to a single load (referred to as single electrode configuration, Figure 2.3c) was compared to the independent performance of the four electrode segments (referred to as segmented electrode configuration, Figure 2.3d) and characterized at five different residence times: 88, 44, 22, 15, and 11 s (corresponding to flow velocities of 0.25, 0.50, 1.00, 1.50 and 2.00 $cm \cdot s^{-1}$, respectively). This approach was chosen since connecting the four electrode segments as a single electrode does not change the total electrode area nor the electrode rinse solution distribution, thus providing a fair comparison. In this third experiment, electrochemical measurements were done using sliding rheostats (4.5 Ω 9 A, Eisco, USA) as a variable external load. Each rheostat was connected to a multimeter (Digital Multimeter VC165, Voltcraft, Germany) monitoring the external load voltage. The segment voltage was measured at the electrodes (Figure S2.3), while the current was measured using a calibrated shunt of 0.1 Ω. The power per segment was calculated from the measured shunt voltage for each segment and the measured segment voltage (equation 2.11). The overall power was calculated by summing all segments powers (P1+P2+P3+P4). The experimental power of each electrode segment was monitored automatically inside the data logger as well as the total power. For the single electrode, the maximum power was determined by sliding the rheostat until the peak in the power curve was reached. For the segmented electrode, the individual rheostats were adjusted manually until the overall power value reached its maximum.

The stack power density was obtained by dividing the power by the total active membrane area. The power density per segment was obtained by dividing the segment power by a quarter of the total active membrane area.

2.3. Results and discussion

2.3.1. Model calibration

Figure 2.4 shows that the calibrated model correctly predicts the power density and energy efficiency for different external loads. The determined model values of the spacer shadow factor (0.61) and salt diffusion coefficient (6.5×10^{-12} $m^2 \cdot s^{-1}$) are in line with the values reported by Veerman et al. [21] and in the normal range for ion exchange membranes [40].

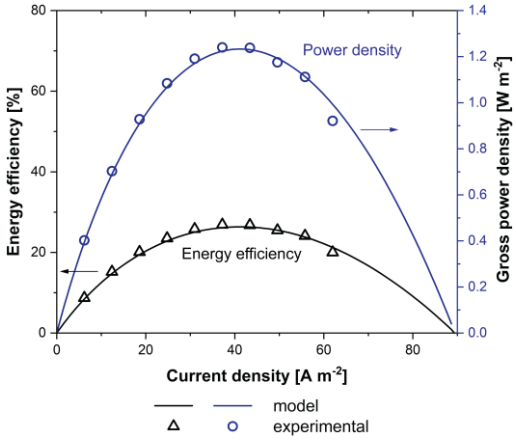

Figure 2.4 Experimental and modelled gross power density and energy efficiency values for a 22 cm x 22 cm cross-flow stack with 155 µm thick spacers at a residence time of 22 s (flow velocity of 1.0 cm·s^{-1}).

2.3.2. The relation between electrode segments

Experimentally obtained I-V curves for each case of one active electrode segment are shown in Figure 2.5 for a residence time of 22 s. The first 60 s period, at OCV conditions, shows a different OCV value for each electrode segment depending on their position. Segment 1 (S1) has the highest potential (1.548 V) because the gradient is the largest in this area. This segment receives fresh seawater and river water, i.e., it is the first contact between both solutions and the first opportunity for ion exchange. And it is then followed by S2 (1.543 V), S3 (1.522 V) and S4 (1.514 V). At this stage, the stack is in stationary condition and no current is extracted, thus, the decrease in potential across the stack indicates undesired water and salt diffusion through the membranes, which is expected when using ion-exchange membranes [19]. This is confirmed by the change in concentration between the inlet and outlet of the river and seawater measured at OCV (Figure S2.4a). The same behaviour was detected in further experiments at different residence times (Table S2.2). The decrease in potential across the electrode segments is more evident at longer residence times since the feedwaters have extended contact periods with the membranes. For a single electrode, these phenomena would only be detected through a change in concentration at the final outlets and a difference between the theoretically calculated and the experimentally measured membrane potential. The segmented electrode configuration allows visualization of the effect of undesired salt and water transport. Moreover, it is visible that the potential of each electrode segment is dependent on its position in the stack.

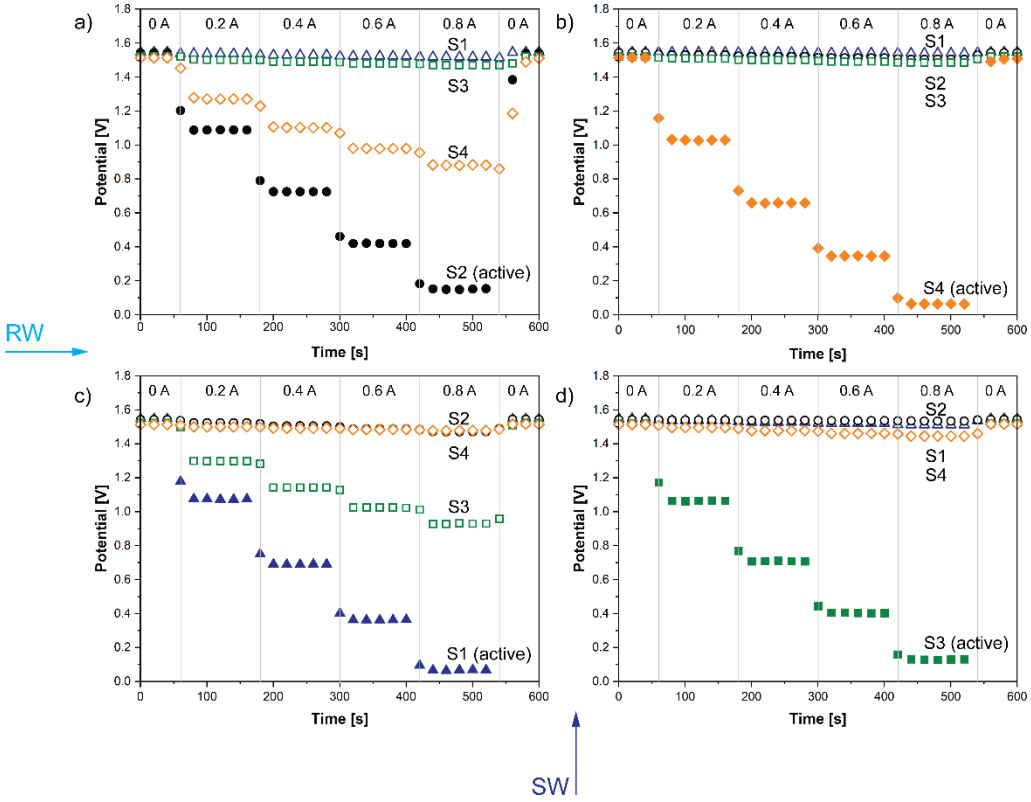

Figure 2.5 Relation between electrode segments at a residence time of 22 s (1.0 cm·s^{-1} flow velocity). Current density steps of 16.5 A·m^{-2} (0.2 A current divided by 11 cm x 11 cm area) were extracted from one segment (solid marker, also indicated in the plot) and the segment voltage response was measured. In the same time frame, the remaining segments (open markers) were measured at OCV conditions. Each plot corresponds to one active electrode segment a) S2 b) S4 c) S1 d) S3, the order was chosen to mimic the position of the segments concerning the RW and SW flow path inside the stack (indicated in the bottom and left by arrows).

Figure 2.5 shows how the electrode segments influence each other when active. When current is extracted from S1 (Figure 2.5c), the OCV of S3 drops. This is caused by the increase in salinity of the river water, which flows from S1 to S3. The potential of S2 exhibits a small decrease compared to the drop in OCV of S3, showing that the salinity drop of the seawater has a smaller influence on the OCV of the adjacent segment rather than the increase in salinity of the river water, following the Nernst equation. Additionally, it is worth noting that the potential of S4 is minimally affected. This shows that the feedwaters and the ions follow a straight flow path inside the stack (Figure 2.3a). Similarly, when S2 generates current (Figure 2.5a), the potential of S4 drops due to the increased salinity of the river water. OCV values of S1 and S3 are not affected, providing a further indication that a straight flow path is present inside the stack. When S3 is active (Figure 2.5d), only S4 has a shallow drop in potential, supporting the conclusion that the salinity drop in the seawater is not crucial for the driving force. Finally, when S4 is generating a current (Figure 2.5b), as expected, the OCV values of

the other segments are not influenced, indicating that the segments do not communicate with each other, i.e., the electrical field is only working in the electrode segment area. These results indicate that the increase in salinity of the river water mainly determines changes in the electromotive force over the active area [28] and that the electric fields introduced by the electrode segments stay separate through the stack when using a limited number of only 10 cell pairs.

2.3.3. Power density distribution model in a single electrode and segmented electrode

The current density inside the RED stack has a non-homogeneous distribution, as the local currents are a function of three parameters: 1) the electromotive force, 2) the internal resistance and 3) the external load. The first two parameters are determined by the local salinity gradient and local concentrations, respectively. This directly affects the local power density output [22,41]. Experimentally this phenomenon can be measured but it is limited to the number of electrode segments available. With a modelling approach, it can be simulated and mapped. For co-flow and counter-flow configurations, the decrease of electromotive force along the flow direction has been shown in several studies [21,24,26,41]. For cross-flow configuration, Vermaas et al. displayed the current density distribution in the active area, albeit for a RED system with ideal membranes [22].

Figure 2.6 compares the gross power density distribution on the active membrane area inside the stack for single electrode configuration (Figure 2.6a), segmented electrode configuration at maximized power per segment (Figure 2.6b), i.e., when the load is sequentially optimized to maximize the power produced by the individual segments (in the order S1, S2, S3, and S4 due to the flow of the feedwaters from one segment to the next), and segmented electrode configuration at maximized overall power (Figure 2.6c), i.e., when the sum of the electrode segments power is maximum. Furthermore, it compares the gross power density contribution (Figure 2.6d) per equivalent segment in the single electrode configuration or per independent segment (segmented electrode configuration). The residence time of 44 s was chosen since the electrode segmentation effect is pronounced at longer residence times. In addition to Figure 2.6, Figure S2.5 illustrates the distribution of the sodium chloride concentration in the river and seawater, the electromotive force, the cell pair resistance, and the current density.

For the single electrode configuration (Figure 2.6a), the electrode segments are electrically connected, and the current is controlled by a single external load (Figure 2.2c). The gross power density value decreases alongside the river water direction (x-axis) since the electromotive force decreases the most with the increase in salinity of the river water (Figure S2.5g), which also results in lower electrical resistance (Figure S2.5j).

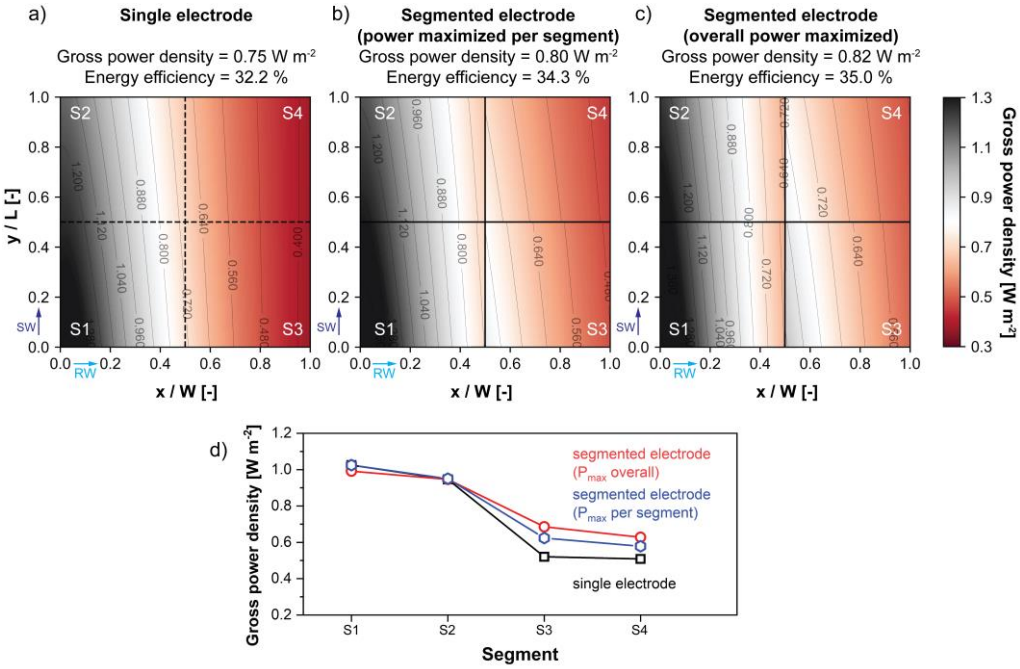

Figure 2.6 Model results for gross power density distribution inside a 22 cm x 22 cm RED stack in a) the single electrode configuration, b) the segmented electrode configuration at maximized power per segment, and c) the segmented electrode configuration at overall maximum power at a residence time of 44 s (flow velocity of 0.5 cm·s^{-1}). The x-axis is the river water path and the y-axis is the seawater path. Note, the grid division in a) is only used to allow an easier comparison with b) and c), as in the single electrode configuration the electrode segments electrically work as one. d) Gross power density contribution per equivalent electrode segment (single electrode) and per electrode segment (segmented electrode at maximized power per individual segment and overall maximum power).

The outcome is different local current densities while the same external load is applied to the stack (Figure S2.5m). The highest gross power density is obtained close to the point where the feedwaters first meet, where the electromotive force is still high, but the electrical resistance of the river water is decreasing due to the rising salt concentration. It can be noted that the current distribution (Figure S2.5m) and the one Vermaas et al. [22] reported are different. This is due to the membrane electrical resistances, they were assumed zero by Vermaas et al., but are considered in the present work. Figures 2.6b and 2.6c show the power distribution using a segmented electrode configuration, with four independent external loads (Figure 2.2d). Again, the gross power density value decreases along the river water due to mixing. However, by adjusting each external load to the internal segment resistance (Fig. S6), the harvested gross power density is higher compared to the single electrode configuration. Fig. S5g-i shows the difference between the electromotive force and the external loads (*E-U* in equation 2.4), which together with the local stack resistance contributes to determining the local current density. In Fig. 6d segments S3 and S4 produce a higher gross power density for both segmented electrode configurations. When adjusting the different loads to reach

the overall maximum power density, S1 is underperforming the equivalent segment in the single electrode configuration. This is because to reach the overall maximum power density, it is beneficial that S1 does not work at its maximum power density, as in Fig. 6b, but preserves part of the salinity gradient for the following electrode segments, thus allowing higher electromotive force in S3 and S4. It may seem counter-intuitive that segments S3 and S4 produce more power when the overall power is maximized rather than when the power per segment is maximized. When the power per segment is maximized the high performance of S1 and S2 comes at the expense of S3 and S4, which experience a lower salinity gradient. At 44 s residence time, the model predicts a 9 % increase in gross power density from a single electrode configuration to the segmented electrode configuration at overall maximum power density. This increase is mainly gained in S3 and S4 (these segments increase power by 24 % and 19 %, respectively). Furthermore, for optimization, it is important to note that the electrode segments work towards the overall maximum power instead of maximizing each segment individually.

2.3.4. The behaviour of a single electrode and a segmented electrode with residence time

In addition to the model results, Figure 2.7 presents a comparison of the experimental and model overall stack gross power densities (Figure 2.7a) and energy efficiencies (Figure 2.7b) for the single electrode and segmented electrode configurations at different residence times when the overall stack power is maximized. In all cases, the model predictions closely resemble the experimental results.

Figure 2.7a shows that the gross power density decreases with increasing residence time. This is consistent with the results from the literature [16,19,28]. The opposite trend is observed in Figure 2.7b, where energy efficiency increases for longer residence times. These trends have been explained by Moreno et al. as the consequence of lower Gibbs free energy per unit time available at longer residence times, in addition to the non-homogenous distribution of electromotive force, cell resistance, and current density in the active membrane area [19].

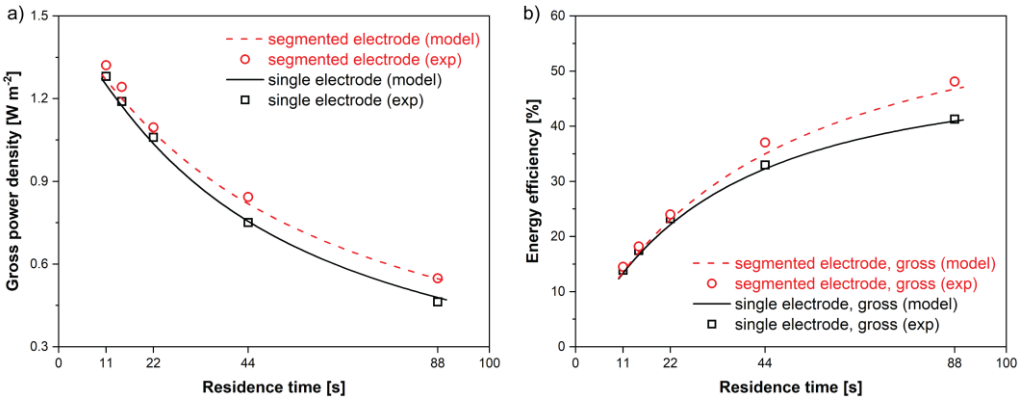

Figure 2.7 a) Gross power density and b) energy efficiency, for single electrode and segmented electrode configurations, as a function of residence time; symbols represent the experimental data (residence time of 11, 15, 22, 44 and 88 s) and the lines represent the model results. Model parameters can be found in Table S2.1.

Additionally, at longer residence times more ion exchange occurs, which results in a lower electromotive force and stack resistance for the segments further away from the water inlets. At longer residence times, for the single electrode configuration, in the region close to the outlets, the locally available electromotive force becomes close to the external voltage load ($E \sim U$), which leads to small current production (equation 2.4), hence only a small power output comes from this region. When the single electrode and the segmented electrode configuration are compared, the adaptation of the external loads to the local electromotive force and local stack resistance (i.e., a lower external load on segments S3 and S4), allows to produce a higher current and therefore a higher power output close to the outlets of the stack. If this is combined with the strategy of saving gradient in the first segments (S1 and S2) to reach the overall maximum power, it explains the higher power production for the segmented electrode configuration compared to the single electrode configuration at all residence times, with a pronounced gain at 44 and 88s.

2.3.5. Electrode segments contribution at different residence times

Data in Figure 2.7 provide the overall stack output, based on the contribution of each electrode segment. The contribution of each electrode is shown in Figure 2.8, providing the voltage load and gross power density for each electrode segment in the segmented electrode configuration at different residence times, when the maximum overall power is achieved.

In Figure 2.8a, for all residence times, the external load voltages on S1 and S2 are similar despite the different extent of ion exchange occurring at different residence times. This indicates that to maximize the overall power segments S1 and S2 work at a sub-optimal point to save gradient for segments S3 and S4. When the feedwaters reach segments S3 and S4, major ion exchange has occurred and the salinity gradient has significantly decreased, with

the highest decrease in S4. Since the salinity gradient is considerably lowered in S3 and S4, the external loads need to be adjusted accordingly. Fig. 8a shows that for increasing residence times, the external load voltages for S3 and S4 are decreasing. To achieve maximum power output on these electrode segments, the required external load voltage is lower than for S1 and S2. It can be noted in Figure S2.7 that the predicted load voltages, with the model, at maximum power density in the segmented electrode configuration closely resembles the experimentally identified set of values. This agreement between the model and experiment highlights the value of the model in guiding the optimization of the external loads. In Figure 2.8b, the gross power density per electrode segment is presented. At short residence times, the power output of the four segments is very similar, but with increasing residence times and consequently increased ion exchange, the power density produced by the electrode segments located further away from the river water inlet (S3 and S4) decreases. Interestingly, at short residence times, the load voltages required to produce similar power densities are lower for S3 and S4 than for S1 and S2. This is the case because S1 and S2 operate with a higher electromotive force, but also higher stack resistance. S3 and S4 have a lower electromotive force available but benefit from the increased conductivity of the river water, leading to lower stack electrical resistance and comparable gross power density for all segments.

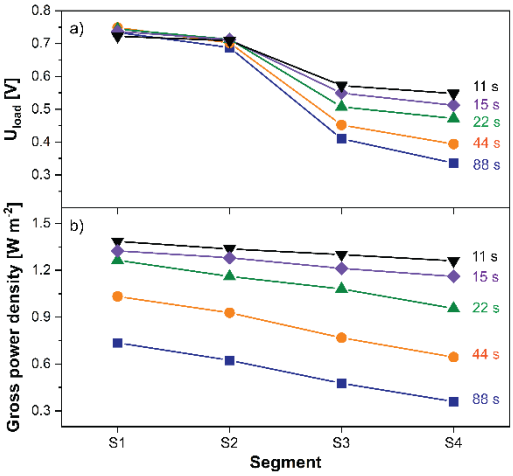

Figure 2.8 Individual segment contribution (experimental) at different residence times (11, 15, 22, 44, and 88 s) when the overall stack power is maximized. a) The voltage drops over the external load voltage per segment. b) Gross power density per electrode segment.

Figure 2.8a shows that the optimal load voltages for S1 and S2 are similar, and the same applies to S3 and S4. The large difference in an optimal external load along the river water and the small difference along the seawater flow direction indicates that segmentation along the river water is more beneficial than along the seawater. This is the case because the electromotive force is most sensitive to the salinity of the river water (Figures S2.5g and S2.5i).

To investigate this hypothesis in further detail, Figure 2.9 presents the model results of a 2 x 2 electrode segmentation (Figure 2.3d) and a 2 x 1 configuration (along the river flow direction only).

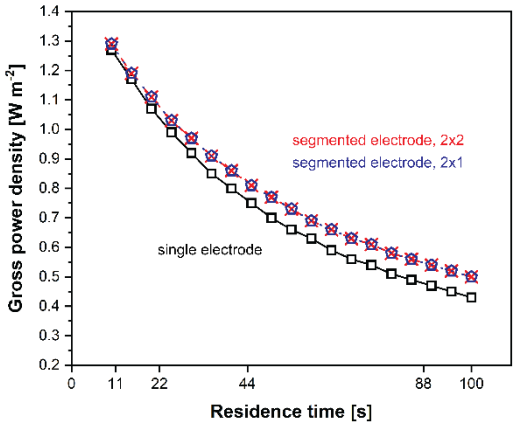

Figure 2.9 Modelled gross power density as a function of the residence time for a single electrode, two electrode segments (2 x 1, in the river water flow direction), and four-electrode segments (2 x 2) in a 22 cm x 22 cm stack.

The results are nearly identical, with only very small differences at high residence times, between the segmented electrode configurations. This confirms that a simpler configuration with electrode segmentation only along the river water direction, as proposed by Vermaas et al [22], would yield the same power increase as segmentation along both river and sea directions. Nevertheless, the additional complexity of a 2 x 2 configuration allows for the operational flexibility required by feedwater switch strategies, i.e., changing seawater for river water and vice versa, which have been proved to be beneficial for fouling management [42].

2.3.6. Net power density and net energy efficiency

Fig. 10a shows the pumping power density, which significantly decreases with increasing residence time as longer residence times imply lower feed flow velocities. At short residence times, the pumping power densities are increasing rapidly due to the increase in pressure drop inside the stack [16]. Meanwhile, at long residence times, a flat region is reached where the pumping losses become negligible, being the ideal working region to avoid pumping losses.

Figure 2.10b shows the net power density, i.e., the gross power density minus the pumping power density, plotted against the net energy efficiency. Electrode segmentation leads to higher net power density and efficiency at residence times longer than 11s. This is the case due to the maximized overall power production. The increased ion exchange for the segmented electrode is evident in the decreased gradient at the stack outlet in Figure S2.4b.

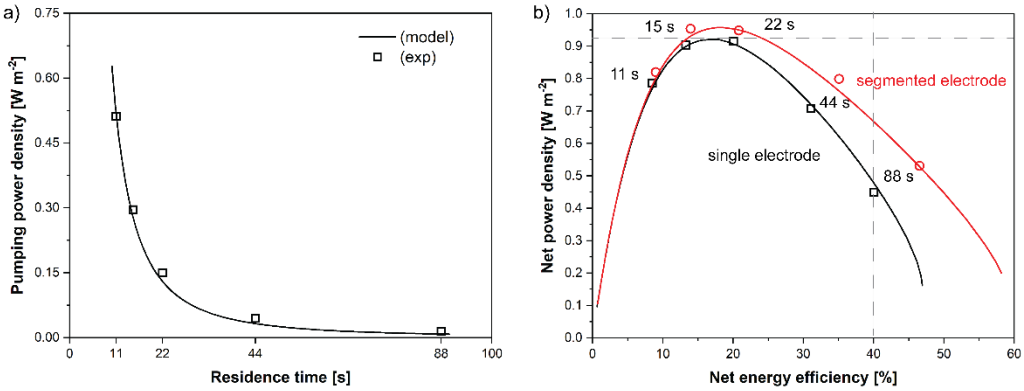

Figure 2.10 a) Pumping power density as a function of residence time. b) Net power density as a function of net energy efficiency for the single electrode and segmented electrode configurations at different residence times. Symbols represent experimental data (residence time of 11, 15, 22, 44 and 88 s) and lines show the model results.

The greatest benefit of applying electrode segmentation is reported in Figure 2.10b. Both configurations achieve maximum net power density at approximately 17 % net energy efficiency and short residence times. This relatively low net energy efficiency is not beneficial for up-scaling RED when the cost of water pre-treatment to decrease fouling is a relevant fraction of the operating costs. To minimize this cost, the energy efficiency should be as high as possible without sacrificing power density. Figure 2.10b shows that electrode segmentation accomplishes this requirement. Comparing both electrode configurations at the net power density at the peak performance for a single electrode (0.92 $W \cdot m^{-2}$), segmentation increases the net energy efficiency from 17 % for the single electrode to 25 % for the segmented electrode (horizontal line in Figure 2.10b), which is a remarkable 43 % relative efficiency increase. This increase in efficiency allows the extraction of the same power from less water, which is likely to reduce the operating costs of a full-scale RED power plant by reducing the need for water pre-treatment. At 40 % net energy efficiency (vertical line in Figure 2.10b) the net power output for the segmented electrode configuration is enhanced by 39 % relative to a single electrode, which is likely to translate in a lower capital cost for a full-scale plant, as a smaller membrane area is required to achieve a given power production target. Although promising, testing in a larger scale RED system, i.e., more cell pairs, fed with natural feedwaters is necessary to confirm the benefits of electrode segmentation on capital and operating costs. For a segmented electrode, the same net energy efficiency can be reached at a shorter residence time. As the process is more efficient, higher net power densities can be achieved. Therefore, the increase in net power density for a segmented electrode results from combining the increase in power due to shorter residence time (more Gibbs free energy available per unit time) and the increased energy extraction enabled by electrode segmentation. This is especially true in the long residence time region (20-90 s), due to the tuning of the external loads allowing additional power production in S3 and S4. Electrode

segmentation thus reduces the trade-off between energy efficiency and power density generation, which is a critical element of the RED process to be considered for large-scale RED plants.

2.4. Conclusions

The present work shows with a validated RED model and experimental investigation that electrode segmentation potentially reduces operating cost or capital expenditure. Operating cost likely decreases by increasing net energy efficiency at a given net power density (43 % relative increase in efficiency), which is beneficial in case of high water pre-treatment costs to control fouling. Capital expenditure likely lowers at high net energy efficiencies by increasing the net power density with electrode segmentation decreasing the membrane area needed.

The highest gain is attained when optimizing the external loads for overall maximum power, rather than sequentially maximizing the power output of individual segments. At 40 % net energy efficiency, the net power output for a segmented electrode is 39 % higher (0.67 $W \cdot m^{-2}$) than a single electrode (0.47 $W \cdot m^{-2}$). This increase in net power density at equal net energy efficiency results from combining the increase in power due to shorter residence time and the increased ion exchange enabled by electrode segmentation. This is especially true in the long residence time region (20-90 s), due to the tuning of the external ohmic loads allowing additional power production in the segments adjacent to the river water outlet.

These experiments were conducted at a laboratory scale with 10 cell pairs. The effect of electrode segmentation in a larger membrane pile needs therefore further study. Experiments and the model confirm that segmenting along the river water direction in a cross-flow stack gives the most benefit, indicating that segmentation can be simplified to two rectangular electrode segments when switching the feedwaters is not required.

2.5. Supporting information

2.5.1. RED stack

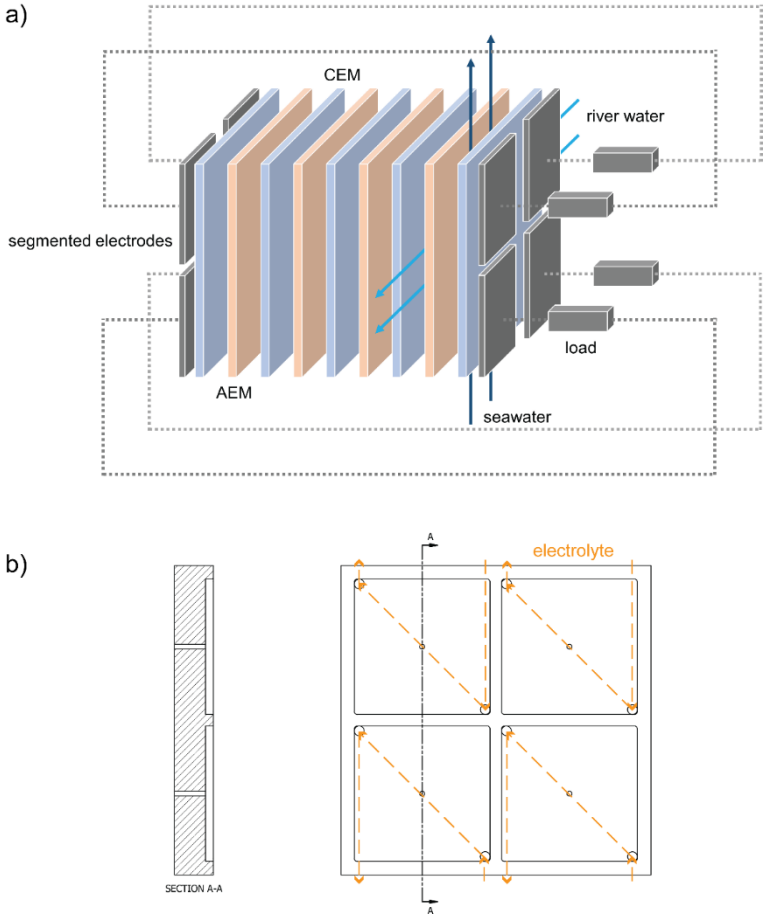

Figure S2.1 a) Schematic representation of the cross-flow stack with segmented electrodes. b) Schematic drawing of the end-plate housing with four electrode segments (not intended as a technical drawing, design and dimension do not reflect the real end-plate). The electrodes are separated by a ridge of 1.5 cm width and the electrolyte solutions are recirculated in four independent circuits. The end-plate housing was designed and made by REDstack BV (The Netherlands).

Table S2.1 Parameters used in the model calculations and procedures to evaluate them.

Parameter	Symbol	Value	Unit	Evaluation procedure
Width of the active area	W	0.22	m	Known stack parameter.
Length of the active area	L	0.22	m	Known stack parameter.
Compartment thickness	d	155×10^{-6}	m	Known stack parameter.
AEM permselectivity	α_{aem}	94.5	%	Literature data [19].
CEM permselectivity	α_{cem}	94.7	%	Literature data [19].
AEM electrical resistance	R_{aem}	1.77×10^{-4}	$\Omega \cdot m^2$	Measurement in a six-compartment cell at 0.5 M NaCl, according to a literature procedure [43].
CEM electrical resistance	R_{cem}	2.69×10^{-4}	$\Omega \cdot m^2$	Measurement in a six-compartment cell at 0.5 M NaCl, according to a literature procedure [43].
Spacer shadow factor	f	0.61	-	The initial value is 0.55, corresponding to the open area of the spacer netting. The value is then adjusted based on I-V data from 22 cm x 22 cm stack with a single electrode.
Average water diffusion coefficient (through the membranes)	D_{H2O}	1.5×10^{-10}	$m^2 \cdot s^{-1}$	Literature data [19]. Permeability is converted into a diffusion coefficient based on the measurement procedure presented in [44].
Average salt diffusion coefficient (through the membranes)	D_{NaCl}	6.5×10^{-12}	$m^2 \cdot s^{-1}$	Calibration with I-V data from 22 cm x 22 cm stack with single electrode.
Membrane thickness	l_m	125×10^{-6}	m	Literature data [19].
Blank resistance	R_{blank}	37.5×10^{-4}	$\Omega \cdot m^2$	Calibration with data from 22 cm x 22 cm stack with single electrode.
Pressure drop coefficient	K_{dP}	0.1945	Pa·s	Calibration with experimental pressure drop data from 22 cm x 22 cm stack with single electrode.

2.5.2. Calibration curve: salt concentration and electrical conductivity

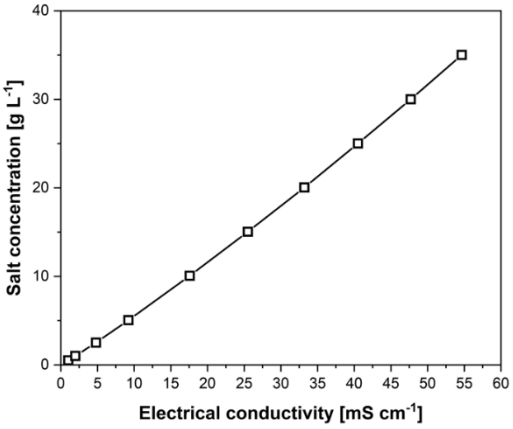

Figure S2.2 Relationship between NaCl concentration and electrical (ionic) conductivity of the solution at 25°C.

2.5.3. Electrical circuit for segmented electrode configuration

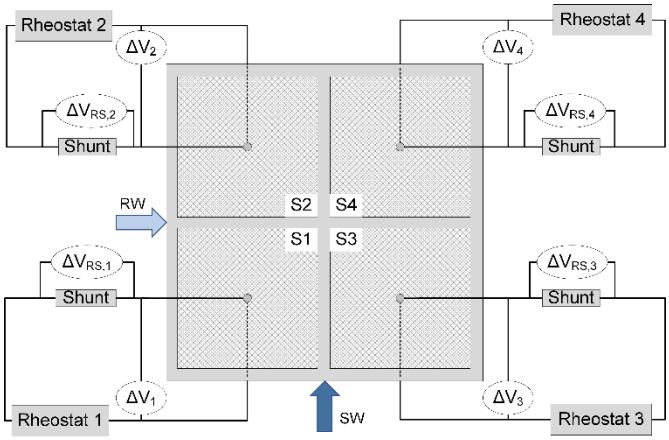

Figure S2.3 Electrical circuit for the segmented electrode stack configuration with separate external loads.

2.5.4. Change in NaCl concentration at the outlet

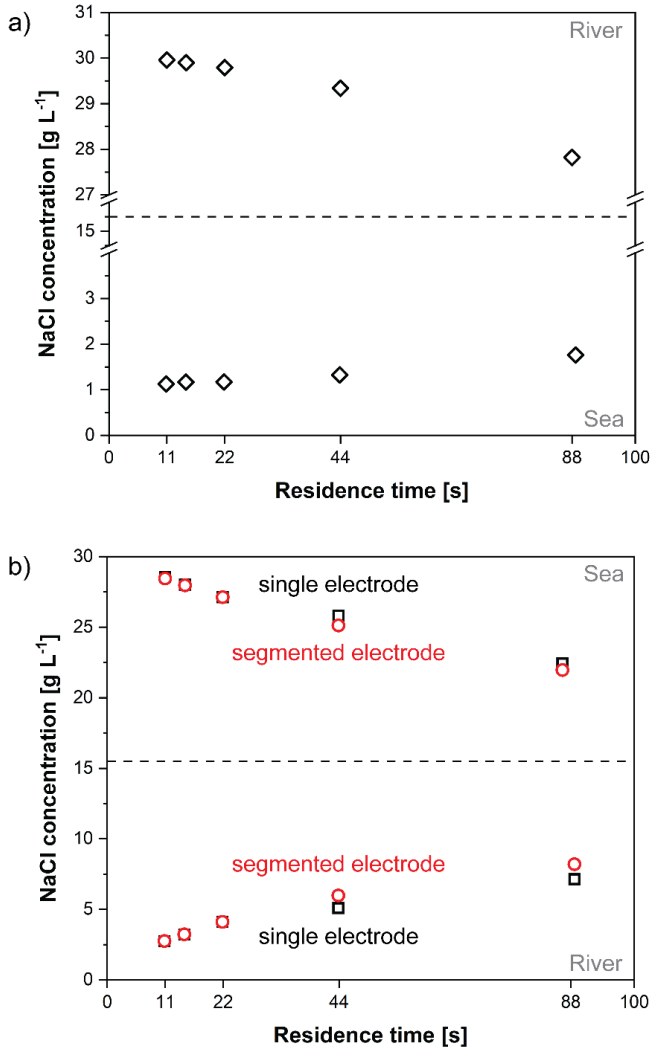

Figure S2.4 Sodium chloride concentration at the river and seawater outlets as a function of the residence time inside the stack. a) stack under OCV conditions (the electrode configuration does not influence this experiment). b) stack working at maximum power density, single and segmented electrode configurations.

2.5.5. Experimental open circuit voltage for a segmented electrode (per segment) and a single electrode at different residence times

Table S2.2 OCV values, in Volts, for each electrode segment of a segmented electrode and a single electrode configuration, at different residence times. The OCV values for each electrode segment/ single electrode were found to be reproducibly different.

	S1	S2	S3	S4	Single Electrode
88 s	1.478	1.458	1.387	1.362	1.400
44 s	1.524	1.513	1.469	1.455	1.473
22 s *	1.542	1.533	1.512	1.499	1.521
15 s	1.552	1.549	1.531	1.526	1.534
11 s	1.552	1.550	1.534	1.532	1.543

* These values differ slightly from the ones in section 2.3.2 since they belong to a different set of experiments.

2.5.6. NaCl concentration, potential, cell pair resistance, and current density plots for 44 s residence time

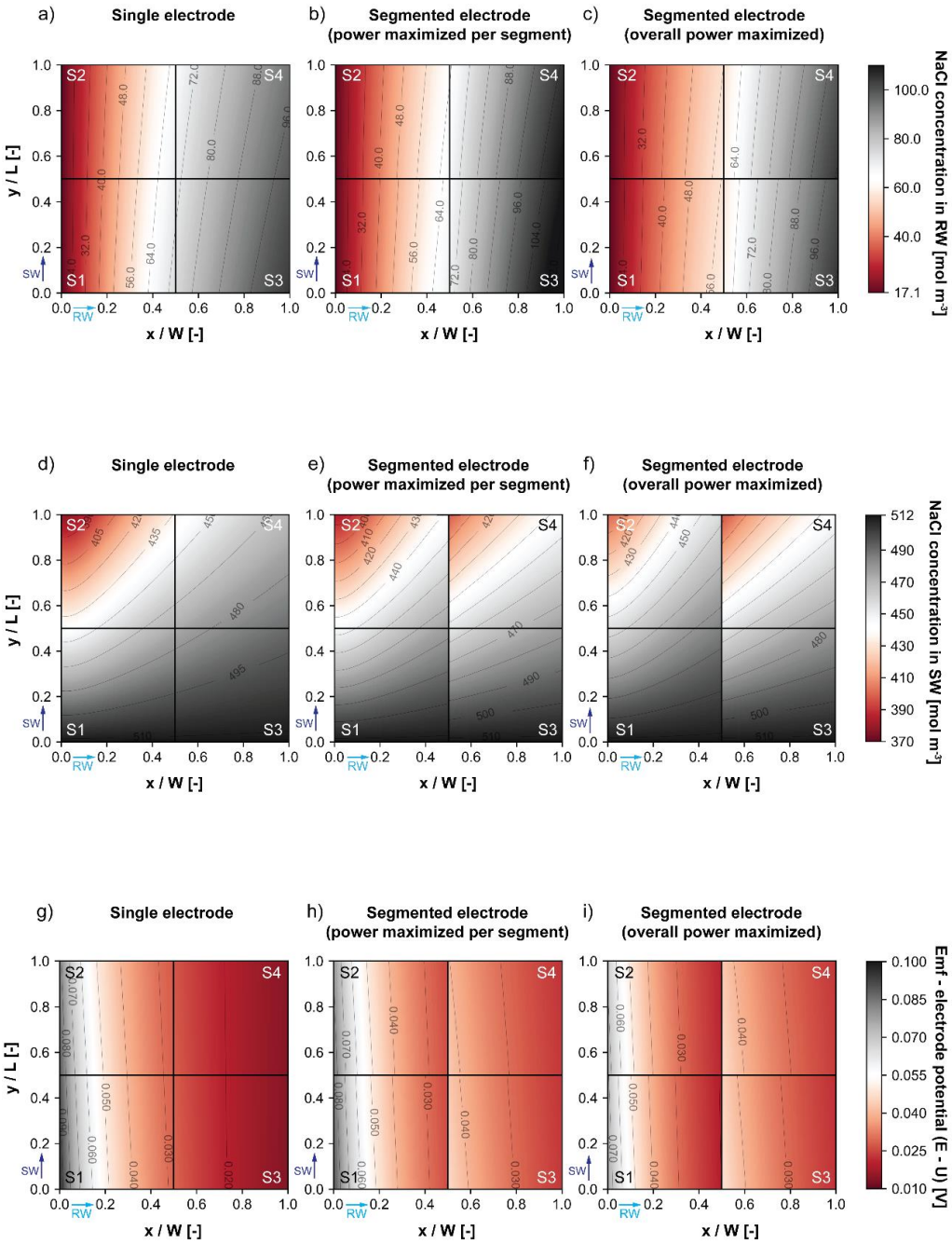

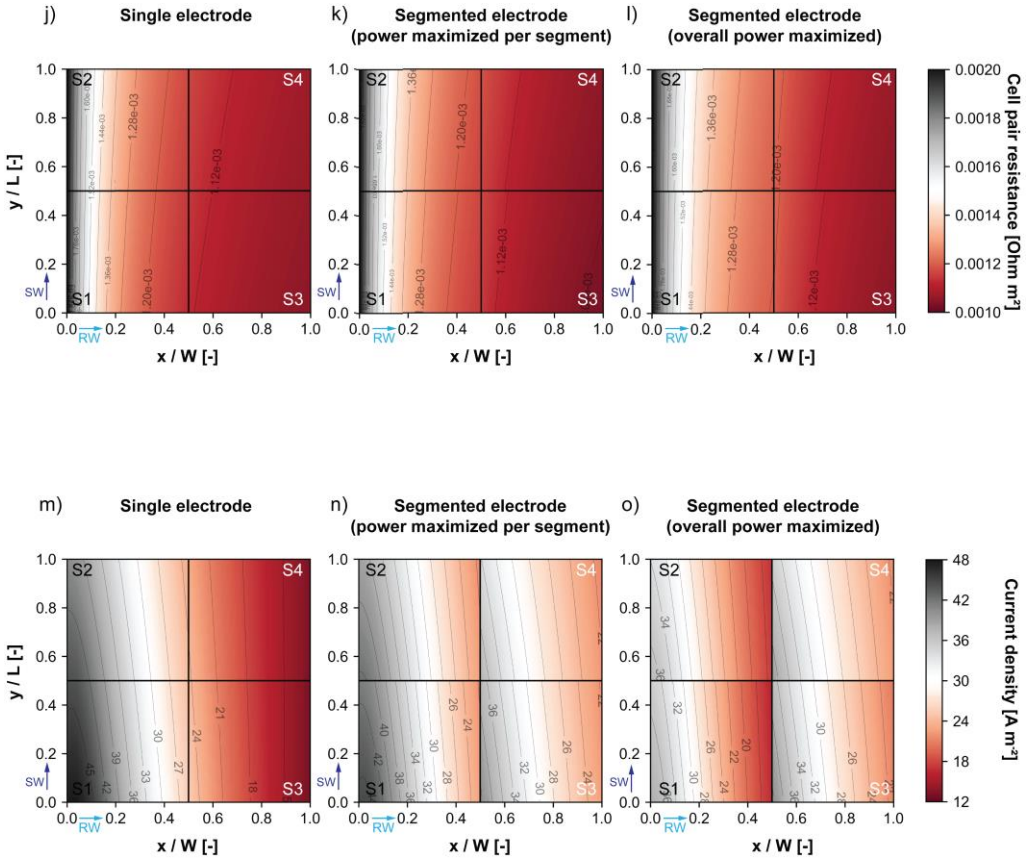

Figure S2.5 Model results for a 22 cm x 22 cm RED stack at a residence time of 44 s (flow velocity of 0.5 cm·s^{-1}). NaCl concentration in river water for **a)** the single electrode configuration, **b)** the segmented electrode configuration at maximized power per segment and **c)** the segmented electrode configuration at overall maximum power. NaCl concentration in seawater for **d)** the single electrode configuration, **e)** the segmented electrode configuration at maximized power per segment, and **f)** the segmented electrode configuration at overall maximum power. Difference between the electromotive force (emf) and the electrode potential (E-U in equation 2.4) for **g)** the single electrode configuration, **h)** the segmented electrode configuration at maximized power per segment, and **i)** the segmented electrode configuration at overall maximum power. Cell pair resistance for **j)** the single electrode configuration, **k)** the segmented electrode configuration at maximized power per segment, and **l)** the segmented electrode configuration at overall maximum power. Current density distribution for **m)** the single electrode configuration, **n)** the segmented electrode configuration at maximized power per segment, and **o)** the segmented electrode configuration at overall maximum power. The x-axis is the river water path and the y-axis is the seawater path. Note, the grid division in a single electrode configuration is only used to allow an easier comparison with a segmented electrode configuration.

2.5.7. Model of the individual segment contribution for different configurations at 44 s residence time

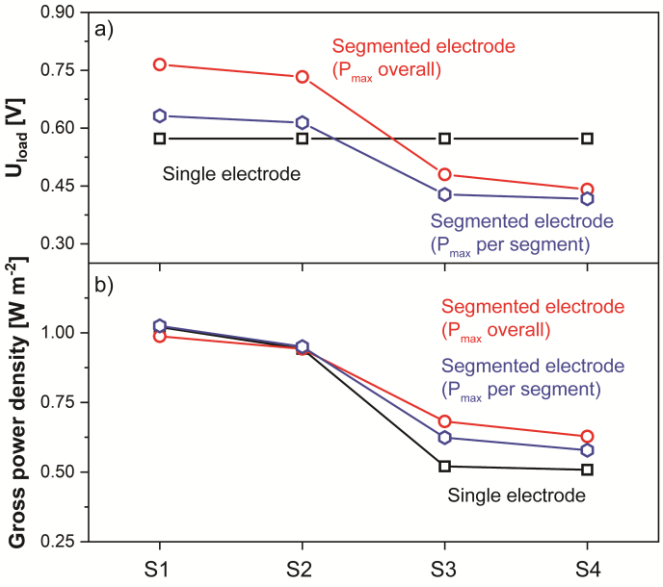

Figure S2.6 Individual segment contribution (model) for a single electrode configuration, a segmented electrode configuration with maximized power per segment, and a segmented electrode configuration with overall maximum power, at 44 s residence time.

2.5.8. External loads voltages

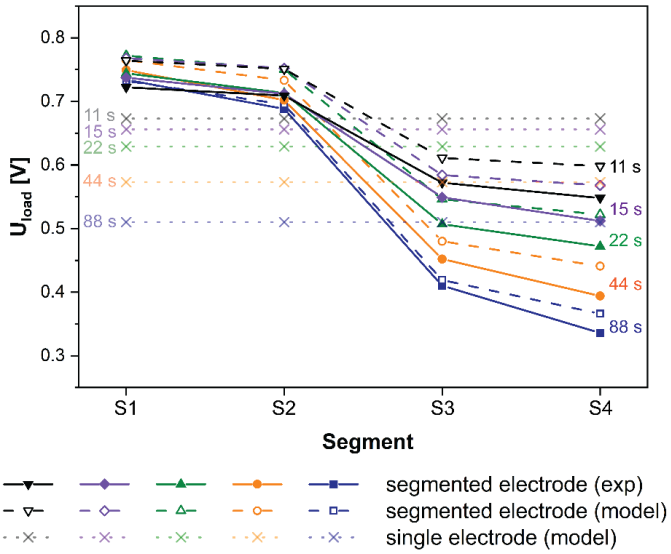

Figure S2.7 External load voltage of the four electrode segments at maximum power density for the five investigated residence times. Full symbols and solid lines for experimental values are shown for a segmented electrode configuration. Empty symbols and dashed lines are given for the model values in a segmented electrode configuration. Crosses and dotted lines for the model values are displayed in a single electrode configuration.

References

[1] U.N.F. Convention on Climate Change, Paris Agreement, (2015). https://unfccc.int/files/essential_background/convention/application/pdf/english_paris_agreement.pdf (accessed January 21, 2020).

[2] W.J. Van Egmond, M. Saakes, S. Porada, T. Meuwissen, C.J.N. Buisman, H.V.M. Hamelers, The concentration gradient flow battery as electricity storage system: Technology potential and energy dissipation, J. Power Sources. (2016). doi:10.1016/j.jpowsour.2016.05.130.

[3] J. Veerman, M. Saakes, S.J. Metz, G.J. Harmsen, Reverse electrodialysis: Performance of a stack with 50 cells on the mixing of sea and river water, J. Memb. Sci. (2009). doi:10.1016/j.memsci.2008.11.015.

[4] J. Kuleszo, C. Kroeze, J. Post, B.M. Fekete, The potential of blue energy for reducing emissions of CO2 and non-CO2 greenhouse gases, J. Integr. Environ. Sci. (2010). doi:10.1080/19438151003680850.

[5] R.E. Pattle, Production of electric power by mixing fresh and salt water in the hydroelectric pile, Nature. (1954). doi:10.1038/174660a0.

[6] R.E. Lacey, Energy by reverse electrodialysis, Ocean Eng. 7 (1980) 1–47. doi:10.1016/0029-8018(80)90030-x.

[7] E. Güler, W. van Baak, M. Saakes, K. Nijmeijer, Monovalent-ion-selective membranes for reverse electrodialysis, J. Memb. Sci. (2014). doi:10.1016/j.memsci.2013.12.054.

[8] H. Gao, B. Zhang, X. Tong, Y. Chen, Monovalent-anion selective and antifouling polyelectrolytes multilayer anion exchange membrane for reverse electrodialysis, J. Memb. Sci. (2018). doi:10.1016/j.memsci.2018.09.035.

[9] X.L. Wang, M. Wang, Y.X. Jia, B.B. Wang, Surface Modification of Anion Exchange Membrane by Covalent Grafting for Imparting Permselectivity between Specific Anions, Electrochim. Acta. (2015). doi:10.1016/j.electacta.2015.06.115.

[10] D.A. Vermaas, M. Saakes, K. Nijmeijer, Power generation using profiled membranes in reverse electrodialysis, J. Memb. Sci. (2011). doi:10.1016/j.memsci.2011.09.043.

[11] D.A. Vermaas, M. Saakes, K. Nijmeijer, Early detection of preferential channeling in reverse electrodialysis, Electrochim. Acta. (2014). doi:10.1016/j.electacta.2013.11.094.

[12] Z. He, X. Gao, Y. Zhang, Y. Wang, J. Wang, Revised spacer design to improve hydrodynamics and anti-fouling behavior in reverse electrodialysis processes, Desalin. Water Treat. (2016). doi:10.1080/19443994.2016.1186569.

[13] J. Moreno, N. de Hart, M. Saakes, K. Nijmeijer, CO 2 saturated water as two-phase flow for fouling control in reverse electrodialysis, Water Res. (2017). doi:10.1016/j.watres.2017.08.015.

[14] E.J. Bodner, M. Saakes, T. Sleutels, C.J.N. Buisman, H.V.M. Hamelers, The RED Fouling Monitor: A novel tool for fouling analysis, J. Memb. Sci. (2019). doi:10.1016/j.memsci.2018.10.059.

[15] D. Pintossi, M. Saakes, Z. Borneman, K. Nijmeijer, Electrochemical impedance spectroscopy of a reverse electrodialysis stack: A new approach to monitoring fouling and cleaning, J. Power Sources. 444 (2019) 227302. doi:10.1016/j.jpowsour.2019.227302.

[16] D.A. Vermaas, M. Saakes, K. Nijmeijer, Doubled power density from salinity gradients at reduced intermembrane distance, Environ. Sci. Technol. (2011). doi:10.1021/es2012758.

[17] S. Pawlowski, T. Rijnaarts, M. Saakes, K. Nijmeijer, J.G. Crespo, S. Velizarov, Improved fluid mixing and power density in reverse electrodialysis stacks with chevron-profiled membranes, J. Memb. Sci. (2017). doi:10.1016/j.memsci.2017.03.003.

[18] I. Choi, J.Y. Han, S.J. Yoo, D. Henkensmeier, J.Y. Kim, S.Y. Lee, J. Han, S.W. Nam, H.J. Kim, J.H. Jang, Experimental investigation of operating parameters in power generation by lab-scale reverse electro-dialysis (RED), Bull. Korean Chem. Soc. (2016). doi:10.1002/bkcs.10810.

[19] J. Moreno, S. Grasman, R. van Engelen, K. Nijmeijer, Up-scaling reverse electrodialysis, Environ. Sci. Technol. (2018). doi:10.1021/acs.est.8b01886.

[20] J. Veerman, J.W. Post, M. Saakes, S.J. Metz, G.J. Harmsen, Reducing power losses caused by ionic shortcut currents in reverse electrodialysis stacks by a validated model, J. Memb. Sci. (2008). doi:10.1016/j.memsci.2007.11.032.

[21] J. Veerman, M. Saakes, S.J. Metz, G.J. Harmsen, Reverse electrodialysis: A validated process model for design and optimization, Chem. Eng. J. 166 (2011) 256–268. doi:10.1016/j.cej.2010.10.071.

[22] D.A. Vermaas, J. Veerman, N.Y. Yip, M. Elimelech, M. Saakes, K. Nijmeijer, High efficiency in energy generation from salinity gradients with reverse electrodialysis, ACS Sustain. Chem. Eng. (2013). doi:10.1021/sc400150w.

[23] M. Ciofalo, M. La Cerva, M. Di Liberto, L. Gurreri, A. Cipollina, G. Micale, Optimization of net power density in Reverse Electrodialysis, Energy. 181 (2019) 576–588. doi:10.1016/j.energy.2019.05.183.

[24] M. Tedesco, A. Cipollina, A. Tamburini, W. van Baak, G. Micale, Modelling the Reverse ElectroDialysis process with seawater and concentrated brines, Desalin. Water Treat. 49 (2012) 404–424. doi:10.1080/19443994.2012.699355.

[25] J.W. Post, C.H. Goeting, J. Valk, S. Goinga, J. Veerman, H.V.M. Hamelers, P.J.F.M. Hack, Towards implementation of reverse electrodialysis for power generation from salinity gradients, Desalin. Water Treat. 16 (2010) 182–193. doi:10.5004/dwt.2010.1093.

[26] M. Tedesco, A. Cipollina, A. Tamburini, G. Micale, Towards 1 kW power production in a reverse electrodialysis pilot plant with saline waters and concentrated brines, J. Memb. Sci. 522 (2017) 226–236. doi:10.1016/j.memsci.2016.09.015.

[27] A. Daniilidis, R. Herber, D.A. Vermaas, Upscale potential and financial feasibility of a reverse electrodialysis power plant, Appl. Energy. (2014). doi:10.1016/j.apenergy.2013.12.066.

[28] J. Veerman, M. Saakes, S.J. Metz, G.J. Harmsen, Electrical power from sea and river water by reverse electrodialysis: A first step from the laboratory to a real power plant, Environ. Sci. Technol. (2010). doi:10.1021/es1009345.

[29] D.A. Vermaas, D. Kunteng, M. Saakes, K. Nijmeijer, Fouling in reverse electrodialysis under natural conditions, Water Res. (2013). doi:10.1016/j.watres.2012.11.053.

[30] A.M. Weiner, R.K. McGovern, J.H. Lienhard V., A new reverse electrodialysis design strategy which significantly reduces the levelized cost of electricity, J. Memb. Sci. 493 (2015) 605–614. doi:10.1016/j.memsci.2015.05.058.

[31] M. Geske, M. Heuer, G. Heideck, Z.A. Styczynski, Current density distribution mapping in PEM fuel cells as an instrument for operational measurements, Energies. (2010). doi:10.3390/en3040770.

[32] M. Noponen, T. Mennola, M. Mikkola, T. Hottinen, P. Lund, Measurement of current distribution in a free-breathing PEMFC, in: J. Power Sources, 2002. doi:10.1016/S0378-7753(01)01063-1.

[33] J.T. Clement, D.S. Aaron, M.M. Mench, In situ localized current distribution measurements in all-vanadium redox flow batteries, J. Electrochem. Soc. (2016). doi:10.1149/2.0241601jes.

[34] A. Bhattarai, N. Wai, R. Schweiss, A. Whitehead, G.G. Scherer, P.C. Ghimire, T.D. Nguyen, H.H. Hng, Study of flow behavior in all-vanadium redox flow battery using spatially resolved voltage distribution, J. Power Sources. (2017). doi:10.1016/j.jpowsour.2017.06.039.

[35] D. Tvrzník, Effect of electrode area on demineralization performance and the distribution of current density in an industrial-scale electrodialysis stack, Desalination. (2017). doi:10.1016/j.desal.2017.03.002.

[36] G. Doornbusch, H. Swart, M. Tedesco, J. Post, Z. Borneman, K. Nijmeijer, Current utilization in electrodialysis: Electrode segmentation as alternative for multistaging, Desalination. 480 (2020) 114243. doi:10.1016/j.desal.2019.114243.

[37] X. Ge, X. Wang, M. Zhang, S. Seetharaman, Correlation and prediction of activity and osmotic coefficients of aqueous electrolytes at 298.15 K by the modified TCPC model, J. Chem. Eng. Data. (2007). doi:10.1021/je060451k.

[38] J. Moreno, E. Slouwerhof, D.A. Vermaas, M. Saakes, K. Nijmeijer, The Breathing Cell: Cyclic Intermembrane Distance Variation in Reverse Electrodialysis, Environ. Sci. Technol. (2016). doi:10.1021/acs.est.6b02668.

[39] J. Moreno, REDstack, Private communication, 2019.

[40] J. Veerman, R.M. de Jong, M. Saakes, S.J. Metz, G.J. Harmsen, Reverse electrodialysis: Comparison of six commercial membrane pairs on the thermodynamic efficiency and power density, J. Memb. Sci. (2009). doi:10.1016/j.memsci.2009.05.047.

[41] M.L. La Cerva, M. Di Liberto, L. Gurreri, A. Tamburini, A. Cipollina, G. Micale, M. Ciofalo, Coupling CFD with a one-dimensional model to predict the performance of reverse electrodialysis stacks, J. Memb. Sci. 541 (2017) 595–610. doi:10.1016/j.memsci.2017.07.030.

[42] D.A. Vermaas, D. Kunteng, J. Veerman, M. Saakes, K. Nijmeijer, Periodic feedwater reversal and air sparging as antifouling strategies in reverse electrodialysis, Environ. Sci. Technol. (2014). doi:10.1021/es4045456.

[43] P. Długołecki, K. Nymeijer, S. Metz, M. Wessling, Current status of ion exchange membranes for power generation from salinity gradients, J. Memb. Sci. (2008). doi:10.1016/j.memsci.2008.03.037.

[44] J.A.W. Van Engelen, Composite membranes, U.S. 9,713,792, 2017.

Chapter 3

Optimizing multistage reverse electrodialysis for enhanced energy recovery from river water and seawater: Experimental and modelling investigation

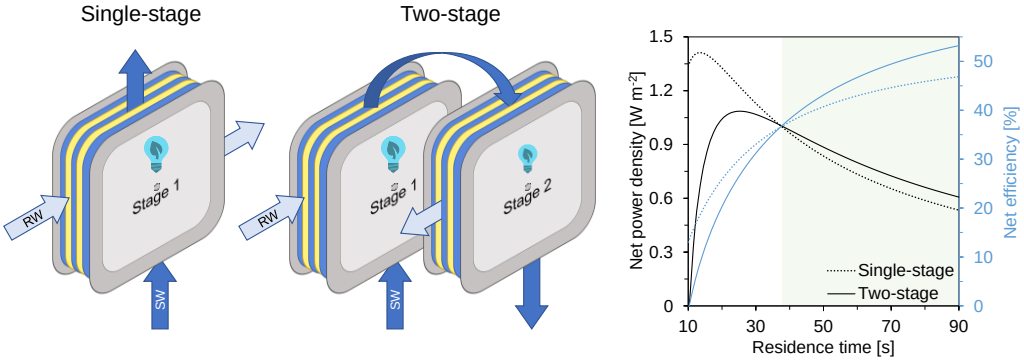

Abstract

Reverse electrodialysis has been established as a promising method to harvest salinity gradient energy. To achieve market viability, an optimum process configuration is needed, in addition to material and stack development, to increase energy efficiency without compromising power density. Multistage reverse electrodialysis is a practical strategy providing several degrees of freedom, such as independent electrical control of the stages, asymmetric staging, and different configurations. This study tests a two-stage configuration experimentally, using seawater and river water (NaCl only), at several residence times and changing the electrical control. Furthermore, the results are compared with a numerical model that is subsequently used to predict the behaviour of alternative multistage configurations. The results show that multistage reverse electrodialysis yields higher gross power density and energy efficiency than a single-stage configuration fed with the same salinity gradient. A new strategy named "saving the gradient" (i.e., lowering the discharge current in the first stage) increased the gross overall performance of the two stages up to 17 % relative to a single-stage and up to 6 % relative to a sequentially optimized two-stage system. Modelling different configurations revealed that only two stages are needed when feeding seawater and river water. When retrieving 40 % net energy efficiency, the net power density for a single stage is 0.86 $W \cdot m^{-2}$ and 0.94 $W \cdot m^{-2}$ for a two-stage system, representing an improvement of 9 %. Multistage reverse electrodialysis is therefore a viable concept to enhance power and energy efficiency and benefits from optimization through electrical control.

This chapter has been published as:

C. Simões, D. Pintossi, M. Saakes and W. Brilman, 2021. Optimizing multistage reverse electrodialysis for enhanced energy recovery from river water and seawater: Experimental and modeling investigation. Advances in Applied Energy, 2, p.100023, https://doi.org/10.1016/j.adapen.2021.100023

3.1. Introduction

Providing renewable and sustainable energy has become a priority to reduce CO_2 emissions and overcome dependence on fossil fuels [1]. With a worldwide technical potential estimated at 984 GW in natural environments (Figure 3.1), salinity gradient energy (SGE) is a promising resource to help fulfil the need for renewable energy [2]. SGE is a CO_2-free, renewable energy source available from mixing waters with different salinity content [3]. It is environmentally friendly since it makes use of the hydrological cycle, and is non-intermittent because the low salinity river water always flows to the saline sea, although with flux fluctuations associated with the season. Reverse electrodialysis (RED) is one of several technologies [4] that can be used to harvest SGE [5], particularly when the feed solutions are seawater and river water [6]. RED is a membrane-based process requiring a RED stack which comprises multiple cell pairs. Each cell pair is composed of one cation exchange membrane (CEM), one low salinity concentration compartment (i.e., river water), one anion exchange membrane (AEM), and one high concentration compartment (i.e., seawater). Ions present in the seawater compartment cross selectively through opposing ion exchange membranes (IEMs): anions cross the AEM from the seawater to the river water, while cations pass the CEM from the seawater to the river water, thereby generating a potential across the membranes, known as the Donnan potential [7]. The ionic current generated inside the stack is converted to an electrical current at the electrodes (enclosing the membrane pile) via redox reactions [9]. The

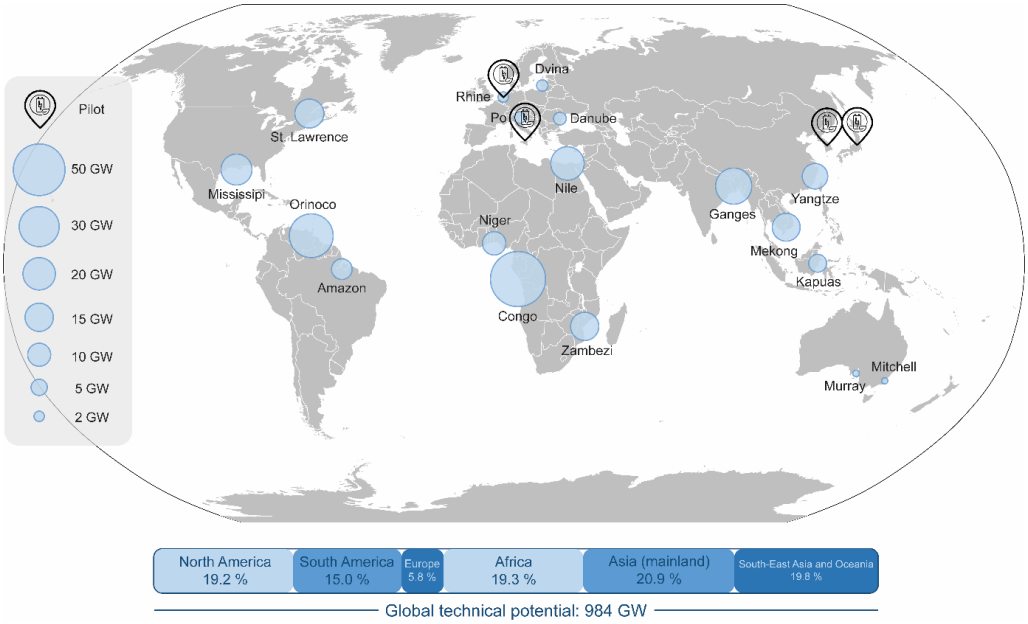

Figure 3.1 World map with marked areas where the RED technology can be potentially implemented to harvest SGE and the location of the four RED pilot-plants. Technical potential data from [8].

maturity of the technology has resulted in four pilot-scale plants at four different locations [10–13]. Figure 3.1 shows the pilot-scale plant locations and how RED can potentially be implemented worldwide to harvest SGE from delta areas where the rivers meet the sea or ocean.

Achieving a continuous production of at least 2 $W \cdot m^{-2}$ net power density at 40 % energy efficiency is considered to make RED competitive with other renewable energy sources [10]. Up to now, power density and energy efficiency have been mainly improved individually by modifying the stack components [14] (i.e., membranes and spacers). However, methods that provide the highest RED power densities, which overcome capital costs, come at the expense of low energy efficiency, which is vital to balance operational costs. Adam et al. evaluated the influence of the trade-off between power and efficiency at the stack level [15].

Working at maximum power conditions limits the produced energy to a maximum of 50 % of the total available energy. This is because half of the available mixing energy is lost via the internal stack resistance, and another small part of the energy is lost as co-ion transport and osmosis through the membranes [16]. Furthermore, the ion-exchange along the stack causes the salinity gradient to decrease from inlet to outlet. Consequently, the electrochemical conditions differ along the stack resulting in potential losses [17]. Our recent study [18] shows electrode segmentation as one strategy to compensate for this effect and to optimize the utilization of the membrane area.

Another proposed strategy to achieve the 2 $W \cdot m^{-2}$ net power density and 40 % net energy efficiency required for market viability is staging the RED operation. With staged RED, process conditions can be adjusted to match stage characteristics resulting in an optimized process. Multistage RED is a promising strategy that allows for independent electrical control of each stage (each stack). Thus, each stage can have a different output voltage, adapting to a change in electromotive force (change in salinity gradient) [17]. In addition to stack voltage independence, which is also achieved with electrode segmentation in a single stage [18], new degrees of freedom are introduced to the RED multistage operation, such as asymmetric staging [19] and the possibility of feed recirculation [20]. This operational mode enables pre-treated water to be used more efficiently by passing it through more than one stage. Such a feature is especially relevant in the case of a limited feedwater supply or high feedwater pre-treatment costs.

The multistage operation has shown benefits in other technologies, such as pressure retarded osmosis [21] and electrodialysis (ED) [22]. Multistage ED allows different currents to be applied to each stage, enhancing desalination degrees while reducing the energy costs associated with the process [23]. Similar benefits of staging are expected in RED: better utilization of the salinity gradient and increased power output.

The concept of multistage RED was introduced in 2009 as a *cascade operation* by Veerman et al. [16]. The authors conducted experiments with a 0.1 m x 0.1 m cross-flow stack with 50 cell pairs to simulate a series multistage RED system. The stack was initially fed with 0.34 g NaCl·L^{-1} and 30.8 g NaCl·L^{-1} to operate the first stage, and the following stages were operated with the preceding stage outlet concentrations. The stack was operated with the same electrical current density of 30 A·m^{-2} every time, reproducing four stages. Staging resulted in decreased cumulative net power density from the single-stage to the four-stage: from 0.61 W·m^{-2} to 0.19 W·m^{-2}. This was due to the increased membrane area (quadrupled) with the same salinity gradient available. Regarding gross energy efficiency, this was relatively improved by over 50 % by operating three stages. The added fourth stage did not further improve the system. Considering pumping losses, the net power output at stage four even became negative. In 2015, Tedesco et al. [20] used a model to simulate cross-flow stacks changing several parameters, including the simulation and comparison of three different three-stage configurations, each with stages of 500 cells. The results showed that more than 1000 W could be obtained using brine (5 M) and brackish water (0.03 M).

Recently, Hu et al. [24] carried out a theoretical study of multistage RED for a RED heat engine system, considering a 0.1 m x 1 m co-flow stack while feeding brine and river water. They compared an independent stage control with a serial control (fixed current) and concluded that, although independent control provided slightly higher power, serial control was more suitable in practice. The same authors [25] followed their theoretical work with an experimental investigation that compared a single-stage RED with multistage RED. They used one 0.1 m x 0.1 m RED stack with 5 cell pairs to simulate a series multistage RED system of up to 16 stages. Different current densities, feed flow velocities, and feed solution concentrations for brine and river water were tested in serial control mode. They concluded that the multistage configuration was superior for RED heat engine systems, as it harvested more SGE and energy efficiencies could reach values five times higher than for a single stage. However, power density values were not discussed and flow directions were not disclosed. In 2020, Veerman [26] published a model-based study in which where co- and counter-flow stacks and co- and counter-flow multistage systems were investigated in RED for maximum efficiency. The study revealed that maximizing the overall power by simultaneously adjusting the electrical current in all stages resulted in the highest efficiencies. However, maximizing the overall power by setting the same current through each stage, which results in a simplified control, produced in an optimized system with almost the same efficiency. So far, studies have been either model-based or tested with one stack simulating stage by stage in co- or counter-flow mode. Running more than one stage at the same time has therefore not been studied. Moreover, researchers have not considered the effect of the residence time when comparing different numbers of stages nor the membrane area. The application of cross-flow stacks in multistage RED has also not been assessed experimentally.

In this study, we explore multistage RED by experimentally connecting two cross-flow stacks and moving away from the laboratory scale (0.1 m x 0.1 m) to the small pilot scale (0.22 m x 0.22 m). We use artificial seawater and river water testing different residence times and different electrical control modes. We investigate how the salinity gradient is utilized throughout the stages by lowering the extracted current in stage 1. With a numerical model [18], now validated with experimental data, we simulate the performance of different multistage configurations with the aim to develop an optimization strategy to increase the energy efficiency.

3.2. Materials and methods

3.2.1. Experimental set-up

Two cross-flow RED stacks (REDstack BV, Sneek, The Netherlands), connected in series, named co-flow multistage (Figure 3.2), were used to investigate the effect of a multistage configuration. The stack design details can be found in the literature [27]. Each stack, with 0.22 m x 0.22 m of active membrane area, contained ten cell pairs (0.968 m^2 of total active membrane area). Each cell pair comprised one FUJIFILM Type 10 CEM and one FUJIFILM Type 10 AEM (FUJIFILM Manufacturing Europe BV, Tilburg, The Netherlands). The membrane properties are reported in Table S3.3. The electrode compartments were closed with two Type 10 CEMs placed at each end, for double-shielding purposes, adding a total of three extra FUJIFILM type 10 CEM [28]. The electrode rinse solution (ERS) volume and colour, which are indicative of possible internal leakage, were controlled. These parameters did not change during the experiments. The membranes were separated by 155 µm thick woven net spacers (Deukum GmbH, Germany). The electrodes at the endplates were 0.22 m x 0.22 m Ti-mesh 1.0 electrodes with a 2.5 µm Pt galvanic coating and were used both as anode and cathode (MAGNETO special anodes BV, Schiedam, The Netherlands). As ERS a mixture of 0.2 M $K_4Fe(CN)_6$, 0.2 M $K_3Fe(CN)_6$, and 0.15 M NaCl was used (96 %, 96 %, and 100 % purity, respectively, VWR Chemicals, Belgium). The ERS was recirculated independently for each stage at a flow rate of 150 $mL \cdot min^{-1}$ using a peristaltic pump (Cole-Palmer, Masterflex L/S Digital drive, USA) with one double pump head to avoid pulsation (Cole-Palmer, Masterflex L/S Two-Channel Easy-Load II, USA).

Artificial feedwaters made of 30 g $NaCl \cdot L^{-1}$ for seawater and 1 g $NaCl \cdot L^{-1}$ for river water (99.9 % purity, Regenit, Esco, Harlingen, The Netherlands) were used to feed the system. Salt concentrations were calculated from measured conductivity values using an experimental calibration curve [18]. Both feedwaters were pumped at an equal rate into the first stage at flow rates of 6.14, 8.18, 12.30, 18.40, and 24.60 $L \cdot h^{-1}$ using diaphragm pumps (Grundfos DDA220, Denmark). For the single-stage configuration, these flow rates correspond to 44, 33,

22, 15, and 11 s residence times; for the two-stage configuration, they correspond to 88, 66, 44, 30, and 22 s residence times. Pulsation dampers (PDS250 PVC/FKM, Prominent GmbH, Germany) were placed between the pumps and the first stage to mitigate the pump pulsation. Also, cartridge filters with 1 µm pore size (Filter Technics, Belgium) were placed before the first stage to reject particles that might be present in the water tanks. Outlet flow rates were measured after the second stage by collecting each outlet for 60 s and weighing it. Between stages, the flow rates were assumed to be the same as at the inlet. Conductivity and temperature were measured in-line (VStar22, Thermo Fisher Scientific, USA) before each stage and at the final outlet for each stream (Figure 3.2). Inlet temperatures were set to 25 °C. Heat losses between stages resulted in an average temperature drop of 0.4 °C at the second stage inlets. Absolute pressures were measured with calibrated sensors (MIDAS SW, JUMO GmbH, Germany) at the same points as the conductivity and the ERS. Data were collected with a data logger (Memograph M, Endress + Hauser, Germany). Finally, each stack was tested individually to assess its performance before being connected in series. These results can be seen in Table S3.1 and Figure S3.1, in the supporting information.

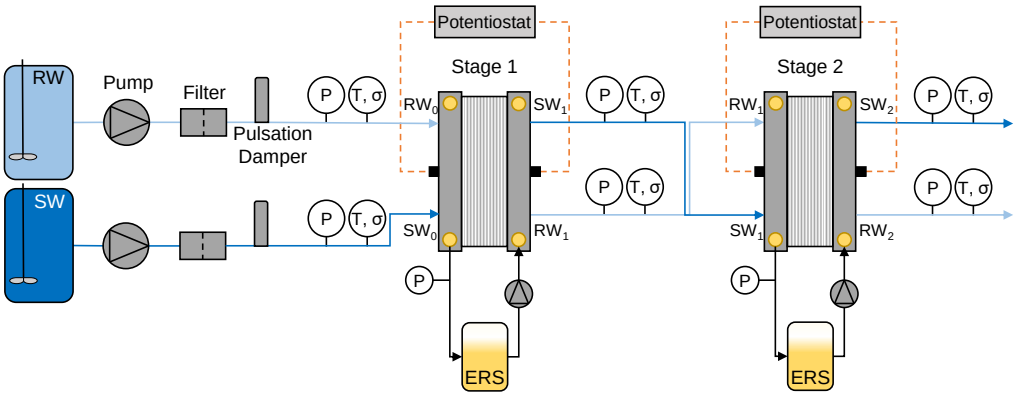

Figure 3.2 Schematic diagram of the experimental set-up in series (two-stage co-flow multistage).

3.2.2. Electrochemical measurements

All electrochemical measurements were made with a multichannel potentiostat (IVIUM n-stat, IVIUM Technologies BV, Eindhoven, The Netherlands) and duplicated. The error between experiments was lower than 3 %. For each flow rate, I-V measurements (i.e., the stack voltage as a function of electrical current) were performed to determine the stage maximum power by applying several discharge currents to the stack and multiplying by the stack voltage. The maximum power was determined sequentially per stage (maximum sequential power). When the I-V measurements were performed for stage 2, stage 1 was stabilized under a fixed discharge current. Since only ten cell pairs were used, the stack voltage was corrected for the voltage loss associated with the electrode reactions, the ERS,

and the three shielding membranes (blank voltage drop). This voltage drop becomes negligible when working with a much higher number of cell pairs in scaled-up systems [29].

Each stage was operated at a constant current corresponding to the I-V curve's maximum power, as an *independent control*. With the stack voltage as a function of the discharge current gross power output, thermodynamic efficiency, and energy efficiency were calculated. Gross power is the voltage output (corrected for the blank voltage drop) multiplied by the extracted current. Thermodynamic efficiency is the gross power divided by the mixing energy (per second) expended in the stage (inlet-outlet). Energy efficiency is the gross power divided by the energy (per second) provided at the inlet. Calculations for the mixing energy can be found in previous work [18]. For multistage calculations, total gross power is the sum of the gross power of each stage, and the energy efficiency is calculated using the total power. Thermodynamic efficiency is calculated per stage since it evaluates the individual stack performance. Pumping power losses were taken into account by multiplying the measured pressure drops across the stacks by the corresponding flow rate. In this way, the net power output can be calculated as the gross power minus the pumping power losses [18]. For the calculation of net energy efficiency, the net power is used. Power density is defined as the power divided by the total membrane area. The response product is introduced as the product of power density and energy efficiency and is used to evaluate the different configurations when both parameters are of equal importance.

3.2.2.1. Electrical control strategy

Two other control strategies were tested in addition to testing both stages with independent control, with each stage at a discharge current corresponding to its maximum power generated. These were *fixed current* (i.e., both stages are working under the same discharge current) and *fixed voltage* (i.e., both stages are working under the same voltage). Figure S3.2 is a schematic of the electrical control strategies. The experiments were conducted at a residence time of 30 s. The independent control was tested as described above. The voltage or current response was measured for the remaining two strategies using the values corresponding to the maximum power from the power curve of stage 1, and with both stages set at the same fixed current or fixed voltage, depending on the strategy.

3.2.2.2. "Saving the gradient" strategy

To optimize individual stage control, discharge currents lower than the maximum power current were extracted from stage 1. This allowed a higher salinity gradient to be available (it was "saved") for stage 2. The experiments were conducted at a residence time of 30 s and the procedure was similar to the independent control. Constant current densities were extracted in stage 1, starting at the 100 % point, which is defined as the extracted current at the maximum power condition. In the following experiments, the discharge current was

lowered in 10 % steps via control of the potentiostat, to 70 %. The discharge current densities corresponding to the new maximum powers of stage 2 were found by making an I-V plot while stage 1 was at a fixed current. Table 3.3 in the results section shows the specific current density values used.

3.2.3. RED model

A model developed in previous work [18] was used to simulate multistage RED. The stacks used for the different stages were identical in geometry and size and operated in cross-flow, in line with earlier work. The model parameters are given in Table S3.3 in the supporting information. The main equations for the RED model are described below.

The electromotive force (V) available at each point in the discretized active area, found with the modified Nernst equation, is expressed by:

$$E_{i,j} = (\alpha_{AEM} + \alpha_{CEM})\frac{RT}{zF} ln\left(\frac{\gamma_{i,j}^{SW} C_{i,j}^{SW}}{\gamma_{i,j}^{RW} C_{i,j}^{RW}}\right) \quad \text{(Eq. 3.1)}$$

where $\boldsymbol{\alpha}$ (-) is the permselectivity of the AEM and the CEM, $\boldsymbol{R}$ (J·mol^{-1}·K^{-1}) is the universal gas constant, $\boldsymbol{T}$ (K) is the absolute temperature, $\boldsymbol{z}$ (-) is the ion valence, $\boldsymbol{F}$ (C·mol^{-1}) is the Faraday constant, $\boldsymbol{\gamma}$ (-) is the molar activity coefficient estimated with the TCPC model of Ge et al. [30], and $\boldsymbol{C}$ (mol·m^{-3}) is the salt concentration.

Including the obstruction factor ($\boldsymbol{obs}$) in equation 3.2 and its determination by fitting experimental data ensured that the spacer shadow factor and the non-ohmic part of the stack resistance were also accounted for. Thus, the area resistance ($\boldsymbol{R_{i,j}^{cell\ pair}}$) was given by:

$$R_{i,j}^{cell\ pair} = R_{AEM} + R_{CEM} + obs\frac{d_{RW}}{\kappa_{i,j}^{RW}} + obs\frac{d_{SW}}{\kappa_{i,j}^{SW}} \quad \text{(Eq. 3.2)}$$

$$\kappa = \Lambda \cdot C \quad \text{(Eq. 3.3)}$$

where $\boldsymbol{R_{AEM}}$ and $\boldsymbol{R_{CEM}}$ (Ω·m^2) are the area electrical resistance of the AEM and the CEM, $\boldsymbol{obs}$ (-) is the obstruction factor and is used as a fitting parameter, $\boldsymbol{d}$ (m) is the river water (RW) and seawater (SW) compartment thickness, $\boldsymbol{\kappa}$ (S·m^{-1}) is the conductivity of the feedwater, and $\boldsymbol{\Lambda}$ (S·m^{-1}·mol^{-1}) is the molar conductivity of NaCl. The experimental values were corrected for the blank resistance; therefore, it was unnecessary to include the blank resistance in the model.

Each stack had a correspondent external load voltage (V). When this load was applied to the stack, the current density (A·m^2) at all points was:

$$J_{i,j} = \frac{E_{i,j} - U_{i,j}^{load}}{R_{i,j}^{cell}} \quad \text{(Eq. 3.4)}$$

The salt flux (mol·m^{-2}·s^{-1}) at each point of the stack was expressed as the sum of current transport and diffusive salt transport through the AEM and CEM:

$$T_{i,j}^{NaCl} = \frac{J_{i,j}}{F} + 2\left(C_{i,j}^{SW} - C_{i,j}^{RW}\right)\frac{D_{NaCl}}{l_m} \quad \text{(Eq. 3.5)}$$

where D_{NaCl} (m^2·s^{-1}) is the average diffusion coefficient of NaCl through the AEM and CEM, l_m (m) is the membrane thickness, and the factor 2 accounts for the diffusion through both the AEM and the CEM.

As a further refinement of the model, the electro-osmosis effect [31] was added to the volumetric flux of water ($T_{i,j}^{H_2O}$ in m·s^{-1}) through the membranes, and was given by:

$$T_{i,j}^{H_2O} = -2\left(C_{i,j}^{SW} - C_{i,j}^{RW}\right)\frac{D_{H_2O}}{l_m}\frac{MW_{H_2O}}{\rho_{H_2O}} + \frac{K_{e,osm}\cdot J_{i,j}}{F}\frac{MW_{H_2O}}{\rho_{H_2O}} \quad \text{(Eq. 3.6)}$$

where D_{H_2O} (m^2·s^{-1}) is the average diffusion coefficient of water through the IEMs, the factor 2 is again introduced to account for the diffusion through both the AEM and the CEM, MW_{H_2O} (kg·mol^{-1}) is the molecular weight of water, ρ_{H_2O} (kg·m^{-3}) is the density of water, and $K_{e,osm}$ (-) is the electro-osmosis coefficient adapted from Galama et al. [32].

The change in concentration in the active area can be described by the sum of the salt transport due to migration and diffusion (co-ions), plus water transport, as in the following partial differential equations (PDEs):

$$\frac{\partial C_{i,j}^{SW}}{\partial y} = -\frac{\Delta x}{\Delta \phi_{SW}}T_{i,j}^{NaCl} + C_{i,j}^{SW}\frac{\Delta x}{\Delta \phi_{SW}}T_{i,j}^{H_2O} = -\frac{W}{\phi_{SW}}T_{i,j}^{NaCl} + C_{i,j}^{SW}\frac{W}{\phi_{SW}}T_{i,j}^{H_2O} \quad \text{(Eq. 3.7)}$$

$$\frac{\partial C_{i,j}^{RW}}{\partial x} = +\frac{\Delta y}{\Delta \phi_{RW}}T_{i,j}^{NaCl} - C_{i,j}^{RW}\frac{\Delta y}{\Delta \phi_{RW}}T_{i,j}^{H_2O} = +\frac{L}{\phi_{RW}}T_{i,j}^{NaCl} - C_{i,j}^{RW}\frac{L}{\phi_{RW}}T_{i,j}^{H_2O} \quad \text{(Eq. 3.8)}$$

where Δx and Δy (m) are the discretization intervals, ϕ is the feed flow rate (m^3·s^{-1}), $\Delta\phi$ (m^3·s^{-1}) is the feed flow rate in Δx or Δy, L (m) is the length of the active area, and W (m) is its width. The two governing PDEs were solved numerically using the Forward Euler method, thus obtaining the matrix of the concentrations at a steady state.

The model was adapted to have multiple stages in series and to set each stage sequentially at its maximum power. Multiple instances of the cross-flow RED stack model were implemented, where the outlet of stage n was the inlet of stage n+1, except for the multistage counter-flow configuration. Furthermore, overall power and energy efficiencies were calculated as described in the experimental methodology. The flowchart and

schematics in the supporting information describe each instance of the cross-flow RED model (Figures S3.3, S3.4 and S3.5). For the multistage option, different linear arrangements of stacks were simulated, as displayed in Figure 3.3.

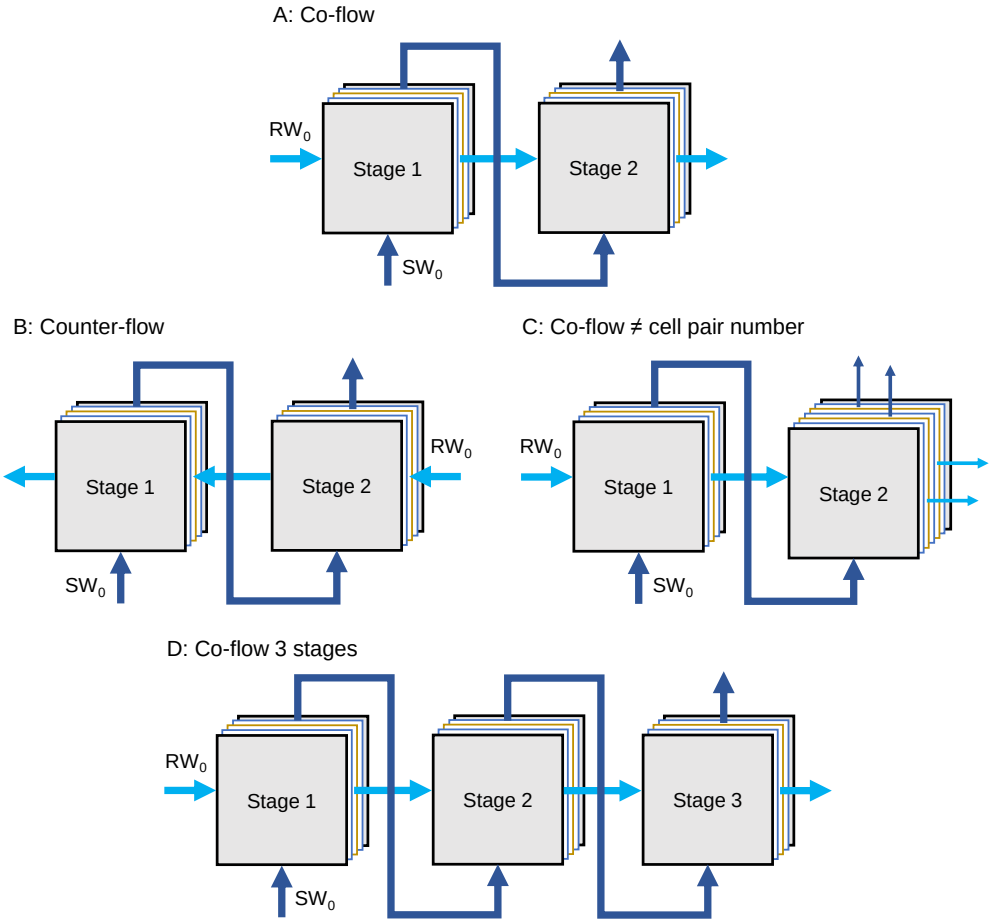

Figure 3.3 Different multistage RED configurations for 0.22 m x 0.22 m cross-flow stacks. A: Two-stage co-flow. B: Two-stage counter-flow. C: Two-stage co-flow, stage 2 with double cell pair number (20 cell pairs). D: Three-stage co-flow.

Other configurations comprise: a change in cell pair number between co-flow stages (Figure 3.3C), e.g., doubling the cell pair number in stage 2, which will increase the stage residence time and is anticipated to increase stack voltage and power generated; and the addition of a third stage (Figure 3.3D). Asymmetric feed flow rates, e.g., in which the seawater residence time is half of the river water residence time, were also simulated (Figure S3.9).

To model the counter-flow configuration (Figure 3.3B), e.g., seawater is fed into stage 1 and river water is fed into stage 2; both stages were modelled simultaneously with a Forward Euler scheme. The inlet concentration of seawater in stage 1 and the inlet concentration of river

water in stage 2 are the boundary conditions. The mixed-cup average of one stage's outlet concentration acts as the inlet concentration for the following stage (Figure S3.5). It should be noted that, due to the interdependence of stages 1 and 2 deriving from the feedwater flow pattern, power optimization is, in this case, not sequential but corresponds to the overall maximum.

For comparison with the experimental results, the simulations' initial concentrations were chosen to be the average of the measured experimental ones, and the pressure drop coefficient (Pa·s) was taken to be equal to each stack experimentally. The initial concentrations were taken as 1 g NaCl·L^{-1} for river water and 30 g NaCl·L^{-1} for seawater, and the pressure drop coefficient was equal to experimental stage 1, to allow comparison between configurations.

3.3. Results and discussion

3.3.1. Residence time influence

The residence time in a single stage is crucial for either high power densities (short residence times) or high energy efficiencies (long residence times) [33]. In this section, the influence of the residence time is investigated for a multistage configuration as depicted in Figure 3.2 and Figure 3.3A, with two stages in co-flow mode. Here, a sequential maximum power optimization is considered; in other words, the maximum power is determined sequentially per stage.

Figure 3.4 shows the gross power density versus current density for stage 1 and stage 2 at various residence times (per stage), with both model and experimental results. The experimentally determined values and the modelling results show good correspondence at several residence times. Although most parameters are kept equal to previous work [18], the obstruction factor and the salt diffusion coefficient are adjusted in the model for the new batch of experiments (obs = 1.25 and D_{NaCl} = 1.5·10^{-12} m^2·s^{-1}, these values are fixed for all simulations in this work). Figure 3.4A shows that short residence times result in higher power densities and higher current densities due to reduced boundary layers and a higher energy input per second [34]. Figure 3.4B shows the power density curve of stage 2, while stage 1 is working at its peak power, determined from Figure 3.4A. Inevitably, stage 2 has a lower power density due to ion transfer in stage 1, leaving less salinity gradient available. This implies that the power density of stage 2 will always be lower than that of stage 1 when the first stage is working at maximum power. Figure 3.4B reveals how stage 2 produces an amount of extra power that will contribute to increasing the process efficiency. Table 3.1 displays the peak discharge currents obtained from Figure 3.4.

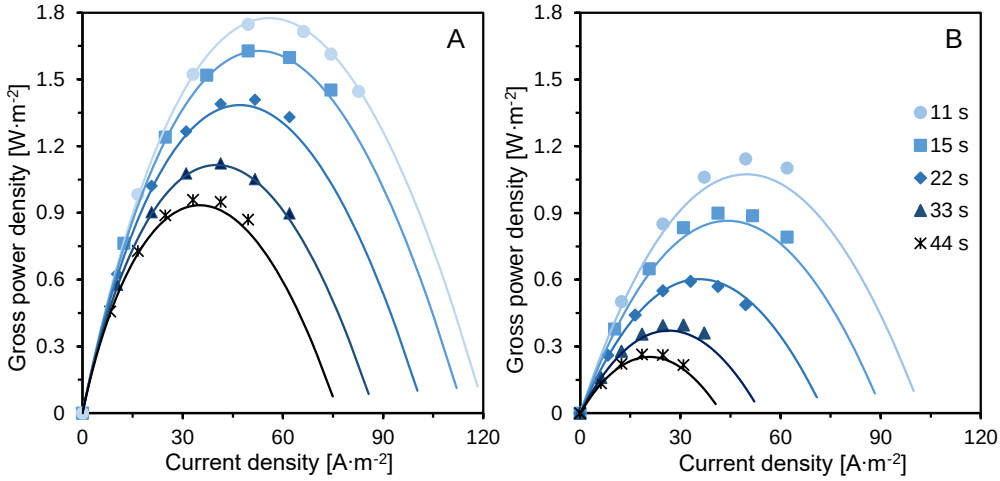

Figure 3.4 A: Gross power density versus current density at different residence times (per stage) for stage 1. B: Gross power density versus current density for stage 2 while stage 1 is working at its maximum power. Symbols represent experimental data; lines represent the model.

Figure 3.5 shows the gross power density, thermodynamic efficiency, and energy efficiency of stages 1 and 2 separately at different residence times. The power density values are most affected between stages due to the lower salinity gradient after stage 1. With a residence time of 11 s, the gross power density decreases from 1.73 $W \cdot m^{-2}$ in stage 1 to 1.14 $W \cdot m^{-2}$ in stage 2; at 44 s, it decreases from 0.95 $W \cdot m^{-2}$ to 0.27 $W \cdot m^{-2}$. This represents a relative decrease in the power density of 34 % and 72 %, respectively.

Table 3.1 Peak discharge currents of stages 1 and 2 obtained from the power curves (set values).

Residence time per stage [s]	$i_{stage\ 1}$ [$A \cdot m^{-2}$]	$i_{stage\ 2}$ [$A \cdot m^{-2}$]
11	56.2	50.8
15	53.2	44.8
22	47.2	34.6
33	41.1	27.8
44	35.8	21.2

To avoid a loss in power density between stages, the multistage configuration should therefore be operated at reasonably short residence times since the salinity gradient available can be kept high (Figure S3.6). However, this is done at the expense of energy efficiency and net power, which are discussed later. Thermodynamic efficiencies are between 50 % and 60 % and increased with residence time. Stage 2 reaches higher values than stage 1 at all residence times. This is due to the higher salinity gradient available at stage 1, making it more susceptible to undesired phenomena such as osmosis and co-ion transport. When most ions are exchanged in stage 1, which favours long residence times, stage 2 achieves the highest

thermodynamic efficiency values since the undesired phenomena will occur to a lesser extent. Figure S3.6 shows the compartments' concentrations quickly converging at long residence times. Energy efficiency values are similar between stages since both stages operate at their maximum power, achieving over 40 % energy efficiency at 44 s. While the use of a short residence time of 11 s increases power density, it reduces energy efficiency values to just 20 %.

As well as showing each stage's behaviour, Figures 3.4 and 3.5 demonstrate that the two-parameter (D_{NaCl} and obs) fitting model shows good agreement with the experimental power density and the derived thermodynamic efficiency and energy efficiency. The model can, therefore, be used for further predictions.

In Figure 3.6, the overall effect of the two-stage co-flow approach is compared to a single stage. Here, both stages' total residence time is taken into account; therefore, the same flow rate will correspond to different total residence times in the single-stage and two-stage configurations.

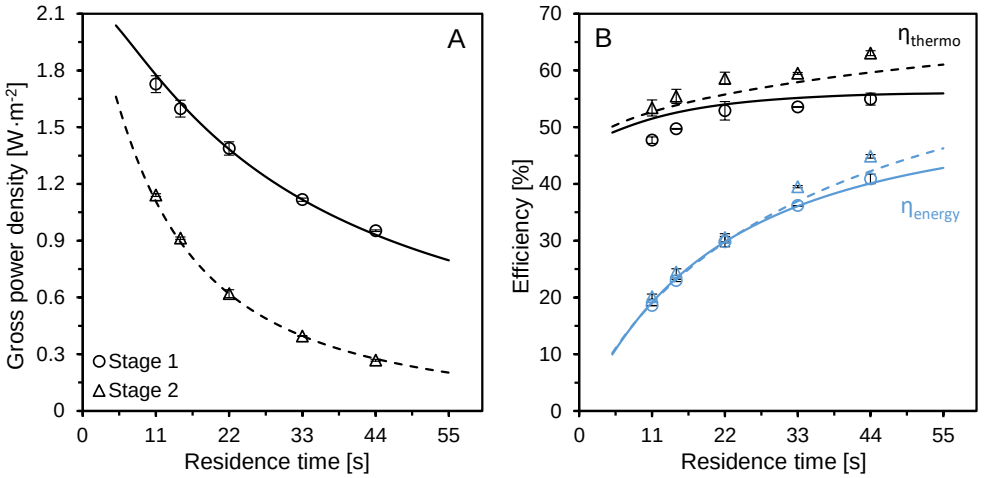

Figure 3.5 Experimental and model gross power densities and efficiencies of stages 1 and 2 at various residence times. Symbols are experimental values (at 11, 15, 22, 33, and 44 s) and lines are model results. Plot A shows the gross power density and plot B shows the thermodynamic efficiency (black) and energy efficiency (blue). Circles and solid lines correspond to stage 1; triangles and dashed lines correspond to stage 2. Error bars are based on two data points; some are not visible due to being smaller than the symbol.

Figure 3.6A shows that the cumulative gross power produced at several residence times is at least doubled when applying multistage. Considering the pumping losses (blue lines and markers), the cumulative net power is reduced in the multistage configuration for the shortest residence times, due to high pumping losses in that region (Figure S3.1) combined with an increasing number of manifolds (i.e., each stage adds a pumping loss to the overall). It should also be noted that stage 2 (stack 2) has slightly higher pumping losses than stage 1

(stack 1), which further decreases the net results of the multistage (Figure S3.1). At more realistic residence times, of longer than 20 s, the cumulative net power density follows the gross power trend, reaching higher values for multistage than for single-stage.

Since the study is conducted using ten cell pairs per stage, the two-stage operation has, in total, twice the membrane area. Hence, Figure 3.6B shows the power density in gross and net values, where both configurations have the total power normalized by the total membrane area (0.968 m^2 for single-stage and 1.936 m^2 for two-stage). The gross power density shows a small increase using two stages, obtained by tuning each external load individually and providing the same benefit as a segmented electrode [18]. On the other hand, net power density values are lower for multistage at most residence times, with a crossover at 66 s.

Figure 3.6C shows both configurations' energy and net energy efficiency. Here the same gain in energy efficiency can be seen as in the gross power density, while the advantage of multistage in net efficiency values is only seen for residence times of more than 55 s. Finally, Figure 3.6D aims to weigh both power density and energy efficiency parameters with the same importance. Thus, the product of the power density and the energy efficiency, namely the "response product", is used as one parameter versus residence time. As seen before, the multistage gross response product is higher than that of the single stage and is related to the individual maximum power tuning of each stage external load. However, it is crucial to evaluate the system pumping losses. The break-even point to benefit from a two-stage application is around 55 s for the cross-flow stacks used.

Considering gross power density and efficiency, the two-stage co-flow configuration yields better performance. Meanwhile, for multistage to surpass single-stage in net power and efficiency values, residence times of over 55 s should be used, considering the pumping losses inherent to the stacks used. This emphasizes the importance of reducing losses related to pumping energy, as multistage pumping losses increase per additional stage. Employing profiled membranes rather than woven spacers [35], increasing the number of cell pairs (more parallel channels) in stage 2, or improved stack design are examples of strategies to reduce pumping losses. Subsequently, the break-even point will be reached at shorter residence times.

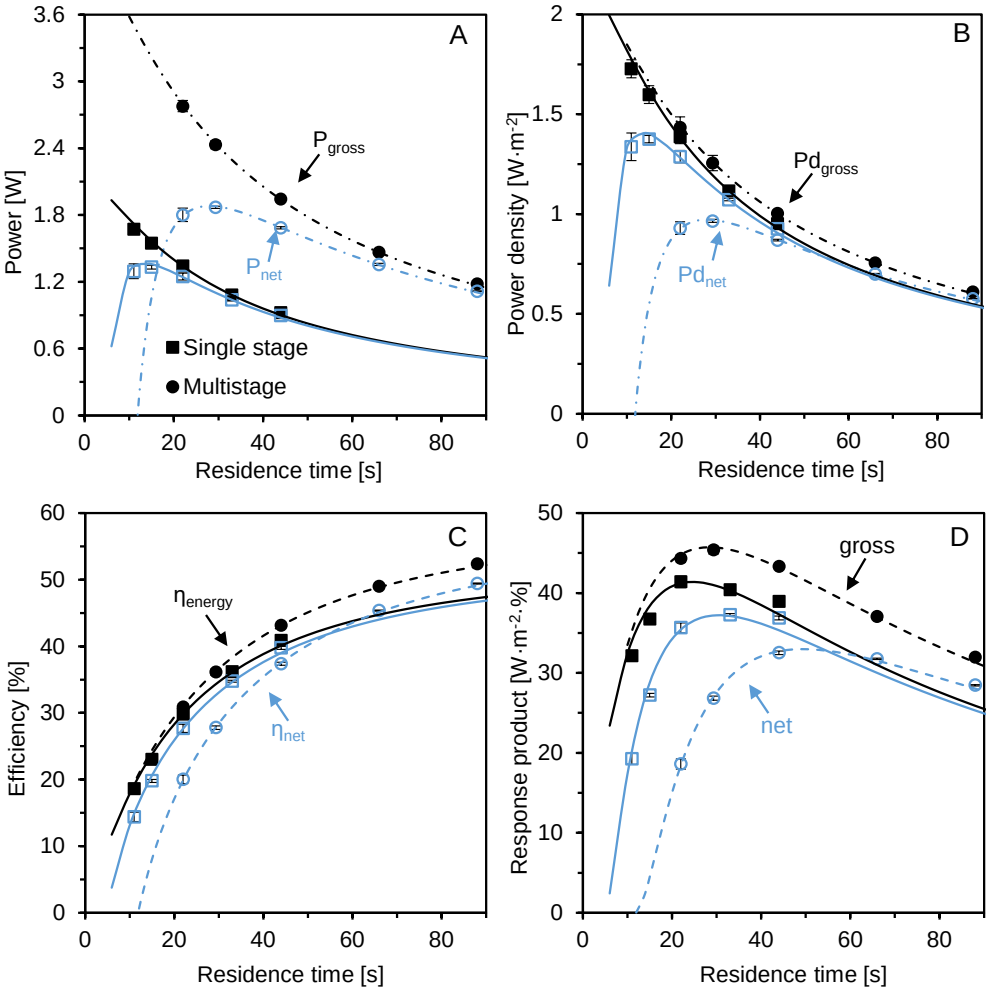

Figure 3.6 Single-stage and multistage performance comparison versus overall residence time. A: Cumulative gross and net power. B: Gross and net power density. C: Gross and net energy efficiency. D: Gross and net response product. Single-stage is represented by squares (experimental) and solid lines (model); multistage is represented by circles (experimental) and dashed lines (model). Gross values are represented in black, and net values are represented in blue. Error bars are based on two data points; some are not visible due to being smaller than the symbol.

3.3.2. Electrical control strategy

Since each stage has its own electrode pair, different electrical control strategies can be applied to a multistage configuration. Hu. et al. [24] studied multistage configurations by modelling the effect between two different control strategies: independent control of the stacks and series-connected (i.e., fixed current) control, using brine and river water as feedwaters. Here, these two control strategies plus fixed voltage control are experimentally

evaluated in Table 3.2 with a two-stage co-flow configuration (Figure 3.3A) at 30 s residence time. Figure S3.2 shows each electrical circuit schematically.

Table 3.2 Power and efficiency resulting from applying different electrical control strategies at 30 s total residence time.

Control	$i_{stage\ 1}$ [A·m^{-2}]	$i_{stage\ 2}$ [A·m^{-2}]	Gross P [W]	Gross Pd [W·m^{-2}]	η energy [%]
Independent	51.4	47.0	2.44 ± 0.04	1.26 ± 0.02	36.2 ± 0.5
Fixed current	51.5	51.3	2.43 ± 0.04	1.26 ± 0.02	36.2 ± 0.5
Fixed voltage	50.8	30.9	2.35 ± 0.02	1.21 ± 0.01	34.9 ± 0.2

The experimental results in Table 3.2 show that, for a residence time of 30 s, an independent control per stack and a fixed current control give essentially the same generated power, which agrees with the results by Hu et al. [24] and Veerman [26]. Therefore, the latter control method could be adopted for a two-stage co-flow configuration to simplify electrical connections. Setting a constant voltage is considered because retrieving the same voltage output from different stages could further simplify electrical connections and avoid voltage conversion losses. Here, there is a decrease in power of 4 %, lost in stage 2, since stage 1 has equal conditions in all three control types. Such an approach could be useful when the losses due to voltage conversion are higher than the lost power at the given flow rate.

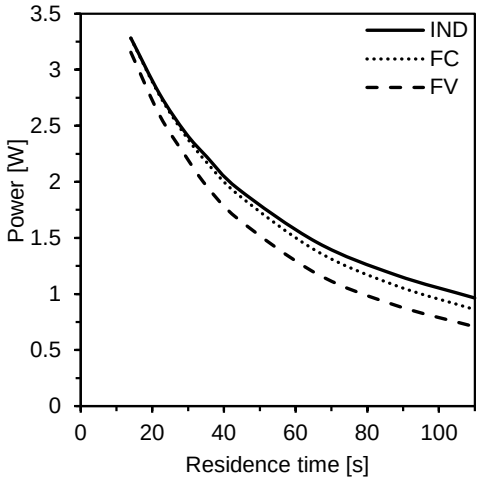

Figure 3.7 Modelled power values of the different electrical control strategies for a two-stage co-flow configuration from 15 s to 110 s residence time. IND – independent control, FC – fixed current control, and FV – fixed voltage control.

Figure 3.7 shows the electrical control strategies using the numerical model at various residence times. Discharge current values are available in Table S3.2. For the residence time

of 30 s, the model results are in close agreement with those achieved experimentally. Operating at short residence times (under 30 s) makes it possible to apply the different strategies while keeping the power losses under 10 %, considering the current and voltage values set for stage 1. Because of the high flow rate (short residence time), the driving force is kept similar across the stack and the stages, resulting in a more homogeneous electromotive force and stack resistance [17]. This results in similar optimal loads between stages 1 and 2, thus fixing current or voltage is acceptable. Longer residence times (over 30 s) are negatively influenced by the change in control since the salinity gradient left for stage 2 is relatively low due to extended ion exchange in stage 1. Thus, extracting the same current might lead to assisted RED: that is forcing the mixing [36]. Aiming at equal voltage output in both stages, when the open circuit voltage of stage 2 is inferior to the set value, will lead to ED in stage 2, therefore providing power to desalinate [37]. A strategy that can be applied to counteract this and to ensure the same output voltage in both stages while optimizing the system is to increase the number of cell pairs in stage 2. This will also result in a higher residence time in stage 2, promoting further ion exchange and decreasing the pressure drop. However, the varying inlet concentration of natural water may limit this application. Such a multistage configuration is sketched in Figure 3.3C.

3.3.3. "Saving the gradient" strategy

A novel strategy to optimize the multistage configuration is "saving the gradient" in stage 1. Instead of exhausting stage 1 at the maximum power, this stage can work at a current density below the maximum power operating point, which allows a higher salinity gradient to be available to stage 2. In stage 2, the maximum power conditions are always applied since the solutions are discarded afterwards.

Table 3.3 Corresponding percentage of the maximum power of stage 1, the set current density at stage 1 and stage 2, and gross power density and energy efficiency values resulting from switching the current.

Status from P_{max} Stage 1	$i_{stage\ 1}$	$i_{stage\ 2}$	Gross power density Stage 1	Gross power density Stage 2	Total gross power density	Change in total gross power density	Total energy efficiency
[%]	[A·m^{-2}]	[A·m^{-2}]	[W·m^{-2}]	[W·m^{-2}]	[W·m^{-2}]	[%]	[%]
100	51.4	47.0	1.58	0.94	1.26±0.02	-	36.2
90	46.3	47.8	1.57	1.00	1.28±0.02	+ 2.0	36.9
80	41.2	48.5	1.53	1.06	1.30±0.02	+ 3.0	37.3
70	36.0	49.1	1.47	1.12	1.29±0.01	+ 2.8	37.2

The beneficial, somewhat counter-intuitive, mechanism of salinity gradient saving is similar to RED with segmented electrodes [18]. Lowering the current extracted on the electrode segments closer to the river water inlet from their maximum power allowed the subsequent

electrode segments to reach higher power individually (higher extracted currents), increasing the overall power. Aiming for overall maximum power is different from maximizing each stage individually. In a two-stage co-flow multistage configuration, the external load of stage 1 can be tuned to reach the overall highest power. Table 3.3 shows the applied current densities for stages 1 and 2 at a 30 s residence time. Even though the stage 1 current density is reduced considerably, the stage 2 current density remains almost constant at maximum power since stage 1 consumes part of the salinity gradient anyway. Table 3.3 also shows the gross power density values of both stages at varying percentages of the current corresponding to the maximum power of stage 1, the total gross power density, the relative change in total power, and the total energy efficiency.

Figure 3.8 shows an increase in power density in stage 2 when the current density extracted in stage 1 (black symbols) is reduced, at 30 s total residence time in a two-stage co-flow configuration (Figure 3A).

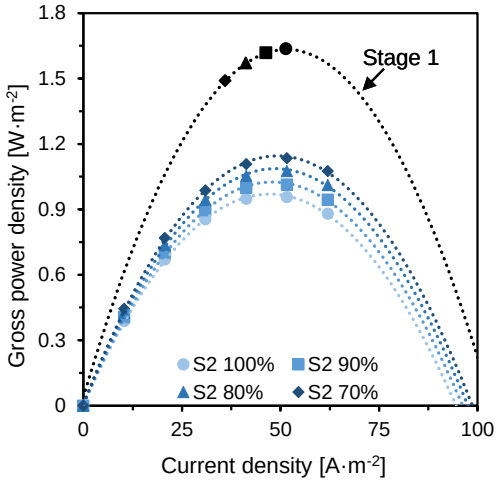

Figure 3.8 Measured gross power density curve versus current density. Different gross power density curves for stage 2 are obtained when the current density of stage 1 is reduced at 30 s total residence time. Black symbols in the stage 1 curve correspond to the current extracted at each percentage (from 100 % to 70 % from right to left). Dotted lines correspond to a second-order polynomial fit.

Decreasing the maximum power density of stage 1 from 100 % to 70 % increases the maximum power density of stage 2 from 0.9 $W \cdot m^{-2}$ to 1.1 $W \cdot m^{-2}$, a more than 20 % relative increase. Although such a procedure decreases the power produced in stage 1, the increased power in stage 2 outweighs the reduction in power produced in stage 1. At 90 % of the maximum current density, the stages work at similar current densities and the power is increased by 2 %. This indicates that the fixed current strategy discussed previously can be applied without incurring power losses by setting the discharge current at a lower value than the value corresponding to the maximum power in stage 1. This follows the findings of

Veerman, where setting the current density yielded higher energy efficiencies [26]. Total gross power and energy efficiency rise by 3 % when stage 1 works at 80 % of its maximum power. By plotting the percentage of the discharge current of stage 1 against the total gross power density (not shown), the optimum overall power density is found when stage 1 works at 77 %. These parameters have a strong relationship, with a correlation coefficient of -0.82. For a residence time of 30 s, the "saving the gradient" strategy only improves the multistage's performance briefly. Therefore, this strategy will not be effective for residence times under 25 s.

Nonetheless, for longer residence times, lowering the current in stage 1 reduces the ion exchange and the salinity gradient's consumption along the stage. This allows for the local current density in stage 1 to become more homogeneous and reduces losses at the electrodes [17]. Saving the gradient shows how the two-stage system can be optimized, providing a clear advantage for the implementation of multistage over the conventional single-stage configuration.

3.3.4. Prospects for additional configurations and application

Multistage provides new degrees of freedom in RED, in addition to the individual load tuning, which electrode segmentation also offers [18]. Between stages, it is possible to implement a different cell pair number or different feedwater arrangements. A straightforward approach to analyse these degrees of freedom is through modelling. With the validated model, different configurations (Figure 3.3) are tested and compared. These include counter-flow multistage with the fresh river water and seawater fed to different stages (Figure 3.3B); co-flow multistage with a change in cell pair number between stages (Figure 3.3C); and the prospect of an additional stage in co-flow (Figure 3.3D).

The net response products for residence times between 10 s and 90 s for these configurations are shown in Figure 3.9, including single and two-stage co-flow (Figure 3.3A). The residence time corresponds to the total time inside the system, and each stage is a 0.22 m x 0.22 m cross-flow stack with ten cell pairs (Table S3.4 shows the residence time distribution). The stages are considered to have equal pumping losses, equal to the pressure drop constant of stage 1 (Table S3.3). Therefore two-stage co-flow (configuration A) yields higher net results in this section than previously shown in Section 3.3.1.

Figure 3.9A and Figure 3.9B single-stage (SS) and counter-flow multistage (B) have the same values. With one stack, only one control is possible, and with counter-flow, the solver routine has to find the converging point of the fed concentrations. However, the co-flow multistage configurations (A, C, and D) have their power calculated per stage in Figure 3.9A. In other words, maximum power is first achieved for stage 1, and then stage 2 is calculated (as done experimentally in Section 3.1). In Figure 3.9B, their power is maximized overall: stage

1 is therefore not at its maximum power (which follows the "saving the gradient" strategy). Comparing the co-flow configurations in Figure 3.9A and 3.9B shows that seeking the overall power yields higher performance, reinforcing the experimental results.

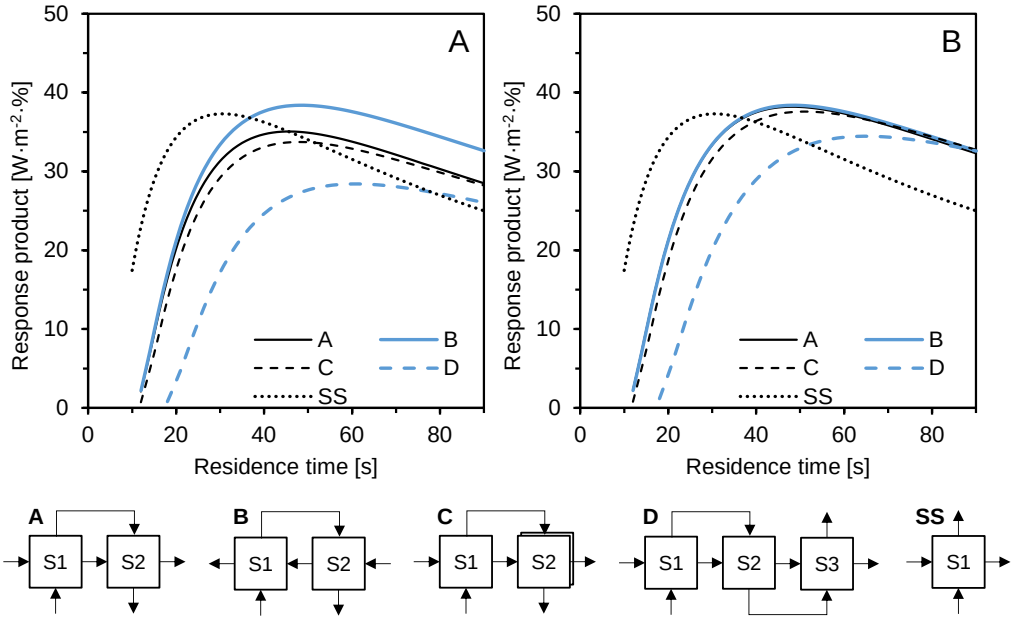

Figure 3.9 Net power density multiplied by the net energy efficiency of different modelled configurations from 10 s to 90 s total residence time. A: Co-flow configurations are modelled sequentially to achieve the maximum power per stage. B: Co-flow configurations are modelled to achieve the overall maximum power. Configuration A: two-stage co-flow; B: two-stage counter-flow; C: two-stage co-flow, stage 2 with double cell pair number (20 cell pairs); D: three-stage co-flow; SS: single-stage.

Compared with the single-stage configuration (Figure 3.9, series SS), all multistage configurations show a higher net response product value at a given residence time. Figure S3.7 shows the net power density and net energy efficiency versus residence time separately. Here, it is possible to differentiate which parameter (net power density or net energy efficiency) contributes the most to increasing the response product. Net power densities in SS are higher than in other configurations for low residence times due to lower pumping losses and reduced membrane area.

In Figure 3.9A, the two-stage counter-flow configuration (B) results in a better performance than the two-stage co-flow for the same conditions (A), especially at residence times longer than 25 s. This is mainly due to the optimization routine of maximizing the power per stage sequentially; in Figure 9B, there is no visible difference between counter-flow and co-flow. Separating the net power density per stage of configuration A and B (Figure S3.8), the stages reach different net power density values. Due to the conditions applied to maximize power, the average net power density is equal. Configuration C has increased membrane area since

it has twice the number of cell pairs in stage 2 and lower pressure losses than configuration A. However, Figure 3.9 shows that increasing the membrane area in stage 2 reduces the response product slightly compared with the other two-stage configurations up to 60 s. Nonetheless, compared with configuration D, which has the same membrane area and inlet flow rates, configuration C shows higher performance, indicating that increasing the membrane area in two stages is preferable to adding a new stage.

Configuration D investigated the prospect of a third stage. Figure 3.9 shows that the additional stage does not benefit the process because of the cumulative pressure drop that another stage brings. Furthermore, most of the salinity gradient between river water and seawater has been exhausted in prior stages, making the third stage redundant. However, for feedwaters with higher salinity gradient, such as brine and river water, where the efficiencies of a single stage are typically very low, adding more stages is a more valid option [24]. Nevertheless, each additional stage will decrease the total net power density compared to an optimized single stage, although it leads to higher energy efficiency.

Since pumping losses are a limiting factor in a two-stage application, feeding asymmetric flow rates between the river water and the seawater is implemented with the overall power approach. Figure S3.9 shows the response product versus the residence time of the river water. The seawater residence time is twice the river water flow rate, as having a lower fraction of seawater can still yield high efficiencies in cross-flow stacks [17]. Considering configuration A, the gross power achieved is around 8 % lower than when using a symmetric flow rate, due to the reduced available energy per second. Nonetheless, this strategy leads to gross energy efficiencies that are 20 % higher because a similar power density is retrieved for a smaller gradient available. The same behaviour is observed in net values. However, an asymmetrical flow rate reaches higher net power densities at short residence times due to the reduced pumping losses of the seawater compartment. Other configurations show the same trend. The response product has higher yields when adopting asymmetrical flow rates.

The key advantage of a multistage configuration is versatility, as it can be adapted to the installation site conditions. The use of artificial seawater and river water allows an understanding of the electrical control and optimization, bringing application one step closer. Other optimizations are also possible, such as different membrane types per stage [38]. For example, a first stage with multivalent permeable membranes facilitates the passage of multivalent ions (i.e., Mg^{2+}, Ca^{2+}), present in natural waters [39] while a second stage with higher permselectivity and low electrical resistance membranes since it might be less prone to fouling.

For application using natural waters, long-term experiments should be conducted to test different membrane types, as done for ED, and higher cell pair numbers, to address membrane lifetime and fouling issues.

The prospect of application is evident when comparing the single-stage operation with the optimized two-stage operation (configuration A, overall maximum power). With short residence times, pumping losses do not compensate for the second stage. Nevertheless, at more reasonable residence times (over 46 s for the studied conditions), the two-stage configuration proves to be efficient, with up to a 17 % improvement in gross power density and energy efficiency, and up to a 14 % improvement in net power density and energy efficiency. When aiming for 40 % net energy efficiency, the net power density retrieved at a single stage is 0.86 $W \cdot m^{-2}$, whereas it is 0.94 $W \cdot m^{-2}$ for a two-stage configuration, representing a relative improvement of 9 % (Figure S3.7). Therefore, when scaling up the technology to include several stacks at the same location, a two-stage system is preferable to two single stages in parallel.

3.4. Conclusions

Multistage reverse electrodialysis allows greater use of the salinity gradient, resulting in a higher gross power density and energy efficiency, the two performance indicators studied in this work. A two-stage configuration resulted in higher gross power density and energy efficiency than a single stage. However, each stage adds pumping losses to the system and the two-stage configuration yields higher net power density and energy efficiency only when stack pressure drops are lowered. An optimization strategy, named "saving the gradient", was tested by lowering the discharge current of stage 1. The strategy improved both power density and energy efficiency when compared to working at the maximum peak current in stage 1. This strategy is increasingly beneficial for lower flow rates since it prevents a major salinity gradient change in the first stage and voltage losses.

The two strategies of sequential power optimization and overall power optimization ("saving the gradient") were evaluated with the developed and validated model for different multistage reverse electrodialysis configurations. All of the co-flow scenarios improve when maximizing the overall multistage power output. For the seawater-river water case, adding a third stage does not yield sufficient net power density, due to the small salinity gradient and increased pumping losses, therefore using two-stages in series is recommended.

This study shows that multistage reverse electrodialysis is a viable concept to enhance power and energy efficiency, and benefits from optimization through "saving the gradient". Its implementation can strengthen the reverse electrodialysis technology for harvesting energy from salinity gradients by reducing pre-treatment costs and generating sufficient power.

3.5. Supporting information

3.5.1. Individual stack comparison and pressure drop behaviour

Table S3.1 Performance parameter values for individual stacks.

Parameter	Stack 1	Stack 2
Residence time [s]	22	22
Gross power density [W·m^{-2}]	1.34	1.34
Net power density [W·m^{-2}]	1.18	1.10
η energy [%]	28.5	28.6
η net [%]	26.0	24.2
η thermo [%]	53.8	54.4

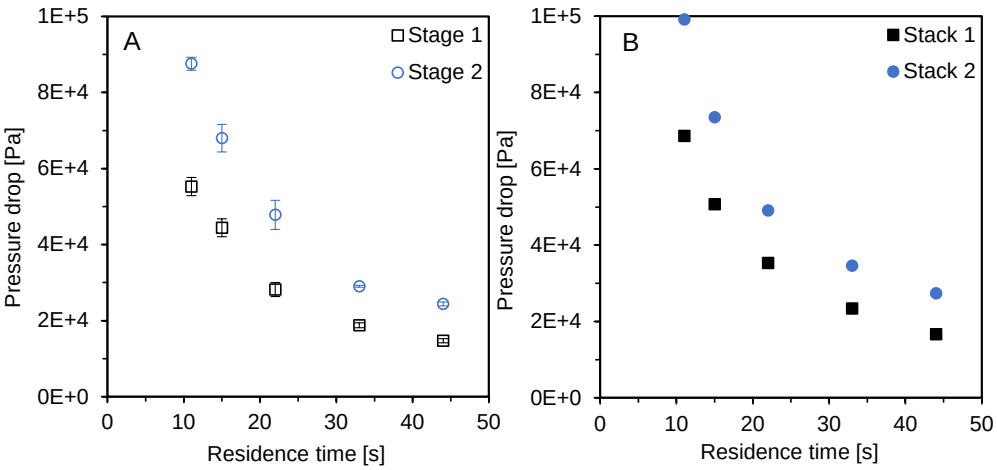

Figure S3.1 A: Pressure drops from each stage with error bars from ten data points. B: Each stack when tested individually.

The difference in pressure drop is a mechanical difference related to the stacks' handmade construction and only impacts net values. This was taken into account when comparing net values.

3.5.2. Electrical control strategies

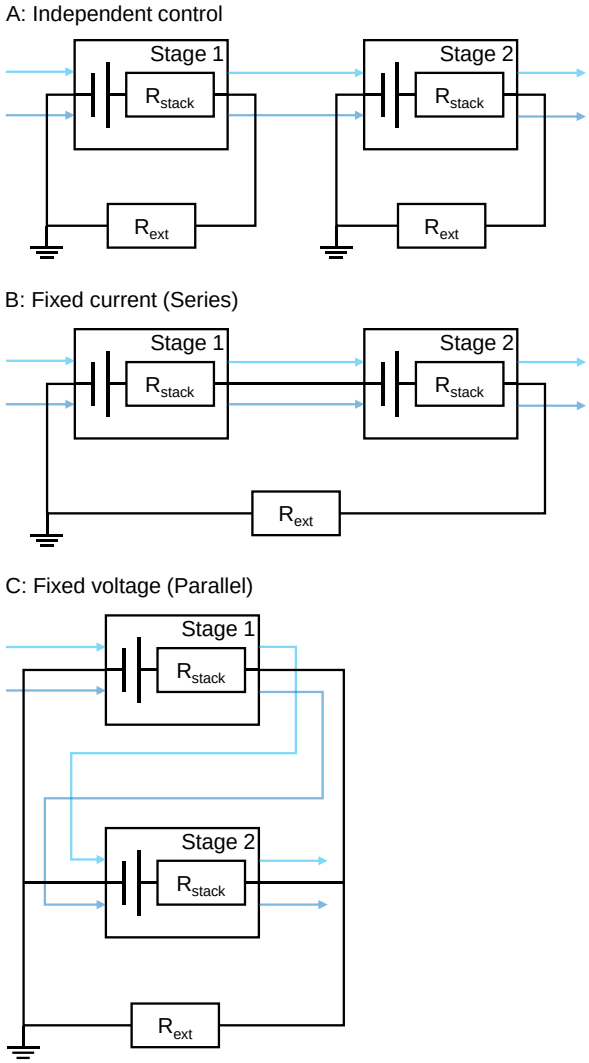

Figure S3.2 Electrical circuit of the different electrical control strategies. A: Independent control. B: Fixed current. C: Fixed voltage. Waters are fed in co-flow for simplification of the schematic. All work is done in cross-flow.

Table S3.2 Discharge currents and retrieved power from a co-flow two-stage configuration with different electrical controls. Fixed current and voltage were set from the maximum power of stage 1.

Independent Residence time [s]	$i_{stage\ 1}$ [A·m^{-2}]	$i_{stage\ 2}$ [A·m^{-2}]	Gross P [W]	Gross Pd [W·m^{-2}]
7	59.1	57.4	3.28	1.70
11	55.9	50.2	2.79	1.44
15	52.8	44.6	2.44	1.26
18	50.4	40.9	2.22	1.15
22	47.0	36.0	1.94	1.00
33	40.1	27.3	1.46	0.75
44	35.0	20.5	1.17	0.60
55	30.9	17.6	0.97	0.50
110	19.6	8.4	0.50	0.26
Fixed current Residence time [s]	$i_{stage\ 1}$ [A·m^{-2}]	$i_{stage\ 2}$ [A·m^{-2}]	Gross P [W]	Gross Pd [W·m^{-2}]
7	59.1	59.1	3.28	1.70
11	55.9	55.9	2.77	1.43
15	52.8	52.8	2.410	1.24
18	50.4	50.4	2.17	1.12
22	47.0	47.0	1.89	0.97
33	40.1	40.1	1.38	0.71
44	35.0	35.0	1.08	0.56
55	30.9	30.9	0.86	0.45
110	19.6	19.6	0.39	0.20
Fixed voltage Residence time [s]	$i_{stage\ 1}$ [A·m^{-2}]	$i_{stage\ 2}$ [A·m^{-2}]	Gross P [W]	Gross Pd [W·m^{-2}]
7	59.1	39.6	3.16	1.63
11	55.9	28.6	2.60	1.34
15	52.8	21.3	2.23	1.15
18	50.4	16.7	1.96	1.01
22	47.0	11.6	1.67	0.86
33	40.1	3.8	1.18	0.61
44	35.0	-0.2	0.90	0.46
55	30.9	-2.5	0.71	0.37
110	19.6	-5.3	0.32	0.17

3.5.3. Model details

Table S3.3 Fixed and fitting (in bold) parameters used in the model calculations and procedures to evaluate them.

Parameter	Symbol	Value	Unit	Evaluation procedure
Width of the active area	W	0.22	m	Known stack parameter.
Length of the active area	L	0.22	m	Known stack parameter.
Compartment thickness	d	155×10^{-6}	m	Known stack parameter.
AEM permselectivity	α_{aem}	94.5	%	Literature data [28].
CEM permselectivity	α_{cem}	94.7	%	Literature data [28].
AEM electrical resistance	R_{aem}	1.77×10^{-4}	$\Omega \cdot m^2$	Measurement in a six-compartment cell at 0.5 M NaCl, according to a literature procedure [40].
CEM electrical resistance	R_{cem}	2.69×10^{-4}	$\Omega \cdot m^2$	Measurement in a six-compartment cell at 0.5 M NaCl, according to a literature procedure [40].
Obstruction factor	***obs***	1.25	-	The value is fitted based on I-V data presented in Figure 3.4.
Average water diffusion coefficient (through the membranes) †	D_{H2O}	1.5×10^{-10}	$m^2 \cdot s^{-1}$	Literature data [28]. Permeability converted into a diffusion coefficient based on the measurement procedure presented in [41].
Average salt diffusion coefficient (through the membranes) †	D_{NaCl}	1.5×10^{-12}	$m^2 \cdot s^{-1}$	Fitting with I-V data presented in Figure 3.4.
Membrane thickness	l_m	125×10^{-6}	m	Literature data [28].
Electro-osmosis coefficient †	$K_{e,osm}$	4		Literature data [32].
Pressure drop coefficient stack 1 *	K_{dP}	0.156	Pa·s	Calibration with experimental pressure drop data from 0.22m x 0.22m stack 1.
Pressure drop coefficient stack 2	K_{dP}	0.245	Pa·s	Calibration with experimental pressure drop data from 0.22m x 0.22m stack 2.

* This value is also used as the standard to simulate multistage configurations, while it is assumed that all stages have the same pressure drop.

† Sensitivity analysis performed on these parameters.

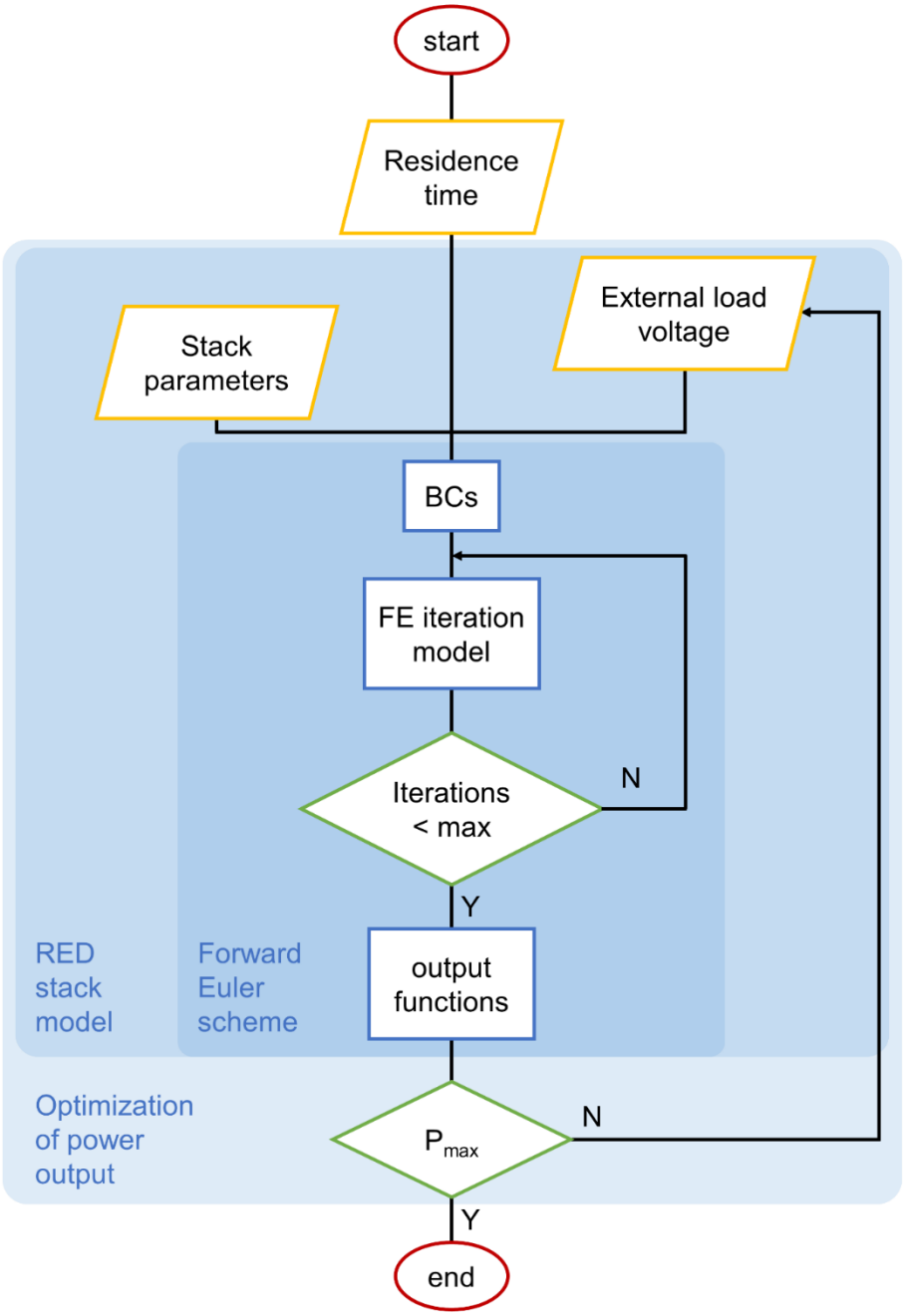

Figure S3.3 Flow chart of RED stack model with optimization of power output per stage.

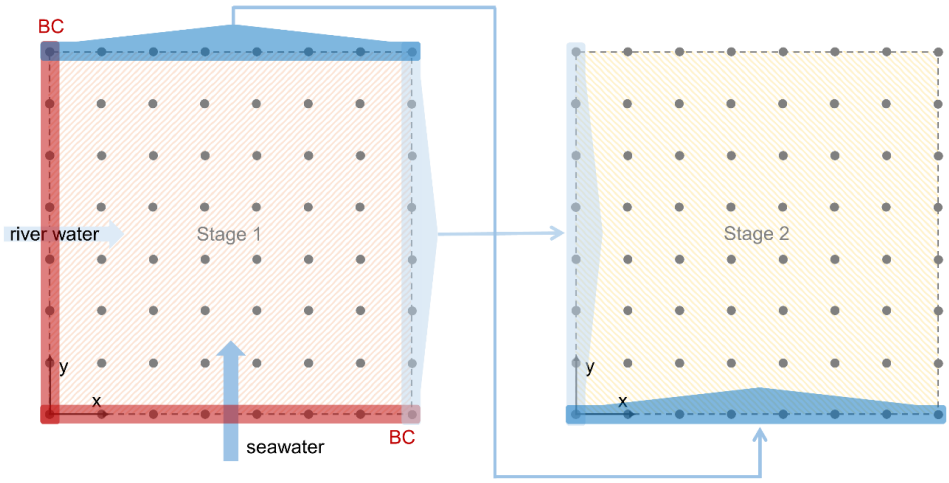

Figure S3.4 Schematic of two-stage co-flow multistage used for configurations A and C. In the case of configuration D, a third stage is added. BC: Boundary condition.

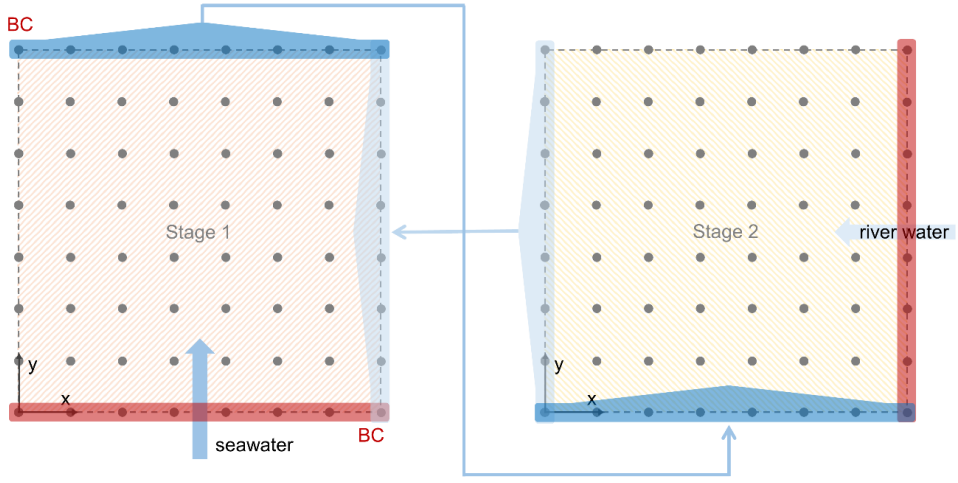

Figure S3.5 Schematic of two-stage counter-flow multistage used for configuration B. BC: Boundary condition.

3.5.4. Concentrations at stages inlets and outlets

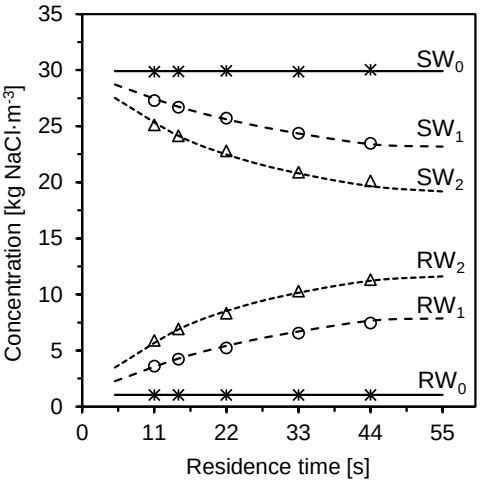

Figure S3.6 Artificial seawater and river water concentrations at the inlet of stage 1 (stars and solid line), the outlet of stage 1/ inlet stage 2 (open circles and dashed lines), and the outlet of stage 2 (open triangles and dotted lines).

3.5.5. Different multistage configurations

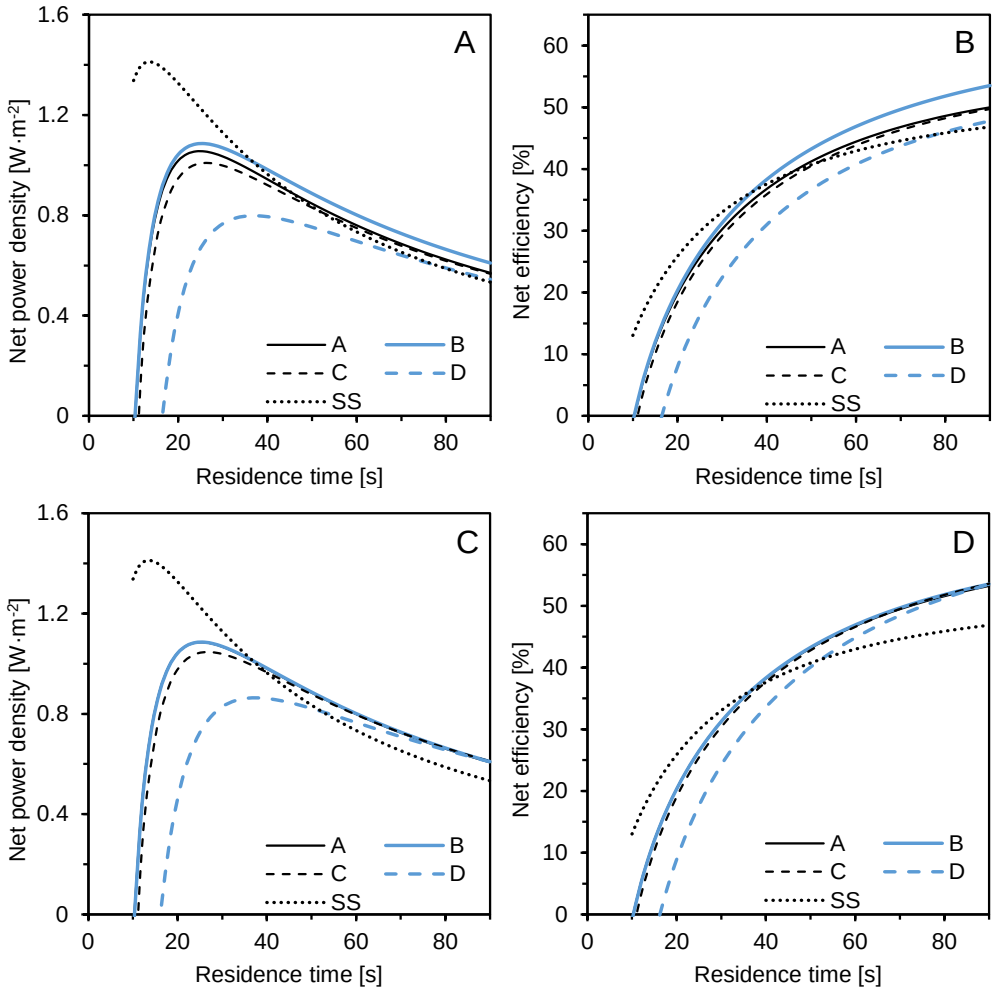

Figure S3.7 Net power density and net energy efficiency of different modelled configurations from 10 s to 90 s residence time. A and B, net power density and net energy efficiency, respectively, for a sequential approach. C and D, net power density and net energy efficiency, respectively, for an overall maximum power approach. The residence time corresponds to the total time inside the system, and each stage is a 0.22 m x 0.22 m cross-flow stack (see Table S3.4 for residence time distribution). Configuration A: Two-stage co-flow; B: Two-stage counter-flow; C: Two-stage co-flow, stage 2 with double cell pair number (20 cp); D: Three-stage co-flow; SS: Single-stage.

Table S3.4 Distribution of the residence time per stage (in fraction) depending on the configuration implemented to reach the same total.

	Stage			Total fraction
Configuration	1	2	3	
A	½	½	-	1
B	½	½	-	1
C	⅓	⅔	-	1
D	⅓	⅓	⅓	1
SS	1	-	-	1

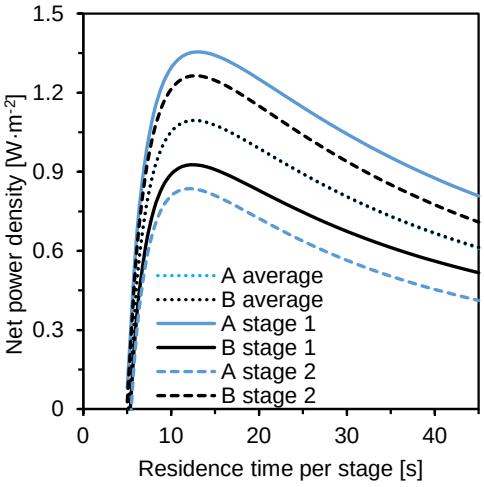

Figure S3.8 Stage 1 and 2 net power density from 5 s to 45 s residence time of configuration A and B (overall power approach). The average net power density for configurations A and B coincide. Note: total residence times for A and B average net power density are twice the residence time per stage.

3.5.6. Asymmetrical flow rate implementation

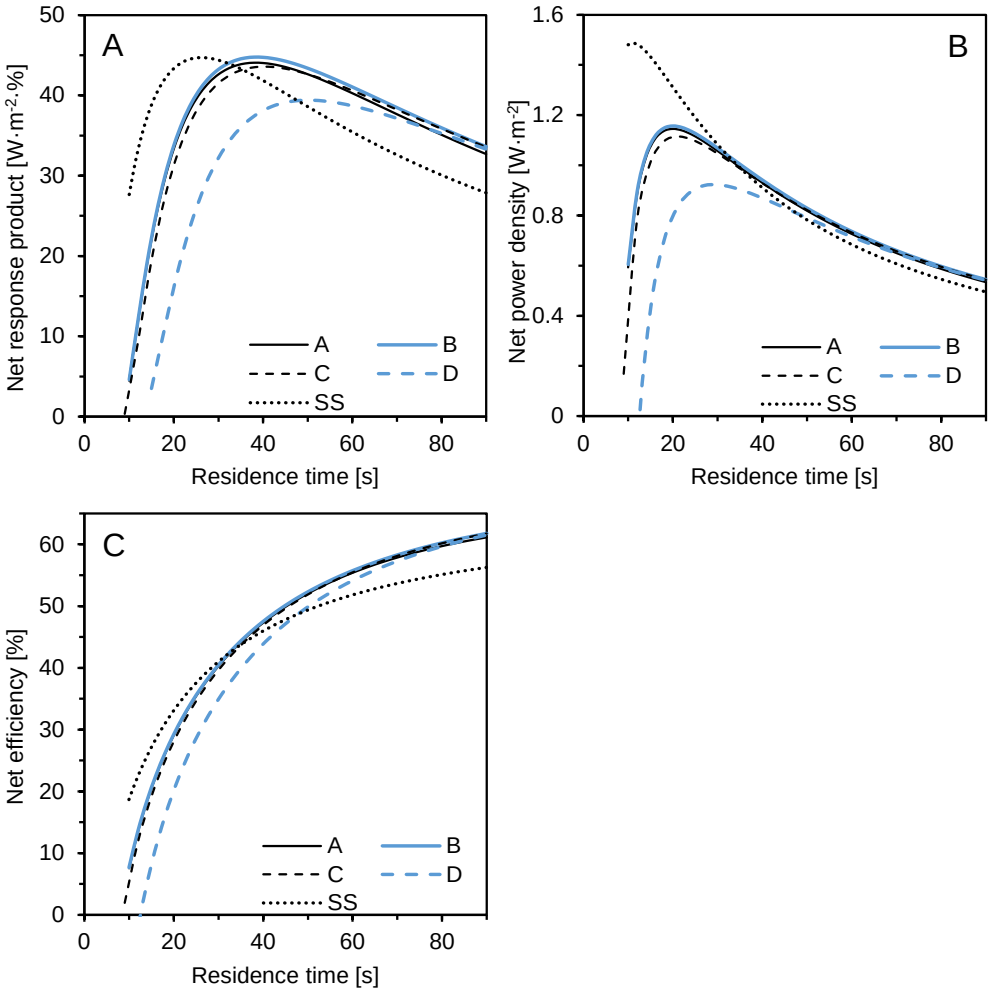

Figure S3.9 Asymmetrical flow rate strategy for the different configurations. The residence time shown relates to the river water compartment from 10 s to 90 s residence time. The seawater has twice the residence time of the river water (half the river water flow rate). The results are for the overall maximum power approach. A: Net response product of the modelled configurations. B: Net power density against residence time. C: Net energy efficiency versus residence time.

References

[1] U.N.F. Convention on Climate Change, Paris Agreement, (2015). https://unfccc.int/files/essential_background/convention/application/pdf/english_paris_agreement.pdf (accessed January 21, 2020).

[2] J. Kuleszo, C. Kroeze, J. Post, B.M. Fekete, The potential of blue energy for reducing emissions of CO2 and non-CO2 greenhouse gases, J. Integr. Environ. Sci. (2010). doi:10.1080/19438151003680850.

[3] R.E. Pattle, Production of electric power by mixing fresh and salt water in the hydroelectric pile, Nature. (1954). doi:10.1038/174660a0.

[4] A. Cipollina, G. Micale, Sustainable Energy from Salinity Gradients, 2016. doi:10.1016/C2014-0-03709-4.

[5] R.E. Lacey, Energy by reverse electrodialysis, Ocean Eng. 7 (1980) 1–47. doi:10.1016/0029-8018(80)90030-x.

[6] J.W. Post, J. Veerman, H.V.M. Hamelers, G.J.W. Euverink, S.J. Metz, K. Nymeijer, C.J.N. Buisman, Salinity-gradient power: Evaluation of pressure-retarded osmosis and reverse electrodialysis, J. Memb. Sci. (2007). doi:10.1016/j.memsci.2006.11.018.

[7] H. Ohshima, S. Ohki, Donnan potential and surface potential of a charged membrane, Biophys. J. (1985). doi:10.1016/S0006-3495(85)83963-1.

[8] J. Kuleszo, The global and regional potential of salinity-gradient power, (2008).

[9] J. Veerman, M. Saakes, S.J. Metz, G.J. Harmsen, Reverse electrodialysis: Evaluation of suitable electrode systems, J. Appl. Electrochem. (2010). doi:10.1007/s10800-010-0124-8.

[10] J.W. Post, C.H. Goeting, J. Valk, S. Goinga, J. Veerman, H.V.M. Hamelers, P.J.F.M. Hack, Towards implementation of reverse electrodialysis for power generation from salinity gradients, Desalin. Water Treat. 16 (2010) 182–193. doi:10.5004/dwt.2010.1093.

[11] M. Tedesco, A. Cipollina, A. Tamburini, G. Micale, Towards 1 kW power production in a reverse electrodialysis pilot plant with saline waters and concentrated brines, J. Memb. Sci. 522 (2017) 226–236. doi:10.1016/j.memsci.2016.09.015.

[12] J.Y. Nam, K.S. Hwang, H.C. Kim, H. Jeong, H. Kim, E. Jwa, S.C. Yang, J. Choi, C.S. Kim, J.H. Han, N. Jeong, Assessing the behavior of the feed-water constituents of a pilot-scale 1000-cell-pair reverse electrodialysis with seawater and municipal wastewater effluent, Water Res. (2019). doi:10.1016/j.watres.2018.10.054.

[13] S. Mehdizadeh, M. Yasukawa, T. Abo, M. Kuno, Y. Noguchi, M. Higa, The effect of feed solution temperature on the power output performance of a pilot-scale reverse electrodialysis (RED) system with different intermediate distance, Membranes (Basel). (2019). doi:10.3390/membranes9060073.

[14] R.A. Tufa, S. Pawlowski, J. Veerman, K. Bouzek, E. Fontananova, G. di Profio, S. Velizarov, J. Goulão Crespo, K. Nijmeijer, E. Curcio, Progress and prospects in reverse electrodialysis for salinity gradient energy conversion and storage, Appl. Energy. (2018). doi:10.1016/j.apenergy.2018.04.111.

[15] A.M. Weiner, R.K. McGovern, J.H. Lienhard V., A new reverse electrodialysis design strategy which significantly reduces the levelized cost of electricity, J. Memb. Sci. 493 (2015) 605–614. doi:10.1016/j.memsci.2015.05.058.

[16] J. Veerman, M. Saakes, S.J. Metz, G.J. Harmsen, Reverse electrodialysis: Performance of a stack with 50 cells on the mixing of sea and river water, J. Memb. Sci. (2009). doi:10.1016/j.memsci.2008.11.015.

[17] D.A. Vermaas, J. Veerman, N.Y. Yip, M. Elimelech, M. Saakes, K. Nijmeijer, High efficiency in energy generation from salinity gradients with reverse electrodialysis, ACS Sustain. Chem. Eng. (2013). doi:10.1021/sc400150w.

[18] C. Simões, D. Pintossi, M. Saakes, Z. Borneman, W. Brilman, K. Nijmeijer, Electrode segmentation in reverse electrodialysis: Improved power and energy efficiency, Desalination. 492 (2020) 114604. doi:10.1016/j.desal.2020.114604.

[19] G.J. Doornbusch, M. Bel, M. Tedesco, J.W. Post, Z. Borneman, K. Nijmeijer, Effect of membrane area and membrane properties in multistage electrodialysis on seawater desalination performance, J. Memb. Sci. (2020). doi:10.1016/j.memsci.2020.118303.

[20] M. Tedesco, P. Mazzola, A. Tamburini, G. Micale, I.D.L. Bogle, M. Papapetrou, A. Cipollina, Analysis and simulation of scale-up potentials in reverse electrodialysis, Desalin. Water Treat. (2015). doi:10.1080/19443994.2014.947781.

[21] D. Bharadwaj, T.M. Fyles, H. Struchtrup, Multistage Pressure-Retarded Osmosis, J. Non-Equilibrium Thermodyn. (2016). doi:10.1515/jnet-2016-0017.

[22] K.M. Chehayeb, K.G. Nayar, J.H. Lienhard, On the merits of using multi-stage and counterflow electrodialysis for reduced energy consumption, Desalination. (2018). doi:10.1016/j.desal.2018.03.026.

[23] G.J. Doornbusch, M. Tedesco, J.W. Post, Z. Borneman, K. Nijmeijer, Experimental investigation of multistage electrodialysis for seawater desalination, Desalination. (2019). doi:10.1016/j.desal.2019.04.025.

[24] J. Hu, S. Xu, X. Wu, D. Wu, D. Jin, P. wang, Q. Leng, Multi-stage reverse electrodialysis: Strategies to harvest salinity gradient energy, Energy Convers. Manag. (2019). doi:10.1016/j.enconman.2018.11.032.

[25] J. Hu, S. Xu, X. Wu, S. Wang, X. Zhang, S. Yang, R. Xi, D. Wu, L. Xu, Experimental investigation on the performance of series control multi-stage reverse electrodialysis, Energy Convers. Manag. 204 (2020). doi:10.1016/j.enconman.2019.112284.

[26] J. Veerman, Reverse Electrodialysis : Co- and Counterflow Optimization of Multistage Configurations for Maximum Energy Efficiency, Membranes (Basel). (2020) 1–13. doi:10.3390/membranes10090206.

[27] J. Moreno, E. Slouwerhof, D.A. Vermaas, M. Saakes, K. Nijmeijer, The Breathing Cell: Cyclic Intermembrane Distance Variation in Reverse Electrodialysis, Environ. Sci. Technol. (2016). doi:10.1021/acs.est.6b02668.

[28] J. Moreno, S. Grasman, R. van Engelen, K. Nijmeijer, Up-scaling reverse electrodialysis, Environ. Sci. Technol. (2018). doi:10.1021/acs.est.8b01886.

[29] A. Culcasi, L. Gurreri, A. Zaffora, A. Cosenza, A. Tamburini, A. Cipollina, G. Micale, Ionic shortcut currents via manifolds in reverse electrodialysis stacks, Desalination. (2020). doi:10.1016/j.desal.2020.114450.

[30] X. Ge, X. Wang, M. Zhang, S. Seetharaman, Correlation and prediction of activity and osmotic coefficients of aqueous electrolytes at 298.15 K by the modified TCPC model, J. Chem. Eng. Data. (2007). doi:10.1021/je060451k.

[31] A. Campione, A. Cipollina, I.D.L. Bogle, L. Gurreri, A. Tamburini, M. Tedesco, G. Micale, A hierarchical model for novel schemes of electrodialysis desalination, Desalination. (2019). doi:10.1016/j.desal.2019.04.020.

[32] A.H. Galama, M. Saakes, H. Bruning, H.H.M. Rijnaarts, J.W. Post, Seawater predesalination with electrodialysis, Desalination. (2014). doi:10.1016/j.desal.2013.07.012.

[33] V.M. Ortiz-Martínez, L. Gómez-Coma, C. Tristán, G. Pérez, M. Fallanza, A. Ortiz, R. Ibañez, I. Ortiz, A comprehensive study on the effects of operation variables on reverse electrodialysis performance, Desalination. 482 (2020) 114389. doi:10.1016/j.desal.2020.114389.

[34] D.A. Vermaas, E. Guler, M. Saakes, K. Nijmeijer, Theoretical power density from salinity gradients using reverse electrodialysis, Energy Procedia. 20 (2012) 170–184. doi:10.1016/j.egypro.2012.03.018.

[35] D.A. Vermaas, D. Kunteng, M. Saakes, K. Nijmeijer, Fouling in reverse electrodialysis under natural conditions, Water Res. (2013). doi:10.1016/j.watres.2012.11.053.

[36] M. Vanoppen, E. Criel, G. Walpot, D.A. Vermaas, A. Verliefde, Assisted reverse electrodialysis—principles, mechanisms, and potential, Npj Clean Water. 1 (2018). doi:10.1038/s41545-018-0010-1.

[37] J. Veerman, M. Saakes, S.J. Metz, G.J. Harmsen, Reverse electrodialysis: A validated process model for design and optimization, Chem. Eng. J. 166 (2011) 256–268. doi:10.1016/j.cej.2010.10.071.

[38] G. Doornbusch, M. van der Wal, M. Tedesco, J. Post, K. Nijmeijer, Z. Borneman, Multistage electrodialysis for desalination of natural seawater, Desalination. 505 (2021) 114973. doi:10.1016/j.desal.2021.114973.

[39] T. Rijnaarts, E. Huerta, W. Van Baak, K. Nijmeijer, Effect of Divalent Cations on RED Performance and Cation Exchange Membrane Selection to Enhance Power Densities, Environ. Sci. Technol. (2017) 13028–13035. doi:10.1021/acs.est.7b03858.

[40] P. Długołecki, K. Nymeijer, S. Metz, M. Wessling, Current status of ion exchange membranes for power generation from salinity gradients, J. Memb. Sci. (2008). doi:10.1016/j.memsci.2008.03.037.

[41] J.A.W. Van Engelen, Composite membranes, U.S. 9,713,792, 2017.

Chapter 4

Scaled-up multistage reverse electrodialysis pilot study with natural waters

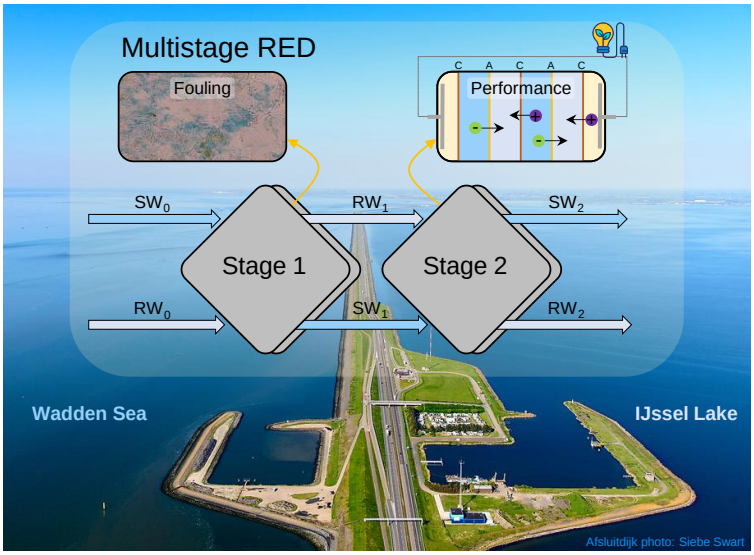

Abstract

A multistage reverse electrodialysis system was studied at the REDstack research facility (the Afsluitdijk, The Netherlands) for over 30 days to describe the performance of such configuration under natural water conditions. The experiments were done with two 0.22 x 0.22 m^2 stacks in series comprising 32 cell pairs (3.1 m^2 of membrane area) for stage 1 and 64 cell pairs (6.2 m^2 membrane area) for stage 2. The total gross power density at the available salinity gradient was stable at around 0.35 $W \cdot m^{-2}$. The total net power density, corrected for the initial pressure drop of the stacks, was 0.25 $W \cdot m^{-2}$ at an energy efficiency of 37 %. Throughout the operation, due to increased stack pressure drop, the actual total net power density lowered to 0.1 $W \cdot m^{-2}$. A distinct behaviour was found for multivalent ions in each stage. For stage 1, Ca^{2+} and SO_4^{2-} were transported from the river water to the seawater side, so-called uphill transport. For stage 2, uphill transport was not found, in line with Donnan potential calculations. Stack autopsy revealed microorganisms with sizes ten times larger than the cartridge filter nominal pore size (5 µm) and biofilm covering part of the spacer open area, both contributing to the increasing pressure drop in the stacks. This study showed that stable gross power densities and high energy efficiencies were obtained from feeding natural waters to a multistage reverse electrodialysis system, independent of fouling. In addition, it emphasized the importance of maintaining pumping power losses low for a viable deployment of the technology.

This chapter has been published as:

C. Simões, B. Vital, T. Sleutels, M. Saakes and W. Brilman 2022. Scaled-up multistage reverse electrodialysis pilot study with natural waters. Chemical Engineering Journal 450 p. 138412, https://doi.org/10.1016/j.cej.2022.138412

4.1. Introduction

Renewable energy sources are a key element in fighting climate change, and CO_2 emissions and, simultaneously help fulfilling world energy requirements. One renewable energy source is salinity gradient energy (SGE), also known as "Blue Energy". SGE results from the chemical potential difference between two solutions of different salinity, for instance, while mixing seawater and river water [1].

Reverse electrodialysis (RED) is an electro-membrane process that harvests the SGE in the form of electrical energy, using cation and anion exchange membranes (CEMs and AEMs) alternately piled in a stack [2]. Spacers keep the membranes apart and make the compartments to flow the feed solutions. Seawater and river water are fed alternately through these compartments. During operation, the concentration gradient across the membranes leads to ion transport from the seawater to the river water compartment and according to their selectivity, CEMs transport cations and AEMs transport anions. The resulting ionic current, generated through the stack, is converted into electric current, usually through redox reactions at the electrode end compartments [3].

The RED process was already introduced in 1954 [4]. However, it only gained more attention in the last two decades due to the call for new renewable energy sources and advances in ion-exchange membranes' performance and fabrication [5]. Despite technological advances during the last decade [6,7], the process has not yet met the targeted power density output of 2 $W \cdot m^{-2}$ and energy efficiency of 40 % at long-term operation [8]. This is particularly true when natural waters are used, demonstrating the need to study natural water systems for the end application. Experiments towards natural seawater and river water applications have investigated the presence of divalent ions (e.g., Ca^{2+}, Mg^{2+}, SO_4^{2-}) which resulted in a decrease in the gross power density compared to NaCl solutions [9–12]. This is due to uphill transport, where divalent ions are exchanged with monovalent ions and are transported against the direction of the concentration gradient, and due to the larger hydration radius of divalent ions which increases the membrane electrical resistance. The use of monovalent selective ion exchange membranes has shown improvements in the gross power density [13–15]. Changes in temperatures have also been assessed, showing that lower temperatures affect negatively the performance of RED [16,17]. Other studies, focused on fouling in natural waters, indicate that, when no anti-fouling strategies are in place, organic matter can decrease the gross power density up to 40 %, whereas inorganic fouling can decrease up to 8 % [18,19]. Anti-fouling strategies, such as water pre-treatment [20], cleaning strategies [21,22] or RED monitors [23,24] show a prospect of solving fouling issues and maintaining low stack pressure drops with the challenge of using less energy. The use of profiled membranes [25,26] was also suggested to decrease stack pressure drops. Another

challenge brought by natural waters is the possible scaling at the electrodes of, for example, $Mg(OH)_2$ and $CaCO_3$, which increased the energetic losses [27]. However, studies combining natural seawater and river water with control strategies, such as electrode segmentation [28] and multistage [29], are missing in the literature.

The multistage RED (MSRED) concept is gaining more attention as it increases the power output, consequently, the energy efficiency, while keeping the gross power density higher when compared to a single stage in the same conditions. MSRED enables different currents per electrode pair, as in electrode segmentation [28]. Moreover, it allows different configurations and materials per stage which can further improve the performance [30]. Veerman, who was the first to propose the MSRED concept in 2009 [31], recently published a model-based study with co- and counter-current flow in different multistage arrangements for maximum efficiency with different electrical controls [32]. Tedesco et al. simulated cross-flow stacks for brine and brackish water mixtures up to three stages and 500 cell pairs per stage, showing more than 1000 W could be obtained [33]. Hu et al. showed through modelling that a multistage series control was more suitable in practice with a counter-flow arrangement for brine and river water concentrations in a RED heat engine system [29]. Their work continued with an experimental investigation where the process efficiency was five times higher than with single-stage, preferably using low feed flow velocities [34]. Referring to natural waters, Wang et al. studied MSRED with natural seawater and brine to improve the process energy efficiency. However, the water composition was left out (only overall concentration was given), the test duration was rather short and only one stack was used to simulate the staging effect [35]. Besides the energy production aspect, MSRED is also used for improving the decolourization efficiency of azo dye wastewater [36], creating a system combined with multi-effect distillation [37] or producing hydrogen [38].

Our previous work investigated the application of MSRED for seawater and river water through modelling and experiments, using 0.5 M and 0.017 M NaCl solutions [30]. We concluded that the total power density and energy efficiency increased with a two-stage configuration using the "saving the gradient" strategy (stage 1 operated at a current density below the stage maximum power density) to achieve an overall higher maximum power. In addition, the pressure drop inherent to the feed compartments played an important role in the staging implementation [30]. Later on, the same multistage model was extended to include magnesium and sulphate ions in solution but it was validated only with single-stage experiments in controlled conditions [39]. The advantages of MSRED were moderated by the presence of divalent ions. The behaviour of multivalent ions in MSRED is limited to the model study and not experimentally verified. Thus, long-term testing of MSRED with natural seawater and river water, connecting two cross-flow stacks in series, where the multivalent ions impact and fouling are evaluated daily, to our knowledge, has never been reported before.

In this study, we show for the first time the performance of two 0.22 x 0.22 m^2 cross-flow stacks connected in series, fed with natural seawater and river water, at a geographically relevant location for RED implementation, over more than 30 days. The goal was to understand the impact of natural waters in an MSRED system concerning performance, ion transport and fouling and dealing with fluctuations associated with nature. Initially, the stacks were individually characterized at the laboratory using pure NaCl solutions (0.5 and 0.017 M NaCl) and, later were transported to the REDstack research facility (Afsluitdijk, The Netherlands), which allowed continuous water supply, and connected in series. During 30 days, the MSRED fed with natural waters was monitored continuously, revealing the fate of the ions (in particular divalent ions) and process performance. After a month of operation, cleaning techniques were tested in an attempt to lower the pressure drop across the stacks. At the end of the operation, a stack autopsy was conducted to evaluate the fouling extension.

4.2. Materials and methods

4.2.1. Experimental setups

Two cross-flow RED stacks were provided and built by REDstack BV (Sneek, The Netherlands). The details of the stack design can be found elsewhere in the literature [40]. The stacks were connected in series with the river and seawater both fed to stack 1 and stack 2 received the outlet streams of stack 1 (Figure 4.1). Stack 1 (or stage 1), which was the first stack receiving the feed waters in the multistage configuration, contained 32 cell pairs (3.098 m^2 of total active membrane area) and stack 2 (or stage 2) contained 64 cell pairs (6.196 m^2 of total active membrane area). The difference in the number of cell pairs resulted from model simulations, a shorter residence time increases the power density on stage 1 and a longer residence time, on stage 2, will exhaust further the salinity gradient increasing the energy efficiency while having lower pumping losses [30]. The active area of a single membrane was 0.22 m x 0.22 m. Each cell pair comprised one CEM (Fumasep FKS-30, Fumatech GmbH, Germany) and one AEM (Fumasep FAS-30, Fumatech GmbH, Germany). The shielding membranes were two fluorinated CEMs (Fumatech F-10150-PTFE, Fumatech GmbH, Germany), one being part of a cell pair and the other as the extra membrane. The ion exchange membranes properties can be seen in Table 4.1. Woven net spacers of 155 µm thickness (Deukum, GmbH, Germany) were used to make the compartments, with 55 % porosity. At the endplates, a pair of 0.22 m x 0.22 m platinized Ti-mesh electrodes were used as anode and cathode (MAGNETO special anodes BV, The Netherlands).

Table 4.1 Ion exchange membranes properties.

Properties	FKS-30	FAS-30	F-10150-PTFE
Thickness (dry) [α] [μm]	25-35	25-35	140 – 150
Permselectivity [α] [%]	> 98	> 90	> 95
Electrical resistance [β] [Ω·cm²]	1.32	0.78	1.8 – 2.9 [γ]
Ion exchange capacity [γ] [meq·g⁻¹]	1.43	1.6 – 2.0	0.7 – 0.9
Dimensional swelling in H2O [α] [%]	< 3	< 2	< 5

[α] Fumatech Technical Data Sheet, provided upon the membrane purchase
[β] Measured in a six-compartment cell at 0.5 M NaCl, according to a literature procedure [41]
[γ] FUELCELL Store Technical Data Sheet, available online (www.fuelcellstore.com/fumatech)

The experiments were conducted first at the laboratory at Wetsus, for stacks validation with NaCl solutions, and later at the REDstack BV research facility (the Afsluitdijk, The Netherlands), where it took place the transition to natural feed waters and set up for two weeks (section 3.1), the 30-day run experiment (section 3.2 and 3.3) and only after the cleaning strategies and fouling investigation (section 3.4).

The electrode rinse solution (ERS), during the laboratory tests and first days of the pilot tests, was a mixture of 0.2 M $K_4Fe(CN)_6$, 0.2 M $K_3Fe(CN)_6$ and 0.15 M NaCl (VWR Chemicals, Belgium) recirculated at 300 mL·min^{-1}. Although it worked in the laboratory and also with natural feed waters at a smaller scale [42,43], the hexacyanoferrate solution was found not to be suitable for scaled-up stacks using natural feed waters. Mg^{2+} and Ca^{2+} ions crossed the CEMs and reacted with OH^- resulting from the reduction of water at the cathode and precipitated as salts. Figure S4.1 shows the visual difference between the initial pristine solution and the used ERS in each stage and, Figure S4.2 shows the scaling found at the autopsy. Therefore, to avoid scaling at the cathode, the ERS was replaced with single-pass seawater. Each electrode compartment for each stage was fed with seawater independently at a rate of 600 mL·min^{-1}. Ag/AgCl reference electrodes were used to measure the potential difference across the membrane pile, excluding the overpotential at the electrodes. In a commercial application, voltages losses due to oxygen, chlorine and hydrogen evolution reactions need to be taken into account (around 1.5 to 2 V) or ERS that avoid such loss should be developed.

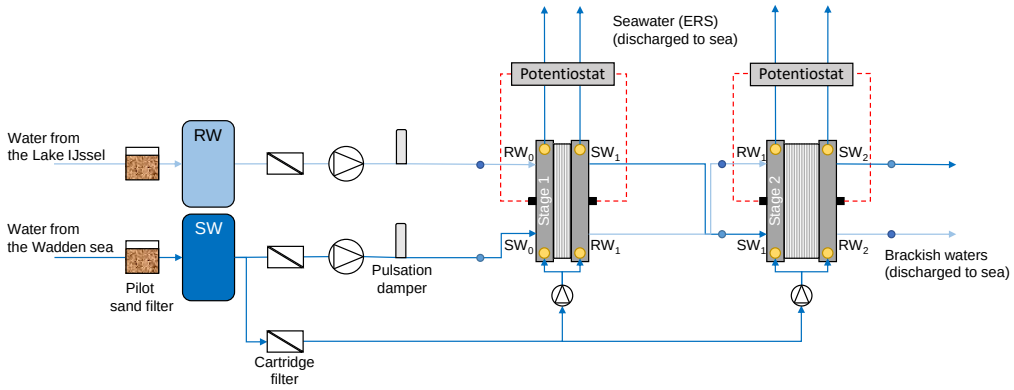

Figure 4.1 Schematic diagram of the experimental setup at the research facility fed with river water (RW) and seawater (SW) and with single-pass seawater as the electrode rinse solution. Dots represent the sampling points in positions 0, 1 and 2. The three-way valves for water switching are not represented for simplicity but were installed before the stage 1 inlet.

The laboratory setup has been described in our previous work [30]. For the pilot setup (Figure 4.1), the river water (RW) and seawater (SW) were pumped at a flow rate of 39.3 $L \cdot h^{-1}$, corresponding to 1.0 $cm \cdot s^{-1}$ in stage 1 and 0.5 $cm \cdot s^{-1}$ in stage 2, unless stated another flow rate. The spacer porosity was not included in the flow velocity calculation. The natural feed waters were automatically switched (changing compartment) every six hours to further mitigate scaling at the electrode compartments. By switching the feed waters, thus the polarity of the stack, cathode and anode were switched periodically, which helped lowering inorganic scaling at the cathode. Both valves installed for water switching were controlled by a Raspberry Pi (Raspberry Pi Foundation, United Kingdom), using an open-source Python code. Temperature and conductivity (Type 8228, Burkert, Germany) were measured inline, before stage 1 (position 0), between stages 1 and 2 (position 1) and after stage 2 (position 2). The pressure drop between inflow and outflow over the stack was measured with absolute pressure sensors (MIDAS SW, JUMO GmbH, Germany). Data were collected with a data logger (Yokogawa, Japan).

At the laboratory, both stacks were fed with pure NaCl solutions (Regenit, Esco, The Netherlands), which consisted of 1 $g \cdot L^{-1}$ for the RW and 30 $g \cdot L^{-1}$ for the SW at 24.5±0.5 °C. These values were chosen for consistency with previous studies with pure NaCl solutions. Afterwards, at the REDstack BV research facility at the Afsluitdijk, The Netherlands, the stacks were fed with natural waters from Lake IJssel (RW) and the Wadden Sea (SW), after being pre-treated with the research facility drum and sand filters, which was the pre-treatment adopted for this study, and a 50 µm/5 µm nominal cartridge filter (Pentek DGD-5005-20, Pentair, USA) placed before the pumps. These waters were sampled at positions 0, 1 and 2 from both RW and SW (Figure 4.1), and were characterized with an Ion Chromatograph (Metrohm Compact IC Flex 930, The Netherlands) for Cl^-, SO_4^{2-}, Na^+, K^+, Mg^{2+} and Ca^{2+}. Before

analysis, the samples were filtered using a 0.45 µm filter (Merck Millipore Millex-LCR, Germany). The typical composition of the natural feed waters, during the experiment, is given in Table 4.2.

Table 4.2 Average natural seawater (SW) and river water (RW) characteristics during the experiment at the Afsluitdijk research facility.

Source	Conductivity [mS·cm⁻¹]	Temperature [°C]	Typical ion concentration [mM]					
			Cl^-	SO_4^{2-}	Na^+	K^+	Mg^{2+}	Ca^{2+}
Wadden Sea (SW)	31.4	18.6	342.5	17.9	283.8	6.2	33.2	6.8
	±4.1	±0.6	±37.6	±1.8	±32.6	±0.8	±3.8	±0.7
Lake IJssel (RW)	0.52	19.0	2.7	0.6	2.3	0.1	0.5	1.1
	±0.02	±0.7	±0.2	±0.1	±0.2	±0.1	±0.1	±0.1

4.2.2. Electrochemical measurements and calculations

The electrochemical measurements were done with a two-channel potentiostat (IVIUM n-stat, IVIUM Technologies BV, The Netherlands) and recorded with the IVIUMsoft software. The potential across the membrane, in volts, was calculated through the Nernst equation:

$$E = \frac{RT}{zF} ln\left(\frac{m_{SW} \cdot \gamma_{\pm,SW}}{m_{RW} \cdot \gamma_{\pm,RW}}\right) \quad \text{(Eq. 4.1)}$$

Where R is the gas constant (J.mol^{-1}.K^{-1}), T is the absolute temperature (K), z is the ion valency (-), F is the Faraday constant (C.mol^{-1}), m is the molality (mol·kg H_2O^{-1}) and $\gamma_\pm$ is the mean salt activity coefficient (-) estimated with the model of Ge et al. [44]. For the case of calculating the theoretical open circuit voltage (OCV), equation 4.1 was adapted to $OCV = E \cdot 2N \cdot \alpha_{IEM}$, where N is the number of cell pairs (-) and α_{IEM} is the average of the AEM and CEM permselectivity (-). The experimental OCV was measured when there was no current applied.

To define the power curve and maximum power density an I-V (current-voltage) measurement was done. It consisted of current steps of -0.5 A (at the Wetsus laboratory), -0.4 A for stage 1 and -0.2 A for stage 2 (with natural waters at the Afsluitdijk) until the cell voltage reached zero. Displaying the results both current and voltage are made positive. The gross power density ($P_{d,gross}$ in W·m^{-2}) of each stage was:

$$P_{d,gross} = \frac{I \cdot U}{A_{mem}} \quad \text{(Eq. 4.2)}$$

Where I is the current applied (A), U is the measured potential (volts) and A_{mem} is the total active membrane area (m^2). The net power density (equation S4.1) only considered pressure drop losses from the stack (equation S4.2). For the total power density ($P_{d,total}$ in W·m^{-2}) of two stages, the contribution of each stage needs to be considered:

$$P_{d,total} = \frac{N_{S1}}{N_T} P_{dS1} + \frac{N_{S2}}{N_T} P_{dS2} \quad \text{(Eq. 4.3)}$$

Where N_T is the total amount of cell pairs (-) and N_{S1} is the amount of cell pairs in stage 1 and N_{S2} is the amount of cell pairs in stage 2. To evaluate the power density and energy efficiency in the long term, the current was fixed during the experiments, after manually employing the "saving the gradient" strategy for the first days [30]. The strategy consisted of stage 1 working at 80 % of its maximum power density and stage 2 at 95 %. Providing a lower current to stage 1 to allow an "extra" salinity gradient for the following stage has proven that more power can be harvested than by setting each stage sequentially at its maximum power [30]. Applied current values and measured response voltage during the 30-day run are shown in Table S4.1.

To verify how much of the available salinity gradient energy was harvested, the energy efficiency was calculated:

$$\eta = \frac{P_{gross}}{\Delta G_{in}} \quad \text{(Eq. 4.4)}$$

Where the P_{gross} is the total gross power (W) and the ΔG_{in} is the Gibbs free energy per second at the inlet (W) [45]. To calculate ΔG, the entropy (ΔS in W·K^{-1}) and the absolute temperature (T in K) are needed.

$$\Delta G = \Delta S \cdot T \quad \text{(Eq. 4.5)}$$

$$\Delta S = S_{mix} - S_{RW} - S_{SW} \quad \text{(Eq. 4.6)}$$

$$S = -R \cdot n_T \cdot \sum_i x_i \ln (x_i \cdot \gamma_i) \quad \text{(Eq. 4.7)}$$

$$i = H_2O, Cl^-, Na^+, K^+, SO_4^{2-}, Mg^{2+}, Ca^{2+}$$

Where n_T is the total number of moles (mol.s^{-1}), x_i is the mole fraction (-) and γ_i corresponds to the single ion activity coefficient of species i (-) as specified above. The single ion activity coefficient of species i, γ_i, was approximated by the mean salt activity coefficient, $\gamma_\pm$, for the following ions: $\gamma_{Cl^-} = \gamma_{NaCl}$, $\gamma_{Na^+} = \gamma_{NaCl}$, $\gamma_{K^+} = \gamma_{KCl}$, $\gamma_{SO_4^{2-}} = \gamma_{Na_2SO_4}$, $\gamma_{Mg^{2+}} = \gamma_{MgCl_2}$ and $\gamma_{Ca^{2+}} = \gamma_{CaCl_2}$. γ_{H_2O} was assumed 1. With Eqs. 4.5,4.6 and 4.7, the available power for mixing is calculated.

4.2.3. Cleaning and autopsy techniques

Cleaning strategies were implemented after more than 30 days of experiment, in an attempt to mitigate the reduction in net power density output. Both stages had visible signs of fouling and presented an increasing pressure drop with time. In the cleaning procedure, the inlet and outlet of the stacks were reversed, since most particulate fouling accumulated in the entrance of the stack and, by reversing the flow direction, this accumulation was pushed out of the stack. Following, the flow was doubled for 5 minutes, forcing the particles out. After that, air sparging was performed, with a configuration of 3 pulses of 2 seconds duration each at 3 bar air pressure. Air sparging is a sudden disturbance on the membrane and spacers surface by introducing compressed air for a short time along with the feedwater flow, to remove a large accumulation of foulants, mostly particulate fouling. During the cleaning procedure, water samples were taken at the outlet of each stack compartment (both river and seawater) and were analysed for suspended solids, according to the Standard Methods for the Examination of Water and Wastewater [46].

The multistage configuration was let to run for two more weeks after the cleaning, and at the end of the experiment, stack 1 was carefully opened and investigated concerning fouling. Since a membrane autopsy was destructive to the stack, stack 2 was kept intact for future research. Pictures of the AEM, CEM, spacers and electrodes were taken and membrane and spacer pieces were cut for optical and electron microscopic investigation, always on an inlet, central area of the membrane. The procedure was the same as described by Vital et al. [20]. In short, membrane and spacer pieces were fixed and dried for microscopy analyses under scanning electron microscopy (SEM) and energy-dispersive X-ray spectroscopy (EDX), while other pieces were stained with Alcian Blue 8 GX 0.1 % solution (Sigma Aldrich, The Netherlands) and observed with phase-contrast microscopy (Olympus BX40, Japan) at 10x and 20x magnification, for visualization of organic fraction of extracellular polymeric substances (EPS) and biofilm [47].

4.3. Results and Discussion

4.3.1. Transitioning between artificial and natural conditions

Both RED stacks were first tested at the laboratory, using pure NaCl solutions and at the same flow velocity (1.0 $cm \cdot s^{-1}$) to ensure reproducibility. Inlet conditions are shown in Table 4.3. OCV values were, 0.131 V and 0.133 V per cell pair for stacks 1 and 2, respectively (Figure 4.2A). These values are close to the calculated theoretical OCV of 0.150 V per cell pair (equation 4.1, assuming permselectivity, $\alpha = 0.95$). The power density versus current density curves were similar (Figure 4.2B). Stack 1 had a 1.5 % higher gross power density; this minor

difference can be attributed to different factors together, such as manual building or ionic shortcut currents from the increased cell pair number in stack 2 [48,49].

Table 4.3 Test description and conditions for each stack/stage. At the laboratory reproducibility tests took place, thus the stacks are studied individually under equal conditions. At the research facility, the stacks, now named stages are already investigated in the two-stage series configuration.

Test	Inlet conditions	SW		RW		Composition	Velocity [cm·s^{-1}]
		σ [mS·cm^{-1}]	T [°C]	σ [mS·cm^{-1}]	T [°C]		
Validation Reproducibility	Stack 1 Lab	47.83	24.9	2.03	24.8	NaCl	1.0
	Stack 2 Lab	47.78	25.3	2.03	25.1	NaCl	1.0
Natural conditions	Stage 1 NW	35.33	19.4	0.66	19.5	Natural	1.0
	Stage 2 NW	29.85	19.7	4.60	19.5	Natural	0.5

When the testing was under natural conditions (Figure 4.2C and 4.2D), the stacks were connected in series (Figure 4.1), and are now referred to as stages 1 and 2. The initial test conditions can be seen in Table 4.3. As a consequence of staging, the salinity gradient available for stage 2 is lower than stage 1, due to the mixing in stage 1. Furthermore, since stage 2 has twice the amount of cell pairs of stage 1, the flow velocity is halved to 0.5 cm·s^{-1}. These two factors account for the 2.3 times lower maximum power density in stage 2, shown in Figure 4.2D. The effect of staging combined with the change in flow velocity seen here is comparable to the literature for NaCl solutions [30]. The maximum gross power density achieved in stack 1 lab was reduced by 41 % with stage 1 NW (Figure 4.2B and 4.2D). This was due to a combination of effects including the lower salinity gradient available which can be seen in Table 4.3 and calculated through equation 4.5, and the presence of multivalent ions like Mg^{2+} and Ca^{2+} (details in section 4.3.3). Vermaas et al. (2014) also reported a decrease of around 50 % in gross power density with $MgSO_4$ (10 %)/ NaCl (90 %) solutions with a total salt concentration of 0.508 M and 0.017 M in artificial seawater and river water [10]. The lower temperature (Table 4.3), known to negatively influence the power density [11,17], further reduced the gross power density. The maximum gross power density of stage 2 NW (Figure 4.2B and 4.2D) was even lower (0.3 W·m^{-2}) because of the reasons mentioned above concerning initial concentration and flow velocity. Transitioning to natural waters shows multiple challenges that cannot be studied simultaneously in the laboratory.

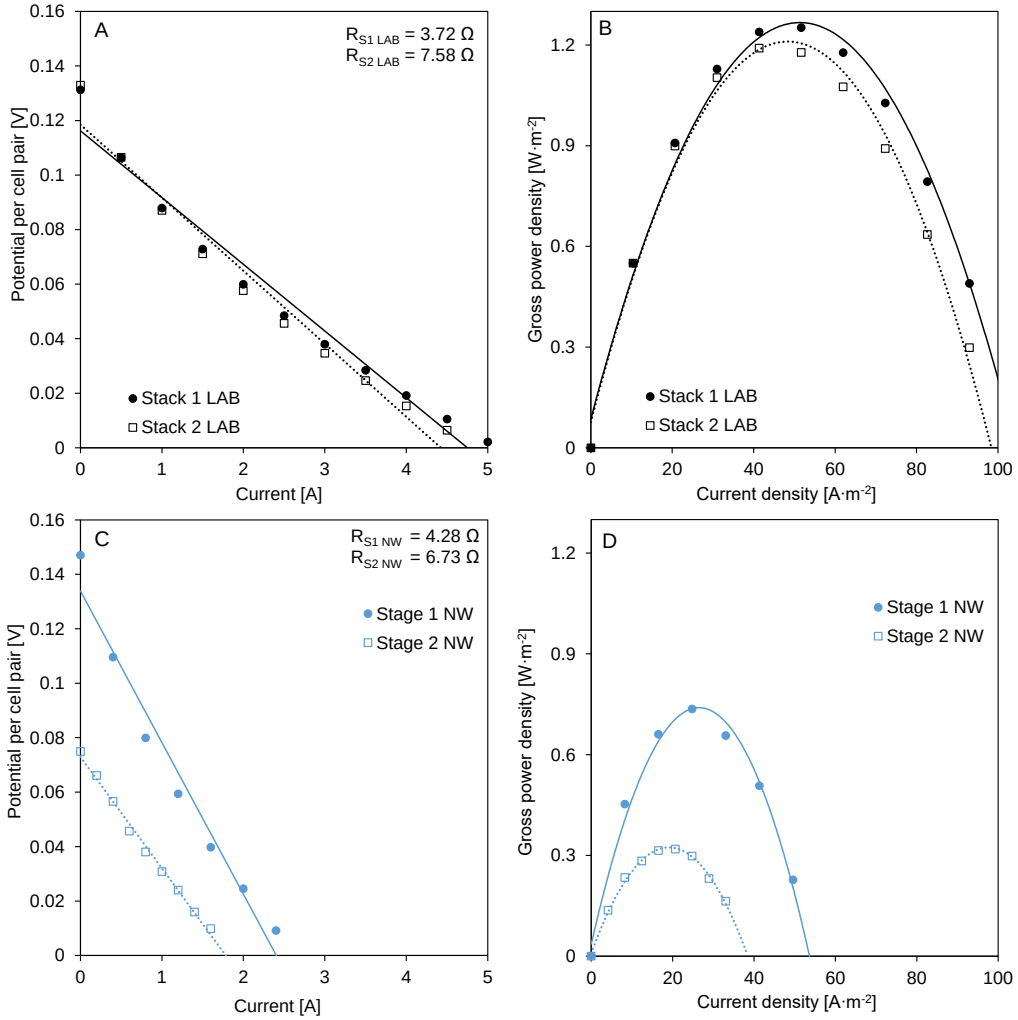

Figure 4.2 (A) I-V curve, stack resistance and (B) gross power density vs current density for stacks 1 (circles and solid lines) and 2 (squares and dotted lines) as tested in the laboratory (LAB, black); (C) I-V curve, stack resistance and (D) gross power density vs current density for stages 1 (circles and solid lines) and 2 (squares and dotted lines) as tested at the research facility with natural waters (NW, blue). Conditions for these results are shown in Table 4.3. In these measurements, ERS was still 0.2 M $K_4Fe(CN)_6$, 0.2 M $K_3Fe(CN)6$ and 0.15 M NaCl. Trend lines are added to guide the eye.

4.3.2. Continuous staging performance over a month

Figure 4.3 shows the gross power density and energy efficiency on the sampling moments for each stage and in total. Throughout the 30-day run, the total gross power density was quite stable at around 0.35 W·m^{-2} (equation 4.3). The contribution of each stage can be seen in Figure 4.3A, averaging 0.55 W·m^{-2} for stage 1 and 0.25 W·m^{-2} for stage 2 (equation 4.2). By reusing the waters in stage 2, thus extending their use at a reduced salinity gradient, and because of the longer residence time in this stage, there was an expected decrease in total

power density. The energy efficiency achieved values above 30 % with a maximum of 37 % (Figure 4.3B, equation 4.4). Such energy efficiencies have not been reported for natural water studies, and are found here to be comparable to theoretical [39,50] and laboratory studies [30,42]. The gross power density and the gross energy efficiency represent a good electrical performance of the multistage configuration. The gross power density would be increased if the salinity gradient of the natural waters was higher.

Some variations in performance as detected were explained by one of the following reasons: First, due to the natural change in salinity gradient between sea and river water (Figure S4.3A) and, second, due to changing the stack operation. For example, on days 27 and 28, an asymmetrical flow rate was tested (shaded green areas in Figures 4.3, 4.4, 4.5 and 4.6), with the seawater flow rate being half of the river water flow rate, or change in current applied (Table S4.1). The temperature varied between 18 and 21 °C. These fluctuations can be seen in Figure S4.3.

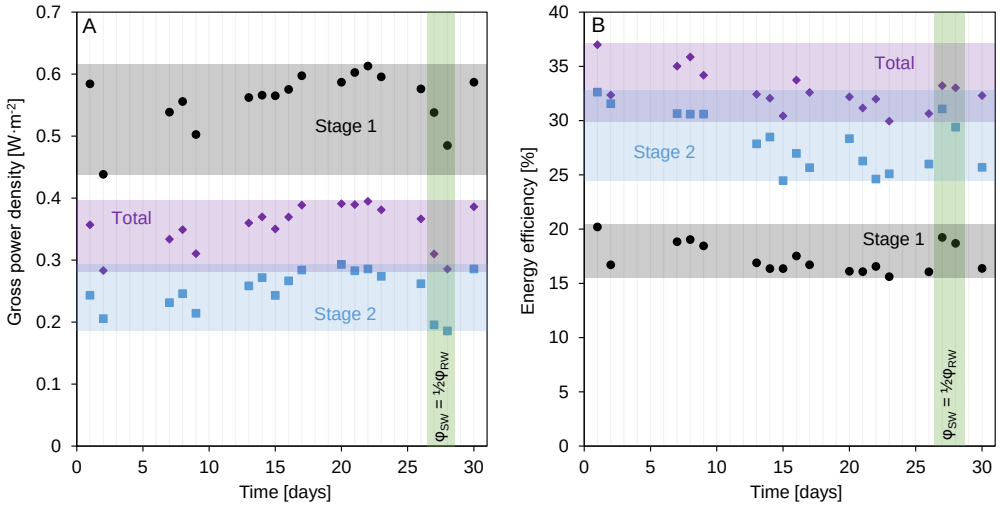

Figure 4.3 Total and stage-related gross power density (A) and gross energy efficiency (B) for the sampling moments: Stage 1 (●), Stage 2 (■) and total (◆). The green shaded area corresponds to two days with an asymmetric flow rate, while RW was kept the same (39.3 L·h^{-1}), and SW was reduced to half (19.6 L·h^{-1}).

Figure 4.4 shows the multistage net power density (equation S4.2) and the pumping power density per stage in two scenarios (equation. S4.1). If we would correct the gross power density only with the pressure drop of that stage to its starting value (0.3 bar for stage 1 and 0.15 bar for stage 2) and kept it constant, the total net power density amounts to 0.25 W·m^{-2}. However, due to an increasing pressure drop in stage 1, at the start of the operation (Figure S4.3), the total net power density was mostly below 0.1 W·m^{-2} (Figure 4.4A). That is also why the constant and actual scenarios' net power density values do not match on day 1 of the 30-day run. Stage 1 was most affected, due to the higher flow velocity, and it was the first in line to experience a pressure drop increase due to fouling (Figure S4.3), reaching, for most days,

pumping power densities higher than the gross power density (Figure 4.4B). Later on, stage 2 also showed an increase in pressure drop, indicating the fouling was not exclusive to stage 1 but remained with positive net power density values. The net power density per stage can be obtained from the difference between Figure 4.3A and Figure 4.4B. In our previous work [30], it was shown that variation of the stack residence time (and hence flow velocity and pressure drop) could be used for the optimization of the net power density production while increasing the energy efficiency. This strategy was not followed in this duration test.

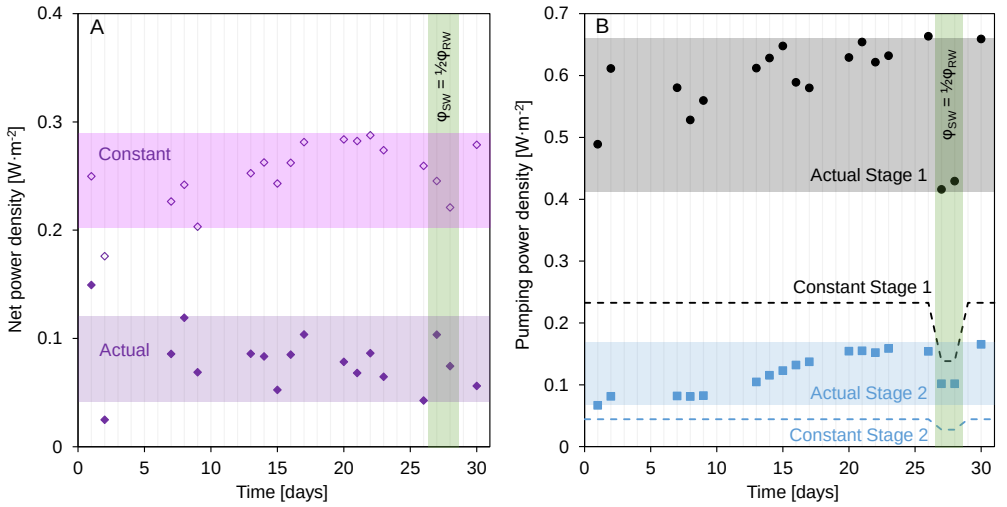

Figure 4.4 (A) Total net power density of the multistage configuration for both the actual pressure drop and in case the pressure drop is taken as a constant and equal to the initial pressure drop. (B) Pumping power density calculated for stage 1 (black) and stage 2 (blue), actual values with symbols and constant values with dashed lines. The scenario actual uses the stage pressure drop at that moment and the scenario constant uses only the initial pressure drop value (Figure S4.5). The green shaded area corresponds to two days with an asymmetric flow rate, while RW was kept the same (39.3 L·h^{-1}), and SW was reduced to half (19.6 L·h^{-1}).

The pressure drop can be partly attributed to visible fouling as algae growth was noticeable in the transparent tubing and the feedwater compartments. More details can be seen during the cleaning and stack autopsy in section 3.4. Interestingly, the gross electrical performance was not affected by the pressure increase and fouling [20]. We conclude that the electrical performance was dependent on the water's composition and concentration and mostly independent of the fouling for the period of testing. The fouling however affected the hydraulic performance, leading to a high loss in net power density output. Efforts towards maintaining the pumping power losses at a lower level in time are therefore needed.

The asymmetrical flow rate, with seawater being half of the river water flow rate, on days 27 and 28 did not show increasing performance values compared to the overall experiment. However, compared to the data points just before and after (days 26 and 30), which share more similar conditions, the energy efficiency increased (Figure 4.3B). Although the gross

power density decreased (Figure 4.3A), the pumping power density lowered (Figure 4.4B) subsequently increasing the net power density for the actual scenario. Thus, for controlled water conditions, the asymmetrical condition could work as an optimization. On the other hand, in a highly dynamic environment, as present in this study, there is no discernible benefit.

4.3.3. Ions behaviour through staging: multivalent ions are transported differently per stage

During the 30-day run, natural waters were sampled at all positions to analyse the transport of ions through staging. The presence of multivalent ions, such as Mg^{2+}, Ca^{2+} and SO_4^{2-}, leads to uphill transport of these ions, as described by Vermaas et al. [10]. Uphill transport occurs when a divalent ion is transported against its concentration gradient (usually from the river water to the seawater side) to obtain equilibrium in chemical potential at both sides of the membrane. This phenomenon results in losses for the RED process, since one divalent ion like Mg^{2+} is exchanged with two monovalent ions like Na^+ at zero net charge.

Figure 4.5 shows the concentration of monovalent ions through the multistage process and the measured conductivity at the inlet (position 0), between the stages (position 1) and at the outlet (position 2). Both for the river and seawater sides, the conductivity coincides with chloride (Cl^-) and sodium (Na^+) concentration, which means that conductivity sensors can correctly indicate the salinity gradient when the natural water is mainly composed of Cl^- and Na^+. This implies that an automated optimization of the RED performance could rely on the conductivity sensors that predict the available salinity gradient. All the monovalent ions show the same trend through staging.

While monovalent ions show a predictable behaviour through staging, multivalent ions have a different pattern. The uphill transport of sulphate (SO_4^{2-}) and calcium (Ca^{2+}) in stage 1 was expected and given in the literature [14,51]. Figures 4.6A and 4.6E show that both SO_4^{2-} and Ca^{2+} concentrations at the river water side decreased from position 0 to 1 (being 0 the inlet and 1 the outlet of stage 1). And the opposite occurred on the seawater side (Figures 4.6B and 4.6F). In the case of magnesium (Mg^{2+}), uphill transport is not present (Figures 4.6C and 4.6D) which is opposite to the literature [14]. In the work by Rijnaarts et al., the uphill transport of divalent ions was studied individually and not as a mixture, while also discarding the presence of Ca^{2+}. The uphill transport of Ca^{2+} can be explained by the smaller hydrated ionic radius of Ca^{2+} (0.412 nm) compared to Mg^{2+} (0.428 nm). Making Ca^{2+} be transported more easily than Mg^{2+}. Guo et al. [11] compared the uphill transport of Mg^{2+} and Ca^{2+} for two different membranes.

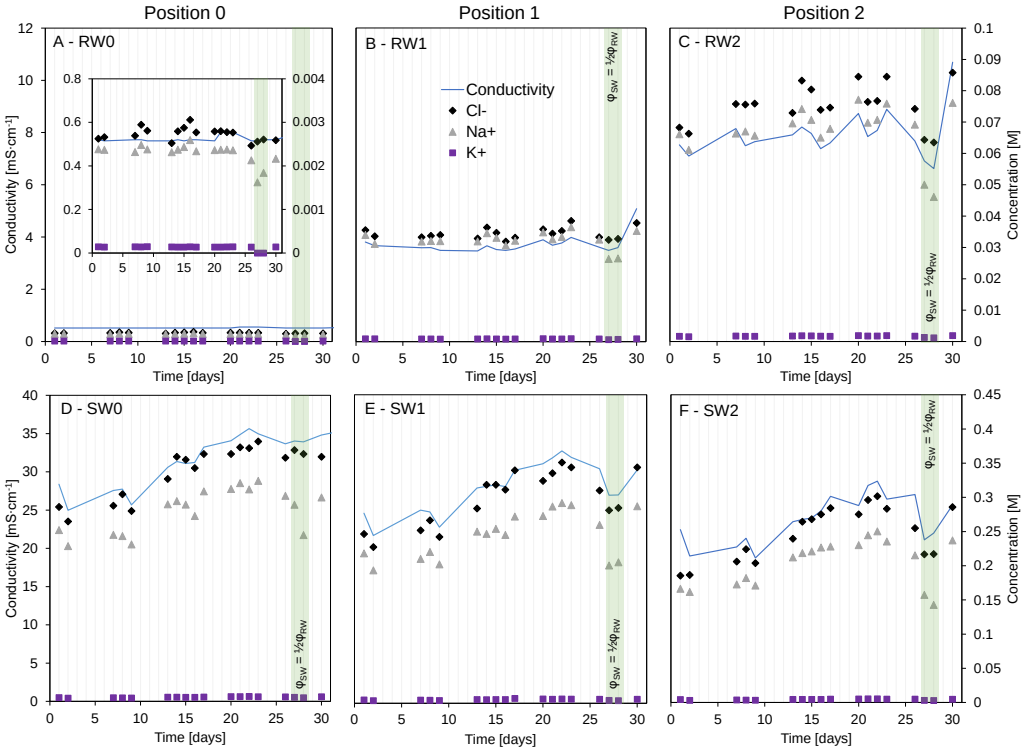

Figure 4.5 Conductivity and concentration of monovalent ions at the inlet (0), between stages (1) and outlet (2) in river water (RW) (A, B and C) and in seawater (SW) (D, E and F) while operating at constant current density. The conductivity is represented with a line. The shaded area corresponds to two days with an asymmetric flow rate, RW was kept the same (39.3 $L \cdot h^{-1}$), and SW was reduced to half (19.6 $L \cdot h^{-1}$).

At lower temperatures, most of the uphill transport was attributed to Ca^{2+} (which was ten times lower in concentration than Mg^{2+} at the river waterside). In our case, Ca^{2+} concentration (1.1 mM) in river water was higher than Mg^{2+} concentration (0.5 mM). The higher concentration and the smaller hydrated radii triggered Ca^{2+} to be preferably exchanged with Na^{+} rather than Mg^{2+}.

Figure 4.6 Sulphate (A and B), magnesium (C and D) and calcium (E and F) concentrations, in mM, in river water (RW, left side graphs) and seawater (SW, right side graphs) at the inlet (0), between stages (1) and outlet (2). Note that the y-axis values differ between graphs. The green shaded area corresponds to two days with asymmetric flow rate, RW was kept the same (39.3 $L \cdot h^{-1}$), and SW was reduced to half (19.6 $L \cdot h^{-1}$).

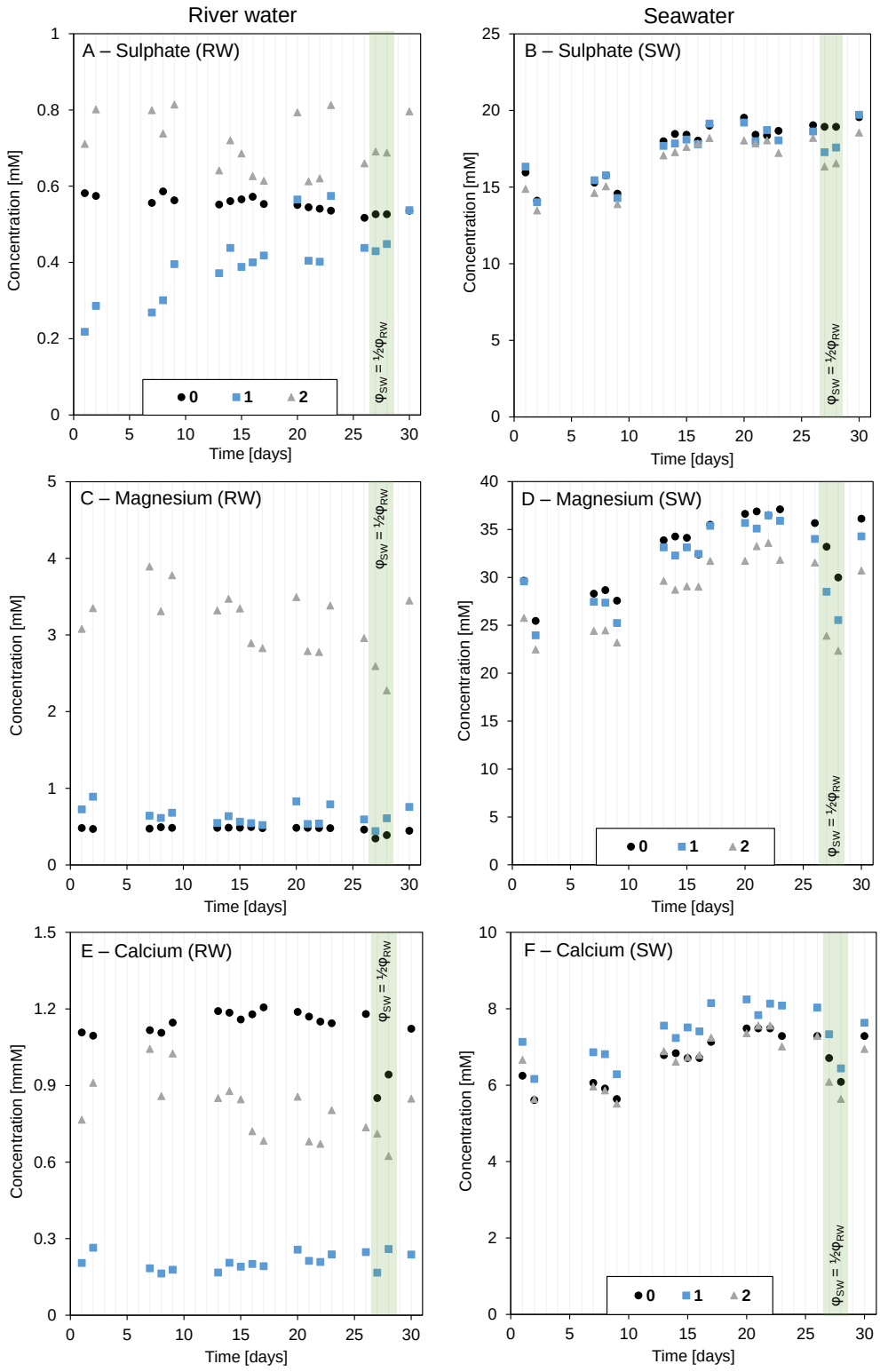
River water
Seawater
A – Sulphate (RW)
B – Sulphate (SW)
C – Magnesium (RW)
D – Magnesium (SW)
E – Calcium (RW)
F – Calcium (SW)
Concentration [mM]
Concentration [mmM]
Time [days]
0
1
2
φSW = ½φRW

In stage 2, the transport pattern of multivalent ions was distinct from the previous stage. From positions 1 to 2, representing the inlet and outlet of stage 2, all ions follow downhill transport, following their concentration gradient, typically from the seawater to river water. Such behaviour has not been reported in the literature so far, given that experiments with multistage and multivalent ions are missing. The absence of uphill transport in stage 2 can be explained by the Donnan equilibrium. In stage 1, the multivalent ions exchange with the monovalent ions to obtain equilibrium in chemical potential between the membrane sides [52]. However, in stage 2, the Donnan potential for each ion is equilibrated at the inlet. Figure 4.7 shows the calculated Donnan potential (equation 4.1) for each ion on day 17 of the experiment. This day was randomly selected from the data. Stage 1 works as a removal step for multivalent ions, comparable to the principle of Donnan Dialysis [53]. The application of Donnan Dialysis as a pre-treatment step for RED was proposed earlier to improve the power density [54]. Since uphill transport was an intrinsic loss only for stage 1, stage 2 could benefit from this, resulting in a relatively better performance on that stage despite the lower salinity gradient.

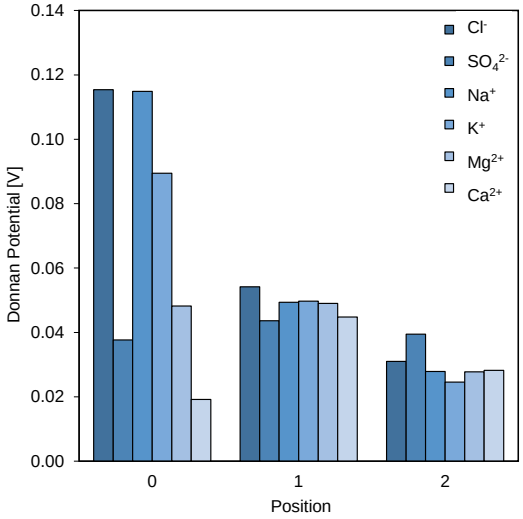

Figure 4.7 Calculated Donnan Potentials (equation 4.1) for the ions at the positions 0, 1 and 2 on day 17 (randomly selected to represent the data). Each bar represents an ion, from left to right: chloride, sulphate, sodium, potassium, magnesium and calcium.

4.3.4. Cleaning and Stack autopsy

The anti-fouling strategies adopted in the pre-treatment were not able to maintain the stacks' pressure drop close to the initial values. Increasing pressure drops lead to higher pumping power losses which decrease the available net power density. Thus, towards the end of the experiment, in an attempt to lower the pressure drop and possibly recover the initial value, three physical cleaning techniques were selected regarding low cost,

sustainability and short system interruption, and applied to both stacks. The cleaning started with reversing the inlet and outlet, followed by increased flow rate and finally air sparging. Results achieved with the application of these cleaning techniques are presented in Figure 4.8.

The fouling removal on both stages was similar, achieving a recovery in pumping power losses of 0.03 $W \cdot m^{-2}$ for stage 1 and 0.01 $W \cdot m^{-2}$ for stage 2, which in both cases represented around 15 % of the pumping power that could be recovered from stage 1 (~ 0.21 $W \cdot m^{-2}$) and stage 2 (~ 0.07 $W \cdot m^{-2}$). A higher removal of fouling on stage 1 was expected since the flow velocity in this stage was higher and it was also more likely to accumulate foulants, as it was the first stack to receive the feed waters. Most likely that could not be detected due to the cleaning being performed only after a long time of operation when fouling build-up was already established and reached similar levels in both stages. When looking at the amount of particulate removed that could be collected in the outlet of the stacks we observed that on the seawater outlet of stage 1 a higher removal was achieved (Figure 4.8). This indicates that more fouling was present and could be removed, even though the numbers presented are normalized for the membrane area, which in stage 2 is double of stage 1. For river water this did not happen, with similar removal in both stages, indicating that the fouling was not affected by the different hydraulic conditions of stages 1 and 2.

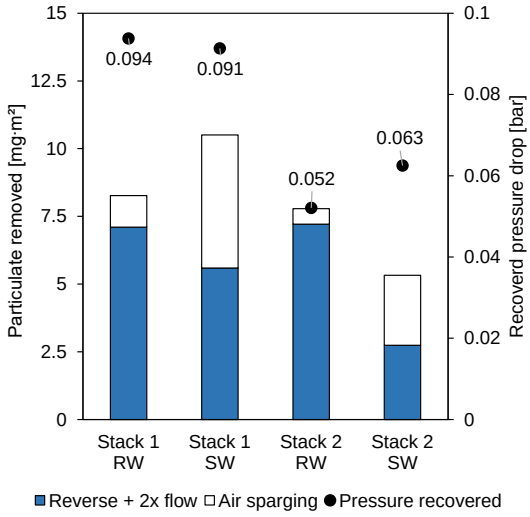

Figure 4.8 Bars represent the amount of particulate fouling removed per stack membrane area for each step of the cleaning procedure: cleaning with reverse and increased flow together and air sparging. The pressure drop that could be recovered from each water compartment at the end of the cleaning is presented with a round symbol on top of the bars (the difference between right before and after cleaning). The pressure drop decrease after the cleaning procedure appeared only to be a small fraction of the pressure drop across the stages after long-term operation.

After the cleaning, two fractions of particulate fouling were analysed, the first one collected after the reverse and increased flow, and the second after air sparging. For the river water compartments of both stages, the particulate removal was greater with the reverse and increase flow than with the air sparging. This probably happened due to the order in which the procedures took place, nonetheless, it showed that this simple technique could already remove a large part of the reversible fouling at a low energy cost and no additional agents had to be added (Figure 4.8). For the seawater compartments of both stages, the removal of foulants with air sparging was similar to the amount achieved with the reverse and increased flow (around 50 % of total particulate removed), showing that the addition of compressed air as a cleaning agent could result in better cleaning. This indicates that the remaining fouling from seawater could still be removed with increased shear stress near the membrane surface as caused by the use of compressed air, tackling a more resistant fouling layer. This shows that a dedicated cleaning procedure has to be applied for a specific type of fouling.

The results show, that the pumping power recovered achieved with the cleaning procedure was quite modest (15 %) compared to the power losses accumulated on the previous days of operation. Implementing the cleaning method earlier in the operation and more frequently, may have prevented the cumulative increase of pressure drop [24]. In addition, other more intensive physical cleanings or chemical cleanings could be considered to reduce the fouling-related pumping power losses [55].

Following the cleaning procedures, the configuration was kept running for two additional weeks to allow fouling regrowth and then stage 1 was opened for fouling investigation. Representative pictures of the membranes and spacers autopsy are shown in Figure S4.6. In the autopsy no particulate fouling was visible, nor types of fouling could be seen by the naked eye, except the presence of organic fouling by humic acids on the AEMs, due to the characteristically brown colour of this type of fouling [43]. The positive charge of the AEMs attracts the negatively charged organic matter commonly found in freshwater bodies, widely known as humic acids, while CEMs do not suffer from this specific type of fouling, due to their negative charge being able to repel such foulants. However, under the microscope, many types of foulant could be identified, as shown in Figures 4.9 and 4.10.

Figures 4.9A, 4.9B and 4.9C show agglomerations of organisms forming large structures, from 1 µm to approximately 50 µm. Most of the structures were identified as green algae, glaucophytes, and diatoms, all of them being commonly present in freshwater bodies [56,57]. The alcian blue dye reacted with biofilm and EPS layer, enabling their visualization and their presence was quite extensive on the surface of the membrane. SEM images, in Figures 4.10A and 4.10B, show similar structures, and biofilm formation can be seen more clearly, with an agglomerate of bacterial cells surrounded by the EPS layer. These types of foulants are

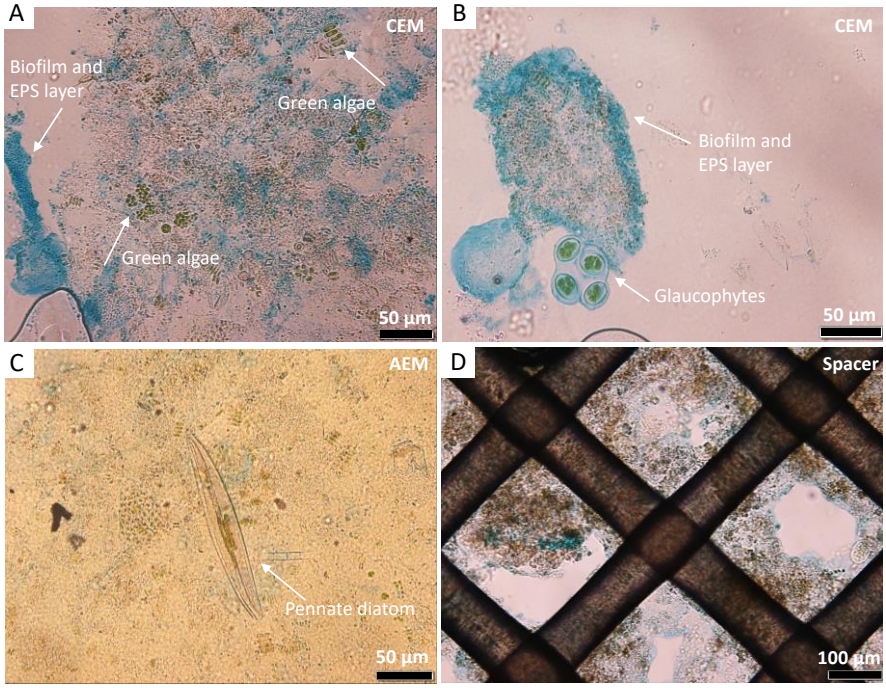

Figure 4.9 Representative microscopic images of algae and other structures found on CEM (A and B), AEM (C) and spacer (D). The scale bar is 50 µm for A, B and C and 100 µm for D.

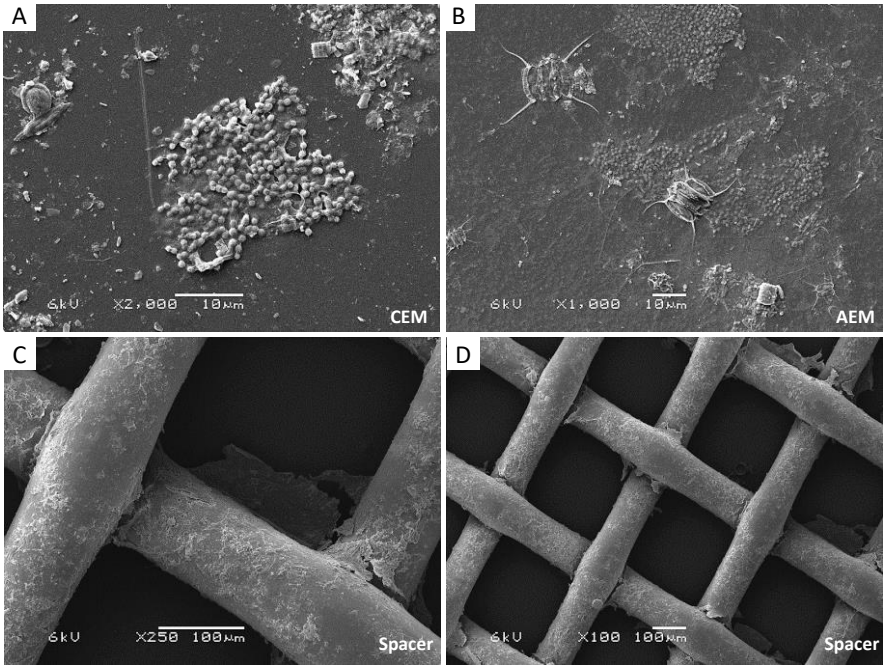

Figure 4.10 Scanning electron microscope representative images of CEM (A), AEM (B) and spacers (C and D). The scale bar is 10 µm for A and B, and 100 µm for C and D.

consistent with the pre-treatment that was employed during the experiment since with a 5 µm filter as the last step of pre-treatment, a large part of particulate fouling was retained and only smaller foulants could pass through. The formation of structures larger than 5 µm resulted from the growth of living organisms and aggregation in communities.

Figures 4.9D, 4.10C and 4.10D also show an accumulation of fouling at the spacers at all four corners of the open mesh area. The presence of fouling reduced the available open area for the feedwaters to pass and consequently led to an increase in pressure drop. The spacers' thickness of 155 µm was remarkably thin and increased the sensitivity to fouling, which may also have contributed to an increase in the pressure on the inlet compartment [58].

Unfortunately, the cleaning procedures were not effective in removing the remaining pressure drop to a large extent, as the type of fouling in this experiment was more intrinsically connected to the membrane surface than loosely particulate deposits. For future studies, an anti-fouling strategy to be applied against biofouling growth could be avoiding sunlight to reach the stacks and tubing. In a darker setting, most microorganisms' metabolism will be slower, preventing growth and accumulation [59]. Although there was a large effect of fouling on the hydraulic performance, the impact of fouling and scaling did not affect the gross electrical performance of the membrane pile, as the gross power density kept stable during the experiment. This positive outcome shows that the electrical optimization of the RED process (e.g., by multistage or electrode segmentation) and the minimization of the hydraulic resistance showed to be independent activities. The main influence of fouling was via the hydraulic resistance, affecting the required pumping power. This issue should be addressed using profiled membranes [25] or (in combination) with a more frequent cleaning procedure directly from the start of the experiment. The anti-fouling strategies (in pre-treatment and cleaning) should also be separately investigated and evaluated in view of their effectiveness, power consumption, system interruption and impact on environmental sustainability [20].

4.4. Conclusions

A multistage reverse electrodialysis system was operated with natural waters, at the Afsluitdijk, The Netherlands, for over 30 days with a stable gross electrical performance. The gross power density was between 0.3 and 0.4 $W \cdot m^{-2}$ and energy efficiency values were between 30 and 37 %. A strong increase in pressure drop in stage 1 was observed in the first weeks, after which the net power density was stable at around 0.1 $W \cdot m^{-2}$. Considering the initial measured pressure drop the net power density would increase to around 0.25 $W \cdot m^{-2}$. Fouling did not affect the gross electrical performance of both stages but led to a higher pressure drop reducing the net power density output. The transport of multivalent ions was different in stage 1 and stage 2. For stage 1, SO_4^{2-} and Ca^{2+} showed uphill transport from river water to seawater, whereas Mg^{2+}, which is often linked to uphill transport in literature, did not. This was explained by the higher concentration of Ca^{2+} than Mg^{2+} in the river water. In stage 2 actually, no uphill transport was observed. The cleaning procedures applied had limited effect on recovering the original pressure drop of the stacks. The stack autopsy revealed, at the membrane surface, microorganism structures larger than the cartridge filter (mean pore size of 5 µm) used as pre-treatment for the natural waters. The agglomeration and growth of these structures in-situ contributed to the increase in pressure drop through time in the compartments, as well as part of the spacers' open area that was covered with (bio)fouling.

Multistage reverse electrodialysis, with two stages in series, showed as a viable configuration to increase the energy efficiency with a stable gross power density, even at the low salinity gradient, available in this duration test. For optimal performance, the electrical control of the stages could be automated, taking into consideration the conductivity at the inlets and actual pressure drop. An improved stack design in combination with pre-treatment of the natural waters and periodical cleaning procedure of the stages is highly recommended, to avoid the power losses associated with the pressure drop increase across the stacks.

4.5. Supporting information

4.5.1. Hexacyanoferrate solution

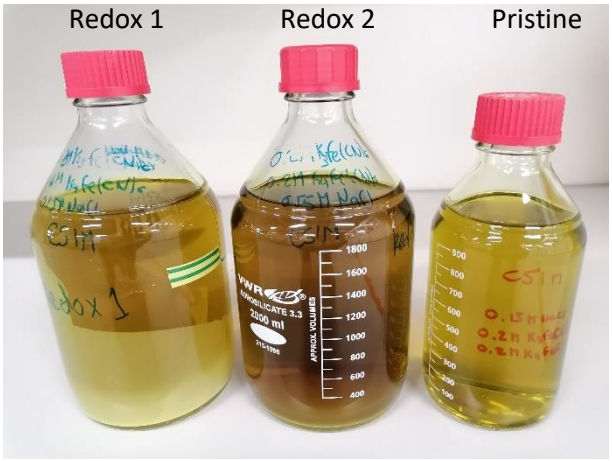

Figure S4.1 Pristine hexacyanoferrate solution (left) compared with the hexacyanoferrate solutions used as ERS at the electrode compartments of stages 1 (right) and 2 (middle) for four days.

The autopsy of the electrodes and spacers adjacent to the electrode compartments showed scaling in different forms, as seen in the pictures in Figure S4.2.

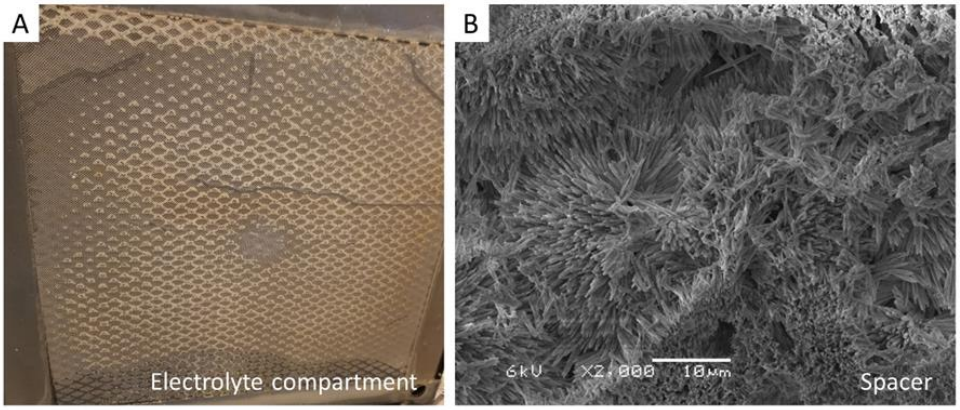

Figure S4.2 (A) Picture of the electrolyte compartment (spacer and electrode behind) and the white scaling on the spacer mesh (scaling). (B) SEM image of the spacer compartment, showing the crystals formed by scaling. With EDX the scaling was identified as $CaCO_3$ deposition.

The scaling was attached to the electrode, to the spacer net and to the shielding membrane on the side facing the electrode. Using EDX, it is more likely that the scaling of the spacers was caused by $CaCO_3$ and on the electrodes scaling was a combination of $Ca(OH)_2$ and

$Mg(OH)_2$. Since no cleaning was performed on the electrodes, the scaling as found may still relate to scaling issues using the hexacyanoferrate electrode rinse solution on the transition to natural waters and, while the single-pass seawater, as ERS, was running without periodically switching the feedwaters (until day 5 of the 30-day run). The electrode scaling was more evident on one side than the other, which reinforces the assumption that this scaling developed at the start of the experiment. Scaling is more prone to occur at the cathode due to an increase in alkalinity. While switching the waters, both electrode compartments act as cathode or anode at some point, making a pH change in the compartment. During the period that the electrode acts as the anode, the precipitates can dissolve due to the formation of acid. To avoid scaling, reversal of polarity every six hours was found effective.

4.5.2. Conditions during the installation phase and the 30-day run

The seawater concentration, and thus conductivity, now and then drastically fluctuated due to the Afsluitdijk locks located at each end of the dyke (Figure S4.3A). These locks open for boats to cross and to discharge extra fresh water from Lake IJssel. For example, between day 0 to day 10 on the 30-day run the locks were frequently opened, due to intense rainfall in the region (Figure S4.4), the seawater conductivity even dropped to 15 $mS \cdot cm^{-1}$. In those moments, given the non-stable behaviour, both stages operated in OCV conditions (Figure S4.3B). These location-specific fluctuations reveal a vulnerability to operating with natural intakes. Note that also at other locations, the conductivity and temperature can change drastically during the seasons or specific weather events [16]. An automated control to adapt the current, given the inlet conductivities, could be a solution for better operation. In the present case, the temperature fluctuated between 18 and 21 °C and between day and night the change was 1 °C (Figure S4.3D).

The stages' pressure drops are shown in Figure S4.3C. The higher initial pressure drop in stage 1 is due to increased flow velocity (1 $cm \cdot s^{-1}$) compared to stage 2 (0.5 $cm \cdot s^{-1}$). Stage 1 was the first to suffer from increased pressure drop since it is also the one receiving the feed waters first. This was probably caused by an accumulation of fouling at the membranes and in the very thin spacer used (155 µm). After the accentuated increase until day 6, for stage 1, water switching was used to mitigate scaling issues at the cathode in both stages. At the same time, this technique also helped with the increasing pressure drop where the rapid increase was replaced by a moderate increase over time and rejuvenated the performance of stage 1 (Figure S4.3B, days 4 to 6). It is hypothesized that the periodical osmotic shock caused by switching the seawater with the river water acted as an anti-fouling technique. It is also after day 6, with the switching, that the pressure drop of stage 2 starts to slowly increase. It seems until there stage 1 was acting like a filter to stage 2, and later the filtering capacity of stage 1 was lost with the switching, thus the fouling was carried to the next stage.

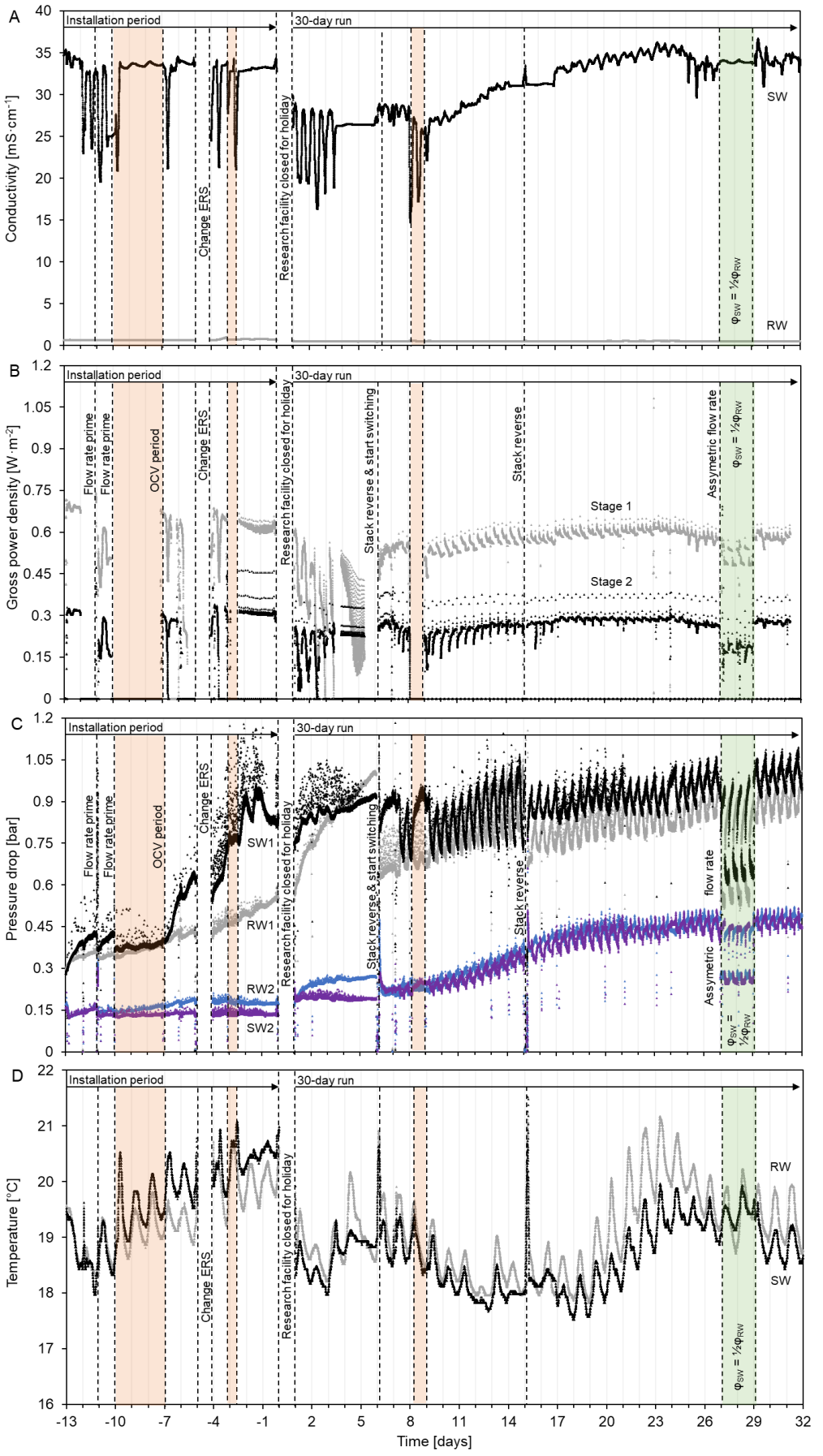
A
Installation period
30-day run
Conductivity [mS·cm⁻¹]
Change ERS
Research facility closed for holiday
SW
RW
φSW = ½φRW
B
Gross power density [W·m⁻²]
Flow rate prime
Flow rate prime
OCV period
Change ERS
Research facility closed for holiday
Stack reverse & start switching
Stack reverse
Assymetric flow rate
Stage 1
Stage 2
C
Pressure drop [bar]
SW1
RW1
RW2
SW2
flow rate
Assymetric
D
Temperature [°C]
Time [days]

Figure S4.3 (A) Inlet seawater (SW) and river water (RW) conductivity, (B) stage 1 and stage 2 gross power density, (C) SW and RW compartments pressure drop for stages 1 and 2, and (D) inlet SW and RW temperature, for the installation period and later 30-day run. When the water switching was active, the waters changed periodically, and with this, the line and colour do not indicate SW or RW but are fixed to the compartment (pressure drop plot). The zig-zag pattern on the pressure drop plot, after water switching, was thought to be caused by an asymmetry between pumps and compartments, but it was not further explored. The orange-shaded areas correspond to OCV moments. The green shaded area corresponds to two days with asymmetric flow rate, RW was kept the same (39.3 $L \cdot h^{-1}$), and SW was reduced to half (19.6 $L \cdot h^{-1}$).

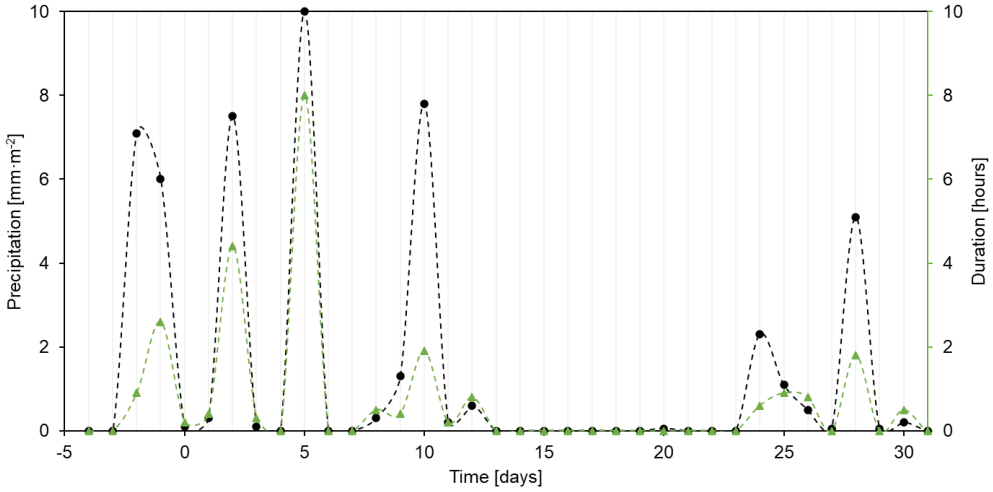

Figure S4.4 Rainfall as registered in Leeuwarden, The Netherlands, 5 days before and during the 30-day experiment [60], this figure does not comprise rainfall data from the installation period.

4.5.3. Pressure drop calculations

The pumping losses, or pumping power density ($P_{d,pump}$ in $W \cdot m^{-2}$), corresponding to the power lost for pumping SW and RW through a stack was calculated as:

$$P_{d,pump} = \frac{\varphi_{RW} \cdot \Delta P_{RW} + \varphi_{SW} \cdot \Delta P_{SW}}{A_{mem}} \quad \text{(Eq. S4.1)}$$

Where $\boldsymbol{\varphi}$ is the flow rate ($m^3.s^{-1}$) and $\boldsymbol{\Delta P}$ is the pressure drop across the compartment (Pa). By measuring the pumping losses, the net power density can be calculated as the difference between gross power and pumping power:

$$P_{d,net} = P_{d,gross} - P_{d,pump} \quad \text{(Eq. S4.2)}$$

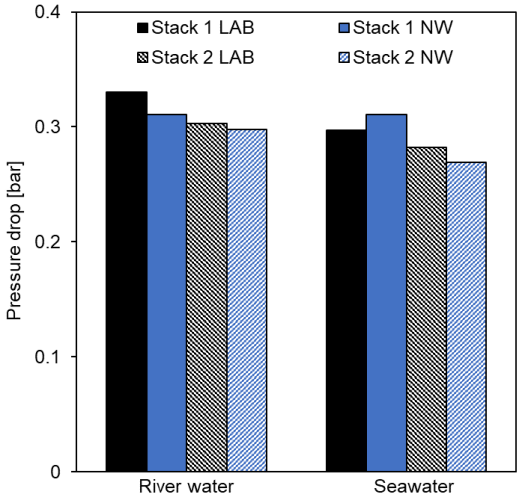

Figure S4.5 Pressure drop of river water and seawater in each stack at 1.0 cm·s^{-1} (39.3 L·h^{-1} for stack 1 and 78.6 L·h^{-1} for stack 2) at the laboratory tests (LAB) and at the pilot plant with natural waters (NW) at initial conditions. Stack 1 = stage 1 and stack 2 = stage 2.

4.5.4. Switch position and current and stack potential measured during the 30-day run

Table S4.1 Switch position and applied current with the respective voltage response at the sampling moments. Since water switching occurred, two positions are defined: position A indicates the original/starting position and position B indicates seawater is in the original river water compartment and vice-versa.

Sample day	Position	I_{S1} [A]	E_{S1} [V]	I_{S2} [A]	E_{S2} [V]
1	A	0.866	2.090	0.519	2.902
2	A	0.866	1.568	0.518	2.456
7	B	0.807	2.067	0.640	2.239
8	A	0.793	2.171	0.583	2.611
9	B	0.759	2.051	0.594	2.234
13	B	0.759	2.294	0.594	2.696
14	B	0.759	2.310	0.594	2.833
15	B	0.759	2.306	0.594	2.533
16	A	0.746	2.389	0.537	3.073
17	A	0.746	2.480	0.537	3.277
20	B	0.759	2.395	0.594	3.055
21	A	0.746	2.502	0.537	3.263
22	A	0.747	2.542	0.537	3.295
23	B	0.759	2.431	0.593	2.860
26	A	0.746	2.392	0.537	3.020
27	B	0.713	2.338	0.407	2.978
28	A	0.747	2.010	0.390	2.951
30	B	0.759	2.395	0.594	2.979

4.5.5. Autopsy

Representative pictures of the membranes and spacer are shown in Figure S4.6. Clean Fumasep FAS-30 and FKS-30 (Fumatech, Germany) membranes are translucent and transparent, as well as a clean spacer net. The membranes and spacers were found to be intact when opening the stacks at the autopsy, with no visible damage. Due to interactions with humic acids, AEMs turned brown after the experiment, while CEMs preserved the same characteristics of a clean membrane looking by the naked eye. On the spacers, some fouling accumulation can be seen on the connections of the mesh, mostly characterized by green light colour due to the presence of algae-like structures.

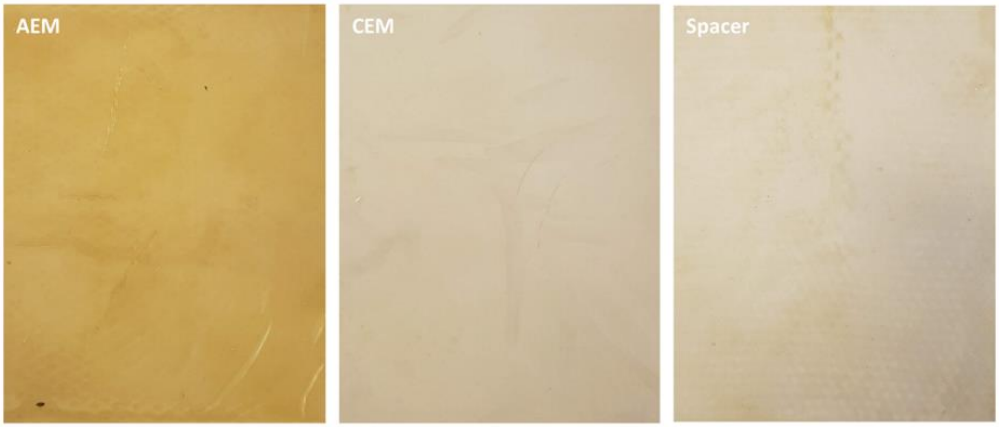

Figure S4.6 Representative pictures of the membranes and spacer. Due to interactions with humic acids, AEMs turned brown after the experiment, while CEMs preserved visually the same characteristics of a clean membrane. On the spacers, some fouling accumulation can be seen on the connections of the net, mostly characterized by green light colour due to the presence of algae.

References

[1] K. Nijmeijer, S. Metz, Chapter 5 Salinity Gradient Energy, Elsevier, 2010. https://doi.org/10.1016/S1871-2711(09)00205-0.

[2] R.E. Lacey, Energy by reverse electrodialysis, Ocean Engineering. 7 (1980) 1–47. https://doi.org/10.1016/0029-8018(80)90030-x.

[3] J. Veerman, M. Saakes, S.J. Metz, G.J. Harmsen, Reverse electrodialysis: Evaluation of suitable electrode systems, J Appl Electrochem. (2010). https://doi.org/10.1007/s10800-010-0124-8.

[4] R.E. Pattle, Production of electric power by mixing fresh and salt water in the hydroelectric pile, Nature. (1954). https://doi.org/10.1038/174660a0.

[5] A. Nazif, H. Karkhanechi, E. Saljoughi, S.M. Mousavi, H. Matsuyama, Recent progress in membrane development, affecting parameters, and applications of reverse electrodialysis: A review, Journal of Water Process Engineering. 47 (2022) 102706. https://doi.org/10.1016/j.jwpe.2022.102706.

[6] Y. Mei, C.Y. Tang, Recent developments and future perspectives of reverse electrodialysis technology: A review, Desalination. (2017). https://doi.org/10.1016/j.desal.2017.10.021.

[7] R.A. Tufa, S. Pawlowski, J. Veerman, K. Bouzek, E. Fontananova, G. di Profio, S. Velizarov, J. Goulão Crespo, K. Nijmeijer, E. Curcio, Progress and prospects in reverse electrodialysis for salinity gradient energy conversion and storage, Appl Energy. 225 (2018) 290–331. https://doi.org/10.1016/j.apenergy.2018.04.111.

[8] J.W. Post, C.H. Goeting, J. Valk, S. Goinga, J. Veerman, H.V.M. Hamelers, P.J.F.M. Hack, Towards implementation of reverse electrodialysis for power generation from salinity gradients, Desalination Water Treat. 16 (2010) 182–193. https://doi.org/10.5004/dwt.2010.1093.

[9] J.W. Post, H.V.M. Hamelers, C.J.N. Buisman, Influence of multivalent ions on power production from mixing salt and fresh water with a reverse electrodialysis system, J Memb Sci. (2009). https://doi.org/10.1016/j.memsci.2008.12.042.

[10] D.A. Vermaas, J. Veerman, M. Saakes, K. Nijmeijer, Influence of multivalent ions on renewable energy generation in reverse electrodialysis, Energy Environ Sci. (2014). https://doi.org/10.1039/c3ee43501f.

[11] Z.Y. Guo, Z.Y. Ji, Y.G. Zhang, F.J. Yang, J. Liu, Y.Y. Zhao, J.S. Yuan, Effect of ions (K+, Mg2+, Ca2+ and SO_4^{2-}) and temperature on energy generation performance of reverse electrodialysis stack, Electrochim Acta. 290 (2018) 282–290. https://doi.org/10.1016/j.electacta.2018.09.015.

[12] A.H. Avci, R.A. Tufa, E. Fontananova, G. di Profio, E. Curcio, Reverse Electrodialysis for energy production from natural river water and seawater, Energy. 165 (2018) 512–521. https://doi.org/10.1016/j.energy.2018.09.111.

[13] E. Güler, W. van Baak, M. Saakes, K. Nijmeijer, Monovalent-ion-selective membranes for reverse electrodialysis, J Memb Sci. (2014). https://doi.org/10.1016/j.memsci.2013.12.054.

[14] T. Rijnaarts, E. Huerta, W. Van Baak, K. Nijmeijer, Effect of Divalent Cations on RED Performance and Cation Exchange Membrane Selection to Enhance Power Densities, Environ Sci Technol. (2017) 13028–13035. https://doi.org/10.1021/acs.est.7b03858.

[15] S. Mehdizadeh, Y. Kakihana, T. Abo, Q. Yuan, M. Higa, Power generation performance of a pilot-scale reverse electrodialysis using monovalent selective ion-exchange membranes, Membranes (Basel). 11 (2021) 1–25. https://doi.org/10.3390/membranes11010027.

[16] E.H. Hossen, Z.E. Gobetz, R.S. Kingsbury, F. Liu, H.C. Palko, L.L. Dubbs, O. Coronell, D.F. Call, Temporal variation of power production via reverse electrodialysis using coastal North Carolina waters and its correlation to temperature and conductivity, Desalination. 491 (2020) 114562. https://doi.org/10.1016/j.desal.2020.114562.

[17] S. Mehdizadeh, M. Yasukawa, T. Abo, M. Kuno, Y. Noguchi, M. Higa, The effect of feed solution temperature on the power output performance of a pilot-scale reverse electrodialysis (RED) system with different intermediate distance, Membranes (Basel). 9 (2019). https://doi.org/10.3390/membranes9060073.

[18] D.A. Vermaas, D. Kunteng, M. Saakes, K. Nijmeijer, Fouling in reverse electrodialysis under natural conditions, Water Res. (2013). https://doi.org/10.1016/j.watres.2012.11.053.

[19] R.S. Kingsbury, F. Liu, S. Zhu, C. Boggs, M.D. Armstrong, D.F. Call, O. Coronell, Impact of natural organic matter and inorganic solutes on energy recovery from five real salinity gradients using reverse electrodialysis, J Memb Sci. 541 (2017) 621–632. https://doi.org/10.1016/j.memsci.2017.07.038.

[20] B. Vital, E. v. Torres, T. Sleutels, M.C. Gagliano, M. Saakes, H.V.M. Hamelers, Fouling fractionation in reverse electrodialysis with natural feed waters demonstrates dual media rapid filtration as an effective pre-treatment for fresh water, Desalination. 518 (2021). https://doi.org/10.1016/j.desal.2021.115277.

[21] D.A. Vermaas, D. Kunteng, J. Veerman, M. Saakes, K. Nijmeijer, Periodic feedwater reversal and air sparging as antifouling strategies in reverse electrodialysis, Environ Sci Technol. (2014). https://doi.org/10.1021/es4045456.

[22] J. Moreno, N. de Hart, M. Saakes, K. Nijmeijer, CO 2 saturated water as two-phase flow for fouling control in reverse electrodialysis, Water Res. (2017). https://doi.org/10.1016/j.watres.2017.08.015.

[23] E.J. Bodner, M. Saakes, T. Sleutels, C.J.N. Buisman, H.V.M. Hamelers, The RED Fouling Monitor: A novel tool for fouling analysis, J Memb Sci. (2019). https://doi.org/10.1016/j.memsci.2018.10.059.

[24] D. Pintossi, M. Saakes, Z. Borneman, K. Nijmeijer, Electrochemical impedance spectroscopy of a reverse electrodialysis stack: A new approach to monitoring fouling and cleaning, J Power Sources. 444 (2019) 227302. https://doi.org/10.1016/j.jpowsour.2019.227302.

[25] D.A. Vermaas, M. Saakes, K. Nijmeijer, Power generation using profiled membranes in reverse electrodialysis, J Memb Sci. (2011). https://doi.org/10.1016/j.memsci.2011.09.043.

[26] S. Pawlowski, T. Rijnaarts, M. Saakes, K. Nijmeijer, J.G. Crespo, S. Velizarov, Improved fluid mixing and power density in reverse electrodialysis stacks with chevron-profiled membranes, J Memb Sci. (2017). https://doi.org/10.1016/j.memsci.2017.03.003.

[27] J.Y. Nam, K.S. Hwang, H.C. Kim, H. Jeong, H. Kim, E. Jwa, S.C. Yang, J. Choi, C.S. Kim, J.H. Han, N. Jeong, Assessing the behavior of the feed-water constituents of a pilot-scale 1000-cell-pair reverse electrodialysis with seawater and municipal wastewater effluent, Water Res. 148 (2019) 261–271. https://doi.org/10.1016/j.watres.2018.10.054.

[28] C. Simões, D. Pintossi, M. Saakes, Z. Borneman, W. Brilman, K. Nijmeijer, Electrode segmentation in reverse electrodialysis: Improved power and energy efficiency, Desalination. 492 (2020). https://doi.org/10.1016/j.desal.2020.114604.

[29] J. Hu, S. Xu, X. Wu, D. Wu, D. Jin, P. Wang, Q. Leng, Multi-stage reverse electrodialysis: Strategies to harvest salinity gradient energy, Energy Convers Manag. (2019). https://doi.org/10.1016/j.enconman.2018.11.032.

[30] C. Simões, D. Pintossi, M. Saakes, W. Brilman, Optimizing multistage reverse electrodialysis for enhanced energy recovery from river water and seawater: Experimental and modeling investigation, Advances in Applied Energy. (2021). https://doi.org/10.1016/j.adapen.2021.100023.

[31] J. Veerman, M. Saakes, S.J. Metz, G.J. Harmsen, Reverse electrodialysis: Performance of a stack with 50 cells on the mixing of sea and river water, J Memb Sci. (2009). https://doi.org/10.1016/j.memsci.2008.11.015.

[32] J. Veerman, Reverse Electrodialysis : Co- and Counterflow Optimization of Multistage Configurations for Maximum Energy Efficiency, Membranes (Basel). (2020) 1–13. https://doi.org/10.3390/membranes10090206.

[33] M. Tedesco, P. Mazzola, A. Tamburini, G. Micale, I.D.L. Bogle, M. Papapetrou, A. Cipollina, Analysis and simulation of scale-up potentials in reverse electrodialysis, Desalination Water Treat. (2015). https://doi.org/10.1080/19443994.2014.947781.

[34] J. Hu, S. Xu, X. Wu, S. Wang, X. Zhang, S. Yang, R. Xi, D. Wu, L. Xu, Experimental investigation on the performance of series control multi-stage reverse electrodialysis, Energy Convers Manag. 204 (2020). https://doi.org/10.1016/j.enconman.2019.112284.

[35] Z. Wang, J. Li, C. Zhang, H. Wang, X. Kong, Power production from seawater and discharge brine of thermal desalination units by reverse electrodialysis, Appl Energy. 314 (2022). https://doi.org/10.1016/j.apenergy.2022.118977.

[36] S. Xu, Q. Leng, X. Wu, Z. Xu, J. Hu, D. Wu, D. Jing, P. Wang, F. Dong, Influence of output current on decolorization efficiency of azo dye wastewater by a series system with multi-stage reverse electrodialysis reactors, Energy Convers Manag. 228 (2021). https://doi.org/10.1016/j.enconman.2020.113639.

[37] J. Hu, S. Xu, X. Wu, D. Wu, D. Jin, P. Wang, Q. Leng, Theoretical simulation and evaluation for the performance of the hybrid multi-effect distillation—reverse electrodialysis power generation system, Desalination. 443 (2018) 172–183. https://doi.org/10.1016/j.desal.2018.06.001.

[38] Y. Zhang, X. Wu, S. Xu, Q. Leng, S. Wang, A serial system of multi-stage reverse electrodialysis stacks for hydrogen production, Energy Convers Manag. 251 (2022). https://doi.org/10.1016/j.enconman.2021.114932.

[39] D. Pintossi, C. Simões, M. Saakes, Z. Borneman, K. Nijmeijer, Predicting reverse electrodialysis performance in the presence of divalent ions for renewable energy generation, Energy Convers Manag. 243 (2021). https://doi.org/10.1016/j.enconman.2021.114369.

[40] J. Moreno, E. Slouwerhof, D.A. Vermaas, M. Saakes, K. Nijmeijer, The Breathing Cell: Cyclic Intermembrane Distance Variation in Reverse Electrodialysis, Environ Sci Technol. (2016). https://doi.org/10.1021/acs.est.6b02668.

[41] P. Długołecki, K. Nymeijer, S. Metz, M. Wessling, Current status of ion exchange membranes for power generation from salinity gradients, J Memb Sci. (2008). https://doi.org/10.1016/j.memsci.2008.03.037.

[42] J. Moreno, S. Grasman, R. van Engelen, K. Nijmeijer, Up-scaling reverse electrodialysis, Environ Sci Technol. (2018). https://doi.org/10.1021/acs.est.8b01886.

[43] T. Rijnaarts, J. Moreno, M. Saakes, W.M. de Vos, K. Nijmeijer, Role of anion exchange membrane fouling in reverse electrodialysis using natural feed waters, Colloids Surf A Physicochem Eng Asp. 560 (2019) 198–204. https://doi.org/10.1016/j.colsurfa.2018.10.020.

[44] X. Ge, X. Wang, M. Zhang, S. Seetharaman, Correlation and prediction of activity and osmotic coefficients of aqueous electrolytes at 298.15 K by the modified TCPC model, J Chem Eng Data. (2007). https://doi.org/10.1021/je060451k.

[45] D.A. Vermaas, J. Veerman, N.Y. Yip, M. Elimelech, M. Saakes, K. Nijmeijer, High efficiency in energy generation from salinity gradients with reverse electrodialysis, ACS Sustain Chem Eng. (2013). https://doi.org/10.1021/sc400150w.

[46] L. S. Clesceri, A. E. Greenberg, A. D. Eaton, Standard Methods for the Examination of Water and Wastewater 22th Edition, 1999.

[47] A.W. Qurashi, A.N. Sabri, Biofilm formation in moderately halophilic bacteria is influenced by varying salinity levels, J Basic Microbiol. 52 (2012) 566–572. https://doi.org/10.1002/jobm.201100253.

[48] J. Veerman, J.W. Post, M. Saakes, S.J. Metz, G.J. Harmsen, Reducing power losses caused by ionic shortcut currents in reverse electrodialysis stacks by a validated model, J Memb Sci. (2008). https://doi.org/10.1016/j.memsci.2007.11.032.

[49] A. Culcasi, L. Gurreri, A. Zaffora, A. Cosenza, A. Tamburini, A. Cipollina, G. Micale, Ionic shortcut currents via manifolds in reverse electrodialysis stacks, Desalination. (2020). https://doi.org/10.1016/j.desal.2020.114450.

[50] N.Y. Yip, D.A. Vermaas, K. Nijmeijer, M. Elimelech, Thermodynamic, energy efficiency, and power density analysis of reverse electrodialysis power generation with natural salinity gradients, Environ Sci Technol. 48 (2014) 4925–4936. https://doi.org/10.1021/es5005413.

[51] D. Pintossi, C.L. Chen, M. Saakes, K. Nijmeijer, Z. Borneman, Influence of sulfate on anion exchange membranes in reverse electrodialysis, NPJ Clean Water. 3 (2020) 1–10. https://doi.org/10.1038/s41545-020-0073-7.

[52] M. Higa, A. Tanioka, K. Miyasaka, Simulation of the transport of ions against their concentration gradient across charged membranes, J Memb Sci. 37 (1988) 251–266. https://doi.org/10.1016/S0376-7388(00)82432-1.

[53] M. Vanoppen, G. Stoffels, C. Demuytere, W. Bleyaert, A.R.D. Verliefde, Increasing RO efficiency by chemical-free ion-exchange and Donnan dialysis: Principles and practical implications, Water Res. 80 (2015) 59–70. https://doi.org/10.1016/j.watres.2015.04.030.

[54] T. Rijnaarts, N.T. Shenkute, J.A. Wood, W.M. De Vos, K. Nijmeijer, Divalent Cation Removal by Donnan Dialysis for Improved Reverse Electrodialysis, ACS Sustain Chem Eng. (2018). https://doi.org/10.1021/acssuschemeng.8b00879.

[55] K. Chon, N. Jeong, H. Rho, J.Y. Nam, E. Jwa, J. Cho, Fouling characteristics of dissolved organic matter in fresh water and seawater compartments of reverse electrodialysis under natural water conditions, Desalination. 496 (2020) 114478. https://doi.org/10.1016/j.desal.2020.114478.

[56] L.O. Villacorte, S.A.A. Tabatabai, N. Dhakal, G. Amy, J.C. Schippers, M.D. Kennedy, Algal blooms: an emerging threat to seawater reverse osmosis desalination, Desalination Water Treat. 55 (2015) 2601–2611. https://doi.org/10.1080/19443994.2014.940649.

[57] T.H. Tan, C.P. Leaw, S. Chee, Y. Leong, L.P. Lim, S.M. Chew, Marine micro-phytoplankton of Singapore , with a review of harmful microalgae in the region, Raffles Bulletin of Zoology. (2016).

[58] J. Choi, W.-S. Kim, H.K. Kim, S.C. Yang, J.-H. Han, Y.C. Jeung, N.J. Jeong, Fouling behavior of wavy-patterned pore-filling membranes in reverse electrodialysis under natural seawater and sewage effluents, NPJ Clean Water. 5 (2022) 1–12. https://doi.org/10.1038/s41545-022-00149-2.

[59] J. Landoulsi, K.E. Cooksey, V. Dupres, Review - Interactions between diatoms and stainless steel: Focus on biofouling and biocorrosion, Biofouling. 27 (2011) 1105–1124. https://doi.org/10.1080/08927014.2011.629043.

[60] https://www.wetterzentrale.de/de/weatherdata_de.php (seen on 9th December 2021)

Chapter 5

Towards Redox Free Reverse Electrodialysis with Carbon-based Slurry Electrodes

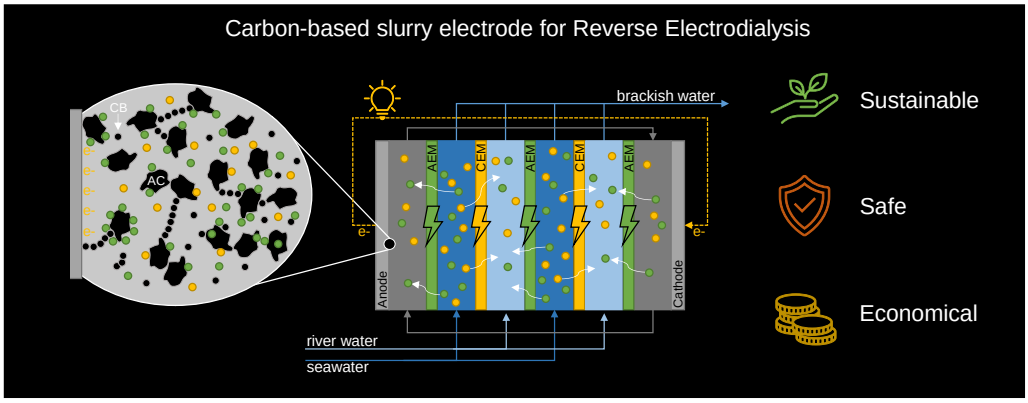

Abstract

Clean and renewable salinity gradient energy can be harvested using reverse electrodialysis (RED). The electrode system is an essential part to convert ionic current into electrical current. In this study, a typical 0.10 x 0.10 m^2 RED stack with a cross-flow configuration was used to test carbon-based slurry electrodes (CSEs) to replace the usual redox solutions, like hexacyanoferrate, to enhance the RED process' sustainability, stability, and economic value. Six different slurry compositions comprising activated carbon, carbon black, and graphite powder were tested. The CSE characteristics were systematically studied by measuring viscosity, electrode compartment pressure drop, maximum current density, stability and performance of power density, and energy efficiency. Using a single membrane configuration the CSE ran continuously for 17 days with a stable output. The application of CSEs for RED, with artificial seawater and river water, using mixing activated carbon and carbon black at a total concentration of 20 wt%, resulted in the best performance with a net power density of 0.7 $W{\cdot}m^{-2}$. Moreover, higher current densities up to 350 $A.m^{-2}$ were tested for ED and shown to be feasible until 150 $A.m^{-2}$. CSEs show promising versatility for different application modes.

A version of this chapter has been published as:

C. Simões, M. Saakes, and D. Brilman 2023. Toward Redox-Free Reverse Electrodialysis with Carbon-Based Slurry Electrodes. Industrial & Engineering Chemistry Research, 62(3), 1665–1675. https://doi.org/10.1021/acs.iecr.2c03567

5.1. Introduction

Reverse electrodialysis (RED) is an emerging technology that generates renewable energy from the mixing of waters with different salinities, such as sea and river water [1]. RED uses a membrane stack comprising alternating anion (AEM) and cation (CEM) exchange membranes. Spacers separate the ion exchange membranes (IEMs) and, at the same time, shape the water compartments where seawater and river water are fed alternately [2]. Due to the salinity gradient and the selective transport of anions and cations through the IEMs, an ionic current is produced at the membrane pile. Generally in RED, this ionic current is converted into an electrical current utilizing dimensionally stable electrodes at the end-compartments. Solutions, such as water, for electrolysis or redox couples, are used for electron transfer. The most used solutions for RED are the Fe^{2+}/Fe^{3+} couple at low pH or hexacyanoferrate $[Fe(CN)_6]^{3-}/[Fe(CN)_6]^{4-}$ mixed with, e.g., 0.25 M NaCl or anthraquinone [3].

Redox couples, like hexacyanoferrate, which is typically used at the laboratory scale, provide a fast charge transfer rate and make the electrode system resistance negligible compared to the membrane pile resistance [4]. However, their sustainability, stability and economic viability are debatable for large-scale application. The Fe^{2+}/Fe^{3+} couple is only stable at pH values below 2 [5], requiring that the shielding membranes, positioned at the ends of the membrane pile, must be resistant to acidic environments. Furthermore, continuous pH monitoring combined with acid dosing is necessary to avoid the precipitation of iron compounds around the cathode [3,4,6]. The $[Fe(CN)_6]^{3-}/[Fe(CN)_6]^{4-}$ couple decomposes in the presence of sunlight and oxygen, it was shown to be unstable under these circumstances and partially releases cyanide ions that, in the case of leakage, can irreversibly bind with the AEMs reducing their performance and harm the environment [3,5,7]. Recently, this couple was also found to be unstable in scaled-up stacks in the presence of Mg^{2+} and Ca^{2+} where scaling occurred [8]. In the case of electrolysis using NaCl solutions (or seawater), gas evolution occurs, and because of the fast kinetics of the chlorine evolution reaction gaseous chlorine gas (Cl_2) evolves at the anode and hydrogen (H_2) gas at the cathode. Chlorine gas is corrosive, while hydrogen gas increases the risk of explosion and must be removed from the system. Furthermore, gas bubbles at the electrode compartments will increase the electrical resistance leading to higher ohmic voltage losses [9]. Therefore, there is a need for an alternative way to transfer electrons.

Static capacitive carbon electrodes have been developed for energy generation in RED (capacitive RED or CRED) [10] and capacitive mixing (CAPMIX) [11], as well as for desalination in electrodialysis (ED) [12] and capacitive deionization (CDI) [13]. These are environmentally friendly since carbon is widely available and in case of leakage, there is no harm to the aquatic environment. The charge transfer mechanism is based on the ions being adsorbed onto the

surface area of the carbon electrodes because of the electrostatic field of the electrical double layer [14], and no faradaic redox reactions occur. However, after adsorption saturation, it is necessary to reverse the polarity to trigger desorption, creating an intermittent charge and discharge process. Using CRED, an interruption in power generation is established as well as a mandatory feed water switch. The power density will be maximum at the start and decrease continuously during one cycle [10]. This shows a limitation to the use of static electrodes, especially in cases where switching the process feed streams for discharge is not possible (e.g., asymmetrical compartments).

A possible solution without necessitating the periodic switch of river water and seawater is the use of carbon-based flow electrodes [15]. The advantages of these flow electrodes compared to redox electrolytes are low cost, easy scalability, harmless to the ion exchange membranes, and non-polluting to the environment [16]. Flow electrodes are widely used in flow capacitive deionization (FCDI) and electrochemical flow capacitors. In FCDI, it is used to continuously desalinate saline streams. By using a capacitive flow electrode, the process of adsorption and desorption can be made continuous and, in the case of desalination, leads to increased salt removal rates [17]. In the case of capacitors, it is used as an energy storage device, by charging and discharging the flow electrode [18]. Several studies have shown a continuous improvement of carbon flow electrodes by optimizing flow rates, preparation procedures, compositions, additives, and regeneration methods [16,19–21]. In RED, the concept of a carbon flow electrode for reverse electrodialysis was first introduced by Liu et al. [22], where a RED stack was used with a capacitive carbon flow electrode at the end-compartments. Liu et al. experimented only with different activated carbon (AC) loads (5 to 15 wt%) and graphite brushes to enhance the contact area. However, the maximum power density achieved was rather low; namely, 0.29 $W \cdot m^{-2}$ using 1.0 and 30.0 g $NaCl \cdot L^{-1}$ solutions as feedwaters at a flow velocity of 1.0 $cm \cdot s^{-1}$.

Carbon-based flow electrodes usually contain carbon percentages lower than 25 wt%, to guarantee flowability in the long term [23]. At higher carbon percentages the flow electrode viscosity, and hence pressure drop, may become prohibitive, although with distinct designs the weight percentage of carbon may be increased [24]. These flow electrodes are composed of micro- to nano-sized particles, with AC being the main carbon material used [17]. Although AC can offer high specific surface areas (~ 1500 to 3200 $m^2 \cdot g^{-1}$), it has poor conductivity. Improvement of the flow electrode's conductivity with additives was successful with the addition of, for example, carbon nanotubes [25] and carbon black (CB) [26], among others [27,28]. Opposite to static capacitive electrodes, flow electrodes do not need a high capacitance since there is a continuous refreshment of the charged or discharged adsorption layer by neutralization of the flow electrode from both electrode compartments in a common mixing vessel or through recirculation from the anode to the cathode [26]. Electrically conductive additives to AC, such as CB, can boost the electrical conductivity of the flow

electrode, and enhance the collision rate between the particles. CB with a low percolation threshold has been engineered to facilitate the charge transfer at a very low percolation threshold [29,30]. To the best of our knowledge, a mixed slurry of AC and CB, or other electrically conductive additives, has not been demonstrated yet with carbon-based slurry electrodes in RED.

In this study, a typical 0.10 x 0.10 m^2 RED stack with a cross-flow configuration was used to test carbon-based slurry electrodes (CSE), as flow electrodes, to replace the usual redox solutions, like hexacyanoferrate, to enhance the RED process in terms of sustainability and stability. The CSE characteristics were systematically studied by measuring composition, viscosity, electrode compartment pressure drop, maximum current density, stability and performance in terms of power density and energy efficiency.

One aim of this study was to study whether a CSE composed of a mix of different carbon particles has improved performance compared to flow electrodes using only activated carbon, by testing using a standard RED stack. Another aim was to run a long-term test (17 days) to show the electrochemical stability of the best-performing CSE. Yet another aim was to evaluate the pressure drop of the CSE related to targeting a low pumping power consumption.

5.2. Materials and methods

5.2.1. Carbon-based slurry electrodes preparation and characterization

Carbon-based slurry electrodes (CSE) were composed of activated carbon, AC (YP-50F, Kuraray Corp., Japan), carbon black CB, (Monarch 800, Cabot, USA) and graphite powder GP, (Graphite fine powder extra pure, Merck, USA) combined with deionized water and NaCl salt (VWR Chemicals, Belgium). The composition of each CSE can be found in Table 5.1. The salt concentration was fixed at 0.25 M NaCl having the average concentration of seawater and river water, to avoid osmosis. The total weight percentage of carbon was not more than 20 %, to ensure flowability. The weight percentage of carbon (wt%) is the mass of carbon divided by the total mass of the slurry. Each CSE was prepared by individually weighting and then mixing all the elements first manually and after, for 12 min, with an UltraTurrax (IKA, T25, Germany) at 12000 rpm. More details regarding the preparation can be found in the supporting information (Table S5.1). Later on, to improve the dispersibility of the CSE, a new CSE with 15 wt% AC, 5 wt% CB and a surfactant, cetyltrimethylammonium bromide (CTAB, Sigma-Aldrich, USA), was prepared.

Table 5.1 Carbon-based slurry electrode composition used in this study.

CSE #	Name	AC [wt %]	CB [wt %]	GP [wt %]	NaCl [M]
1	20AC	20	0	0	0.25
2	15AC5CB	15	5	0	0.25
3	10AC10CB	10	10	0	0.25
4	10AC5CB	10	5	0	0.25
5	10CB	0	10	0	0.25
6	15AC5GP	15	0	5	0.25

The AC, CB and GP were characterized before making the CSEs. Samples were dried at 65 °C for 24h prior to analysis, for Scanning Electron Microscopy (SEM) to evaluate the surface morphology (JSM-6480LV, JEOL, Japan). All samples were degassed under a nitrogen atmosphere for 2 h at 300 °C in a degassing apparatus (VacPrep 061, Micromeritics, Norcross, GA, USA). Subsequently, nitrogen gas adsorption (TriStar 3000, Micromeritics, Norcross, GA, USA) at -196 °C was used to determine the specific surface area and pore size of the samples according to the BET analysis. From the slurries, samples were taken to determine the viscosity using a modular compact rheometer (MCR 102, Anton Paar, Austria) at shear rates from 1 to 400 s^{-1}, at 22 °C. All slurry samples were shaken before being introduced into the rheometer to assure homogeneity. The results of these characterizations can be found in supporting information.

5.2.2. Experimental setup

A 0.10 x 0.10 m^2 cross-flow stack (REDstack B.V., The Netherlands) was used. The design can be found in literature [31]. Each end plate had a Ti-mesh 1.0 electrode with 2.5 µm Pt coating to act as a current collector (MAGNETO Special Anodes BV, The Netherlands). Silicon gaskets were used for sealing. The electrode configuration for the flow electrodes was the same as used for the hexacyanoferrate solutions to make a direct comparison with previous research (Figure 5.1). Only the end membranes used in this test are anion exchange membranes (AEMs).

For single membrane tests, schematized in Figure 5.2A, one AEM was used (0.01 m^2 membrane area). If natural waters are supplied, an AEM is needed to block divalent cations to pass from the feedwaters to the flow electrode. And, while using CTAB, this membrane is also desirable. In laboratory tests, using only NaCl-containing solutions a cation exchange membrane (CEM) can also be used as a shielding membrane or must be used in the case of hexacyanoferrate solutions. For the RED operation (Figure 5.2B), the stack contained 10 cell pairs, with a total membrane area of 0.20 m^2. All AEMs and CEMs were Type 10 (FujiFilm Manufacturing Europe B.V., The Netherlands) and were conditioned in 0.5 M NaCl solution for 24h before being used in the RED stack (characteristics are shown in Table S5.2). To

separate the membranes, 155 µm thick woven spacers with 55 % porosity with integrated silicon sealing were used (Deukum GmbH, Germany).

Figure 5.1 Flow geometry of the electrode compartment: Pt/Ti mesh on top, perpendicular flow field below, a manifold both for the inlet and for the outlet, all contained in plastic housing. The dark colour of the electrode originates from its use with the carbon-based slurry electrode.

A secondary electrochemical cell was used in the system to measure inline the CSE resistance using electrochemical impedance spectroscopy (EIS). This cell contained a single flow channel of 1.5 cm thickness and 22 cm^2 area with two graphite plates that functioned as cathode and anode (Figure S5.1).

The CSE was recirculated at 300 $mL \cdot min^{-1}$ using a peristaltic pump with one double pump head (Cole-Palmer, Masterflex L/S Two-Channel Easy-Load II, USA) at the end compartments. Recirculation of the CSE was done in parallel to evaluate the anode and the cathode individually, and the outlets were mixed in the glass bottle. Yet, the anode and cathode can also be connected in series. The slurry was continuously stirred with a propeller stirrer at 600 rpm (CAT, R18, Germany) in the mixing bottle, to promote neutralization of the charged particles and homogeneity. Ag/AgCl reference electrodes (ProSense, The Netherlands) and pH sensors (Digital Orbisint, Endress + Hauser, Germany) were added at the outlet of the anode and the cathode compartments. The absolute pressure was measured with calibrated sensors (MIDAS SW, JUMO GmbH, Germany) at the inlet and outlet of the anode and cathode compartments. Data were collected with a data logger (Memograph M, Endress + Hauser, Germany).

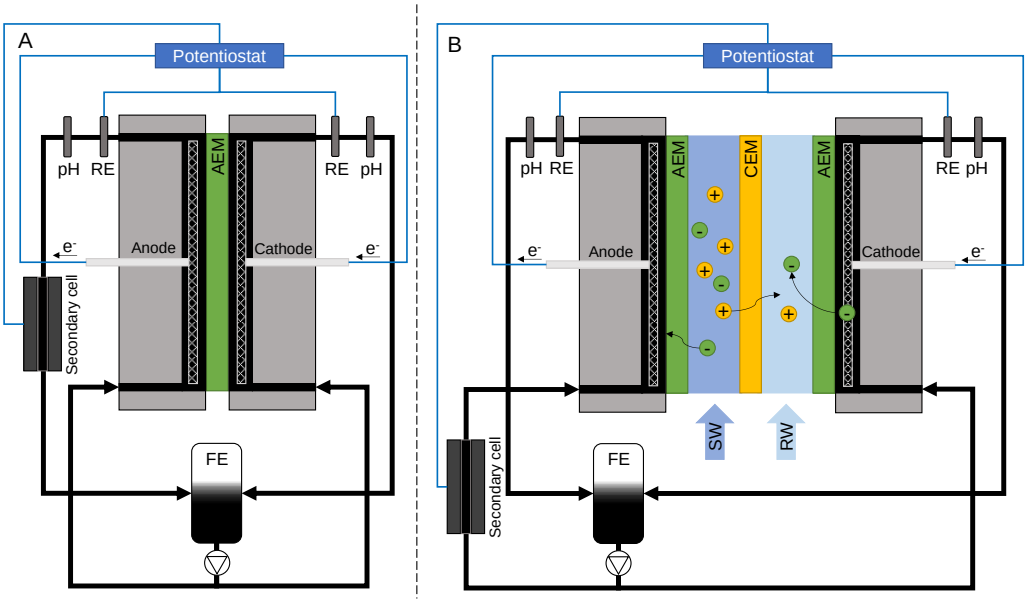

Figure 5.2 Schematic view of the experimental setup. (A) for single membrane tests and (B) for multiple cell pair tests (one cell pair is shown for simplicity). Carbon particles will become positively charged at the anode and negatively charged at the cathode.

For complete RED operation, artificial seawater and river water with 30.0 g·L^{-1} and 1.0 g·L^{-1} NaCl (Regenit, Esco, The Netherlands) were pumped into the water compartments at a superficial flow velocity of 1.0 cm·s^{-1} (without accounting for the porosity of the spacer). The feedwater system can be found in previous work [32]. The outlet flow rates were measured gravimetrically. The temperature and conductivity were measured at the inlet and outlet of each stream (Vstar22, Thermo Fisher Scientific, USA), to quantify the degree of mixing. At the same points, the absolute pressure of each stream was recorded with calibrated sensors (MIDAS SW, JUMO GmbH, Germany). The inlet temperature was set to 25.0 °C (heat losses through the tubing were registered).

5.2.3. Electrochemical measurements

First, electrochemical measurements were performed with a single membrane configuration (Figure 5.2A) to evaluate the anode and cathode potential of the CSE, electrochemical stability and flowability. The open circuit voltage (OCV), the current-voltage (I-V) curve, the maximum current at 1.15 V, and the stack potential at 50 A.m^{-2} were measured using a potentiostat (IVIUM n-stat, IVIUM Technologies BV, The Netherlands).

The OCV is the stack potential when no current is applied, for the single membrane the cell voltage should be zero volts. The I-V curve consisted of current density steps of 10 A·m^{-2} for 1 min until 1.2 V was reached. The maximum current density was defined as the current density that could be achieved at 1.15 V cell voltage during a short period of 10 min. This value was

chosen to be below the water-splitting voltage of 1.23V, which is undesirable since it can lead to gas formation. Lastly, the slurries were tested with an applied fixed current density of 50 $A{\cdot}m^{-2}$ for 20 h to evaluate the CSE stability. The value of the current density was chosen to include typical current density values of RED. After the 20 h fixed current density test, the I-V curve and maximum current density at 1.15 V were repeated.

Second, the electrochemical measurements were performed in a 10-cell pair RED stack (Figure 5.2B), to evaluate the suitability of each CSE with the RED process. The OCV, the I-V curve and the performance test were measured with the potentiostat. The I-V curve consisted of current density steps of 5 $A{\cdot}m^{-2}$ for 2 min until the stack potential reached 0 V. From the I-V curve the power density versus current density curve was calculated. The current density at the maximum power density was tested for one hour. With the stack voltage as a function of the maximum current density, the gross power output, thermodynamic efficiency, and energy efficiency were calculated. Gross power is the stack voltage output (in this case not corrected for the voltage losses at the electrodes) multiplied by the extracted current. Thermodynamic efficiency is the gross power divided by the mixing energy (per second) expended in the stack (inlet-outlet). Energy efficiency is the gross power divided by the energy (per second) provided at the inlet. Calculations for the mixing energy (ΔG) can be found in previous work [32]. The tests above were done twice for each slurry.

Lastly, using CSE 2, electrodialysis experiments were performed for desalination purposes. The same setup was used but now feeding seawater to both water compartments. Different current densities, from 50 to 350 $A{\cdot}m^{-2}$, were applied to the stack having the stack voltage measured with the potentiostat (IviumStat.h, IVIUM Technologies BV, The Netherlands).

To determine the flow electrode resistance, while the measurements at the main cell took place, electrochemical impedance spectroscopy was applied at the secondary electrochemical cell (Figure S5.1), with a frequency range from 1 Hz to 250 kHz using another channel of the same multichannel potentiostat.

5.3. Results and Discussion

5.3.1. Physical properties of the carbon-based slurry electrodes

Three types of carbon were selected to prepare the carbon-based slurry electrodes (CSEs). Activated carbon (AC) was the main material used for carbon electrodes for both static and flow electrodes [16]. Carbon black (CB) and graphite powder (GP) are known to enhance charge transfer by facilitating the collision between particles and increasing the flow electrode conductivity, compared to pure AC electrodes [26,33,34]. Table 5.2 shows the BET analysis results of the selected carbons.

Table 5.2 BET analysis results for specific, external, and internal surface area (SA) and average pore size of AC, CB and GP. Figure S5.2 contains more specific results regarding the BET analysis.

Carbon type	Specific SA [$m^2 \cdot g^{-1}$]	External SA [$m^2 \cdot g^{-1}$]	Internal SA [$m^2 \cdot g^{-1}$]	Av. pore size [nm]
AC (YP-50F Kuraray)	1665.5	100.2	1565.3	3.6
CB (Monarch 800 Cabot)	233.1	168.3	64.7	21.8*
GP (Pure Merck)	11.7	11.2	0.5	10.9

* This value is not consistent with the literature, bigger pore size than the particle size, probably because the pore size detected is between agglomerated particles

The specific surface area of AC was at least seven times higher than for the CB used and 142 times higher than for the GP used, as seen in Table 5.2, providing a higher absorption surface. Most of the surface area of AC is internal, while for the other two it is mostly external. The measured value for the CB average pore size was due to the agglomeration of carbon black particles, which is also seen in the SEM images (Figure S5.4). CB particles have sizes between 5 to 20 nm [35,36], thus a pore size larger than the particle size cannot be correct. However, by agglomeration, the CB particles form primary and secondary structures as detected in SEM images and can range up to 10 µm (Figure S5.4) [35]. A sturdy mixing is necessary to effectively have very finely divided CB particles. For AC and GP SEM images are also found in the supporting information (Figures S5.3 and S5.5).

Two physical parameters of special interest in flow electrodes are the slurry viscosity since flowability is key for a good distribution/mixing, and the pressure drop at the electrode compartment. A low-pressure drop is required to keep the energetic costs associated with pumping the slurry acceptable.

Figure 5.3 shows the relation between the slurry viscosity (at 400 s^{-1} shear rate) and the average pressure drop as measured by flowing through the electrode compartment at 300 $mL \cdot min^{-1}$. A linear relation was found between viscosity and pressure drop as predicted by theory. Figure S5.6, in supporting information, provides a shear rate range from 50 to 400 s^{-1} for each flow electrode. CSEs are thixotropic fluids (non-Newtonian fluids) or shear-thinning fluids since they become less viscous with agitation/stress [37]. Looking at each CSE composition more relations were found. Increasing the CB content in the sample (comparing CSEs 1, 2 and 3) also increased the slurry viscosity, while adding GP reduced the viscosity (CSE 1 and 6). Reducing the carbon weight percentage, as expected [26], reduced the viscosity of the CSE. Although CB is much more viscous than AC or GP, the CSE 5 viscosity was lower but still close to the value of CSE 4 and CSE 6. The CSEs that presented lower viscosity and consequently lower pressure drop are more suitable since less energy is spent pumping the CSE. Lastly, although a relation was found between viscosity and pressure drop since these

are thixotropic fluids, it is relevant to directly measure the pressure drop to estimate the power spent pumping the CSE as the flow rate used will influence the shear rate.

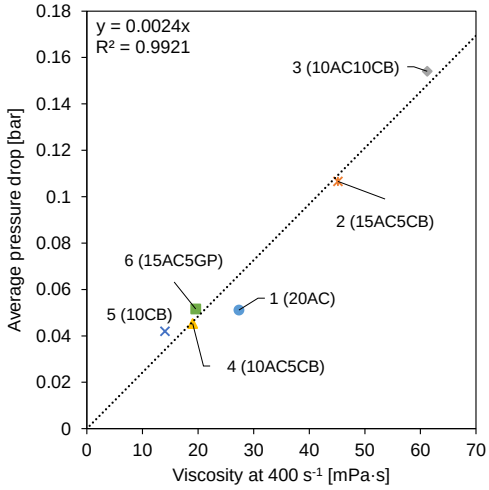

Figure 5.3 Relation between CSE viscosity (at 400 s^{-1} shear rate) and the average electrode compartment pressure drop. Pressure drop values are based on initial measurements.

5.3.2. Performance with a single membrane

The CSE performance was further evaluated electrochemically in a single membrane setup (Figure 5.2A). Using the secondary cell, each CSE electronic conductivity was measured as shown in Figure 5.4. Higher conductivity leads to lower electrical resistance which is ideal to decrease voltage losses at the electrodes of the RED stack.

In the secondary cell, the conductivity of 0.5 M NaCl was also measured, this resulted in a value of 44.3 ± 1.2 $mS \cdot cm^{-1}$. Estimating for 0.25 M NaCl solution, the conductivity is around 22 ± 2 $mS \cdot cm^{-1}$, as in low NaCl concentrations solutions the relation between conductivity and concentration is rather linear [32]. Comparing these two values with the obtained in Figure 5.4, for all CSEs, the addition of carbon clearly enhances the electronic path, leading to conductivity values similar to a 0.5 M NaCl solution.

Since all CSEs contained the same NaCl concentration flowing through the same cell, the differences seen in conductivity in Figure 5.4 can be attributed directly to the carbon composition of each flow electrode. Increasing the content of CB increases the flow electrode conductivity (comparing CSE 1, CSE 2 and CSE 3). The replacement of AC with CB allowed a percolation threshold at lower weight percentages [38]. In Figure S5.7 it is possible to see the electrical conductivity of CB slurries increasing with the increase in weight percentage, from pure H_2O to 11 wt% CB. The type of CB used, Monarch 800, percolated at 1 wt% with 0.1 $mS \cdot cm^{-1}$ conductivity, showing suitability as an effective electric conductive [39].

Looking at CSE 1 and CSE 6, the addition of GP, however, did not enhance the conductivity, therefore the GP used showed not to be a suitable conductive additive for our tests. The mixing of different carbon materials and amounts can lead to

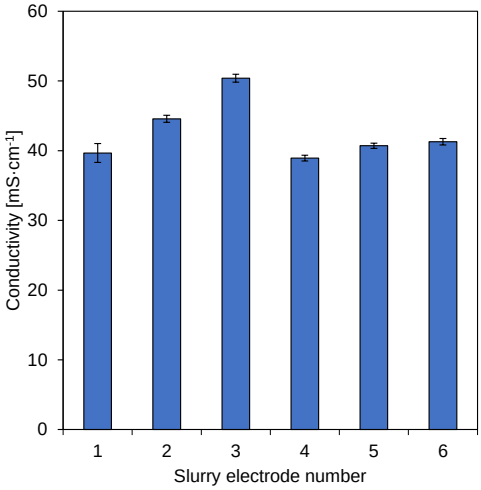

Figure 5.4 Carbon-based slurry electrode conductivity measured in the secondary cell (Figure S5.1). 1 – 20 % AC; 2 – 15 % AC + 5 % CB; 3 – 10 % AC + 10 % CB; 4 – 10 % AC + 5 % CB; 5 – 10 % CB and 6 – 15 % AC + 5 % GP, all weight percentages and with 0.25 M NaCl in solution.

different interactions, this was also seen by Cohen et al [40]. Mixing AC with fluidized bed electrodes enhanced the conductivity of the combined electrode compared to the two materials separated. On the other hand, the combination of carbon nano-tubes with the fluidized bed electrodes resulted in a lower conductivity for the combined compared to the carbon nano-tubes alone. Using only 10 wt% of CB (CSE 4) resulted in a CSE with the same conductivity as 20 wt% AC (CSE 1). CSE 4 presented the lowest conductivity (38.9 $mS \cdot cm^{-1}$) and adding an extra 5 wt% CB showed a positive effect on the conductivity as for CSE 3 (50.4 $mS \cdot cm^{-1}$). The use of CB enhanced the flow electrode's electric conductivity, thus decreasing the electrical resistance. The suitable weight percentage will depend on several factors together such as viscosity, conductivity and dispersibility [41].

To measure the hydrodynamical and electrochemical stability of the flow electrodes, each flow electrode was pumped continuously for 20 h at 50 $A \cdot m^{-2}$ current density. The cell potential, pH of anolyte and catholyte and the anode and cathode compartment pressure drop were recorded during this 20 h period and are shown in Figure 5.5.

In Figure 5.5 a fluctuation in cell voltage can be seen in all cases. The CSEs that do not contain CB (CSE 1 and 6) showed a linear increase in potential over time (except for the last hours of CSE 1 where a sudden increase was detected). The continuous increase in potential may lead to values above the water electrolysis voltage (~ 1.23 V), after a few days of

operation if this trend continues. This voltage will trigger oxygen and hydrogen evolution, as well as chlorine gas evolution. This will result in extra potential losses at the electrodes (due to the reactions and gas bubbles formation). Therefore, it is undesired, and these are not considered electrochemically stable. Regarding pH and compartment pressure drop, these two CSEs seem to be stable. CSE 2 showed a particular positive behaviour by slightly improving over time concerning the decreasing cell potential and also showed a constant pH and pressure drop.

For CSE 3, the pressure drop at the electrode compartments decreased over time, as could be caused by the partial settling of the carbon in the tubing, making the flowable fraction less viscous and containing less carbon. This could explain also why the cell potential slightly increases. The pH remained similar in both the anode and cathode compartments, meaning no electrolysis occurred. CSE 4 showed peaks in the measured cell potential but also recovered. Interestingly, the potential peaks seem to match the small pressure drop peaks, therefore it could be an influence of the pump. The pH was also kept similar in this case. Using only CB, in CSE 5, it was not possible to avoid side reactions and the pH at the cathode and anode differentiated, indicating water splitting at the current collectors. Furthermore, the potential and pressure drop fluctuated over time.

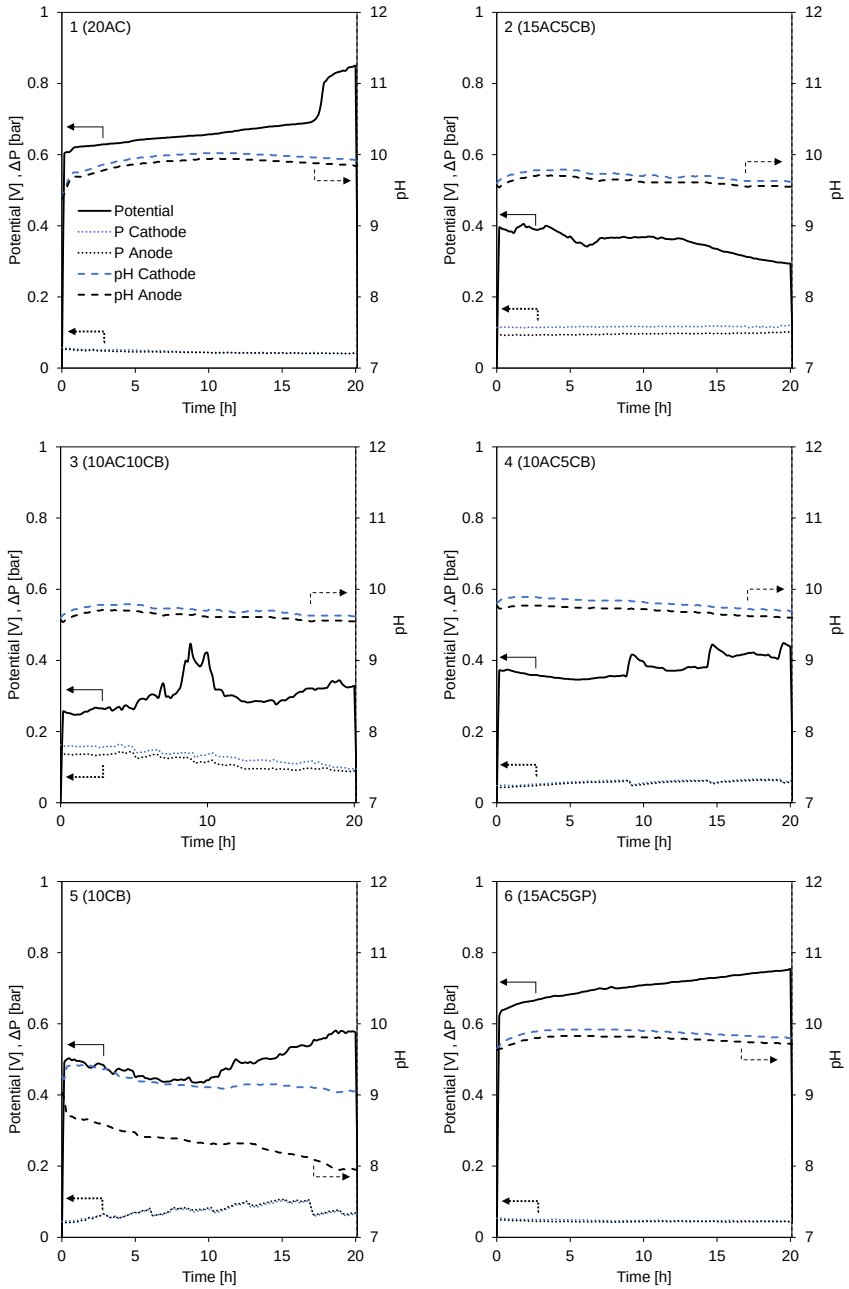

Figure 5.5 Stability test over 20 h with each carbon-based slurry electrode using a single membrane setup at constant current density (50 $A \cdot m^{-2}$). The left vertical axis represents the cell potential (solid line) and anode and cathode compartment pressure drop (dotted lines), and the right vertical axis represents the pH (dashed line) of the cathode (black) and anode (blue).

Figure 5.5 unveils that by monitoring the flow electrodes for 20 h, the physical and electrochemical characteristics changed. Furthermore, we conclude that flow electrodes

containing a mixture of AC and CB offer improved operational conditions with low cell potential and no pH changes.

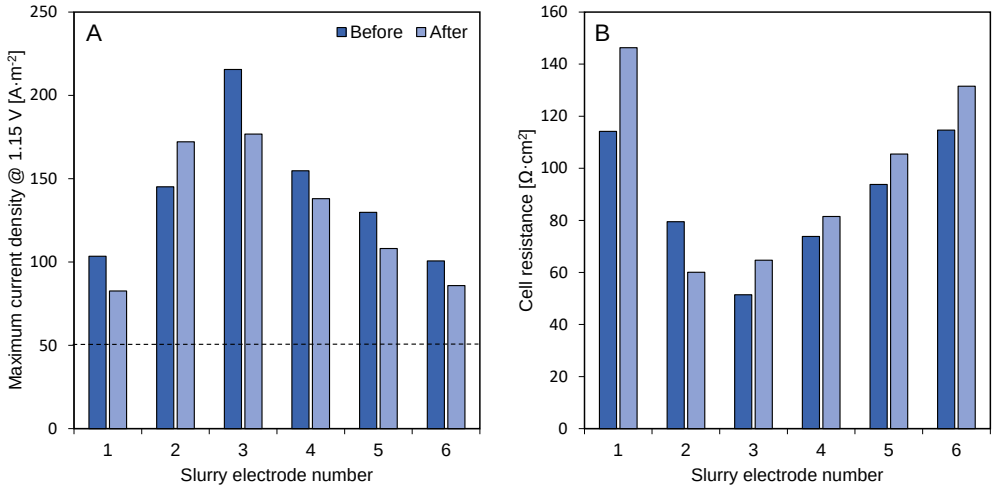

Figure 5.6 (A) Maximum achieved current density at constant cell potential (1.15 V) and (B) cell resistance taken from the I-V plot for each carbon-based slurry electrode before and after the 20-hour constant current test for a single membrane setup. 1 – 20 % AC; 2 – 15 % AC + 5 % CB; 3 – 10 % AC + 10 % CB; 4 – 10 % AC + 5 % CB; 5 – 10 % CB and 6 – 15 % AC + 5 % GP, all weight percentages and with 0.25 M NaCl in solution.

The maximum current density sustained by each flow electrode before reaching the water-splitting voltage and the cell resistance, before and after the 20 h testing are shown in Figure 5.6. Figure 5.6A reveals that all the tested flow electrodes reached current densities above 50 $A \cdot m^{-2}$ at 1.15 V, which is typically a high current density value suitable for RED. An operational current density above 150 $A \cdot m^{-2}$ is found for CSE 2 and 3, which also opens the possibility to other applications where higher current densities are needed, such as electrodialysis and this is discussed therefore in section 3.5. Except for CSE 2, the CSE showed decreasing current density over time by up to 20 %. This is consistent with the cell electrical resistance increase, seen in Figure 5.6B.

Given the fluctuation in cell voltage and cell resistance shown in Figures 5.5 and 5.6, CSE 2 was selected for a long-duration test with a single membrane. This CSE was chosen because it was improving over 20h, being interesting to see if it would stabilize and if so, at what performance level. Figure 5.7 shows the recorded potential response for a constant current density (of 50 $A \cdot m^{-2}$) through a period of 17 days of a newly made CSE 2.

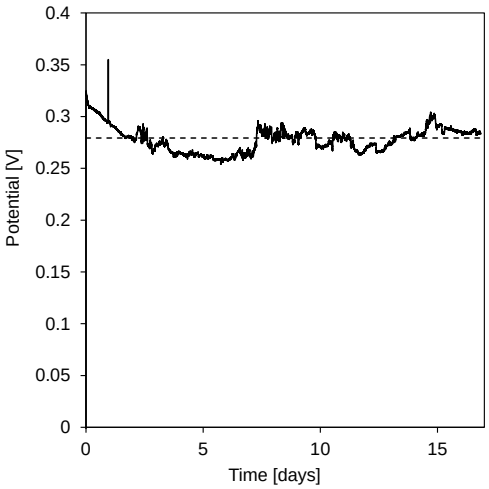

Figure 5.7 Cell potential measured during a 17-day experiment with a single membrane with CSE 2 (15wt% AC + 5wt% CB + 0.25 M NaCl) at 50 $A \cdot m^{-2}$. The potential peak after one day was due to sampling. As sampling disturbed the measuring system and reduced the active volume, no more samples were taken.

During the first two days, there was a clear decrease in the cell potential, thus the cell resistance was also decreasing. This was consistent with the results from Figures 5.5 and 5.6, probably due to some grinding of the AC/CB mixture leading to finer particles. Figure 5.7 proves that it is possible to continuously pump the slurry around for at least 17 days (without redispersing with the UltraTurrax) and to maintain a rather stable cell potential. The fluctuation detected initially flattened through time. Although the pressure drop was not measured continuously, there were no signs of clogging during the experiment.

5.3.3. Performance with a RED stack

Since it was shown in the previous section that the CSEs can sustain enough current density for RED, these were tested in an actual RED stack (Figure 5.2B). Figure 5.8 shows for each CSE the obtained power density for the RED stack and the corresponding energy and thermodynamic efficiencies. The stack comprised a limited number of 10 cell pairs, therefore the resistance attributed to the electrode compartments (including the flow electrode) and the extra shielding membrane still contributed significantly to the gross power output, see Figure 5.8A.

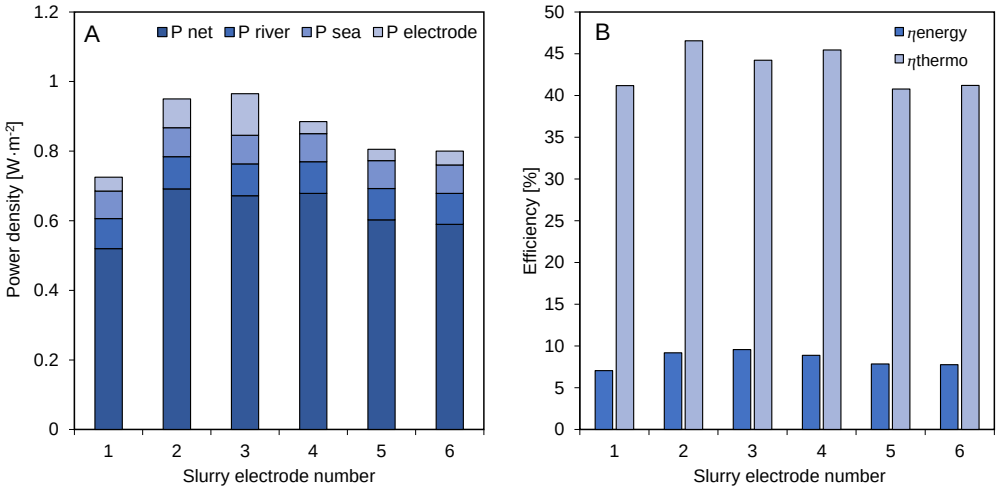

Figure 5.8 (A) RED performance in terms of gross and net power density, power loss for the river compartment, power loss for the seawater compartment, and power loss for the electrode compartments; (B) energy and thermodynamic efficiency for the tested carbon-based slurry electrodes for a RED stack with 10 cell pairs. 1 – 20 % AC; 2 – 15 % AC + 5 % CB; 3 – 10 % AC + 10 % CB; 4 – 10 % AC + 5 % CB; 5 – 10 % CB and 6 – 15 % AC + 5 % GP, all weight percentages and with 0.25 M NaCl in solution.

In Figure 5.8A, the gross power density (aiming for maximum power) is given for the CSEs as used. We found that the power output was stable during the experimental run time. The I-V and power curves can be found in Figure S5.8. Since no other condition was changed, apart from the CSE composition, the change in gross power density is due to the different electrical resistance of the CSEs. The obtained results in Figure 5.8A agree with the single membrane experiments where the slurries with higher electrical resistance in Figure 5.6B (CSE 1, 5 and 6) showed less gross power density being produced.

Furthermore, Figure 5.8A categorizes the contributions to the net power density (losses at the river water, the seawater, and the electrode compartments). The power density lost by pumping the sea and river water was constant in all cases, the difference remained in the flow electrode pumping power density contribution which varied according to the viscosity of the CSE. This led to a very similar net power density of 0.69, 0.67 and 0.68 $W \cdot m^{-2}$ for CSE 2, 3 and 4, respectively. Nonetheless, it must be emphasized that the number of cell pairs (10) is small, and therefore for a larger number of cell pairs, both the pumping power losses at the electrodes and the electrode resistance will be negligible compared to the pumping power loss at the water compartments and total cell pair resistance [10]. Thereby, according to this test, all CSEs, except CSE 5 due to change in pH under current, could still be suitable for RED.

The energy efficiencies obtained, in Figure 5.8B, were for all cases between 7 and 10 %. This is common for small stacks and can be mostly attributed to the short residence time of 10 s [2,42]. Not correcting the power density for the voltage losses at the electrodes given only 10

cell pairs also lowers the energy efficiency. Longer residence times would increase the energy efficiency but reduce the power density [42]. Other known strategies that can increase the efficiency are electrode segmentation [32] or multistage [43] without sacrificing the power density, and can also be implemented with carbon-based slurry electrodes. The thermodynamic efficiencies were above 40 % in all cases and were close to the theoretical maximum of 50 % while aiming also for maximum power [44], which was the case in these experiments.

5.3.4. Comparison to other alternatives

To further determine the suitability of the best slurries presented in this study (CSE 2, CSE 3 and CSE 4), Table 5.3 compares and evaluates these CSEs with other known electrode systems for RED. The stack properties and water residence time influence the gross power density; therefore these parameters are first described. Electrode rinse solutions, such as iron chloride, have a technological potential like hexacyanoferrate solutions, therefore these are not specified in this evaluation. An extensive evaluation of suitable electrode systems for RED has been reported by Veerman et al [3]. For comparison, the following parameters are used: gross power density, water switching needed (intermittency) and technological potential. The technological potential includes sustainability, safety, scalability, economical sustainability (e.g., materials costs) and performance (e.g., gross power density), as assessed by us. More details can be found in Table S5.3.

From analysing Table 5.3, it is concluded that the most promising electrode systems are the slurries with AC and CB, in particular, CSE2 and CSE3 because they provide the best properties in terms of good electrochemical and physical performance, sustainability and safety, scalability, low pressure losses at the electrode compartment and no need to switch the river water and seawater flow contrary to CRED, and the low cost of the carbon materials (Table S5.3). The gross power density results with NaCl, CRED or F-CAPMIX are more than 3 times lower than the obtained with CSEs. This may indicate that the electrode compartment voltage losses are higher in these systems. Furthermore, CRED and F-CAPMIX have the disadvantage of being intermittent. The hexacyanoferrate system provides the highest gross power density, however, due to stability and environmental concerns, it is not a suitable option.

The pumping losses for the CSE are influenced by the electrode compartment geometry. Recent studies revealed serpentine flow field geometries for the electrode caused pressure losses such high that net power density values even became negative [45]. In this study, the pressure drop loss was negligible for the flow electrodes, even though the electrode compartments were not further adapted for a slurry. That may still be improved in a dedicated study, also aiming to scale-up to larger stacks.

The use of a surfactant was studied as an option to stabilize the slurries. In this case, CTAB was used, aiming to improve the CSE's dispersibility and avoid settling of the mixed carbon slurry (if necessary). However, the addition of such a surfactant was found to affect negatively the CSE electrochemical performance as the overpotential increased over time. The addition of 7.8 wt% CTAB significantly improved the stability of the mixed CB-AC slurry. However, the use of such surfactants will result in safety and sustainability issues as redox solutions and should be avoided.

Towards a full economic optimization of the electrode compartment, replacing the current collector from Ti/Pt mesh with graphite plates would drastically decrease the costs associated with the electrode compartment, as well as contribute to a more sustainable process by reducing the use of scarce materials like platinum and reducing the chance of water electrolysis which is catalysed by platinum by taking away the catalytic action of platinum towards water splitting into oxygen and hydrogen. During this research, the use of graphite plates was attempted. However, the current collector modification towards a graphite insert plate while keeping the rest of the RED stack structure intact was not yet successful. This was due to the change of a mesh electrode for a flat plate electrode resulting in a flow path with a poor mixing degree and lack of support for the membrane pile. More work in this area is recommended.

Table 5.3 Comparison and evaluation of different electrode systems for conventional RED (with $[Fe(CN)_6]^{3-/4-}$ or NaCl), CRED, F-CAPMIX and CSE-RED.

Electrode compartment	Stack details	Residence time [s]	Cell pair number	Flow rate Electrode rinse solution [mL/min]	Gross power density [W·m^{-2}]	Intermittent use of seawater and river water	Technological Potential*	Reference
0.25M NaCl	0.1 x 0.1 m^2 200 µm spacer Neosepta CMX/AMX	10	30	200	0.230	No	+/-	[10]
CRED (90 wt% AC + 10 wt% PVDF)		6 #	10	200	0.760	Yes	+/-	[10]
FE-RED (10 wt% AC + 0.5M NaCl + brushes)	0.0007 m^2 250 µm spacer Neosepta CMX/AMX	n.d.	4	20	0.260	No	+	[22]
F-CAPMIX (5 wt % AC + 0.6M NaCl)	0.00138 m^2 360 µm spacer Neosepta CMX/AMX	n.d.	n.a.	25	0.175	Yes	-	[46]
0.2M $K_3Fe(CN)_6$ 0.2M $K_4Fe(CN)_6$ 0.25M NaCl	0.1 x 0.1 m^2 155 µm spacer Type 10 Fujifilm	10	10	150	1.220	No	-	This study
CSE 2 (15 wt% AC + 5 wt% CB + 0.25M NaCl)		10	10	300	0.945	No	+	This study
CSE 3 (10 wt% AC + 10 wt% CB + 0.25 M NaCl)		10	10	300	0.973	No	+/-	This study
CSE 4 (10 wt% AC + 5 wt% CB + 0.25 M NaCl)		10	10	300	0.905	No	+	This study
CSE 2 with surfactant		10	10	300	0.800	No	-	This study

* Technological potential evaluated by the authors in terms of sustainability and safety, feasibility, economics and performance (-, +/-, +).

Accounting with spacer porosity

RED tests used 1 and 30 g NaCl·L^{-1} for sea and river water, respectively. F-CAPMIX used either 35 g NaCl·L^{-1} or deionized water in the central compartment.

n.d. – not defined; n.a. – not applicable

5.3.5. Electrodialysis experiment

The relatively high current densities obtained in the single membrane test allow and stimulate the CSEs to be used in other applications besides flow capacitive deionization, F-CAPMIX or RED. Therefore, using CSE 2, a short test using the same cross-flow RED stack was performed under electrodialysis (ED) conditions, feeding seawater at the inlets. Figure 5.9 shows the stack voltage, Coulombic efficiency, and pH change at different current densities.

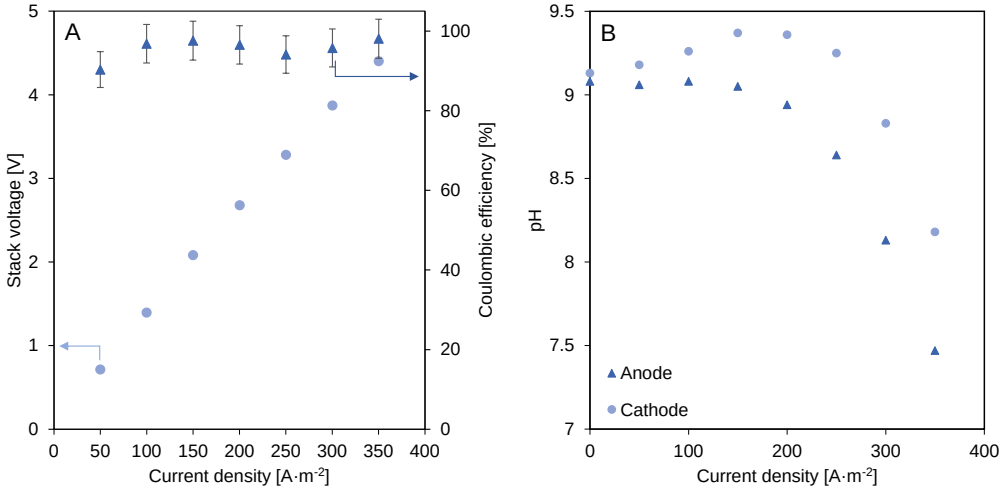

Figure 5.9 (A) Stack voltage and Coulombic efficiency for ED mode at different current densities using CSE 2. (B) Anode and cathode pH change with current density applied.

The measured stack voltage was linear with the applied current density and no limiting voltage was detected. The Coulombic efficiency achieved values of 90 % in all cases. This value might be overestimated due to the conversion between conductivity ($mS \cdot cm^{-1}$) to concentration ($mol \cdot L^{-1}$), while not considering the water transport as the outlet flow rate was not measured. The Coulombic efficiency was calculated according to Doornbusch et al [47]. However, the pH measurements at the anode and cathode showed that at current densities above 150 $A \cdot m^{-2}$, electrolysis occurred with the anode becoming acidic and the cathode becoming alkaline. The reason for the drop in pH at the cathode above 200 $A \cdot m^{-2}$ is not known. The application of CSEs for electrodialysis is advantageous for a continuous process without redox reactions, particularly in specific configurations in which waters cannot be reversed due to, for example, the use of bipolar membranes or the need to keep the solution in a determined compartment. The results show potential application, nonetheless, a dedicated study on carbon-based slurry electrodes for ED is advised.

5.4. Conclusions

Carbon-based slurry electrodes (CSEs) were tested to move towards redox free reverse electrodialysis as these slurry electrodes allow a continuous reverse electrodialysis process in a more clean and sustainable way. Several compositions of CSEs were tested including mixing activated carbon with carbon black or graphite powder as conductive additives. The CSEs were characterized both physically and electrochemically. From these tests, the CSEs that performed best comprised a mixture of activated carbon and carbon black (CSE 2, CSE 3 and CSE 4) presenting low electrode losses and stable electrical performance. However, in the case of a higher loading of carbon black (10 wt%, CSE 3), the viscosity increased considerably, thereby increasing pumping losses for the electrode compartments. By achieving current densities higher than 150 $A \cdot m^{-2}$ with CSE 2, CSEs can also be used for desalination with electrodialysis. It is recommended to further test these CSEs to evaluate the effect of multivalent ions present in the seawater and river water and validate the long-term operational stability.

5.5. Supporting Information

5.5.1. Slurry preparation

For each carbon-based slurry electrode, 700 mL of deionized water was used. First, a third of the water was poured into a beaker. Then the carbons were weighted and placed in the same beaker. Slowly the rest of the water was poured into the beaker. Finally, the NaCl was weighted and added to the mixture. The slurry was mixed manually, using a spoon to avoid the powders to spread. Once the powders were mixed, the slurry was firmly mixed for 12 minutes using an UltraTurrax (IKA, T25, Germany) at 12000 rpm. After preparation, a sample was taken for viscosity measurements and the remaining slurry was tested first in the single membrane configuration and later in the RED stack.

Table S5.1 CSEs composition used for the experiments.

Slurry	Composition (g)					
	H_2O	NaCl	AC	CB	GP	Total
1.AC20	700.00	10.21	177.55	0.00	0.00	887.76
2.AC15.CB5	700.00	10.21	133.16	44.39	0.00	887.76
3.AC10.CB10	700.00	10.21	88.78	88.78	0.00	887.76
4.AC10CB5	700.00	10.28	83.56	41.78	0.00	835.62
5.CB10	700.00	10.26	0.00	78.92	0.00	789.18
6.15AC.GP5	700.00	10.21	133.16	0.00	44.39	887.76

5.5.2. Ion exchange membranes characteristics

Table S5.2 Characteristics of the ion exchange membranes. Information provided by the manufacturer.

Membrane	Manufacturer	Dry thickness [μm]	Electrical resistance [Ω·cm²]	Permselectivity [%]
Type 10 AEM	FujiFilm	125	1.7	95
Type 10 CEM	FujiFilm	135	2.0	99

5.5.3. Secondary cell to perform Electrochemical Impedance Spectroscopy

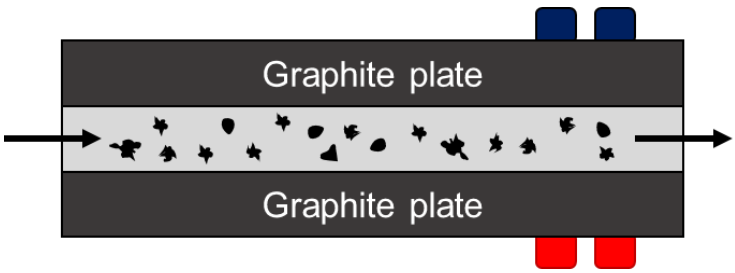

Figure S5.1 One chamber electrochemical cell used for EIS

5.5.4. Brunauer-Emmett-Teller (BET) analysis

Samples were degassed under a nitrogen atmosphere for 2 h at 300 °C in a degassing apparatus (VacPrep 061, Micromeritics, Norcross, GA, USA). The degassing was needed to remove adsorbed gases and water from the pores of the sample material. Subsequently, nitrogen gas adsorption (TriStar 3000, Micromeritics, Norcross, GA, USA) at -196 °C (77 K) was used to determine the specific surface area of the samples according to the BET model.

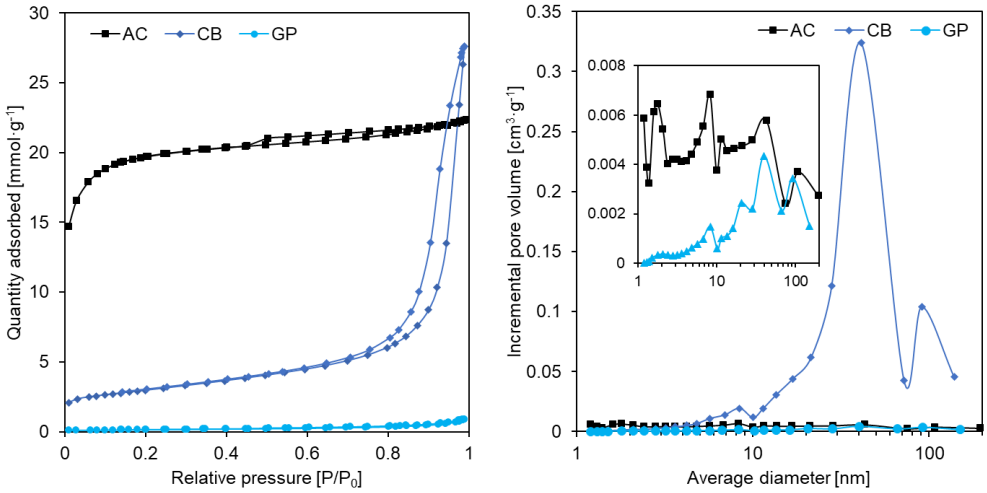

Figure S5.2 (A) Absorption and desorption rate of each carbon and (B) incremental pore volume.

5.5.5. Scanning electron microscopy (SEM) of raw carbons

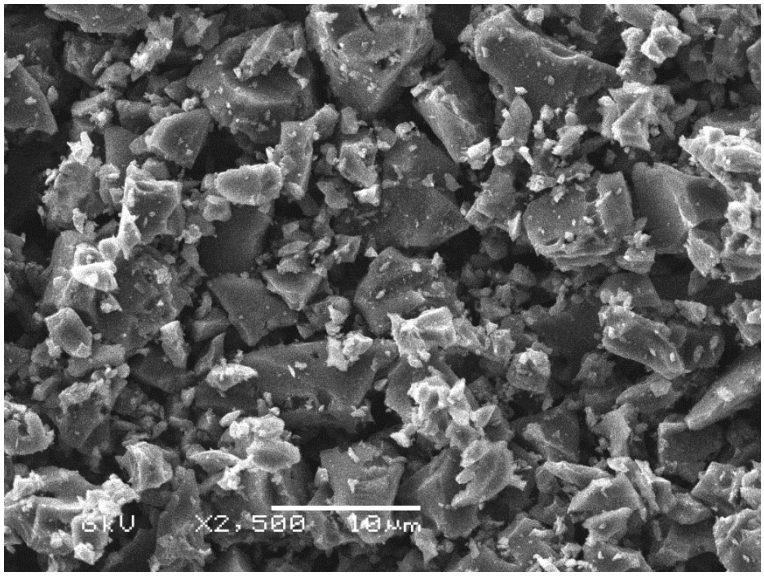

Figure S5.3 Activated Carbon (x2500)

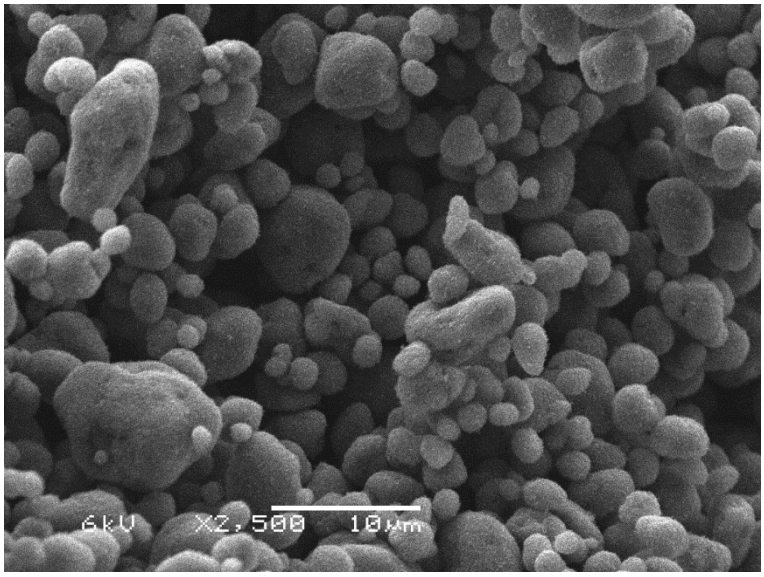

Figure S5.4 Carbon black agglomerates (x2500)

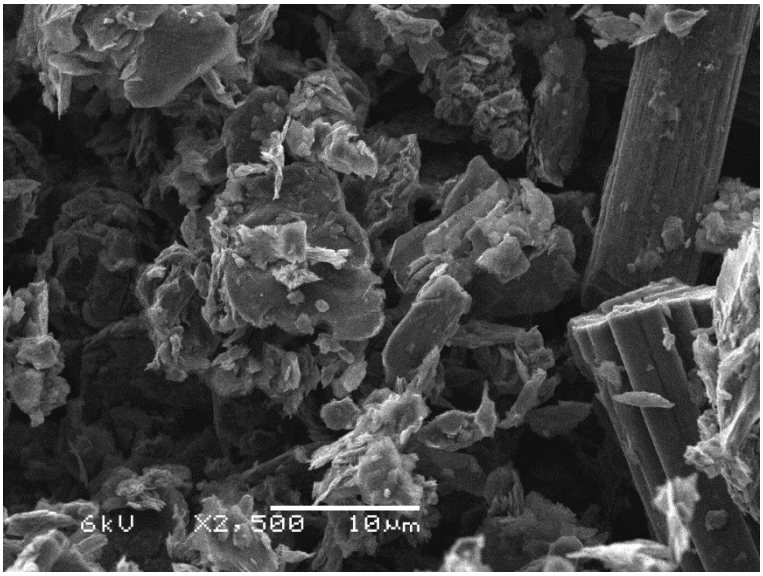

Figure S5.5 Graphite powder (x2500)

5.5.6. Viscosity measurements

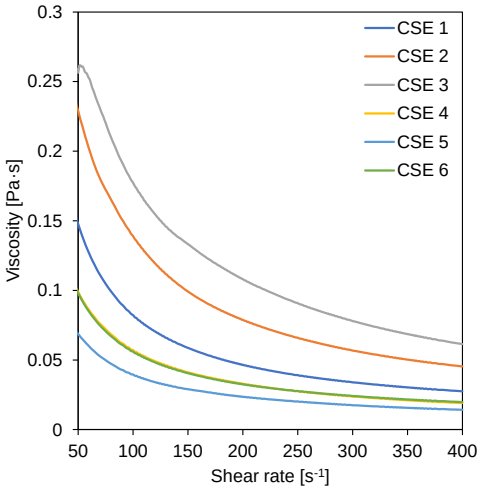

Figure S5.6 Carbon-based slurry electrodes viscosity at shear rates from 50 to 400 s^{-1}.

5.5.7. Carbon black electrical conductivity

The test of the carbon black (CB) electrical conductivity was conducted by pumping the solution through the secondary cell only at 300 mL·min^{-1}. The solution initially consisted of one litre of pure H_2O and for every three measurements 1wt% of CB was added until 11 wt% was achieved. After 0.25 M NaCl was added to the sample to quantify the salt effect, as shown in position 12, Fig, S7, the carbon slurry composition was 11 wt% CB + 0.25 M NaCl instead of 12 wt% CB.

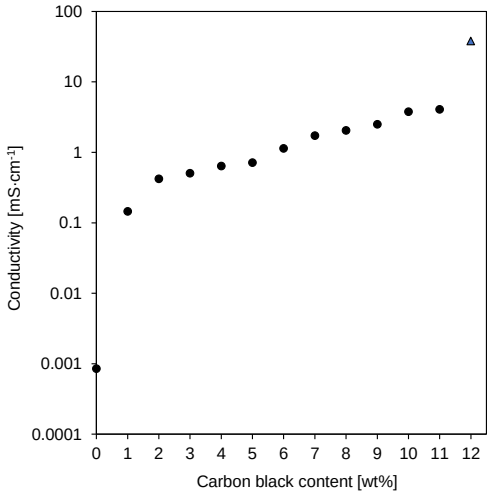

Figure S5.7 Electrical conductivity of different carbon black weight percentages in pure H_2O. The last point (12 wt%) relates to a composition with 11 wt% CB + 0.25 M NaCl.

5.5.8. I-V and Power curve for each carbon-based slurry electrode in a 10-cell pair REDstack

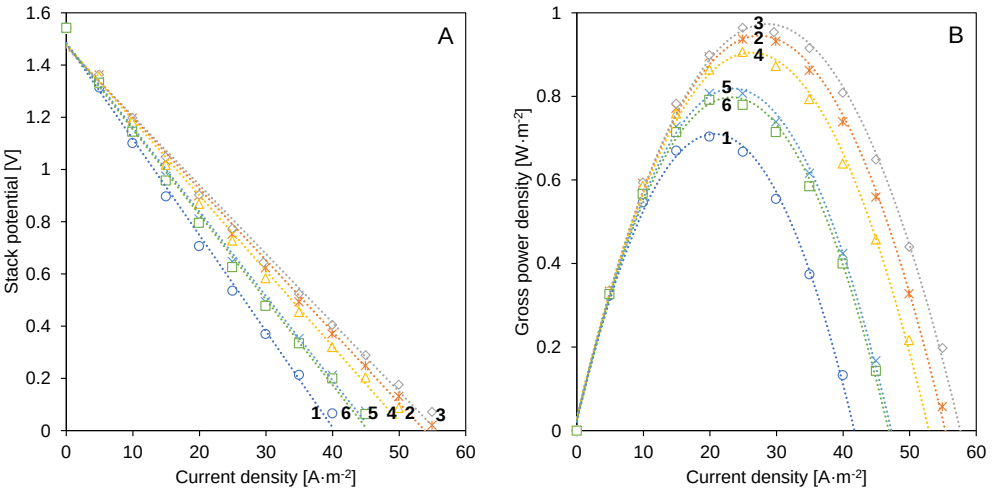

Figure S5.8 (A) I-V and (B) power curve changing carbon-based slurry electrode at the electrode compartment for a RED stack with 10 cell pairs. 1 – 20 % AC; 2 – 15 % AC + 5 % CB; 3 – 10 % AC + 10 % CB; 4 – 10 % AC + 5 % CB; 5 – 10 % CB and 6 – 15 % AC + 5 % GP, all weight percentages and with 0.25 M NaCl in solution.

5.5.9. Comparison to other alternatives

Table S5.3 Cost and hazards of the materials used for the electrode system.

Materials	Costs [€/kg]	Hazards at the electrode comp.	References
$K_3Fe(CN)_6/K_4Fe(CN)_6$	~ 400	Cyanide formation, scaling, harmful to the aquatic environment	[48],[49]
NaCl	~ 0.7	Cl_2 and H_2 evolution, scaling	[50]
PVDF	~ 1840	None	[51]
Activated Carbon	~ 10	None	[52]
Carbon Black	~ 3	None	[53]
CTAB	~ 270	Very toxic for the aquatic environment, corrosive	[54]

References

[1] J.W. Post, J. Veerman, H.V.M. Hamelers, G.J.W. Euverink, S.J. Metz, K. Nymeijer, C.J.N. Buisman, Salinity-gradient power: Evaluation of pressure-retarded osmosis and reverse electrodialysis, J Memb Sci. 288 (2007) 218–230. https://doi.org/10.1016/j.memsci.2006.11.018.

[2] J. Veerman, M. Saakes, S.J. Metz, G.J. Harmsen, Reverse electrodialysis: Performance of a stack with 50 cells on the mixing of sea and river water, J Memb Sci. 327 (2009) 136–144. https://doi.org/10.1016/j.memsci.2008.11.015.

[3] J. Veerman, M. Saakes, S.J. Metz, G.J. Harmsen, Reverse electrodialysis: Evaluation of suitable electrode systems, J Appl Electrochem. 40 (2010) 1461–1474. https://doi.org/10.1007/s10800-010-0124-8.

[4] J. Jang, Y. Kang, J.H. Han, K. Jang, C.M. Kim, I.S. Kim, Developments and future prospects of reverse electrodialysis for salinity gradient power generation: Influence of ion exchange membranes and electrodes, Desalination. 491 (2020) 114540. https://doi.org/10.1016/j.desal.2020.114540.

[5] O. Scialdone, C. Guarisco, S. Grispo, A.D. Angelo, A. Galia, Investigation of electrode material - Redox couple systems for reverse electrodialysis processes. Part I: Iron redox couples, Journal of Electroanalytical Chemistry. 681 (2012) 66–85. https://doi.org/10.1016/j.jelechem.2012.05.017.

[6] A. D'Angelo, M. Tedesco, A. Cipollina, A. Galia, G. Micale, O. Scialdone, Reverse electrodialysis performed at pilot plant scale: Evaluation of redox processes and simultaneous generation of electric energy and treatment of wastewater, Water Res. 125 (2017) 123–131. https://doi.org/10.1016/j.watres.2017.08.008.

[7] E. Jaszczak, Ż. Polkowska, S. Narkowicz, J. Namieśnik, Cyanides in the environment—analysis—problems and challenges, Environmental Science and Pollution Research. 24 (2017) 15929–15948. https://doi.org/10.1007/s11356-017-9081-7.

[8] C. Simões, B. Vital, T. Sleutels, M. Saakes, W. Brilman, Scaled-up multistage reverse electrodialysis pilot study with natural waters, Chemical Engineering Journal. 450 (2022) 138412. https://doi.org/10.1016/j.cej.2022.138412.

[9] J. Hyung, H. Kyo, H. Jeong, S. Yong, B. Joo, Y. Nam, C. Soo, Electrode system for large-scale reverse electrodialysis : water electrolysis , bubble resistance , and inorganic scaling, J Appl Electrochem. 49 (2019) 517–528. https://doi.org/10.1007/s10800-019-01303-4.

[10] D.A. Vermaas, S. Bajracharya, B.B. Sales, M. Saakes, B. Hamelers, K. Nijmeijer, Clean energy generation using capacitive electrodes in reverse electrodialysis, Energy Environ Sci. 6 (2013) 643. https://doi.org/10.1039/c2ee23562e.

[11] B.B. Sales, M. Saakes, J.W. Post, C.J.N. Buisman, P.M. Biesheuvel, H.V.M. Hamelers, Direct power production from a water salinity difference in a membrane-modified supercapacitor flow cell, Environ Sci Technol. 44 (2010) 5661–5665. https://doi.org/10.1021/es100852a.

[12] A. Campione, A. Cipollina, E. Toet, L. Gurreri, I.D.L. Bogle, G. Micale, Water desalination by capacitive electrodialysis: Experiments and modelling, Desalination. 473 (2020) 114150. https://doi.org/10.1016/j.desal.2019.114150.

[13] M.A. Anderson, A.L. Cudero, J. Palma, Capacitive deionization as an electrochemical means of saving energy and delivering clean water. Comparison to present desalination practices: Will it compete?, Electrochim Acta. 55 (2010) 3845–3856. https://doi.org/10.1016/j.electacta.2010.02.012.

[14] E. Avraham, M. Noked, I. Cohen, A. Soffer, D. Aurbach, The Dependence of the Desalination Performance in Capacitive Deionization Processes on the Electrodes PZC, J Electrochem Soc. 158 (2011) P168. https://doi.org/10.1149/2.078112jes.

[15] X. Zhao, H. Wei, H. Zhao, Y. Wang, N. Tang, Electrode materials for capacitive deionization : A review, Journal of Electroanalytical Chemistry. 873 (2020) 114416. https://doi.org/10.1016/j.jelechem.2020.114416.

[16] J. Wang, J. Dai, Z. Jiang, B. Chu, F. Chen, Recent progress and prospect of flow-electrode electrochemical desalination system, Desalination. 504 (2021) 114964. https://doi.org/10.1016/j.desal.2021.114964.

[17] S. il Jeon, H.R. Park, J.G. Yeo, S. Yang, C.H. Cho, M.H. Han, D.K. Kim, Desalination via a new membrane capacitive deionization process utilizing flow-electrodes, Energy Environ Sci. 6 (2013) 1471–1475. https://doi.org/10.1039/c3ee24443a.

[18] J.W. Campos, M. Beidaghi, K.B. Hatzell, C.R. Dennison, B. Musci, V. Presser, E.C. Kumbur, Y. Gogotsi, Investigation of carbon materials for use as a flowable electrode in electrochemical flow capacitors, Electrochim Acta. 98 (2013) 123–130. https://doi.org/10.1016/j.electacta.2013.03.037.

[19] S. Dahiya, B.K. Mishra, Enhancing understandability and performance of flow electrode capacitive deionisation by optimizing configurational and operational parameters: A review on recent progress, Sep Purif Technol. 240 (2020) 116660. https://doi.org/10.1016/j.seppur.2020.116660.

[20] S.N. Ashrafizadeh, A. Ganjizade, A. Navapour, A brief review on the recent achievements in flow-electrode capacitive deionization, Korean Journal of Chemical Engineering. 38 (2021) 1–7. https://doi.org/10.1007/s11814-020-0677-0.

[21] Y.U. Shin, J. Lim, C. Boo, S. Hong, Improving the feasibility and applicability of flow-electrode capacitive deionization (FCDI): Review of process optimization and energy efficiency, Desalination. 502 (2021) 114930. https://doi.org/10.1016/j.desal.2021.114930.

[22] F. Liu, O. Coronell, D.F. Call, Electricity generation using continuously recirculated flow electrodes in reverse electrodialysis, J Power Sources. 355 (2017) 206–210. https://doi.org/10.1016/j.jpowsour.2017.04.061.

[23] K.B. Hatzell, M. Boota, Y. Gogotsi, Materials for suspension (semi-solid) electrodes for energy and water technologies, Chem Soc Rev. 44 (2015) 8664–8687. https://doi.org/10.1039/c5cs00279f.

[24] G.J. Doornbusch, J.E. Dykstra, P.M. Biesheuvel, M.E. Suss, Fluidized bed electrodes with high carbon loading for water desalination by capacitive deionization, J Mater Chem A Mater. 4 (2016) 3642–3647. https://doi.org/10.1039/c5ta10316a.

[25] H. Li, L. Pan, T. Lu, Y. Zhan, C. Nie, Z. Sun, A comparative study on electrosorptive behavior of carbon nanotubes and graphene for capacitive deionization, Journal of Electroanalytical Chemistry. 653 (2011) 40–44. https://doi.org/10.1016/j.jelechem.2011.01.012.

[26] J. Ma, C. Zhang, F. Yang, X. Zhang, M.E. Suss, X. Huang, P. Liang, Carbon Black Flow Electrode Enhanced Electrochemical Desalination Using Single-Cycle Operation, Environ Sci Technol. 54 (2020) 1177–1185. https://doi.org/10.1021/acs.est.9b04823.

[27] J. Oladunni, J.H. Zain, A. Hai, F. Banat, G. Bharath, E. Alhseinat, A comprehensive review on recently developed carbon based nanocomposites for capacitive deionization: From theory to practice, Sep Purif Technol. 207 (2018) 291–320. https://doi.org/10.1016/j.seppur.2018.06.046.

[28] M. Mourshed, S.M.R. Niya, R. Ojha, G. Rosengarten, J. Andrews, B. Shabani, Carbon-based slurry electrodes for energy storage and power supply systems, Energy Storage Mater. 40 (2021) 461–489. https://doi.org/10.1016/j.ensm.2021.05.032.

[29] P. Liang, X. Sun, Y. Bian, H. Zhang, X. Yang, Y. Jiang, P. Liu, X. Huang, Optimized desalination performance of high voltage flow-electrode capacitive deionization by adding carbon black in flow-electrode, Desalination. 420 (2017) 63–69. https://doi.org/10.1016/j.desal.2017.05.023.

[30] T.J. Petek, Enhancing the Capacity of All-Iron Flow Batteries: Understanding Crossover and Slurry Electrodes, 2015. http://rave.ohiolink.edu/etdc/view?acc_num=case1428057617 (accessed August 15, 2022).

[31] J. Moreno, N. de Hart, M. Saakes, K. Nijmeijer, CO 2 saturated water as two-phase flow for fouling control in reverse electrodialysis, Water Res. 125 (2017) 23–31. https://doi.org/10.1016/j.watres.2017.08.015.

[32] C. Simões, D. Pintossi, M. Saakes, Z. Borneman, W. Brilman, K. Nijmeijer, Electrode segmentation in reverse electrodialysis: Improved power and energy efficiency, Desalination. 492 (2020) 114604. https://doi.org/10.1016/j.desal.2020.114604.

[33] K. Fang, H. Gong, W. He, F. Peng, C. He, K. Wang, Recovering ammonia from municipal wastewater by flow-electrode capacitive deionization, Chemical Engineering Journal. 348 (2018) 301–309. https://doi.org/10.1016/j.cej.2018.04.128.

[34] S. Yang, H. Park, J. Yoo, H. Kim, J. Choi, M.H. Han, D.K. Kim, Plate-Shaped Graphite for Improved Performance of Flow-Electrode Capacitive Deionization, J Electrochem Soc. 164 (2017) E480–E488. https://doi.org/10.1149/2.1551713jes.

[35] S. Khodabakhshi, P.F. Fulvio, E. Andreoli, Carbon black reborn: Structure and chemistry for renewable energy harnessing, Carbon N Y. 162 (2020) 604–649. https://doi.org/10.1016/j.carbon.2020.02.058.

[36] P. Greenwood, R.H. Thring, R. Chen, Conductive materials for polymeric bipolar plates: Electrical, thermal and mechanical properties of polyethylenecarbon black/graphite/magnetite blends, Proceedings of the Institution of Mechanical Engineers, Part L: Journal of Materials: Design and Applications. 227 (2013) 226–242. https://doi.org/10.1177/1464420712454059.

[37] C. Tropea, A. L. Yarin, J. F. Foss, eds., Springer Handbook of Experimental Fluid Mechanics, Springer, 2007.

[38] T.J. Petek, J.E. Soc, T.J. Petek, N.C. Hoyt, R.F. Savinell, J.S. Wainright, Characterizing Slurry Electrodes Using Electrochemical Impedance Spectroscopy, J Electrochem Soc. 163 (2016) A5001–A5009. https://doi.org/10.1149/2.0011601jes.

[39] H. Parant, G. Muller, T. le Mercier, J.M. Tarascon, P. Poulin, A. Colin, Flowing suspensions of carbon black with high electronic conductivity for flow applications: Comparison between carbons black and exhibition of specific aggregation of carbon particles, Carbon N Y. 119 (2017) 10–20. https://doi.org/10.1016/j.carbon.2017.04.014.

[40] H. Cohen, E. Eli, M. Jǒgi, M.E. Suss, Suspension Electrodes Combining Slurries and Upflow Fluidized Beds, ChemSusChem. 9 (2016) 1–5. https://doi.org/10.1002/cssc.201601008.

[41] M.B. Dixit, D. Moreno, X. Xiao, M.C. Hatzell, K.B. Hatzell, Mapping Charge Percolation in Flowable Electrodes Used in Capacitive Deionization, ACS Mater Lett. 1 (2019) 71–76. https://doi.org/10.1021/acsmaterialslett.9b00106.

[42] J. Moreno, S. Grasman, R. van Engelen, K. Nijmeijer, Up-scaling reverse electrodialysis, Environ Sci Technol. 52 (2018) 10856–10863. https://doi.org/10.1021/acs.est.8b01886.

[43] C. Simões, D. Pintossi, M. Saakes, W. Brilman, Optimizing multistage reverse electrodialysis for enhanced energy recovery from river water and seawater: Experimental and modeling investigation, Advances in Applied Energy. 2 (2021) 100023. https://doi.org/10.1016/j.adapen.2021.100023.

[44] J. Veerman, J.W. Post, M. Saakes, S.J. Metz, G.J. Harmsen, Reducing power losses caused by ionic shortcut currents in reverse electrodialysis stacks by a validated model, J Memb Sci. 310 (2008) 418–430. https://doi.org/10.1016/j.memsci.2007.11.032.

[45] D. Kim, H. Kwon, G.H. Cho, H. Kim, H. Seo, Y.G. Jung, J. Choi, H. Kim, J. Yoo, D. Lee, I. Hwang, U. Paik, T. Song, H. Park, S.C. Yang, Importance of channel dimension for flow-electrode flowing in flow-electrode capacitive mixing (F-CapMix): Evaluation of net power density under high-pressure-drop conditions, Sep Purif Technol. 290 (2022) 120859. https://doi.org/10.1016/j.seppur.2022.120859.

[46] H. Kim, J. Choi, N. Jeong, H.J. Im, J.G. Yeo, S. il Jeon, W.G. Chun, D.K. Kim, S. Yang, Electrochemical Analysis of High-Performance Flow-Electrode Capacitive Mixing (F-CapMix) under Different Operating Conditions, ACS Sustain Chem Eng. 9 (2021) 9199–9208. https://doi.org/10.1021/acssuschemeng.1c00848.

[47] G. Doornbusch, H. Swart, M. Tedesco, J. Post, Z. Borneman, K. Nijmeijer, Current utilization in electrodialysis: Electrode segmentation as alternative for multistaging, Desalination. 480 (2020) 114243. https://doi.org/10.1016/j.desal.2019.114243.

[48] Potassium hexacyanoferrate(III), https://www.sigmaaldrich.com/NL/en/product/mm/104973, (consulted on 26.08.2022)

[49] Potassium hexacyanoferrate(II) trihydrate, https://www.sigmaaldrich.com/NL/en/product/mm/104984, (consulted on 26.08.2022)

[50] ESCO tableted salt REGENIT 25kg, https://sanresurs.lv/en/esco-sals-tabletes-filtriem-regenit-25kg-(vacija), (consulted on 26.08.2022)

[51] Poly(vinylidene fluoride), https://www.sigmaaldrich.com/NL/en/product/aldrich/182702,(consulted on 26.08.2022)

[52] Lithium Ion Battery Conductive Powder YP50F YP80F Active Carbon Super Capacitor Activated Carbon With High Quality, https://www.alibaba.com/product-detail/Lithium-Ion-Battery-Conductive-Powder-YP50F_1600275023235.html?spm=a2700.details.0.0.61e137b6RuGzcn,(consulted on 30.08.2022)

[53] Black Pearl 800 Cabot Carbon Black, https://carbonblack.en.made-in-china.com/product/SKLmYIiJugRT/China-Black-Pearl-800-Cabot-Carbon-Black.html, (consulted on 30.08.2022)

[54] Hexadecyltrimethylammonium bromide, https://www.sigmaaldrich.com/NL/en/product/sigma/h5882,(consulted on 26.08.2022)

Chapter 6

Outlook and general conclusions

6.1. Introduction

This thesis focused on optimizing the reverse electrodialysis process for energy generation centring on the salinity gradient available between seawater and river water. The studied topics were at the system level, the electrical control, and at the stack level, the electrode system. First, the optimization was done regarding the electrical control by segmenting the electrodes (Chapter 2) or staging two electrically independent stacks (Chapters 3 and 4). Both configurations showed an improvement in gross power density and energy efficiency, especially when the overall maximum power was targeted. The overall maximum power was optimized by tailoring the external load to each electrode segment or stack and making the best use of the salinity gradient available. Second, the optimization was performed at the electrode system by employing carbon-based slurry electrodes (Chapter 5) for charge transfer instead of redox solutions. This prevented the evolution of unwanted electrode reactions like hydrogen gas formation at the cathode and chlorine gas formation at the anode and makes the process safer and more sustainable.

Chapter 6 is dedicated to combining the knowledge gained in the previous chapters with other RED developments to understand the process achievability, energetic trends, sustainability and future directions.

6.2. Reverse electrodialysis achievability

Previous studies indicated that mixing seawater and river water could theoretically achieve 4 $W \cdot m^{-2}$ to even 8 $W \cdot m^{-2}$ of gross power density in the case of membranes without electrical resistance and 100 % permselectivity [1]. However, experimentally obtained gross power densities above 2 $W \cdot m^{-2}$ from feeding seawater and river water are rare. The maximum achieved gross power density reported in literature [2] was 2.2 $W \cdot m^{-2}$ with artificial waters, at a flow velocity of 4 $cm \cdot s^{-1}$. This resulted in a negative net power density due to the pumping power losses at such high flow velocity. Previous reported theoretical calculations [1] only accounted for the maximum gross power density that the salinity gradient could deliver on the first moment of mixing. At the point that the salt gradient was still intact. However, these theoretical calculations lacked, for example, the effect of flow rate, stack length, spacers, and osmotic water transport through the membranes. The highest gross power density should be in line with achieving the highest net power density. Thus it is important to balance between maximizing the gross power density, optimizing the use of the available salinity gradient, and minimizing pumping power losses [3].

Employing the Donnan potential-based model developed in Chapters 2 and 3, the RED achievability from mixing seawater and river water is discussed. The ion exchange

membranes (IEMs) have a direct influence on the gross power density. Figure 6.1 shows the gross power density for a 0.22 x 0.22 m^2 cross-flow stack, as a function of the membrane electrical resistance and permselectivity. The flow velocity, fixed at 1.5 $cm \cdot s^{-1}$ (15 s residence time), is representing a realistic value to obtain high gross power densities, without an extreme loss in pumping power densities. The simulation was performed using 155 µm thick spacers and the correction for the pumping losses was -0.174 $W \cdot m^{-2}$, as taken from the experimental work of Chapter 4 [4].

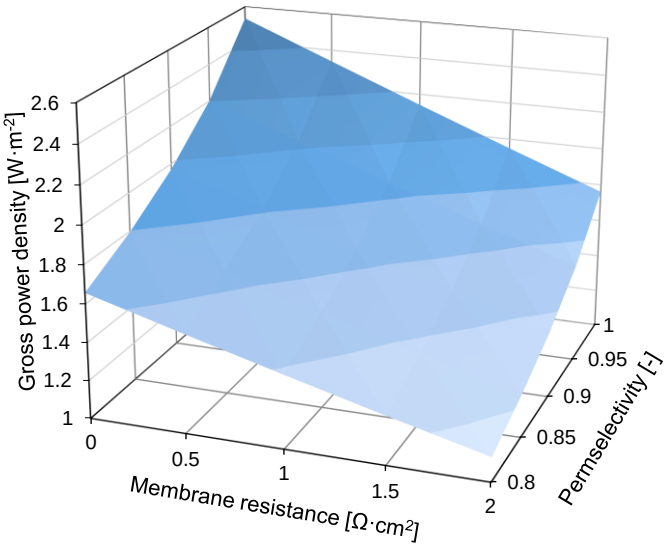

Figure 6.1 Simulated gross power density for a 0.22 x 0.22 m^2 cross-flow stack at a flow velocity of 1.5 $cm \cdot s^{-1}$ (15 s residence time) while varying the membrane electrical resistance and permselectivity. The inlet concentrations are 0.017 M and 0.500 M NaCl, the obstruction factor is 1.65 (based on experimental results, [4]), the spacer thickness is 155 µm, and the pumping power density is 0.174 $W \cdot m^{-2}$ (based on experimental results, [4]).

Considering perfect membrane conditions (which correspond to imaginary membranes with zero electrical resistance and 100 % permselectivity) the calculated maximum gross power density is 2.54 $W \cdot m^{-2}$. Therefore, for the set flow velocity and spacer properties, this is the upper theoretical value. This value is much lower than the theoretical value initially published [1] since it includes the effects of the stack length, flow rate, and spacer geometry. Considering net power density, this corresponds to 2.36 $W \cdot m^{-2}$. Most commercially available IEMs fall in the range of 0.7 – 2.0 $\Omega \cdot cm^2$ electrical resistance and 0.9 – 0.98 permselectivity [5], which means the gross power density ranges between 1.4 – 2.0 $W \cdot m^{-2}$. To achieve 2 $W \cdot m^{-2}$ net power density, current commercial membranes need to have much lower electrical resistance and a higher permselectivity.

Table 6.1 shows membrane properties for the IEMs used in previous chapters, Fumatech FKS-30 & FAS-30 (named FUMA) and Fujifilm AEM & CEM Type 10 (named FUJI) and two case scenarios, an ideal scenario where the IEMs have the best characteristics found in the literature [6,7] and a perfect scenario where the IEMs have 100 % permselectivity and null electrical resistance.

Table 6.1. Membrane properties used in the calculation of the stack performance. For the ideal membranes, values of permselectivity, electrical resistance and thickness were taken from Jiang et al [6] and the salt and water diffusion coefficients were taken from Veerman et al [7].

Parameter	Symbol	Unit	FUMA	FUJI	Ideal	Perfect
Permselectivity	α	%	92	94.6	97	100
Thickness	l_m	m	$30x10^{-6}$	$125x10^{-6}$	$10\ x10^{-6}$	$10\ x10^{-6}$
Electrical resistance AEM	R_{aem}	$\Omega \cdot m^2$	$0.78x10^{-4}$	$1.77x10^{-4}$	$0.2\ x10^{-4}$	0
Electrical Resistance CEM	R_{cem}	$\Omega \cdot m^2$	$1.32x10^{-4}$	$2.69x10^{-4}$	$0.3\ x10^{-4}$	0
Water diffusion coefficient	D_{H2O}	$m^2 \cdot s^{-1}$	$1.93x10^{-10}$	$1.5x10^{-10}$	$5.8x10^{-11}$	0
Salt diffusion coefficient	D_{NaCl}	$m^2 \cdot s^{-1}$	$2.64x10^{-12}$	$1.5x10^{-12}$	$1.8x10^{-14}$	0

Modelling the performance of a 0.22 x 0.22 m^2 stack for the different IEMs while varying the residence time is shown in Figure 6.2. The stack parameters used in the calculations are described in Table 6.2.

Table 6.2. General parameters used in the calculation of the stack performance.

Parameter	Symbol	Value	Unit
Width of the active area	W	0.22	m
Length of the active area	L	0.22	m
Compartment thickness	d	$155x10^{-6}$	m
Temperature	T	298	K
River water initial concentration	c_{RWo}	17.1	mol NaCl$\cdot m^{-3}$
Seawater initial concentration	c_{SWo}	500.0	mol NaCl$\cdot m^{-3}$
Residence time	τ	[5 – 65]	s
Flow rate per cell pair	Φ	7 – 90	mL$\cdot min^{-1}$
Flow rate per cell pair	Φ	$[1.16 – 15]x10^{-6}$	$m^3 \cdot s^{-1}$
Obstruction factor	obs	1.65	-
Electro-osmosis coefficient	$K_{e,osm}$	4	-
Pumping losses (function of RT)	P_{pump}	$0.071^{-0.034\tau} + 1.006^{-0.136\tau}$	W$\cdot m^{-2}$

Figure 6.2A shows the gross power density as a function of the residence time. The short residence times provide higher power densities. However, Figure 6.2B reveals the importance of incorporating power losses by pumping. If infinite flow rates would be used, the pumping power density would be significantly higher than the gross power density, resulting in a

negative net power density. Thus, all the power produced would be used for pumping and no net power would be left for energy generation.

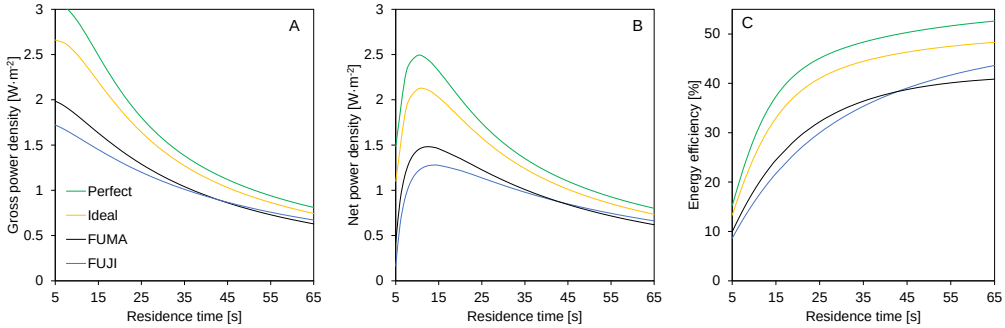

Figure 6.2 Different IEMs' performance at different residence times. (A) Gross power density; (B) Net power density; (C) Energy efficiency. Simulated for a 0.22 x 0.22 m² cross-flow stack, the inlet concentrations are 0.017 M and 0.5 M NaCl, the obstruction factor is 1.65, the spacer thickness is 155 μm, and the pumping power density is based on experimental results. Model inputs are listed in tables 6.1 and 6.2.

When aiming for ideal membranes, instead of perfect membranes, it results only in small losses (around -0.12 $W{\cdot}m^{-2}$ and – 1.8 % at 15 s). Comparing both FUJI and FUMA membranes to the other scenarios, there is an obvious improvement needed to achieve 2 $W{\cdot}m^{-2}$ net power density. For now, a maximum net power density of 1.48 $W{\cdot}m^{-2}$ is obtained with FUMA. The FUMA membranes have better performance at lower residence times because of their lower electrical resistance, while at longer residence times FUJI has better results because of the higher permselectivity and lower water permeability. Higher permselectivity contributes to less co-ion transport. Lower water permeability results in less water transported through osmosis avoiding to some extent the dilution of the seawater. Figure 6.2C describes the energy efficiency of the different IEMs. By improving the membrane characteristics, the energy efficiency increases along with the power density. So, for the same amount of feedwater more power is harvested with membranes with lower electrical resistance and a higher permselectivity. Realistically, in a single stack, a net power density of around 1.5 $W.m^{-2}$ seems achievable, with an energy efficiency of 25 % feeding sodium chloride solutions. Targeting a net power density of 2.0 $W.m^{-2}$ and 40 % energy efficiency requires a lower ohmic resistance of the ion exchange membranes while keeping the water transport low and the permselectivity high.

What is the optimal stack?

When upscaling reverse electrodialysis, there is a need to fix a stack design. Based on the knowledge gathered throughout this thesis and previous studies, an optimal stack for energy production from sea and river water is anticipated in this section, considering sodium chloride solutions (0.017 M and 0.500 M NaCl). During this thesis, two new configurations were

proposed to optimize the RED process: electrode segmentation (Chapter 2) and multistage operation (Chapters 3 and 4).

Electrode segmentation increased both power density and energy efficiency without any trade-off. It was also shown that electrode segmentation could be done just in the direction of the river water, which would also facilitate the electrical control. However, two questions remain for electrode segmentation and upscaling: (a) what is the influence of the electrode area lost by having physical separation of the electrodes? and (b) will electrode segmentation optimization be visible in stacks with thousands of cell pairs?

For the first issue, electrode segmentation was tested with a 0.22 x 0.22 m^2 stack with 10 cell pairs in series. Segmenting the electrode resulted in four electrode segments with a total area of 0.04 m^2 while a non-segmented electrode had 0.0484 m^2. This means that the electrode area was reduced by almost 20 %. If the stack is further upscaled to a size of, for example, 0.5 x 0.5 m^2, four electrode segments would result in 0.2304 m^2 and a non-segmented electrode in 0.25 m^2. The loss in total electrode area would be lower (~ 8 %). The effect of this geometric area reduction on gross power production was not quantified in this work. Nonetheless, when there is a power loss by reducing the electrode area, the negative impact in percentage would be lower with further upscaling.

For the second issue, "will electrode segmentation optimization be visible in stacks with thousands of cell pairs?". At a higher number of cell pairs the electrical field lines may diverge, and the segmentation effect might not be effective for the whole membrane pile. Electrode segmentation was tested with only ten cell pairs; thus, this dimensional influence of a much larger number of cell pairs remains unclear. When stacks with several thousands of cell pairs are available it would be interesting to revisit the segmented electrode option.

Multistage configurations were shown to increase the energy efficiency. With this, a reduction of the cost impact of any feedwater pre-treatment method is feasible. Increased energy efficiency translates into better utilization of the feedwaters However, the increased energy efficiency came with a trade-off in net power density, since by installing a second stage, the power penalty in pressure drop losses across the stacks is also increased.

Considering the three approaches (the two above and a standard cross-flow single-electrode stack) for the case of harvesting energy from seawater and river water, a stack with four electrode segments should provide the best results. This was seen in Chapter 2, where electrode segmentation increased both energy efficiency and power density compared to a single stage. Multistage can reach the same optimized level in gross power density and energy efficiency. However, to be alluring, the stack pressure drop needs to be further reduced or higher salinity gradient sources should be explored for a higher total power density (e.g., brine/freshwater).

In any stack configuration, reducing pumping losses is necessary. Replacing spacers, as separators to create water compartments, with profiled membranes is a desired feature that has been pointed out in the literature [3,8]. Spacers are, usually, a non-conductive mesh reducing (shadowing) part of the active membrane area, increasing the friction for the water flowing through the compartment and are prone to develop fouling [9]. With profiled membranes, the profile on the membrane is made from the same ion exchange material as the IEM, removing the spacer's shadow effect. Rectangular profile geometries for a parallel flow field have proven to lower pumping power losses as well as reduce fouling accumulation [3]. However, chevron, pillar and overlapped crossed filaments geometries might increase the pressure drop of the stack and are more sensitive to fouling and less sensitive to cleaning [10,11]. The spacing and geometry of the profile on the membrane will greatly influence the pressure drop losses. Furthermore, the profile should allow in-situ cleaning to restore performance losses due to fouling.

For the same residence time, the gross power density is independent of the stack's dimension. The stack's dimension, however, changes the net power density result. Figure 6.3 shows the (gross, net and pumping) power density change with the length considering an open channel, profiled membranes and a net-woven spacer.

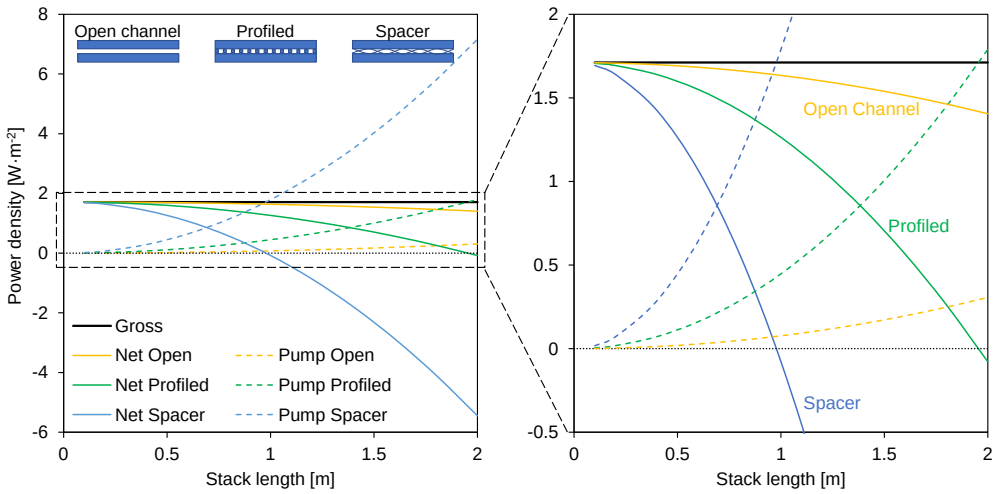

Figure 6.3 Effect of the stack size, from 0.1 m to 2 m, on the pressure drop between two flat plates (Open channel), rectangular profiled membranes (Profiled) and 155 µm net-woven spacers (Spacer). The width is equal to the length. The right panel is a magnification of the left one. The gross power density is taken for a residence time of 15 s, using FUMA membranes and the parameters of Table 6.2. Gross – gross power density; Net – Net power density; Pump – Pumping power density.

The pressure drop in the channel was obtained using the equation for the pressure drop between two flat plates [12].

$$\Delta p = \frac{12\mu . L . \varphi}{W . d^3} \quad \text{(Eq. 6.1)}$$

Where, μ is the viscosity of water (Pa·s), L is the length of the flow path (m), φ is the flow rate ($m^3 \cdot s^{-1}$), W is the width of the flow path (m) and d is the height of the flow path (m). For the Spacer scenario, a factor of 23.4 was used (fitting experimental data [4] to pressure drop calculated for an open channel) and for the Profiled scenario, for which a factor of 5.85 was used (four times lower than for using spacers, as established by Vermaas et al [3]). With the pressure drop (Δp, Pa) and the flow rate (φ, $m^3 \cdot s^{-1}$), the pumping power (P_{pump}, W) is calculated.

$$P_{pump} = \Delta p \cdot \varphi \quad \text{(Eq. 6.2)}$$

Figure 6.3. highlights the relation between the size of the compartment and the net power density. With the existing woven spacers of 155 µm, stacks longer than 1 m, in length and width, will have negative net power density. Although smaller stacks lead to less pumping losses and higher net power densities, it is not feasible to install numerous small stacks to up-scale, as other costs are also involved. These costs can be stack housing, tubing, connectors, electrical control and monitoring devices, which increase with a very large number of smaller stacks to produce essentially the same amount of power. On the other hand, increasing the length (and width) leads to lower net power outputs. The stack size needs to be defined considering both the application and the power losses through pumping. For example, one stack (one cell pair considered) with 0.5 m length (and width) will deliver the same net power (0.63 W) as circa nineteen 0.1 m length stacks in the spacer scenario. If no pumping losses would exist with scaling up, it should replace twenty-five 0.1 m length stacks. Figure 6.3. also shows that the implementation of profiled membranes could save half of the pumping power losses while increasing the net power density. A hydraulic loss with scaling up is present even in the case of an empty channel.

In most studies, an equal (50:50) flow rate ratio of seawater and river water is adopted. However, it has been identified that an asymmetrical flow rate can bring benefits [13]. Using again a 0.22 x 0.22 m^2 cross-flow stack configuration with 155 µm spacers, the optimal flow rate fraction is analysed in Figure 6.4. The simulation parameters are taken from Table 6.2 using FUMA membranes (Table 6.1), and without taking credits for possible improvements with electrode segmentation.

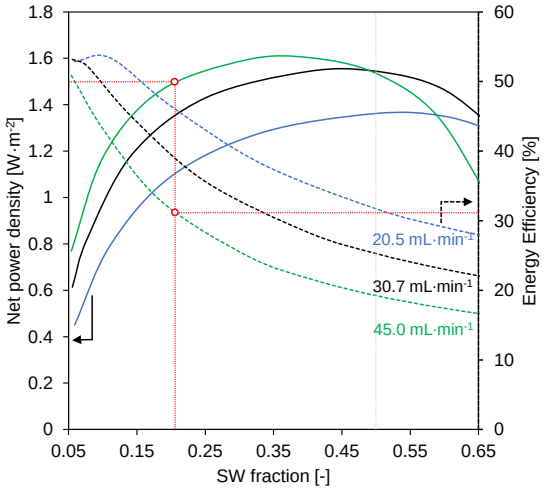

Figure 6.4 Net power density (solid line) and energy efficiency (dashed line) changing the seawater (SW) fraction. The SW fraction is calculated as $f = \varphi_{SW}/(\varphi_{SW} + \varphi_{RW})$. The river water (RW) flow rate per cell pair was accessed in three instances: 20.5 (22 s residence time, blue), 30.7 (14.67 s residence time, black) and 45.0 mL·min^{-1} (10 s residence time, green). The cross-flow stack has an area of 0.22 x 0.22 m^2 with 155 µm spacers and the pumping power density is based on experimental results.

Figure 6.4 shows that a symmetrical flow rate (f = 0.5) does not necessarily lead to an optimal scenario. The optimal performance will always depend on the site conditions and costs. For example, if aiming for a net power density of 1.5 W·m^{-2}, this can be obtained with an RW flow rate of 45 mL·min^{-1} and an energy efficiency of 31 % (red points in Figure 6.4). More importantly, the fraction of SW is reduced to 0.21 which corresponds to pump only 12 mL·min^{-1}. This is a significant reduction in the SW usage compared to the 0.50 fraction scenario for the same RW flow rate. At a site where pre-treatment costs for SW are significant, such optimization will pay off. With the implementation of electrode segmentation, it is expected to increase both net power density and energy efficiency, when compared to Figure 6.4.

For the electrode system, Chapter 5 highlighted the application of carbon-based slurry electrodes to RED stacks as the most promising method for safe and more sustainable electrode reactions. The combination of such slurry electrode systems with segmented electrodes, although not tested, is feasible as well. The use of smaller electrode compartments may even improve the slurry distribution through the electrode compartment. A computational fluid dynamics (CFD) study is recommended for future stack development, aiming for a good flow distribution with lower pressure drop and preventing the risk of clogging at the electrode compartments. This CFD study should be followed by an experimental study of the best outcomes. Slurries have a higher viscosity than electrode rinse solutions based on redox couples, therefore, good flowability and distribution through the

compartment should be assured. For the slurry composition, carbon blacks with a low percolation threshold are recommended in combination with activated carbon.

Other features to consider are a stack housing and tubing that do not pass the sunlight. Limiting light exposure should reduce the microorganism activity and keep biofouling at lower levels. A darker tubing, when exposed to direct sunlight, will cause the streams to heat up and higher temperatures increase the power density [14].

In conclusion, in the case of a scenario of seawater and river water as feedwaters (for simplicity we considered NaCl only), the use of one 0.5 x 0.5 m^2 stack with four electrode segments is recommended, having profiled membranes with characteristics described in Table 6.1 in the Ideal column, an asymmetrical flow rate (i.e., 45 $mL \cdot min^{-1}$ for RW and 12 $mL \cdot min^{-1}$ for SW, per cell pair) and carbon-based slurry electrodes at the end compartments. The maximum cell pair number will depend on strategies to reduce ionic shortcut currents [15], but with a smart stack design, a pile of thousands of cell pairs is feasible.

The evaluation above is done for the case of mixing seawater with river water. However, if the available salinity gradient is much larger, such as between brine and freshwater, the optimal stack may differ. For instance, for a larger salt gradient, multistage configurations might lead to better results. Furthermore, the brine supply might be the limiting feed solution, and the flow rates need to be adjusted accordingly.

6.3. Sustainability

Analogous to the implementation of any new technology, the implementation of salinity gradient energy facilities poses changes for the surrounding environment. Together with being driven by a renewable source of energy, the technology itself should also be sustainable. In this section, the environmental impacts and sustainability of the installation of a RED facility are discussed.

The environmental impacts vary per location of installation and life cycle phase. The location of installation relates to the involving habitat and area occupation and is specific per installation. The phases in the life cycle of the plant are generally categorized as construction, operation ("use phase") and decommissioning ("end of life") [16]. The scale of operation will also influence the impact. Here it is assumed that the impact increases linearly with scale.

During construction, the ecosystem might be disrupted, but this can be reversed once the stress factors are stopped. Stress factors include, for example, noise, habitat changes and the release of pollutants like emission of CO_2 and N emission. This should be a short-term disturbance to marine life, and comparable to other coastal constructions [16]. Integrating a RED facility in previously built facilities, such as pumping stations, can reduce the impact on

the surrounding environment as well as construction costs for the facility. Seyfried et al. indicated that the construction of the facility brings the most impact on the environment [16], like for other renewable energy technologies. A specific feature of RED facilities is the use of IEMs. Manufacturing IEMs introduces high risks of carcinogenic emissions (up to 2.52 kg benzene equivalent per MWh) and ecotoxicity (up to 94 kg 2,4-D equivalent per MWh), due to the anion exchange membrane (AEM) monomer production. A further concern is eutrophication (up to 0.153 kg N equivalent per MWh) due to the use of trimethylamine to aminate the AEMs [17]. The chemistry behind the AEMs production is the most affecting factor in the Life Cycle Assessment (LCA) of a RED plant, underlining the importance of the development of AEMs with lower environmental impact. For example, by using different non-amination synthesis routes for AEM fabrication [18].

Throughout the operation period, in the long term, there might be alterations to marine life. The influent pumping, pre-treatment and effluent discharge were looked at in detail at the Afsluitdijk Blue Energy pilot plant in The Netherlands. Four-year research was conducted to evaluate the surrounding effects of Blue Energy [19]. The use of wedge-wire screens to avoid the suction of large zooplankton, fish and macrofauna at the intake was successful. However, fish larvae and shrimps could still cross this first filtration step. For pre-treatment, the use of rapid sand filtration allowed the return of macrofauna without harm, however, it could cause damage or death to fish larvae and shrimps. The biggest impact detected was on the space needed for the intake, using the wedge-wired screens. No effects were detected on migratory fish behaviour and mussel cultures. The study also indicated that most of the pre-treatment-related negative impacts could be limited by a proper design. The brackish water discharge only changed the salinity closer to the discharge area, without significant impact on the Wadden sea. RED facilities implemented in natural environments will blend in optimally since these are typically locations with an ecosystem accustomed to a certain salinity change.

Another aspect concerning the operation is the IEMs lifetime. Although there are not many studies regarding the lifetime of IEMs, they are estimated to last between 7 to 10 years [20]. This IEM lifetime may depend on many factors, such as current density, solution composition and temperature. It is expected that over the years the membranes will age and will lose some of their initial properties (such as permselectivity) [21]. Consequently, the power output will be reduced and at some point, there is a need for replacing the IEMs. This not only increases membrane usage but also raises the question about the afterlife of the IEMs.

In the literature, the focus is typically on how to improve the membrane properties. However, few words are written about what to do with aged membranes. The possible applications for old IEMs should be evaluated to determine the circularity of IEMs, through production from renewable resources, recycling or reuse in other products [22].

Lastly, during a decommissioning phase, the best case is to repurpose the facility and recycle stack materials. The stress factors will be similar to those in the construction phase in case of demolition of the facility.

The LCA performed by Mueller et al [17] unveils that energy generation through RED is well-positioned compared to other energy sources. In nine categories evaluated (acidification, ecotoxicity, eutrophication, global warming, ozone depletion, photochemical oxidation, carcinogenic, non-carcinogenic and respiratory effects) the best-case scenario for RED (both from seawater/river water or with brines) resulted in lower impact values than onshore wind, rooftop and ground solar energy and natural gas. As an example, the Global Warming Potential of the RED technology was identified to be 14.2 kg CO_2 equivalent per MWh produced, while for onshore wind it was 23.8 kg CO_2 [17]. The other sources mentioned above presented even higher values. For RED, the construction phase is responsible for most of these emissions. Through the sensitivity analysis, the categories of ecotoxicity, eutrophication and carcinogenic effects have room for improvement which mainly relies on the manufacturing of the AEM, as it generates over 50 % of the impact in these categories [17].

6.4. Development agenda

6.4.1. Ion Exchange Membranes

IEMs development can be done on multiple fronts. The previous sections have identified the need to further improve the membrane characteristics, such as electrical resistance and permselectivity and the demand for sustainable membrane materials for production. Nonetheless, two other IEM features should be deliberated in the future. These are profiling of IEMs to increase contact area and decrease pumping losses, and designing IEMs that endure the presence of multivalent ions, to avoid uphill transport and increased electrical resistance.

The fabrication of profiled IEMs is not yet done on a commercial scale, unlike several types of flat sheet IEMs. Profiled membranes can be fabricated in different ways: hot (thermal) pressing (batch process), membrane casting, and 3D printing (photopolymerization). Hot (thermal) pressing is mostly done with heterogeneous membranes [8], and usually, profiling can improve the characteristics of the membranes. Heterogeneous membranes are far from ideal for RED since they have high electrical resistance values [23]. An example of homogeneous membranes is the profiled Nafion membrane reported by Tzanetakis et al [24]. The Nafion membrane was hot pressed under wet conditions to lower the glass transition temperature. Membrane casting is more suitable for homogeneous membranes. The liquid membrane is poured into a mould that will define the profile characteristics. However, this

method can take several hours for solvent evaporation and it may be difficult to release the membranes from the mould, which is problematic for large-scale production.

Using 3D printing is an interesting alternative since it can be carried out at room temperature and solvent free. Moreover, it can be coupled easily with CFD studies as the drawings for printing are the same as for simulations. Still, the profile might lack good resolution and show errors of replication [25]. Typically, the printing is done on top of a flat membrane, which leads to a two-step process, taking more time for production. Towards large-scale production and commercialization, the profiling techniques need to evolve to a single step to make the membrane production process fast enough. Fujifilm produced in pilots some exemplars of profiled homogeneous membranes with overlapped crossed filaments or pillar structures as profile geometry [26]. However, these profiled membranes are not yet available commercially nor the process of making is disclosed.

Further tuning the selectivity of IEMs can provide benefits for RED as in natural waters not only Na^+ and Cl^- ions are present. Multivalent ions (i.e., Mg^{2+}, Ca^{2+} and SO_4^{2-}) increase the electrical resistance of standard IEMs and lead to uphill transport [27]. These two phenomena decrease the gross power density. Therefore, the choice of the IEMs and their selectivity will influence power production. To reduce the influence of multivalent ions at the membrane level two routes are considered.

The first route is the development of multivalent permeable membranes, which allow all counter-ions to be transported across the membranes without increasing the membrane's electrical resistance (i.e., 1.2 $\Omega \cdot cm^2$ for FUJI T1) [28]. At the same time, a lower open circuit voltage might be observed, compared to standard membranes, indicating a lower permselectivity (around 4 % less) [29]. These types of membranes are suitable for reducing the trapping of multivalent ions by increasing their diffusion rate through the membrane. With this purpose, they can easily be implemented in RED [29] or ED processes [30]. So far, multivalent permeable membranes have only been reported in the studies mentioned. Although they deliver higher power densities for RED compared to other membrane types, they are not yet commercialized.

The second route, monovalent selective membranes for RED, presents higher electrical resistances (3.1 $\Omega \cdot cm^2$ for Neosepta Cation Monovalent Selective, CMS [28]) but also higher permselectivity, as well as cation selectivity (i.e., cation selectivity for CMS of Na^+/Mg^{2+} is 34, while values for a standard IEM is around 3 [28]). Given these properties, monovalent selective membranes increase the gross power density compared to a standard IEM in the presence of multivalent ions [29]. This could be a more attractive route since monovalent selective membranes are also used for other technologies, such as batteries and membrane capacitive deionization [31]. For example, it is expected that the separation of Li^+ and Mg^{2+}, for Li-ion batteries for electric vehicles, to be a driver to the development of low-resistance

monovalent cation exchange membranes [32]. Nonetheless, the monovalent selective membrane should be, in the end, adapted to RED [33].

Both multivalent permeable membranes and monovalent selective membranes might lead to similar power densities [28]. However, the comparison should be made not only by considering the power density but also by considering costs, materials used and options to profile.

6.4.2. Energetic trends and Levelized cost of energy

Modern society depends on a vast energy supply to power everything from communications, transportation, medical care and monitoring to everyday chores. In the past 50 years, global energy demand has increased by 156 % [34]. Besides years of global crisis (i.e., 2009, 2020), the electrical power demand constantly grows. This has also consequences for energy prices and energy security since punctual events can create instability and a shortage of energy, which leads to increased energy prices. Figure 6.5 shows the average electrical energy price (in €/kWh, wholesale) in different European countries between 2020 and 2022.

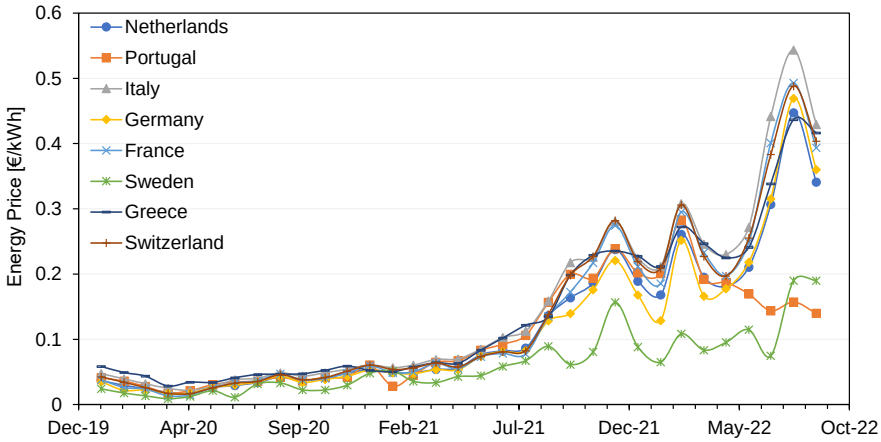

Figure 6.5 Average monthly electrical energy wholesale prices in selected countries in the European Union (EU) from January 2020 to September 2022 [35].

Due to the economic recovery (post-pandemic) in 2021 and the Russian-Ukrainian war started in March 2022, the electrical energy prices, which remained far below 0.1 €/kWh in 2020, abruptly increased achieving a record of 0.54 €/kWh in August 2022 in Italy, with many other countries on the same track. The lack of energy security generated speculation over the electrical energy price affecting most European countries. This opens an opportunity for new renewable energy technologies that struggle to enter the electrical energy market due to a considered high Levelized cost of energy (LCOE). Table 6.3 shows the LCOE of several energy technologies.

Table 6.3. Levelized cost of energy (LCOE) by technology in 2021 [36].

Energy technology	Cost [€ / kWh]
Fossil fuels	0.05 – 0.18
Concentrated solar power	0.11
Offshore wind	0.08
Geothermal	0.07
Bioenergy	0.07
Solar photovoltaic	0.05
Hydropower	0.05
Onshore wind	0.03

The LCOE of RED has been calculated in various studies, resulting in values between 0.3 to 6.8 €/kWh depending on the study conditions [20,37–39]. The two major factors contributing to the very broad interval are the estimated membrane price and the net power density produced. These assessments are also summarized in a review by Chae et al [40]. In a brief estimation, projecting a ten-year payback period, with a RED stack producing 1.5 $W \cdot m^{-2}$ net power density and a membrane price of 10 €/m^2 (total investment of 30.5k €) the LCOE for RED is 0.13 €/kWh. If the membrane price is instead 20 €/m^2 (total investment of 50k €), the LCOE increases to 0.21 €/kWh, or if the net power density delivery is reduced to 1 $W \cdot m^{-2}$ the LCOE also increases to 0.19 €/kWh. Both effects combined would result in an LCOE of 0.30 €/kWh. These calculations indicate that the LCOE of RED is above other renewable energy sources, as shown in Table 6.3, but the LCOE of RED is still below the current electrical energy wholesale prices. More importantly, as RED is not yet a mature technology, there is the opportunity to accomplish lower LCOE prices, as predicted in the literature. Estimations for the future cost price range between 0.02 and 0.17 €/kWh [20,37,41,42].

As discussed in this thesis, a strong argument in favour of RED is the continuous energy output being able to complement intermittent solar and wind power in their downtimes. RED can work as a large-scale, base-load electrical energy generation system by providing electrical power without fluctuations. Such characteristic gets more valued in the electrical energy market, resulting in a high renewable energy certificate (REC) for RED [40]. This means electrical energy providers might be willing to pay more for technologies with the added value of stable electrical power output. If necessary, RED can also work as a dispatchable electrical energy generation source since it is possible to program and control on demand and is available quickly dispatching in a couple of minutes.

6.4.3. Efficient control under dynamic conditions

The electrical power output is dependent on the voltage and current of the stack. Only one single operating point will have the maximum power output. If the resistive load connected to the RED system is fixed but other variables may change (i.e., concentration or

temperature), the maximum power will not be always achieved. This was also seen during the pilot experiments with natural waters described in Chapter 4, where intense rainfall in summer resulted in the dilution of seawater. Using a constant current discharge of the RED stack, as applied by a galvanostatic operation, led to negative stack voltages causing the experiment to stop temporarily. Therefore, the implementation of a smart electrical control to assess performance and assure maximum power is an essential tool for a RED facility.

To operate RED under dynamic conditions, two strategies are proposed. First, the knowledge gained for maximum power output control for photovoltaic cells can be translated to RED. Maximum power point tracking (MPPT) is the process of adjusting the load characteristic as the surrounding conditions change. As mentioned in Chapter 1, the current-voltage (I-V) curve of the RED stack is used to determine the maximum power that can be achieved. This is also how the MPPT technology works, with frequent I-V curve measurements, to determine at which current or voltage the photovoltaic cell, or in our case the RED stack, should operate. Yet, this method has two drawbacks. The first one is that measurement of the I-V curve will cause a short disruption in electrical power production. A solution could be to add a RED test cell, being a very small-scale stack to measure the power variation and provide information to the control of larger RED stacks (when implemented to full scale). A second challenge is that in the case of segmentation or multistage the algorithm would need to be further refined and finding the new optimum could take several minutes of disruption. Developing advanced algorithms that use a model-based control is expected to address this.

A promising approach is foreseen in blending RED models and electrical power output optimizers. RED models have evolved through the years and are predicting more accurately the behaviour of the process. Combining the RED model with a power output optimizer, with the right parameter inputs, such as inlet concentration or conductivity, temperature and flow rates, the model would be able to correctly predict what load (or loads in case of segmented electrodes and/or multistage) to apply such that the maximum power output is retrieved. It is not only valid for simple cases such as a single standard stack but also for more complex operations such as electrode segmentation and multistage when aiming for the overall maximum power output by using “saving gradient” strategies. At the same time, the RED model can detect if there are defects or problems with a given stack. This model-based optimization approach will enable monitoring and optimize the process of electrical energy harvesting with RED without interruptions. Additionally, the suggestion above of having a smaller stack to monitor the conditions as an independent second check is still viable to double-check future model-based electrical power output optimizations.

6.5. Concluding remarks

The Outlook presents the future challenges and key points to improve RED technology for electrical energy generation. The further optimization of IEMs remains the main challenge for RED becoming an economically viable option for renewable electrical energy generation. IEMs need further improvements, from price to lifetime, and from the use of more sustainable materials to even lower electrical resistance, higher permselectivity and less water transport. Efforts to produce better-performing and more sustainable membranes should therefore be the future focus.

During this thesis a validated RED model using NaCl solutions allowed us to evaluate the process configurations (i.e., multistage) and conditions (i.e., flow rate). With further model improvement (i.e., membrane properties varying with temperature or with different ions present like Ca^{2+}, Mg^{2+} and SO_4^{2-}) it can be implemented for monitoring during operation using natural waters. Experiments with scaled-up stacks of 0.22 x 0.22 m^2 demonstrated that the implementation of electrode segments for both increased power density and energy efficiency was successful, whilst the implementation of multistage showed the necessity for reducing further the cross-flow stack's pressure drop. Testing a two-stage cross-flow configuration of 0.22 x 0.22 m^2 with natural waters revealed that the gross power density was not affected by (bio)fouling, but predominantly by multivalent ions. Also, multivalent ions uphill transport was only affecting the first stage. The feasibility of a sustainable carbon-based slurry electrode with carbon black and activated carbon was also demonstrated at the laboratory scale with stacks of 0.10 x 0.10 m^2, reducing voltage losses at the electrodes compared with sodium chloride solutions and preventing chlorine, oxygen and hydrogen evolution.

Lastly, the gained knowledge presented in this thesis contributes to the application of RED in the future, worldwide, either on a large scale, near a river delta, or on small scale, as part of a closed loop in the industry with brines.

References

[1] P. Długołecki, K. Nymeijer, S. Metz, M. Wessling, Current status of ion exchange membranes for power generation from salinity gradients, J Memb Sci. (2008). https://doi.org/10.1016/j.memsci.2008.03.037.

[2] D.A. Vermaas, M. Saakes, K. Nijmeijer, Doubled power density from salinity gradients at reduced intermembrane distance, Environ Sci Technol. (2011). https://doi.org/10.1021/es2012758.

[3] D.A. Vermaas, M. Saakes, K. Nijmeijer, Power generation using profiled membranes in reverse electrodialysis, J Memb Sci. (2011). https://doi.org/10.1016/j.memsci.2011.09.043.

[4] C. Simões, B. Vital, T. Sleutels, M. Saakes, W. Brilman, Scaled-up multistage reverse electrodialysis pilot study with natural waters, Chemical Engineering Journal. 450 (2022) 138412. https://doi.org/10.1016/j.cej.2022.138412.

[5] R.A. Tufa, S. Pawlowski, J. Veerman, K. Bouzek, E. Fontananova, G. di Profio, S. Velizarov, J. Goulão Crespo, K. Nijmeijer, E. Curcio, Progress and prospects in reverse electrodialysis for salinity gradient energy conversion and storage, Appl Energy. 225 (2018) 290–331. https://doi.org/10.1016/j.apenergy.2018.04.111.

[6] C. Jiang, H.# Masem, Y. Li, Y. Wang, T. Xu, Ion Exchange Membranes for Electrodialysis: A Comprehensive Review of Recent Advances, 2014. http://www.astom-corp.jp/en/product/02.html#03.

[7] J. Veerman, R.M. de Jong, M. Saakes, S.J. Metz, G.J. Harmsen, Reverse electrodialysis: Comparison of six commercial membrane pairs on the thermodynamic efficiency and power density, J Memb Sci. (2009). https://doi.org/10.1016/j.memsci.2009.05.047.

[8] S. Pawlowski, J.G. Crespo, S. Velizarov, Profiled ion exchange membranes: A comprehensible review, Int J Mol Sci. 20 (2019) 165. https://doi.org/10.3390/ijms20010165.

[9] P. Długołecki, J. Dabrowska, K. Nijmeijer, M. Wessling, Ion conductive spacers for increased power generation in reverse electrodialysis, J Memb Sci. (2010). https://doi.org/10.1016/j.memsci.2009.10.011.

[10] S. Pawlowski, T. Rijnaarts, M. Saakes, K. Nijmeijer, J.G. Crespo, S. Velizarov, Improved fluid mixing and power density in reverse electrodialysis stacks with chevron-profiled membranes, J Memb Sci. (2017). https://doi.org/10.1016/j.memsci.2017.03.003.

[11] S. Pawlowski, V. Geraldes, J.G. Crespo, S. Velizarov, Computational fluid dynamics (CFD) assisted analysis of profiled membranes performance in reverse electrodialysis, J Memb Sci. 502 (2016) 179–190. https://doi.org/10.1016/j.memsci.2015.11.031.

[12] G.K. Batchelor, An Introduction to Fluid Dynamics, Cambridge University Press, 2000. https://doi.org/10.1017/CBO9780511800955.

[13] D.A. Vermaas, J. Veerman, N.Y. Yip, M. Elimelech, M. Saakes, K. Nijmeijer, High efficiency in energy generation from salinity gradients with reverse electrodialysis, ACS Sustain Chem Eng. (2013). https://doi.org/10.1021/sc400150w.

[14] Z.Y. Guo, Z.Y. Ji, Y.G. Zhang, F.J. Yang, J. Liu, Y.Y. Zhao, J.S. Yuan, Effect of ions (K+, Mg2+, Ca2+ and SO42−) and temperature on energy generation performance of reverse electrodialysis stack, Electrochim Acta. 290 (2018) 282–290. https://doi.org/10.1016/j.electacta.2018.09.015.

[15] J. Veerman, J.W. Post, M. Saakes, S.J. Metz, G.J. Harmsen, Reducing power losses caused by ionic shortcut currents in reverse electrodialysis stacks by a validated model, J Memb Sci. (2008). https://doi.org/10.1016/j.memsci.2007.11.032.

[16] C. Seyfried, H. Palko, L. Dubbs, Potential local environmental impacts of salinity gradient energy: A review, Renewable and Sustainable Energy Reviews. 102 (2019) 111–120. https://doi.org/10.1016/j.rser.2018.12.003.

[17] K.E. Mueller, J.T. Thomas, J.X. Johnson, J.F. DeCarolis, D.F. Call, Life cycle assessment of salinity gradient energy recovery using reverse electrodialysis, J Ind Ecol. 25 (2021) 1194–1206. https://doi.org/10.1111/jiec.13082.

[18] K.F.L. Hagesteijn, S. Jiang, B.P. Ladewig, A review of the synthesis and characterization of anion exchange membranes, J Mater Sci. 53 (2018) 11131–11150. https://doi.org/10.1007/s10853-018-2409-y.

[19] P. Herman, Z. Jager, L. van Walraven, S. Grasman, J. Wijsman, L. van Duren, R. Siebers, Onderzoek Omgevingseffecten Blue Energy - Synthese van vier jaar onderzoek, 2020.

[20] A. Daniilidis, R. Herber, D.A. Vermaas, Upscale potential and financial feasibility of a reverse electrodialysis power plant, Appl Energy. (2014). https://doi.org/10.1016/j.apenergy.2013.12.066.

[21] R. Ghalloussi, W. Garcia-Vasquez, N. Bellakhal, C. Larchet, L. Dammak, P. Huguet, D. Grande, Ageing of ion-exchange membranes used in electrodialysis: Investigation of static parameters, electrolyte permeability and tensile strength, Sep Purif Technol. 80 (2011) 270–275. https://doi.org/10.1016/j.seppur.2011.05.005.

[22] A. Lejarazu-Larrañaga, S. Molina, J.M. Ortiz, R. Navarro, E. García-Calvo, Circular economy in membrane technology: Using end-of-life reverse osmosis modules for preparation of recycled anion exchange membranes and validation in electrodialysis, J Memb Sci. 593 (2020) 117423. https://doi.org/10.1016/j.memsci.2019.117423.

[23] V.I. Zabolotskii, S.A. Loza, M. v. Sharafan, Physicochemical Properties of Profiled Heterogeneous Ion-Exchange Membranes, Russian Journal of Electrochemistry. 41 (2005) 1053–1060. https://doi.org/10.1007/s11175-005-0180-2.

[24] N. Tzanetakis, W.M. Taama, K. Scott, R.J.J. Jachuck, The effect of corrugated membranes on salt splitting, J Appl Electrochem. 33 (2003) 411–417. https://doi.org/10.1023/A:1024428106739.

[25] C. Capparelli, C.R. Fernandez Pulido, R.A. Wiencek, M.A. Hickner, Resistance and Permselectivity of 3D-Printed Micropatterned Anion-Exchange Membranes, ACS Appl Mater Interfaces. 11 (2019) 26298–26306. https://doi.org/10.1021/acsami.8b04177.

[26] L. Gurreri, A. Filingeri, M. Ciofalo, A. Cipollina, M. Tedesco, A. Tamburini, G. Micale, Electrodialysis with asymmetrically profiled membranes: Influence of profiles geometry on desalination performance and limiting current phenomena, Desalination. 506 (2021) 115001. https://doi.org/10.1016/j.desal.2021.115001.

[27] D.A. Vermaas, J. Veerman, M. Saakes, K. Nijmeijer, Influence of multivalent ions on renewable energy generation in reverse electrodialysis, Energy Environ Sci. (2014). https://doi.org/10.1039/c3ee43501f.

[28] T. Rijnaarts, E. Huerta, W. van Baak, K. Nijmeijer, Effect of Divalent Cations on RED Performance and Cation Exchange Membrane Selection to Enhance Power Densities, Environ Sci Technol. (2017) 13028–13035. https://doi.org/10.1021/acs.est.7b03858.

[29] J. Moreno, V. Díez, M. Saakes, K. Nijmeijer, Mitigation of the effects of multivalent ion transport in reverse electrodialysis, J Memb Sci. (2018). https://doi.org/10.1016/j.memsci.2017.12.069.

[30] G. Doornbusch, M. van der Wal, M. Tedesco, J. Post, K. Nijmeijer, Z. Borneman, Multistage electrodialysis for desalination of natural seawater, Desalination. 505 (2021) 114973. https://doi.org/10.1016/j.desal.2021.114973.

[31] T. Luo, S. Abdu, M. Wessling, Selectivity of ion exchange membranes: A review, J Memb Sci. 555 (2018) 429–454. https://doi.org/10.1016/j.memsci.2018.03.051.

[32] W. Shi, X. Liu, C. Ye, X. Cao, C. Gao, J. Shen, Efficient lithium extraction by membrane capacitive deionization incorporated with monovalent selective cation exchange membrane, Sep Purif Technol. 210 (2019) 885–890. https://doi.org/10.1016/j.seppur.2018.09.006.

[33] A.T. Besha, M.T. Tsehaye, D. Aili, W. Zhang, R.A. Tufa, Design of monovalent ion selective membranes for reducing the impacts of multivalent ions in reverse electrodialysis, Membranes (Basel). 10 (2020). https://doi.org/10.3390/membranes10010007.

[34] BP, Statistical Review of World Energy 2022, 2022. https://www.bp.com/en/global/corporate/energy-economics/statistical-review-of-world-energy/downloads.html (accessed September 2, 2022).

[35] Bruna Alves, Monthly electricity prices in selected EU countries 2020-2022, (2022). https://www.statista.com/statistics/1267500/eu-monthly-wholesale-electricity-price-country/ (accessed November 2, 2022).

[36] IRENA, Renewable Power Generation Costs in 2021, Abu Dhabi, 2022. www.irena.org.

[37] F. Giacalone, M. Papapetrou, G. Kosmadakis, A. Tamburini, G. Micale, A. Cipollina, Application of reverse electrodialysis to site-specific types of saline solutions: A techno-economic assessment, Energy. 181 (2019) 532–547. https://doi.org/10.1016/j.energy.2019.05.161.

[38] M. Turek, B. Bandura, Renewable energy by reverse electrodialysis, Desalination. 205 (2007) 67–74. https://doi.org/10.1016/j.desal.2006.04.041.

[39] A.M. Weiner, R.K. McGovern, J.H. Lienhard V., A new reverse electrodialysis design strategy which significantly reduces the levelized cost of electricity, J Memb Sci. 493 (2015) 605–614. https://doi.org/10.1016/j.memsci.2015.05.058.

[40] S. Chae, H. Kim, J. Gi Hong, J. Jang, M. Higa, M. Pishnamazi, J.-Y. Choi, R. Chandula Walgama, C. Bae, I.S. Kim, J.-S. Park, Clean Power Generation from Salinity Gradient using Reverse Electrodialysis Technologies: Recent Advances, Bottlenecks, and Future Direction, Chemical Engineering Journal. (2022) 139482. https://doi.org/10.1016/j.cej.2022.139482.

[41] H. Kim, S.C. Yang, J. Choi, J.O. Kim, N. Jeong, Optimization of the number of cell pairs to design efficient reverse electrodialysis stack, Desalination. 497 (2021). https://doi.org/10.1016/j.desal.2020.114676.

[42] J.W. Post, C.H. Goeting, J. Valk, S. Goinga, J. Veerman, H.V.M. Hamelers, P.J.F.M. Hack, Towards implementation of reverse electrodialysis for power generation from salinity gradients, Desalination Water Treat. 16 (2010) 182–193. https://doi.org/10.5004/dwt.2010.1093.

Acknowledgements | Dankwoord | Agradecimentos

"If everyone is moving forward together, then success takes care of itself." – Henry Ford

The accomplishment presented in this thesis was not a one-person job. Thus, I would like to express my gratitude and acknowledge the ones involved directly or indirectly to this successful outcome. Wim and Michel, my first thank you is for both of you. I appreciate all the guidance and support through these years. I am glad that we could make such a great team!

Wim, we have always a good communication. I enjoyed receiving your "what if…" questions that made rethink some approaches and improve my reasoning. Thank you for triggering me to give a bit more. I appreciated your support regardless the distance between Leeuwarden and Enschede.

Michel, I could always count on you from the quick feedback to any piece of writing or presentation to all the detailed explanations in the laboratory, or the Friday afternoon experiments. You are a fountain of ideas which inspired me to be more curious. Many of our conversations gave me new perspectives in subjects beyond reverse electrodialysis and electrochemistry.

Harm, thank you for all the help with the setup and experiments. Your interest on how the experiments were going and advice on the equipment to use made the life in the laboratory much easier.

Michele, thanks for keeping an eye on me. You are one of the people that made the PhD journey possible for me and, through the years, you give me encouraging but down to earth advices. Zarko, you also made the PhD journey possible from the moment the internship for my master thesis at Wetsus was proposed. I am happy we keep in touch and collaborating through all these years.

Cees, Johannes, and Bert, you are the pillars of Wetsus, and without such a great coordination such a great place would not exist. I am grateful there is. I hope Wetsus continues to be the joyful working place it was for me.

To the Blue Energy theme, it was a pleasure to work within this theme, also bittersweet that the theme came to an end in 2022. For me this means the research part is done, now it is time to put it out there. Thanks to Jordi, Simon, Kristan, Don, Menno, Hendrik and Marcel for the help and input to my research. Special thanks to Joost! The REDnews is a noteworthy journal, and I am glad I could help in some editions. Jan Post, thank you for the words of advice and help. Tom, thanks for the feedback in some writing and help with student supervision. Diego, it was great to have you around for half of the journey and that we could

collaborate so much. Emad, it was nice to have you around in the lab and that we could share many ideas and doubts.

At the UT, I would like to thank my group, Sustainable Process Technology, although I was far away and mostly online, I felt always welcome. A special thanks to Michel and Louis, for carefully scheduling my presentations, and to Yvonne for all the help. Surika, Evelyn and Enas, sharing the group and Wetsus with you gave different discussions and shared feelings.

Pedro, Eliana, Lars, Mario and Nynke, I would like to thank for trusting me to guide you during your thesis and for helping me in this research. I believe the future reserves you all a lot of success!

A particular thank you to the ones behind the scenes, from technical to cooking! Gerben, Catharina, Karin, Gerrit, Rienk, John, Ernst, JJ, Jan, Jan Willem, Lisette, Jelmer, Mieke, Wiebe, Johan, Wim, Nynke, Alexander, Anke, Marnejaeike, Jannie, Roely, you have all contributed for a smooth time at Wetsus. Thank you, Antoine, and Caroline, for all the input at the fouling meetings.

Having a good office environment can be helpful to strive, as well as to getting distracted with nerfguns… Andrew, we met very short in the office, but it was a pleasure to take your place. Gonçalo, meu compatriota, os nossos momentos tugas valeram ouro. Thomas, you can make everything a sort of game or competition, but I might say these were fun challenges. Shuyana, from sharing the office to sharing the defence day, I am happy that we agreed to finish together, I do miss our office talks! Ruizhe, we got closer through the years in the office, thank you for taking care of my plant. Victor, it was great to have you in the office always so cheerful. Daniele, I was very happy you came to the office, so I stopped being the newest, plus in a related topic! I enjoyed our discussions and that we could understand each other struggles. Wiecher and Swarupa we did not have much time together in the office, but it was always a nice atmosphere there. To the most recent office mates, Lester, Shih-Hsuan and Berke you made me feel a senior PhD, but it was about time, good luck with the rest of your research. Besides the office, a lot of time was spent on the laboratory, so I would like to thank my setup neighbours for the good times there, Antony and Slawek.

A couple activities at Wetsus brought me close with many people. Like the PV 2019, Jan de Groot, Gerben, Catharina, Qingdian, Mariana, Chris, Xiaoxia, Carlo, Alicia, and Nelleke, we were the best PV! Gerben en Catharina, wat gezellige conversaties we in de keuken hadden. It was also a pleasure to be part of the Wetsuits, and I enjoyed to sometimes engage in the cycling activities (Cycling with Hakan is fun! Cycling with Roel is cool! Cycling with Gijs is nice! Cycling with João is lauw!) and with all the other patient cyclists, Philipp, Sam, Qingdian, Ruizhe, Antony, Wokke, Caspar, Jolanda, Shih-Hsuan, Angel, and Sanne. Thank you for being patient with my slowness. Also, without any related activity but thank you for the good times, Paulina,

Vanessa, Ruben (also for teaching how to use the rheometer!), Klaudia, Sebastian, Edward, Rose, Yang, Rita, Hector, Marta and Rodrigo.

Good friendships came as result of this thesis. Mariana, que nunca nos falte comida e a amizade uma da outra, sempre presente mesmo quando viajavas. Emanuel, obrigada por estares sempre pronto para uma pausa e gostava que não estivesses tão longe. Raquel, que continuemos a partilhar os milestones da vida. João, para mim és o exemplo do equílibrio em pessoa e a tua determinação é algo que admiro. Sara, estás sempre pronta para tudo, para quando a próxima alheira? Wokke, nothing like a good walkie-talkie to cheer up (en lekker eten!). Marianne, I get enthusiastic with your enthusiasm about things. Qingdian, it is always good to go to you and talk like we talked yesterday, even though most times is not the case. Riky you are a funny guy, keep the jokes coming! Francisca, I am happy that we meet, even though it was in the weirdest house ever!

Estar noutro país deixa sempre saudade, Cláudia, Nuno, Chico, Nelson, Xana, Bruno, Inês, obrigada por fazerem voltar a casa sentir que nunca me fui embora ou por fazerem os Países Baixos serem mais portugueses.

Aos meus paranymphs, um obrigado especial pelo apoio nesta fase final. Kostadin, já não dá para contar os anos pelos dedos, obrigada por estares sempre disponível para me receber e por teres aceite este desafio. Bárbara, estamos juntas do início ao fim desta história que é o PhD, obrigada por estares sempre lá e ainda bem que nos tivemos uma à outra para celebrar vitórias e partilhar frustações.

Aan mijn Nederlandse familie, Mieke, Jan, Bart, Fleur, en Claire, bedankt dat jullie me zo snel deel van de familie hebben laten voelen.

Querida família, obrigada por todo o apoio, que vem desde que eu nasci. Se estou onde estou hoje, vocês são responsáveis por grande parte disso! Mãe, pai, avó Fernanda, Miguel e Raquel, obrigada! Não é fácil estar longe, mas a distância só é grande se a fizermos grande. Obrigada, e muitas saudades, avô Ferdi e avó Maria.

Dori e Darwin, muita gente não vai perceber, mas não há abraço mais terapêutico que os vossos!

Gijs, er zijn niet genoeg woorden om je steun en liefde te beschrijven. Jij bent mijn veilige thuis. Dat we ons leven blijven delen en ik kijk uit naar vele jaren gelukkig samen.

About the Author

Catarina Simões, born in 28th of April 1995, in Almada, Portugal. In 2013, she began her studies with a combined Bachelor's & Master's in Chemical and Biochemical Engineering at the Science and Technology Faculty of NOVA University Lisbon, Portugal. In 2018, she graduated after defending her Master's thesis in "Bipolar Membrane Based Energy Storage System: The Acid-Base Flow Battery", work performed at Wetsus, European Centre of Excellence for Sustainable Water Technology, in Leeuwarden, The Netherlands. In the same year, with a growing interest in electrochemistry, she started her PhD research on "Reverse electrodialysis for renewable energy generation" at Wetsus, in collaboration with the Sustainable Process Technology group from the University of Twente, The Netherlands. During her PhD research, in 2019, she was awarded the Best Poster at the NPS16 symposium, The Netherlands.

List of Publications

Simões, C.*, Pintossi, D.*, Saakes, M., Borneman, Z., Brilman, W., & Nijmeijer, K. (2020). Electrode segmentation in reverse electrodialysis: Improved power and energy efficiency. Desalination, 492, 114604. https://doi.org/10.1016/j.desal.2020.114604

Simões, C., Pintossi, D., Saakes, M., & Brilman, W. (2021). Optimizing multistage reverse electrodialysis for enhanced energy recovery from river water and seawater: Experimental and modeling investigation. Advances in Applied Energy, 2, 100023. https://doi.org/10.1016/j.adapen.2021.100023

Pintossi, D., Simões, C., Saakes, M., Borneman, Z., & Nijmeijer, K. (2021). Predicting reverse electrodialysis performance in the presence of divalent ions for renewable energy generation. Energy Conversion and Management, 243 (March). https://doi.org/10.1016/j.enconman.2021.114369

Simões, C., Vital, B., Sleutels, T., Saakes, M., & Brilman, W. (2022). Scaled-up multistage reverse electrodialysis pilot study with natural waters. Chemical Engineering Journal, 450, 138412. https://doi.org/10.1016/j.cej.2022.138412

Simões, C., Saakes, M., & Brilman, D. (2023). Toward Redox-Free Reverse Electrodialysis with Carbon-Based Slurry Electrodes. Industrial & Engineering Chemistry Research, 62(3), 1665–1675. https://doi.org/10.1021/acs.iecr.2c03567

Conferences and symposiums

(Poster) Netherlands Process technology Symposium 16, Eindhoven, Netherlands (October 2019) Awarded Best Poster

(Poster) 17th Poster Day: Membrane Technology, Essen, Germany (February 2020)

(Presentation) International Congress on Membranes & Membrane Processes, online (December 2020)

(Presentation/Poster/Organization) 13th European Symposium of Electrochemical Engineering, online (June 2021)

(Poster) Wetsus Congress, Leeuwarden, Netherlands (September 2021)

(Presentation) Wetsus Internal Congress, Leeuwarden, Netherlands (November 2021)

(Presentation) Desalination for the Environment (EDS), Las Palmas, Spain (June 2022)

(Presentation) 13th Conference of the Aseanian Membrane Society, Singapore (July 2022)

This research has been carried out in the Sustainable Process Technology group at the University of Twente, The Netherlands. This work was performed in the cooperation framework of Wetsus, European Centre of Excellence for Sustainable Water Technology (www.wetsus.nl). Wetsus is co-funded by the Dutch Ministry of Economic Affairs and Ministry of Infrastructure and Environment, the European Union Regional Development Fund, the Province of Fryslân and the Northern Netherlands Provinces. This work is part of a project that has received funding from the European Union's Horizon 2020 research and innovation programme under the Marie Skłodowska-Curie grant agreement No 665874.

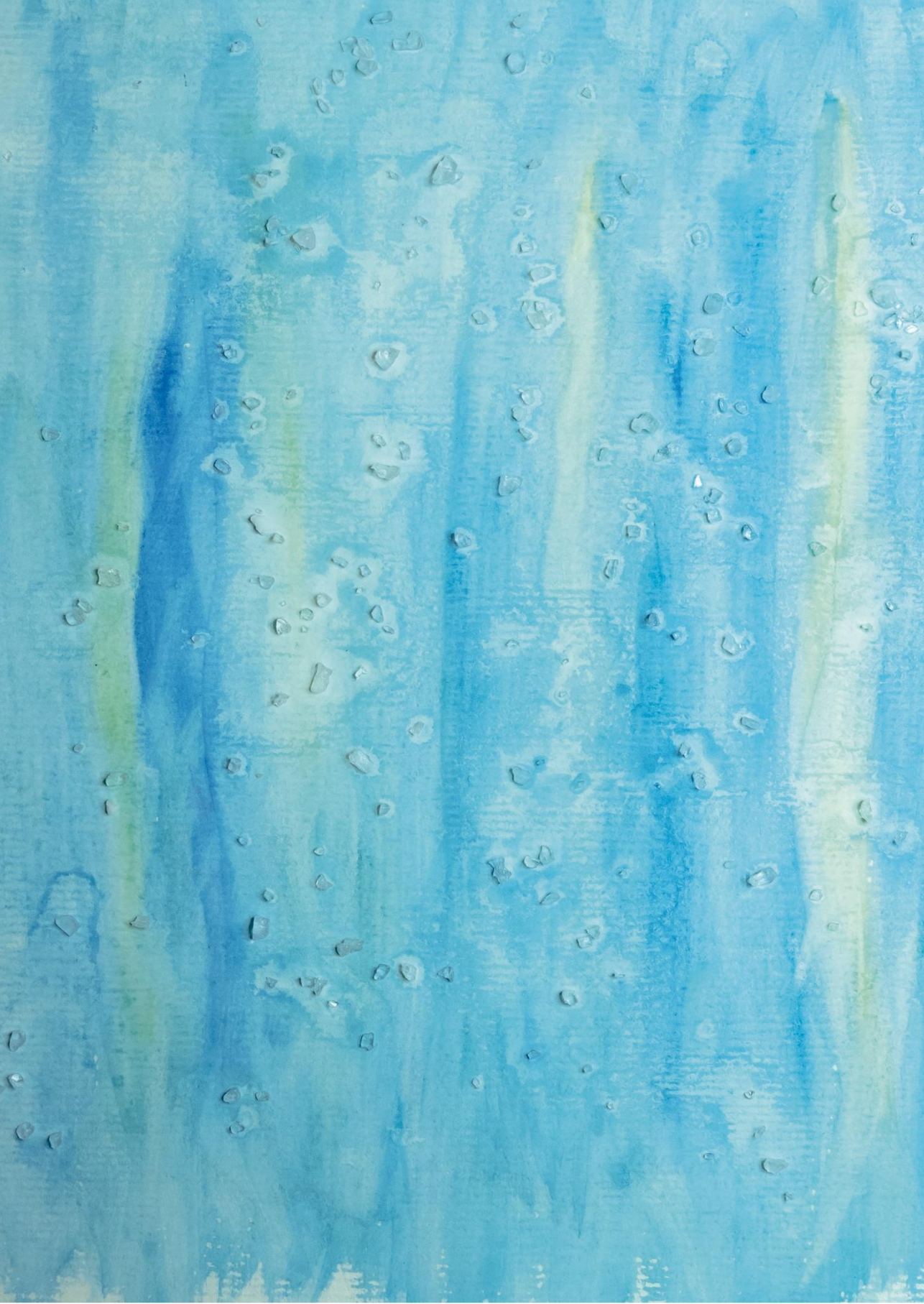

Propositions

accompanying the PhD thesis "*Advances in Reverse Electrodialysis for Renewable Energy Generation*"

to be defended on the 10th of March 2023 at 14:45 hrs

by Catarina Cerqueira da Silva Simões

1. "Saving the gradient" by electrode segmentation or multistaging lowers potential losses in a reverse electrodialysis stack. (This dissertation)

2. Testing reverse electrodialysis with natural waters results in pragmatic approaches. (This dissertation)

3. Implementing carbon slurries to replace potentially harmful solutions at the electrode compartments makes reverse electrodialysis safer. (This dissertation)

4. Having the right research tools but not knowing how to fully use them is a missed opportunity.

5. Promoting renewable energy systems without assessing their impact on ecosystems is greenwashing.

6. Defining the meaning of the word "chemical" is not straightforward leading to irrational fears about chemistry.

7. Publishing fees in scientific publications should be avoided since money is not a standard for good research.

8. Multidisciplinary working environments allow collaborations to naturally occur.

9. The human being is rather adaptable to situations with a great tendency to return to old habits.

10. Aiming for a local food diet is better for sustainability than a plant-based diet.